Matthias Bleckmann

Itinerant to localized views on *f*-electron systems: A multiprobe study

Cuvillier Verlag Göttingen
Internationaler wissenschaftlicher Fachverlag

Itinerant to localized views on f-electron systems: A multiprobe study

Von der Fakultät für
Elektrotechnik, Informationstechnik, Physik
der Technischen Universität Carolo-Wilhelmina
zu Braunschweig

zur Erlangung des Grades eines
Doktors der Naturwissenschaften
(Dr. rer. nat.)

genehmigte

Dissertation

von

Matthias Bleckmann

aus Herford

Bibliografische Information der Deutschen Nationalbibliothek
Die Deutsche Nationalbibliothek verzeichnet diese Publikation in der Deutschen Nationalbibliografie; detaillierte bibliografische Daten sind im Internet über http://dnb.ddb.de abrufbar.
1. Aufl. - Göttingen : Cuvillier, 2009
Zugl.: (TU) Braunschweig, Univ., Diss., 2009

978-3-86727-952-9

1. Referent: Prof. Dr. Stefan Süllow
2. Referent: Prof. Dr. Andreas Eichler

eingereicht am: 16. Januar 2009

mündliche Prüfung (Disputation) am: 3. April 2009

Nonnenstieg 8, 37075 Göttingen
Telefon: 0551-54724-0
Telefax: 0551-54724-21
www.cuvillier.de

1. Auflage, 2009
Gedruckt auf säurefreiem Papier

978-3-86727-952-9

Vorabveröffentlichungen der Dissertation

Teilergebnisse aus dieser Arbeit wurden mit Genehmigung der Fakultät für Elektrotechnik, Informationstechnik, Physik, vertreten durch den Betreuer der Arbeit, in folgenden Beiträgen veröffentlicht:

Publikationen:

- M. Bleckmann, O. Prokhnenko, K. Gofryk, D. Kaczorowski, and S. Süllow: *Structural properties of the heavy fermion antiferromagnet* UPd_2Sb, J. Magn. Magn. Mat., **316** (2007) e435.

- M. Bleckmann, A. Buchsteiner, N. Stüßer, K. Gofryk, D. Kaczorowski, and S. Süllow: *Antiferromagnetic structure of* UPd_2Sb, Physica B, in print.

Tagungsbeiträge:

- Joint European Magnetic Symposia (JEMS) 2006 in San Sebastian, Spanien: *Structural properties of the heavy fermion antiferromagnet* UPd_2Sb (Poster).

- Frühjahrstagung der Deutschen Physikalischen Gesellschaft 2007 in Regensburg: *Structural properties of* PrB_6 (Poster).

- Magnetic Fields for Science 2007 in Cargese, Frankreich: *The effect of disorder in the heavy fermion compound* UPt_2Si_2(Vortrag).

- International Conference on Strongly Correlated Electron Systems (SCES) 2008 in Buzios, Brasilien: *Antiferromagnetic structure of* UPd_2Sb (Poster).

Contents

List of Figures

1 Introduction

Nowadays, many modern materials, such as high-temperature superconductors, geometrically frustrated oxides and low-dimensional magnets, are discussed in terms of strong correlations in complex systems. Common to these materials is that their unique properties arise from many-body effects. In particular, in this field strongly correlated electron materials represent one of the major topics. Here, to obtain more insight in this - on behalf of theory - still poorly understood research area, model systems are needed in order to advance our knowledge on correlated electron materials in particular and correlation physics in general. In this situation, the physics of heavy fermion systems, as archetypical strongly correlated electron systems, is one key to better understand such behavior.

As a result of electronic correlations, heavy fermion systems display a wide range of exotic features, such as

- quantum phase transitions and non-Fermi liquid behavior, *e.g.* in $CeCu_{5.9}Au_{0.1}$ [1–5];
- unconventional superconductivity, *e.g.* in UPt_3 [6];
- "hidden order" phases, as observed in URu_2Si_2 [7].

Inherent to heavy fermions is the vicinity to a magnetic instability as a result of the hybridization J between conduction and localized f electrons. The physical ground state properties of heavy fermions as function of the strength of hybridization is schematically summarized in the so-called Doniach phase diagram. With decreasing hybridization these materials transform from an intermediate valence state for large J values into a stable f-shell system, and in between crossing the Kondo regime. In the Kondo regime, the hybridization between conduction and f-electrons is the source for strong correlations between the electrons. As long as no magnetic order occurs, this behavior can be described in terms of Fermi liquid behavior.

Upon further reduction of the hybridization, at a critical hybridization value J_c magnetic order sets in. At J_c the physics of heavy fermion systems is determined by quantum fluctuations, hence the name quantum critical point (QCP). At the QCP exceptional physical properties are observed, such as non-Fermi liquid behavior with a resistivity deviating from Fermi liquid behavior. Experimentally, in most cases magnetically ordered heavy fermion system can be tuned by external control parameters such as pressure or magnetic fields through such a quantum critical point.

On the low hybridization side of the Doniach phase diagram are systems with localized f-electrons. These f-electrons can potentially order, resulting in magnetically ordered structures composed of dipolar moments. Further, higher multipole moments, in particular quadrupolar moments, can also exhibit ordered structures and control the physical ground state properties.

One of the main open topics concerning heavy fermions is the interplay between crystallographic disorder and the correlated electron state. Enhanced disorder effects are arising from correlations between the charge carriers. Furthermore, non-Fermi liquid behavior is predicted and observed for moderately structural disordered systems in the vicinity of a quantum critical point.

In contrast, for strongly localized or completely delocalized systems pronounced disorder effects are not expected. An investigation of the effect of disorder on the degree of itinerancy appears to be of interest. Therefore, in this thesis materials with a varying level of itinerancy are investigated with respect to the physical ground state properties. In particular, materials studied here are ranging from Ce intermetallics like $CePt_3B$, U heavy fermion systems such as UPd_2Sb, and UPd_2Sn, or systems previously considered to be strongly localized, *viz*., UPt_2Si_2 and UPd_3. Finally, a truly localized f-electron material, PrB_6, is studied regarding its properties.

The outline of this thesis is as follows:

In **Chapter 2** a brief introduction in the theory of heavy fermion systems is provided. The competition between magnetic RKKY interaction and Kondo interaction is summarized in the Doniach phase diagram. The properties of the Fermi liquid model are summarized and concepts accounting for non-Fermi liquid behavior are pointed out. Finally, a brief introduction into quadrupolar ordering will be provided.

In **Chapter 3** the experimental methods used in this thesis are described and illustrated using measurements on the alloying series $\mathrm{CePt_3B_{1-x}Si_x}$. Bulk property studies from previous works, in particular susceptibility, specific heat and electronic transport, on $\mathrm{CePt_3B}$ reveal a first transition into an antiferromagnetic and secondly at lower temperatures into a weak ferromagnetic phase. In addition, here the bulk properties of the alloyed samples $\mathrm{CePt_3B_{0.8}Si_{0.2}}$ and $\mathrm{CePt_3B_{0.6}Si_{0.4}}$ have been investigated. Using these measurements the phase diagram of $\mathrm{CePt_3B_{1-x}Si_x}$ has been generated. In order to verify the scenario deduced from the bulk property study and to determine the magnetic structure neutron scattering experiments on $\mathrm{CePt_3B}$ have been carried out. Surprisingly, in our neutron scattering experiments no evidence of neither antiferromagnetic nor ferromagnetic order has been found. Subsequently, μSR measurements have been carried out to successfully prove the existence of bulk magnetism in $\mathrm{CePt_3B}$. In addition, at the end of Chapter 3 an introduction into resonant x-ray scattering is given to provide the basis for the experiments presented on $\mathrm{PrB_6}$.

In **Chapter 4** two closely related material classes are investigated, namely $\mathrm{UPd_2Sb}$ and $\mathrm{UPd_{2-x}Sn}$. First, a review of the properties of the Heusler compounds $\mathrm{UT_2M}$ (T: d electron element, M heavier element such as In, Sn Sb or Pb) investigated so far is presented. In the following, the heavy fermion system $\mathrm{UPd_2Sb}$ is investigated by means of neutron scattering experiments. From these data, it is shown that unconventional semi-conductor like behavior of the resistivity can be accounted for by structurally disordered regions in the sample. The antiferromagnetic structure has been determined and the neutron scattering experiments reveal an interplay of structural disorder and magnetism. The influence of structural disorder on the Fermi liquid properties has been investigated on a series of compounds $\mathrm{UPd_{2-x}Sn}$, with different stoichiometric composition ($x = 0$, 0.02 and 0.04) and different heat treatments. Using these experimental results the predictions on disorder induced non-Fermi liquid behavior in the vicinity of a quantum critical point and the influence of structural disorder on the Hall effect have been investigated.

Chapter 5 is dedicated to the moderately mass enhanced compound $\mathrm{UPt_2Si_2}$. Previously, $\mathrm{UPt_2Si_2}$ has been discussed as a local moment antiferromagnet, which ought to be describable by a crystal electric field level scheme. In our reinvestigation of the low temperature electronic transport properties strong evidence has been found, that $\mathrm{UPt_2Si_2}$ is better understood in terms of an itinerant system rather than a localized one. This evidence of delocalized f-electron behavior has been supported by susceptibility and resistivity measurements in high magnetic fields. Furthermore, a new phase diagram, based on high magnetic field magnetization and resistivity measurements, has been generated and new field induced phases have been observed. Altogether, these findings imply that $\mathrm{UPt_2Si_2}$ has to be discussed as a delocalized f-electron system with the unusual physical properties arising from Fermi surface effects.

Chapter 6 discusses the influence of Pt doping on the properties of antiferroquadrupolar ordered intermetallic $\mathrm{UPd_3}$. The phase diagram of $\mathrm{U(Pd_{1-x}Pt_x)_3}$ has been generated by means of specific heat, electronic transport and susceptibility measurements. We show that $\mathrm{UPd_3}$ is very sensitive to Pt doping, *i.e.*, a very small amount of Pt in $\mathrm{UPd_3}$ destroys the quadrupolar ordered phases. Moreover, the magnetic phase diagram of $\mathrm{U(Pd_{1-x}Pt_x)_3}$, $x = 0.005$, has been obtained by means of susceptibility and resistivity measurements in different applied magnetic fields. Furthermore, a newly observed splitting in the susceptibility between zero-field cooled and field cooled measurements with the magnetic field applied along the crystallographic c-axis is detected, which possibly is associated to a quadrupolar and magnetic transition.

In **Chapter 7** the results of a detailed study of the rare earth hexaboride $\mathrm{PrB_6}$ by means of resonant x-ray scattering is presented. $\mathrm{PrB_6}$ undergoes two phase transitions, the first one from a paramagnetic into an incommensurate, antiferromagnetically ordered phase and at lower temperatures a second one into a commensurate antiferromagnetic phase. In this study, structural Bragg peaks are investigated for all three phases and evidence of a lattice distortion in the commensurate phase has been provided. Furthermore, detailed investigations on magnetic and charge Bragg peaks have been carried out. The Bragg peaks associated with charge ordering have been examined in all three phases. In addition, the type of magnetic ordering in the commensurate and incommensurate phase has been determined.

2 Fundamentals of heavy fermion systems

2.1 Heavy fermion systems

Heavy fermion systems represent an archetypical class of strongly correlated electron systems. Most of the heavy fermion systems contain materials with partly filled $4f$- or $5f$-shells like Ce, Yb, U, and Np. Well-known and extensively investigated examples are $\mathrm{CeAl_3}$, $\mathrm{CeCu_2Si_2}$, $\mathrm{UPt_3}$ or $\mathrm{CeCu_6}$ [8–11].

For a characterization of the essential properties of these materials it is useful to distinguish between two temperature regimes with a qualitatively different behavior of the electron system. The transition between these two regimes is not sharp, therefore a temperature T_{co} is introduced as a measure for the crossover between the two regimes.

Above T_{co} the electrons behave like a weakly interacting ensemble of local f-moments and conduction electrons. In contrast, in the low temperature regime the electrons behave like a collection of electrons with strongly enhanced effective mass, the heavy fermion quasiparticles, that scatter one another. For $T < T_{\mathrm{co}}$, such behavior results from the hybridization between the local f-electrons and the delocalized conduction electrons. The strength of this hybridization is given via Fermi's golden rule

$$\Gamma = \pi V^2 N(E_{\mathrm{F}}), \tag{2.1}$$

with $N(E_{\mathrm{F}})$ representing the density of states at the Fermi Energy E_{F}, and V as an average of the hybridization matrix element.

Regarding the hybridization strength Γ three regimes can be distinguished:

- $\Gamma \ll E_0 \rightarrow$ stable $4f$-shell,
- $\Gamma < E_0 \rightarrow$ Kondo regime,
- $\Gamma \geq E_0 \rightarrow$ intermediate valence regime,

where E_0 is the binding energy of an unperturbed f^n state. In the first case, the hybridization is relatively small, and therefore the mixing of localized and delocalized states can be neglected. The magnetic properties can be described using a Heisenberg exchange, taking into account the f-level crystal field splitting induced by the local f-ion symmetry. With a residual magnetic exchange, as a consequence very often long range antiferromagnetic ordering is observed for materials residing in this parameter range.

In the Kondo regime $\Gamma < E_0$, in comparison to the intermediate valence regime $\Gamma \geq E_0$, a stable f-state is present. Hence, only small deviations from an integer valence state of the f-ion can be found. In this range, hybridization between localized and delocalized electrons controls the behavior of the materials. Then, at temperatures below T_{co}, an extremely enhanced Pauli susceptibility appears because of the large effective electron mass, in contrast to the Curie-Weiss behavior occurring for temperatures higher than T_{co}.

In the last case, the intermediate valence regime, a strong mixing of f-electrons and conduction electrons is present. Therefore, the f-states are unstable, with a non-integer valency, resulting in a non-magnetic ground state. Still, in contrast to ordinary metals a typically one order of magnitude enhanced Pauli susceptibility is observed as a result of electronic hybridization.

The label "Kondo" for the second regime derives from the so-called Kondo effect [12]. Originally, it describes a situation in which dilute magnetic moments, embedded in a metallic host matrix, are screened by the conduction electrons of the surrounding matrix below a certain temperature T_{K}. Hence, a non-magnetic singlet ground state, with the singlet consisting of the local moment spin and the oppositely aligned spins of the conduction electron screening cloud, is formed. The tell-tale mark of this kind of singlet formation is an increase of the resistivity at temperatures somewhat below T_{K} with $\rho \propto \ln(T/T_{\mathrm{K}})$ for decreasing temperature, and a resistive saturation at lowest temperatures with $\rho \propto (1 - (T/T_{\mathrm{K}})^2)$ [13].

An equivalent situation is believed to exist in heavy fermions for $\Gamma < E_0$, *i.e.*, in the Kondo regime. In these systems the f-electron atoms reside on a regular sublattice of the crystal structure, hence the label "Kondo lattice". With the hybridization Γ the conduction electrons are coupled to the f-electrons, leading to screening processes analogous to the single ion Kondo effect.

For high temperatures ($T > T_{\mathrm{K}}$) the physical properties of such systems are those of ordinary f-electron local moment systems. Below T_{K}, screening processes develop, yielding a behavior which initially resembles that of the single ion Kondo effect, with for instance a strongly enhanced Pauli susceptibility. Only, as temperature is further lowered, stark deviations from the single impurity Kondo model appear due to phase correlations between the different Kondo scattering centers. With the periodicity of the f electron sublattice the Kondo singlets can form a Bloch wave state, resulting in a decreasing resistivity with decreasing temperature, in contrast to the single impurity model. This low temperature coherent state is well described by Fermi liquid theory.

Further, in contrast to dilute Kondo systems, in a Kondo lattice the interactions between the magnetic moments can no longer be neglected. For f electron systems these interactions are of the Ruderman-Kasuya-Kittel-Yosida (RKKY) type. Within the so-called "Doniach model" [14] the energy scale related to this coupling strength, which promotes long-range magnetic order, is given by

$$k_{\mathrm{B}}T_{\mathrm{RKKY}} \propto |\Gamma N(E_{\mathrm{F}})|^2, \tag{2.2}$$

with k_{B} - Boltzmann factor, T_{RKKY} - temperature characterizing RKKY-exchange strength, E_{F} - Fermi energy, $N(E_{\mathrm{F}})$ - density of states at the Fermi level and Γ - hybridization between conduction and localized electrons.

On the other hand, the Kondo interaction, which tends to suppress magnetic order, has to be taken into account, and for which the corresponding energy scale evolves like

$$k_{\mathrm{B}}T_{\mathrm{K}} \propto \exp\frac{-1}{|\Gamma N(E_{\mathrm{F}})|}, \tag{2.3}$$

with T_{K} - temperature characterizing Kondo coupling.

As a result, there are two competing energy scales, one promoting magnetic order, the other suppressing it. The combined behavior is schematically summarized in the "Doniach phase diagram" (Fig. 2.1) (originally derived within molecular field approximation of the periodic Anderson model for a one dimensional system of $S = 1/2$ spins). As a consequence of the competition there is a critical hybridization value Γ_c, which separates a spin compensated state of strong hybridization with $|\Gamma N(E_{\mathrm{F}})| > |\Gamma_{\mathrm{c}} N(E_{\mathrm{F}})|$ from a weakly hybridized state with magnetic order for $|\Gamma N(E_{\mathrm{F}})| < |\Gamma_{\mathrm{c}} N(E_{\mathrm{F}})|$. Heavy fermions are located close to the magnetic instability at Γ_c, where the competition between the Kondo and the RKKY interaction is strongest.

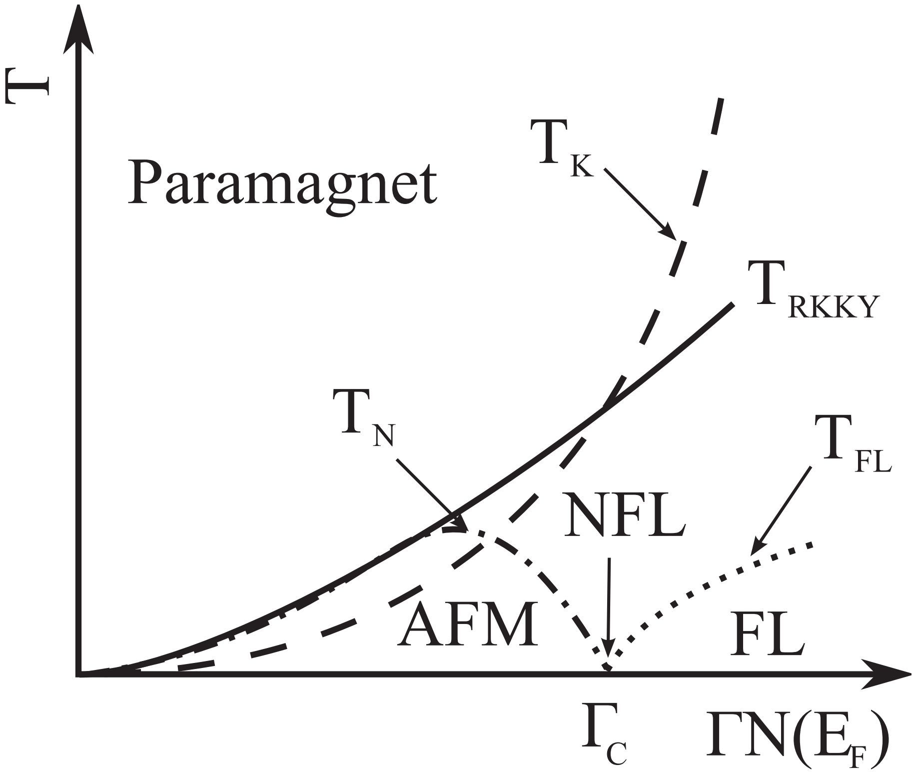

Figure 2.1: The Doniach phase diagram of the one-dimensional Kondo-lattice [15]; for details see text.

2.2 Fermi liquid and non-Fermi liquid theory

In contrast to most common metals where the conduction electrons are considered as independent and non-interacting particles, in strongly correlated electron systems the electron-electron interaction cannot be neglected. In order to deal with this issue, with the Fermi liquid theory the concept of fermionic quasiparticles is introduced. According to energy and momentum conservation and Pauli exclusion principle low energy excitations (*e.g.*, an additional electron at a wave vector $\boldsymbol{k}$ with $|\boldsymbol{k}| = k > k_\mathrm{F}$ and $k - k_\mathrm{F} \ll k_\mathrm{F}$, where k_F is the Fermi wave vector) of the Fermi sea are very stable with a lifetime of $\tau_k \approx (k - k_\mathrm{F})^2$. Furthermore, there is a one-to-one mapping of the low energy eigenstates of these quasiparticles to the eigenstates of a system of non-interacting electrons. The total energy of a system of weakly excited quasiparticle states with respect to the various occupation numbers of states (with momentum $\boldsymbol{k}$ and spin projection $\sigma = \pm$) is given by

$$E = E_{\mathrm{G}} + \sum_{\boldsymbol{k},\sigma} \epsilon(\boldsymbol{k})\delta n_{\boldsymbol{k},\sigma} + \sum_{\boldsymbol{k},\sigma;\boldsymbol{k'},\sigma'} f(\boldsymbol{k},\sigma;\boldsymbol{k'},\sigma')\delta n_{\boldsymbol{k},\sigma}\delta n_{\boldsymbol{k'},\sigma'}, \tag{2.4}$$

with E_{G} - ground state energy. $\epsilon(\boldsymbol{k}) \approx v_{\mathrm{F}}(k - k_{\mathrm{F}})$ is the quasiparticle dispersion, which is parameterized by $v_{\mathrm{F}} = k_{\mathrm{F}}/m^*$, where m^* is the effective mass of the quasiparticle. The last term in Eq. 2.4 incorporates the self-interaction among the quasiparticles.

For many heavy fermion systems it has been demonstrated that their properties can be understood within the Fermi liquid theory, with an effective mass m^* which is 2 to 3 orders of magnitude larger than the free electron mass (hence the name “heavy fermions”). However, while the Fermi liquid theory has successfully been applied in the context of heavy fermion physics, in recent years many compounds out of this class of materials have been found which show deviations from Fermi liquid behavior in their basic physical properties, and therefore have attracted a lot of interest. These systems have been labeled non-Fermi liquid systems (commonly abbreviated as NFL systems). Currently, there are various models to account for non-Fermi liquid behavior in f electrons systems, of which the most important ones will be briefly summarized:

- Multichannel Kondo effect: The f electrons are overscreened with more than one conduction electron per f electron site stemming from different conduction bands or channels. The overcompensation gives rise to non-Fermi liquid behavior [16, 17].
- The disordered Kondo model scenario: Because of structural disorder, different f electrons in a system have different Kondo temperatures, resulting in a distribution of Kondo temperatures in this system, this way leading to non-Fermi liquid anomalies in various physical properties [18].
- Griffiths phase model: Similarly, in the Griffiths phase model - as a result of crystallographic disorder - magnetic cluster of different sizes appear in the paramagnetic phase in the proximity to a quantum critical point

(QCP). Magnetic fluctuations associated to these clusters yield non-Fermi liquid behavior [19, 20].

- Vicinity of a quantum critical point: In the vicinity of a QCP the physical properties are determined by excitations generated by quantum fluctuations rather than single fermion excitations, yielding a non-Fermi liquid behavior [21, 22]. In this context, in recent years two different scenarios of the relevant processes have been developed.

  In the first scenario, the spin density wave scenario, the Kondo temperature T_{K} stays finite for all values of an external parameter controlling the ground state. Hence, the local moments are quenched at finite temperatures. The physics close to the QCP is determined by quantum spin fluctuations. In the spin density wave scenario only for a few quasiparticles along "hot lines", which are connected by the ordering vector of the antiferromagnetism $\boldsymbol{Q}$, the inelastic scattering is strong, whereas in the remaining "cold regions" it is weak [23].

  In the second scenario, the local breakdown of the Fermi liquid, the competition between the Kondo effect and the antiferromagnetism leads to a breakdown of the Kondo effect, yielding a suppression of an effective Kondo temperature to $T = 0$. This causes a local destruction of the Fermi liquid at the quantum phase transition, and results in strong scattering over the whole Fermi surface [24].

  Both, the phase diagrams for the spin density wave and local breakdown of the Fermi liquid scenarios are qualitatively depicted in Fig. 2.2 (a) and (b), respectively. $\mathrm{CeCu}_{6-x}\mathrm{Au}_x$ and $\mathrm{YbRh_2Si_2}$ are discussed as materials which display a local breakdown of the Fermi liquid [25, 26], the spin density wave scenario is used to explain the observations in $\mathrm{CePd_2Si_2}$, $\mathrm{CeNi_2Ge_2}$, and $\mathrm{CeIn_3}$ [23, 27–29].

2.3 Quadrupolar ordering

Aside from the Kondo physics at $\Gamma < E_0$, also very stable f electron shells in the limit $\Gamma \ll E_0$ may lead to interesting and exotic phenomena and ground state properties. Especially, in localized f electron systems the ordering cannot only be of dipolar nature (*i.e.*, magnetic), but also higher order multipole

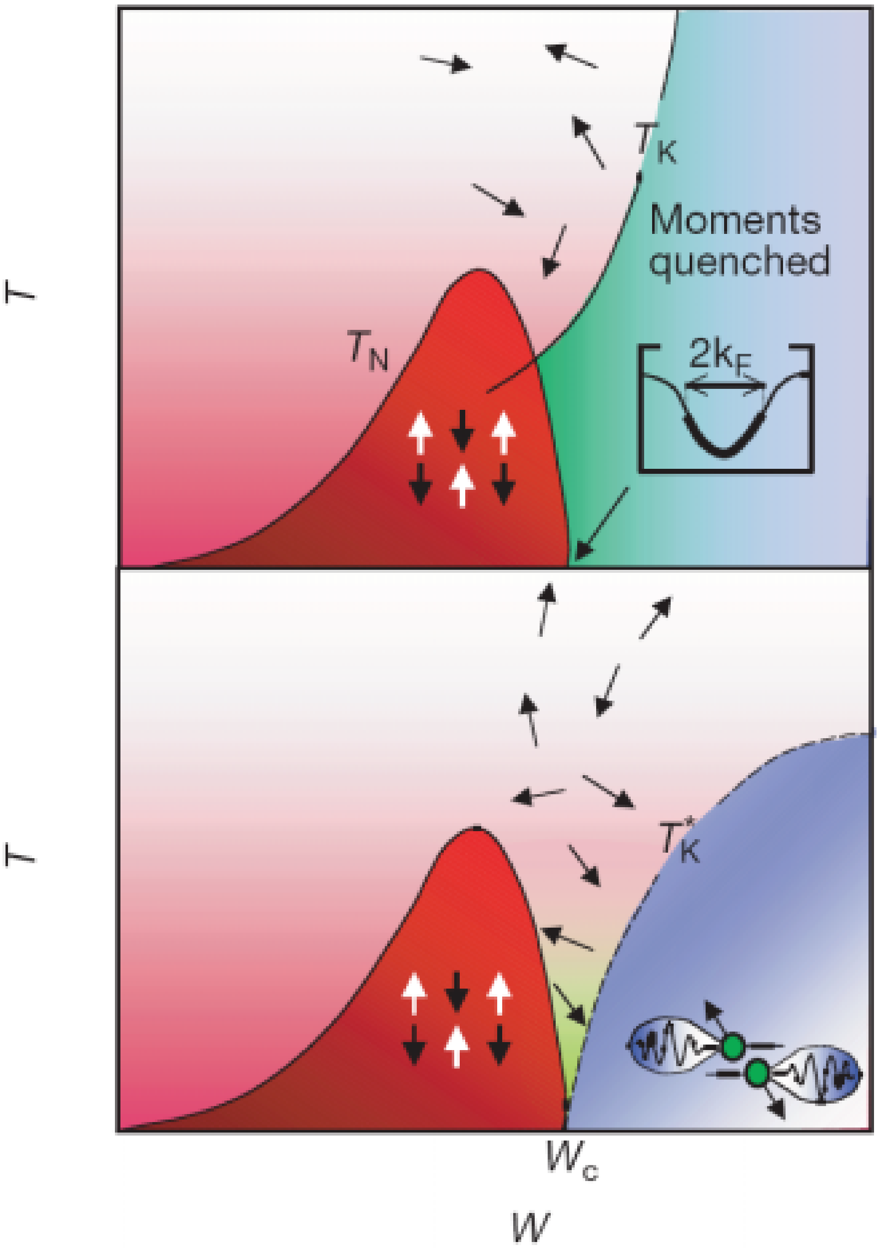

Figure 2.2: Sketches of the phase diagram for two different scenarios of NFL behavior, that is *i.e.*, spin density wave and local breakdown of the Fermi liquid at the quantum critical point; taken from [26], for details see text.

moments such as quadrupolar ordering etc. may be realized and can lead to complex phase diagrams. Furthermore, the existence of quadrupolar moments can be of relevance to Kondo systems as well. The asymmetric charge distribution is screened by conduction electrons which may result in the so-called quadrupolar Kondo effect and give rise to non-Fermi liquid behavior as discussed in terms of the overcompensated two channel Kondo effect.

The interaction which leads to an ordering of quadrupolar moments can have different sources. It can arise from biquadratic exchange due to the presence of the orbital moment [30, 31], analogous to the Heisenberg type bilinear coupling between magnetic dipoles, or from magnetoelastic coupling, corresponding to a direct coupling between lattice deformation and the f shell [32]

Although multipole ordering has attracted a lot of interest in recent years, a full and detailed theory is still lacking. First treatments have been presented recently [33], but due to the complexity in the treatment of multipole degrees of freedom only limited progress in theoretical calculations has been obtained so far. In consequence, most of the theoretical studies have been limited to a phenomenological treatment of such ordering phenomena.

3 A case study: Basic properties of $CePt_3B$

In this chapter a short introduction of the measurement methods used in this work will be given. In doing so, to illustrate what kind of information can be gathered from the various experimental techniques corresponding studies on a material out of the heavy fermion range, $CePt_3B$, and the related alloying series $CePt_3B_{1-x}Si_x$ will be presented. Finally, additional experimental techniques used in the context of studies of quadrupolar systems will be discussed.

3.1 Basic properties of $CePt_3B$

$CePt_3B$, which has been studied for the first time in Ref. [34], is isostructural to the recently discovered heavy fermion superconductor $CePt_3Si$ [35]. For almost 30 years, heavy fermion superconductors have attracted a lot of interest because of the possible realization of unconventional superconducting pairing mechanisms and symmetries of the superconducting state.

In conventional superconductors the coupling of two electrons to a Cooper pair is mediated by an exchange of virtual phonons. This effect is explained in much detail within the **B**ardeen-**C**ooper-**S**chrieffer theory. The superconducting order parameter in common BCS-type superconductors mirrors the full lattice symmetry.

However, in heavy fermion superconductors the BCS theory seems not to be valid, instead unconventional superconducting pairing states and symmetries may occur. For instance, in these systems a pairing mediated by spin fluctuations is discussed [29]. As well, in unconventional superconductors the symmetry of the order parameter is broken under symmetry operations of the crystal lattice.

Moreover, $CePt_3Si$ is the first heavy fermion superconductor without a center of symmetry in the crystallographic lattice. In such systems a spin triplet state of Cooper pairs is believed to be excluded [36]. However, for $CePt_3Si$ an anomalously large superconducting upper critical field B_{c2} has been observed experimentally [35], and which has been taken as indication for a spin-triplet pairing, in apparent conflict with the statement from Ref. [36]. As yet, this issue concerning the superconducting state in $CePt_3Si$ has not been resolved.

Complicating matters is the antiferromagnetically ordered phase below $T_N = 2.2\,\mathrm{K}$, with an ordered moment of $0.16\,\mu_B$ (ordering vector $\boldsymbol{k} = (0\ 0\ \frac{1}{2})$), embedding the superconducting state, and whose role has not fully been understood so far [35, 37, 38]. In this context, various scenarios regarding the nature of the superconducting state have been proposed in recent years, with mixed singlet-triplet pairing states as the most prominent and exotic models [39, 40].

Unlike $CePt_3Si$, $CePt_3B$ does not show superconductivity. Both systems, $CePt_3Si$ and $CePt_3B$, crystallize in the $P4mm$ structure, see Fig. 3.1 [35, 41]. For $CePt_3B$ lattice parameters $a = 4.0051(7)$ Å and $c = 5.0760(8)$ Å and for $CePt_3Si$ $a = 4.072(1)$ Å and $c = 5.442(1)$ Å have been found [35, 41].

Moreover, $CePt_3B$ exhibits two magnetic transitions at $T_C = 6\,\mathrm{K}$ and $T_N = 7.8\,\mathrm{K}$ [34, 41, 42]. While the upper transition temperature is antiferromagnetic, a study of the magnetic bulk properties reveals a weakly ferromagnetic behavior below the lower transition temperature, with a ferromagnetically ordered moment of $0.08\,\mu_B/\mathrm{Ce\,atom}$. The most straightforward interpretation of such a low ferromagnetic moment, together with a high temperature Curie-Weiss like behavior in the susceptibility with an effective moment of $\mu_{eff} = 2.3\,\mu_B$ and an antiferromagnetic Curie-Weiss temperature of $\Theta_{CW} = -12\,\mathrm{K}$, would be that below T_C the magnetic state is antiferromagnetically ordered with comparatively large (order of one μ_B) magnetic moments, together with a canting of the moments causing the weak ferromagnetic response. Such a canting could possibly result from the lacking inversion symmetry of the crystal structure, as under these conditions an additional exchange mechanism, the magnetic coupling via Dzyaloshinskii-Moriya (DM) interaction, might become relevant.

In combination with the Heisenberg exchange, given by

$$H_{\mathrm{Heisenberg}} = \sum_{\mathrm{i,j}} J_{\mathrm{ij}} \boldsymbol{s}_{\mathrm{i}} \cdot \boldsymbol{s}_{\mathrm{j}},$$

with J_{ij} - magnetic exchange coupling and $\boldsymbol{s}_i$ and $\boldsymbol{s}_j$ - neighboring spins, the

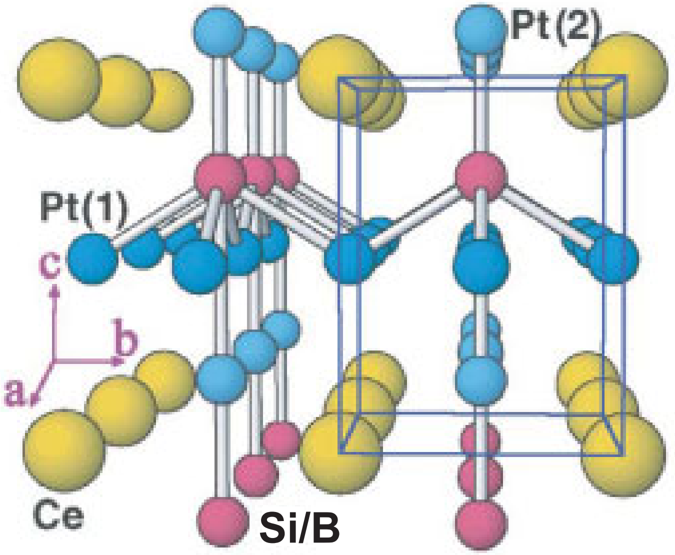

Figure 3.1: Crystal structure of $CePt_3B$ and $CePt_3Si$ (from [35]); for details see text.

Dzyaloshinskii-Moriya interaction term given by

$$H_{\mathrm{DM}} = \sum_{\mathrm{i,j}} \boldsymbol{D}_{\mathbf{ij}}(\boldsymbol{s}_{\mathbf{i}} \times \boldsymbol{s}_{\mathbf{j}}),$$

with $\boldsymbol{D}_{\mathbf{ij}}$ - Dzyaloshinskii-Moriya vector, is known to often cause canted or helical magnetic structures. Although such a scenario regarding the magnetically ordered state appears to be quite likely realized in the case of $CePt_3B$, as yet a direct and microscopic determination of the symmetry of the antiferromagnetic phase is lacking.

Furthermore, in order to understand the ground state properties of heavy fermion systems, it is a common procedure to carry out doping experiments, this way to change the electronics of the material in a controlled fashion and exerting chemical pressure to some degree. With $CePt_3B$ being isostructural to $CePt_3Si$, an alloying series $CePt_3B_{1-x}Si_x$ for $0 \leq x \leq 1$ can be studied and hence the complete phase diagram from unconventional superconductivity to possible canted local moment antiferromagnetism is accessible, allowing to draw conclusions about the physics of the pure ternary system. Therefore, in order to clarify the magnetic structure of $CePt_3B$ and to unravel the phase diagram of $CePt_3B_{1-x}Si_x$ a set of microscopic and bulk measurements will be presented in the following.

The samples $CePt_3B_{1-x}Si_x$ studied here have been prepared by mixing the elements in stoichiometric ratio. Subsequently, the polycrystalline material was produced by melting the constituents under argon atmosphere in a water-cooled copper crucible using a high frequency generator.

3.2 Bulk methods

3.2.1 Magnetization

If not noted, all low field magnetization and susceptibility measurements presented in this work have been performed in a commercial DC-SQUID. The pulsed high field magnetization measurements on UPt_2Si_2 will be discussed in the corresponding chapter. The magnetization density $\boldsymbol{M}(\boldsymbol{H})$ at $T = 0\,\mathrm{K}$ of a volume V in a homogeneous magnetic field $\boldsymbol{H}$ is defined as

$$M(H) = -\frac{1}{V}\frac{\partial E_0(H)}{\partial H}. \tag{3.1}$$

For simplicity it is assumed that $\boldsymbol{M}$ is parallel to $\boldsymbol{H}$. The magnetic susceptibility is defined as

$$\chi = \frac{\partial M}{\partial H}. \tag{3.2}$$

For sufficiently low magnetic fields, and provided no ferromagnetic ordering occurs, the magnetization M is linear in H and therefore the susceptibility is reduced to $\chi = M/H$. With these definitions, the magnetic behavior of materials can be grouped into two different types, as distinguished by the susceptibility χ behavior:

Diamagnetism In completely filled orbitals the spin- and orbital angular momentum of the electrons are compensated. The magnetic moment is induced by an external field and directed antiparallel to this field, the susceptibility is negative:

$$\chi_{\mathrm{dia}} < 0, \tag{3.3}$$

This behavior is called the Larmor diamagnetism.

Paramagnetism Paramagnetism stems from magnetic moments which are aligned in an external field and point parallel to this field, hence the susceptibility is positive:

$$\chi_{\mathrm{para}} > 0. \tag{3.4}$$

In a material with only partially filled orbitals there may exist localized magnetic moments. In an applied field, these moments are aligned in the direction parallel to the field. The total angular momentum $\boldsymbol{J}$ is the sum of spin $\boldsymbol{S}$ and orbital angular momentum $\boldsymbol{L}$:

$$\boldsymbol{J} = \boldsymbol{L} + \boldsymbol{S}. \tag{3.5}$$

As long as there is no interaction between the magnetic moments, the susceptibility is given by the Curie law

$$\chi_{\mathrm{Langevin}} = \frac{C}{T}, \tag{3.6}$$

with the Curie constant C.

Also the spins of the free electrons in a metal can contribute to the paramagnetism (Pauli paramagnetism). In a magnetic field the energy of the conduction electrons is increased or reduced by $|\mu_{\mathrm{B}}\boldsymbol{B}|$, depending on the direction of the spins with respect to the magnetic field. As both spin-up and spin-down electrons have the same Fermi energy, more electrons have a spin parallel to the magnetic field than antiparallel, yielding a net magnetization in field direction. The paramagnetic Pauli susceptibility is given by

$$\chi_{\mathrm{Pauli}} = \mu_0 \mu_{\mathrm{B}}^2 N(E_{\mathrm{F}}), \tag{3.7}$$

with $N(E_{\mathrm{F}})$ the density of states at the Fermi energy. As the Fermi temperature is very high in comparison to the temperatures used in experiments, $N(E_{\mathrm{F}})$ and hence the Pauli susceptibility, are nearly temperature independent.

> Most of the systems discussed in this work are heavy fermion systems. Due to the strong electronic correlations the low temperature properties are understood using Fermi liquid theory. Within Fermi liquid theory the magnetic susceptibility can be written as
>
> $$\chi_{\text{Pauli}} = \frac{m^* k_{\text{F}} \mu_{\text{B}}^2}{\pi^2 (1 + F_0^\alpha)}, \tag{3.8}$$
>
> with the Landau parameter $F_0^\alpha \propto f(k \uparrow, k' \uparrow) - f(k \uparrow, k' \downarrow)$. Here, $f(k\sigma, k'\sigma)$ is the quasiparticle interaction function between two quasiparticles characterized by their wavevectors k, k' and spins σ.

Furthermore, magnetic moments in a solid environment very often interact with each other, resulting in ordered magnetic structures. Two basic examples are ferromagnetism (all magnetic moments are pointing in the same direction) and antiferromagnetism (neighboring magnetic moments are antiparallel). The interaction between the magnetic moments can be the result of different processes, such as RKKY exchange interaction or magnetic superexchange.

3.2.1.1 Magnetic properties of $CePt_3B_{1-x}Si_x$

$CePt_3B$ exhibits two magnetic phase transitions at low temperatures [34]. The first one at $T_{\text{N}} = 7.8\,\text{K}$ is assumed to be a transition into an antiferromagnetically ordered structure, the second one at $T_{\text{C}} \approx 6\,\text{K}$ shows ferromagnetic characteristics. For the latter transition a substantial sample dependence is reported, with Lackner *et al.* obtaining a value of $T_{\text{C}} = 4.5\,\text{K}$ [42].

For one specific sample, the inverse magnetic susceptibility χ^{-1} versus the temperature T, as measured in Ref. [34], is plotted in Fig. 3.2. At high temperatures, using a Curie-Weiss fit Süllow *et al.* [34] found an effective Ce moment of $2.3\,\mu_{\text{B}}$ and a Curie-Weiss temperature Θ_{CW} of $-12\,\text{K}$. Such behavior would be consistent with local moment antiferromagnetism at low temperatures. The inset of Fig. 3.2 shows that a kink, followed by a plateau, is observed at $\sim 8\,\text{K}$. Below $7\,\text{K}$ χ^{-1} decreases further and finally saturates at low temperatures. These two anomalies have been associated to the magnetic transitions referred to above.

The overall susceptibility behavior of the sample $CePt_3B$ examined in this work is similar to that reported in Ref. [34]. This is illustrated in Fig. 3.3,

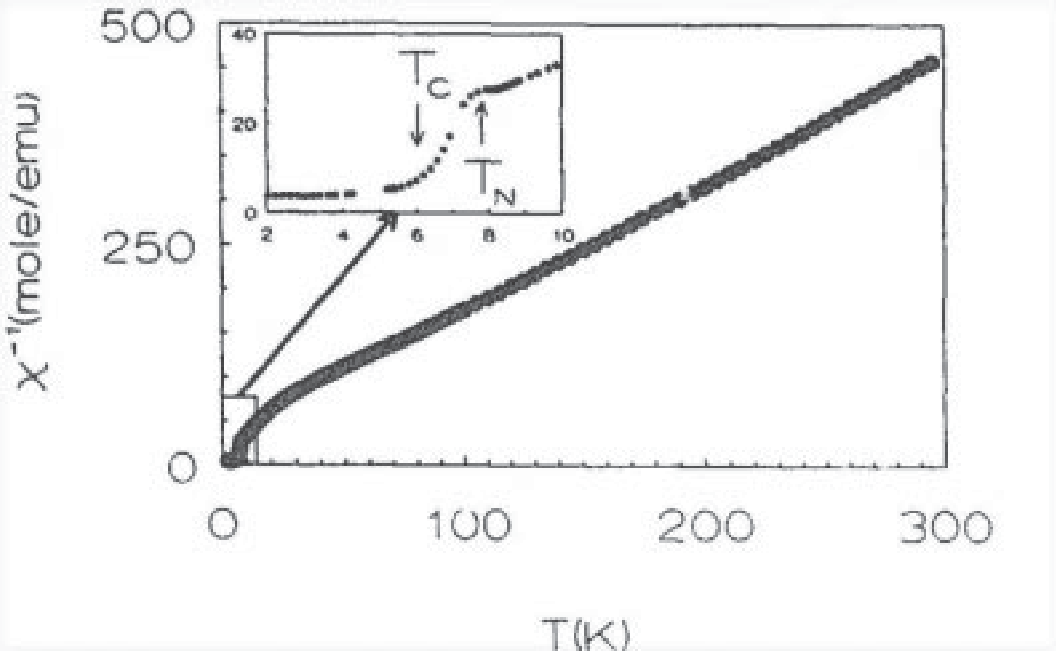

Figure 3.2: Temperature dependence of the inverse suseptibility χ^{-1} of $CePt_3B$ (from Ref. [34]); for details see text.

where the temperature dependence of the inverse susceptibility measured in a residual field of $13.3 \cdot 10^{-4}\,\mathrm{T}$ at low temperatures is plotted. From the construction displayed in Fig. 3.3 the two transition temperatures have been determined to $T_{\mathrm{C}} = 5.8\,\mathrm{K}$ and $T_{\mathrm{N}} \sim 8\,\mathrm{K}$ (marked by arrows in Fig. 3.3).

For basic sample characterization, the susceptibility of the alloyed samples $CePt_3B_{1-x}Si_x$, with $x = 0.2, 0.4$, has also been measured in a residual field of $8.68 \cdot 10^{-4}\,\mathrm{T}$, see Fig. 3.4. The susceptibility behavior in the paramagnetic phase is similar to that of $CePt_3B$. However, in $CePt_3B_{0.8}Si_{0.2}$ only one magnetic transition remains clearly observable, while in $CePt_3B_{0.6}Si_{0.4}$ clear signatures of both magnetic transitions have disappeared.

In Fig. 3.5 the low temperature region of the inverse susceptibility χ^{-1} for the three samples $CePt_3B_{1-x}Si_x$, with $x = 0, 0.2$, and 0.4 is depicted. From the constructions indicated in the plot the transition temperatures are derived and marked by arrows.

From the same procedure as used for $CePt_3B$ (see Fig. 3.3) the upper transition temperature of $CePt_3B_{0.8}Si_{0.2}$ has been determined to $T_{\mathrm{N}} = 4.8\,\mathrm{K}$. For this sample as for $CePt_3B_{0.6}Si_{0.4}$ an accurate determination of T_c is not possi-

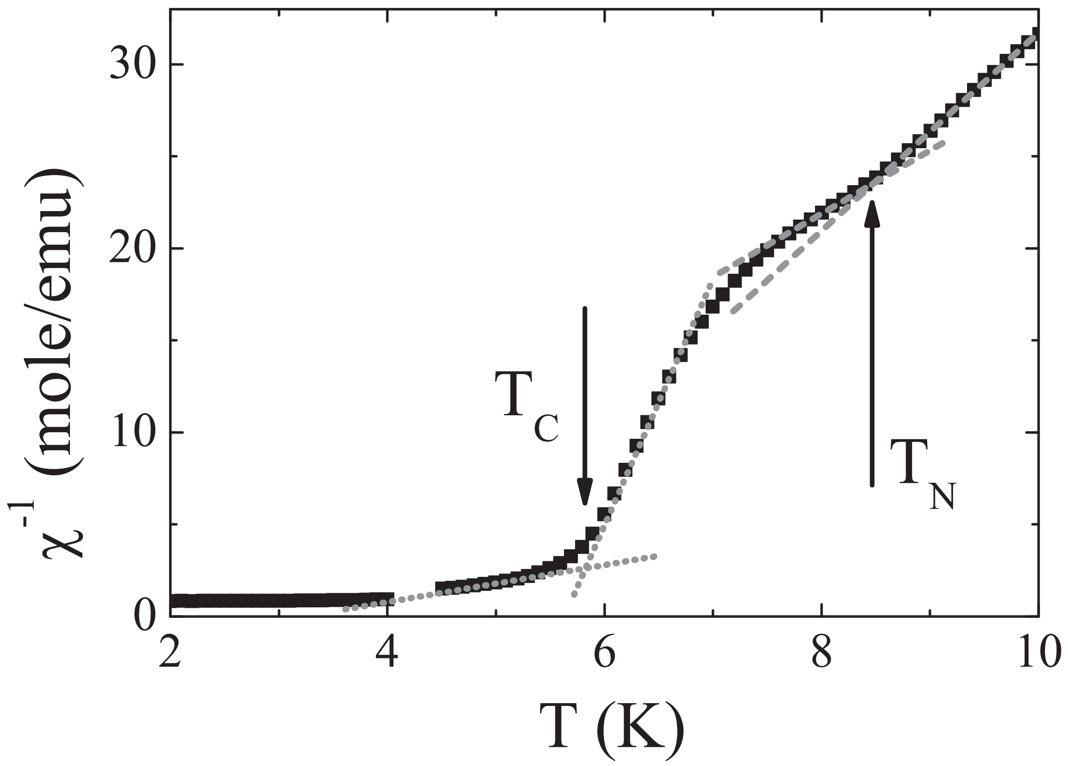

Figure 3.3: Temperature dependence of the inverse susceptibility χ^{-1} of the sample CePt$_3$B examined in this work. The linear construction to determine T_C and T_N is shown by the dotted and dashed gray lines. The transition temperatures are marked by arrows; for details see text.

ble as the lowest accessible temperature of the SQUID magnetometer is $1.8\,\mathrm{K}$. However, an estimate of T_c is possible using a linear extrapolation as shown in the plot. For comparison, for CePt$_3$B, employing this procedure, a transition temperature T_C of $5.6\,\mathrm{K}$ is obtained, in reasonable agreement with the values obtained from other experimental techniques or procedures to analyze the susceptibility data, see Fig. 3.5. Correspondingly, for the alloyed sample T_C values of $1.8\,\mathrm{K}$ for CePt$_3$B$_{0.8}$Si$_{0.2}$ and $1.1\,\mathrm{K}$ for CePt$_3$B$_{0.6}$Si$_{0.4}$, respectively, are obtained (Fig. 3.5).

Furthermore, magnetization measurements at low temperatures have been carried out on CePt$_3$B$_{1-x}$Si$_x$, $x = 0, 0.2, 0.4$. The magnetization *vs.* magnetic field for CePt$_3$B is depicted in Fig. 3.6. Below T_C a hysteresis is observable in the field sweeps, which has vanished in the $8\,\mathrm{K}$ data. To quantify the temperature dependent evolution of the ferromagnetic moment associated to the

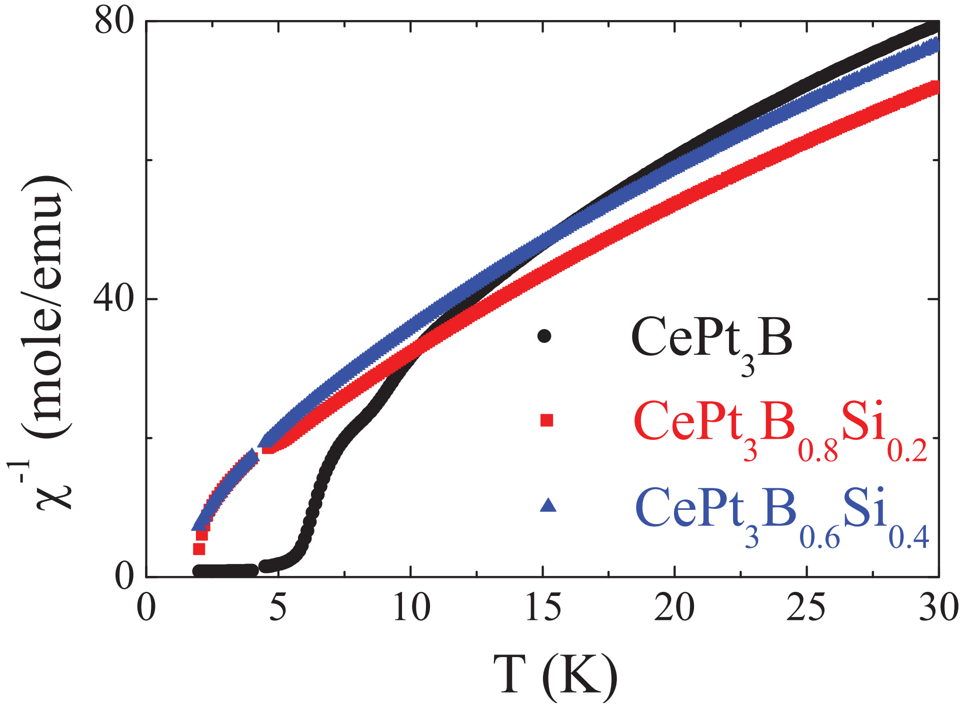

Figure 3.4: Temperature dependence of the inverse susceptibility χ^{-1} of $CePt_3B$ and the alloyed samples $CePt_3B_{1-x}Si_x$, $x = 0.2, 0.4$; for details see text.

phase below T_C, the average value of the extrapolated remanent magnetization at $B = 0\,T$ has been determined and summarized in Fig. 3.7. Again an extrapolation of the temperature dependence of the remanent magnetization yields a transition temperature T_C of $5.5\,K$, in good agreement with the previously described procedures to determine T_C, see Fig. 3.7.

For the alloyed samples $CePt_3B_{1-x}Si_x$, $x = 0.2, 0.4$, no hysteresis is observed down to $1.8\,K$ (Fig. 3.8 a. and b.). Thus, for the alloyed samples, no ferromagnetic ordering is observed down to $1.8\,K$.

3.2.2 Resistivity

For metallic heavy fermion systems the electrical resistivity usually represents a probe of the ground state properties. Hence, it is a very useful tool to investigate these compounds.

As long as disorder related processes are not dominant, assuming the valid-

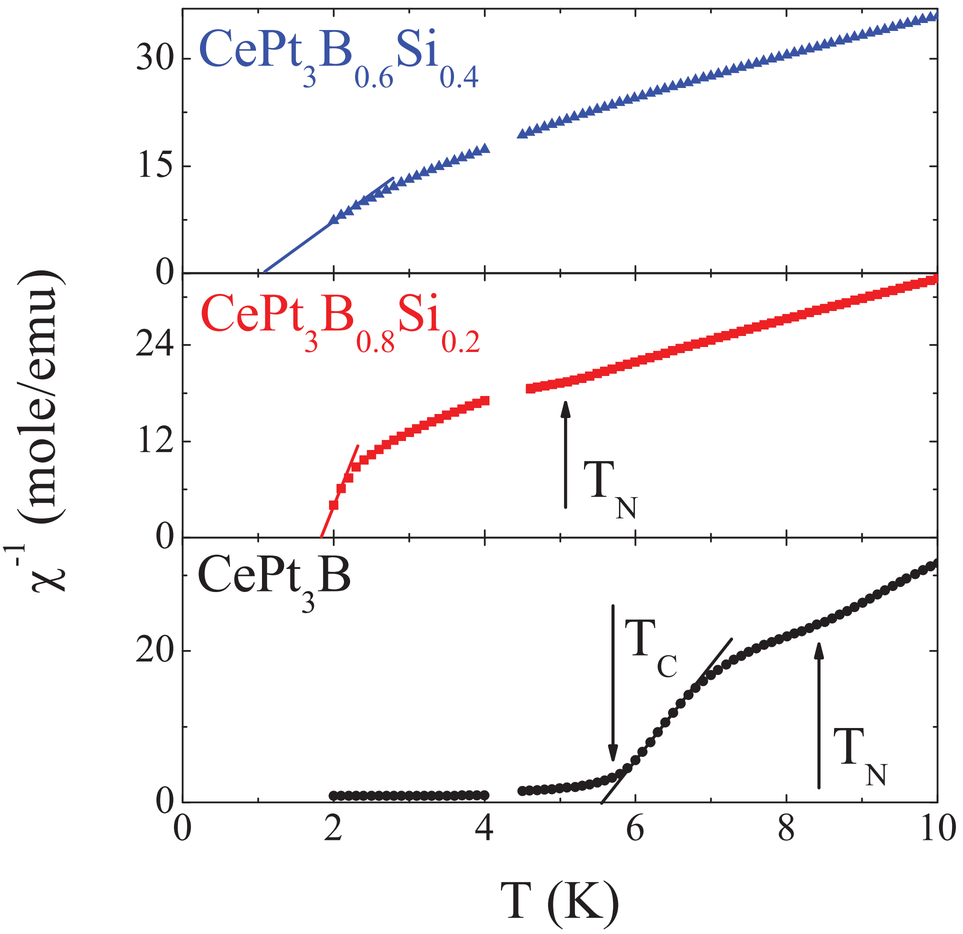

Figure 3.5: Enlarged view of the low temperature region of the inverse susceptibility χ^{-1} of CePt$_3$B and the alloyed samples CePt$_3$B$_{1-x}$Si$_x$, $x = 0.2, 0.4$; for details see text.

ity of Matthiessen's rule, *i.e.*, scattering processes are independent from each other for heavy fermion metals, the temperature dependence of the electrical resistivity $\rho(T)$ is given by

$$\rho(T) = \rho_0 + \rho_{\text{ph}}(T) + \rho_{\text{mag}}(T).$$

ρ_0 represents the residual resistivity from impurity scattering, $\rho_{\text{ph}}(T)$ from phonon scattering and $\rho_{\text{mag}}(T)$ that of scattering from magnetic moments.

Relevant limiting cases for $\rho_{\text{ph}}(T)$ are $T \gg \Theta_{\text{D}}$, yielding a behavior $\rho_{\text{ph}}(T) \propto T$, and a characteristic $\rho_{\text{ph}}(T) \propto T^5$ for $T \ll \Theta_{\text{D}}$.

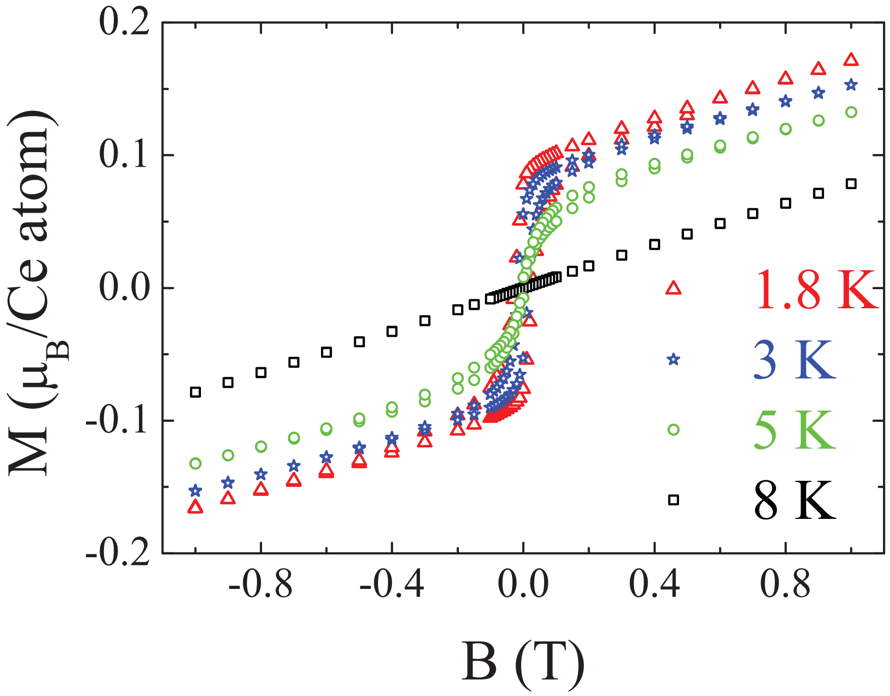

Figure 3.6: Magnetic field dependence of the magnetization of $CePt_3B$; for details see text.

In the basic models of magnetic scattering, $\rho_{\mathrm{mag}}(T)$ is constant above a magnetic transition temperature T_{mag} [43]. For real systems, however, this is often not the case, and the temperature dependence of magnetic fluctuations need to be considered in detail. While on a qualitative level there are lots of insights into the associated resistive behavior, there is only a very limited number of analytical descriptions.

Sufficiently far below T_{mag} the electrical resistivity is given by a magnon scattering term

$$\rho_{\mathrm{mag}}(T) = AT^y.$$

Here, y depends on the type of magnetic ordering, *e.g.* $y = 2$ for ferromagnetic magnons [44], $y = 5$ for antiferromagnetic magnons [44]. The excitation of antiferromagnetic magnons in the presence of a spin excitation gap can be described by

$$\rho(T) = \rho_0 + \frac{DT}{\Delta}\left[1 + \frac{2T}{\Delta}\right]\exp\left(-\frac{T}{\Delta}\right),$$

with ρ_0 - impurity scattering, Δ - spin excitation gap value [45].

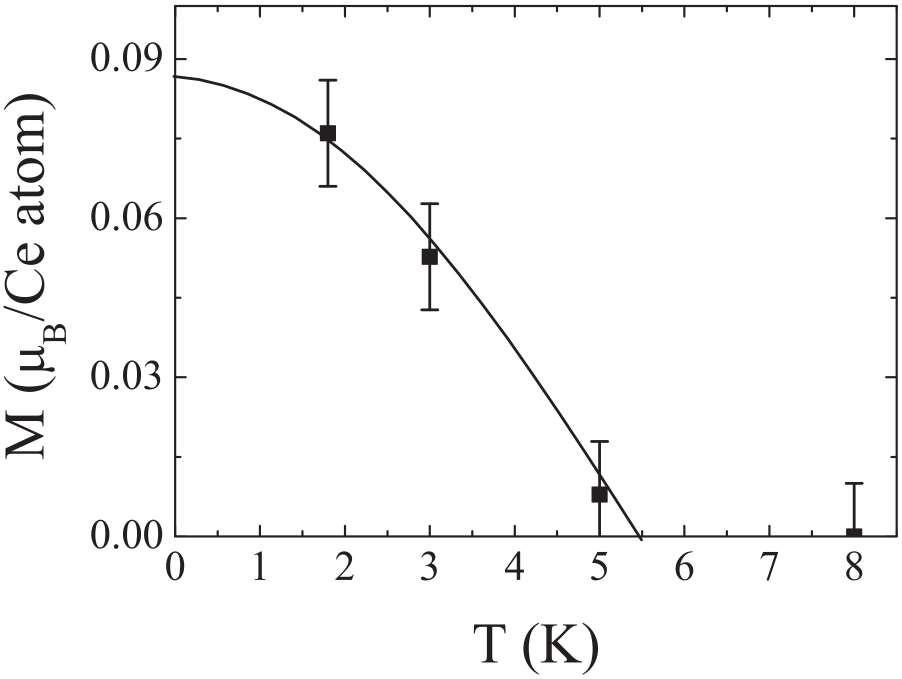

Figure 3.7: The remanent ferromagnetic moment *vs.* temperature of CePt$_3$B. The solid line is an extrapolation; for details see text.

In heavy fermion systems the Kondo scattering of the conduction electrons, correlation effects at low temperatures and the crystal field have to be taken into account. In the high temperature range, *e.g.*, $T > T_K$ the resistivity can be calculated from the Heisenberg Hamiltonian ($s - f$ model):

$$H = -2J\boldsymbol{s}\boldsymbol{S},$$

J - exchange coupling parameter, $\boldsymbol{s}$ - spin state of the conduction electron and $\boldsymbol{S}$ - magnetic ion spin. For $T > T_K$, Kondo found a logarithmic increase of the resistivity

$$R_{\mathrm{imp}}(T) = \rho_0 \left[1 - JN(E)\ln\frac{k_B T}{\Delta}\right],$$

$N(E)$ - density of states , Δ - width of the Friedel virtual bound state [46].

In heavy fermion systems the magnetic ions are arranged in a regular lattice. Due to the periodicity of the Kondo lattice, coherence of the electrons is observed. In the coherent state, the system can be described by Fermi liquid theory. Within the framework of Fermi liquid theory the low temperature behavior

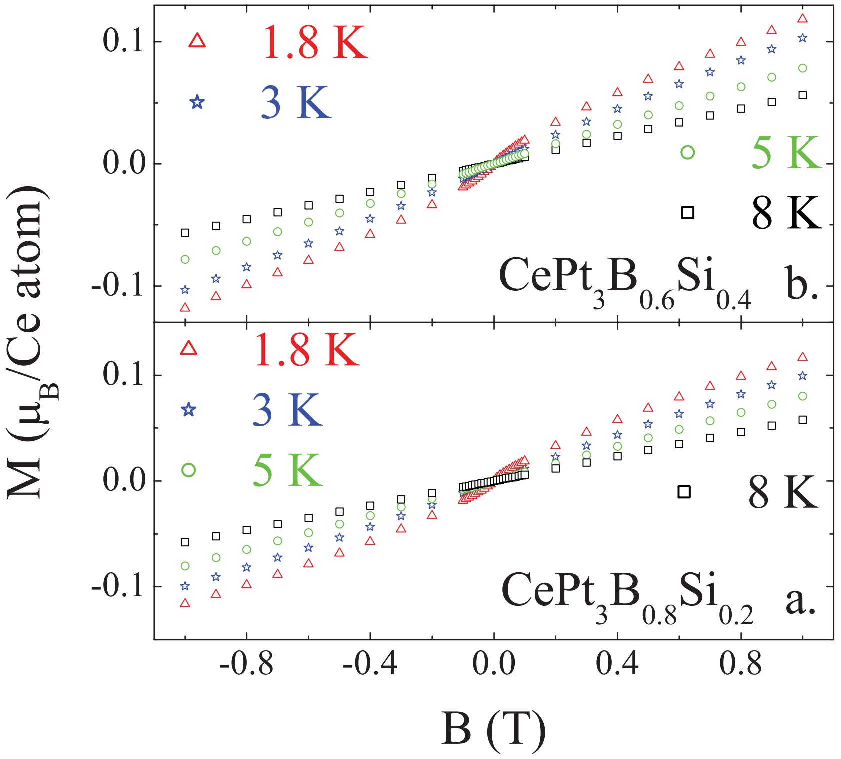

Figure 3.8: Magnetic field dependence of the magnetization of $CePt_3B_{1-x}Si_x$, $x = 0.2$ (a.) and 0.4 (b.).

($T < T^*$) of the resistivity in heavy fermions evolves like $\rho(T) = \rho_0 + AT^2$, where A is a coefficient proportional to the square of the density of states at the Fermi energy $N(E_F)$. Further, A is related to the Sommerfeld parameter γ by the empirical Kadowaki-Woods relation $A/\gamma^2 \sim 10\ \mu\Omega\text{cmK}^2\text{mole}^2\text{J}^{-2}$.

In the last two decades many materials have been found which show a "non-Fermi liquid" (NFL) behavior. For these materials a resistive behavior $\rho(T) = \rho_0 + AT^y$ with $y < 2$ has been observed. The different models to account for such behavior are described briefly in Chapter 2.2. Here, only the interplay between resistivity and structural disorder will be discussed in more detail.

The observation of NFL behavior in the resistivity in the vicinity of a quantum critical point (QCP) may result from small amounts of disorder [23]. The scattering at antiferromagnetic (AFM) spin fluctuations is most effective along so called “hot lines”, *e.g.*, regions on the Fermi surface which are connected by the scattering vector $\boldsymbol{Q}$. In a clean sample these regions are short-circuited by “cold” regions, *e.g.* regions where the scattering rate is small. If disorder is introduced into the system this mechanism does not work anymore as impurity scattering leads to an averaging of the scattering rates over the Fermi surface, resulting in non-Fermi liquid behavior, with resistive exponents $y < 2$ at low temperatures [23].

Moreover, in disordered system without electronic correlations, disorder induced localization effects have to be considered. Anderson demonstrated in his calculation [47], that a certain amount of perturbation in the periodic potential of the lattice can lead to a localization of the charge carrier wave function. The envelope of such a localized state is given by

$$|\Psi(\bar{r})| \sim \exp\left(\frac{|\bar{r} - \bar{r_0}|}{\zeta}\right),$$

where ζ is the correlation length.

For this type of localization the system becomes insulating for $T \rightarrow 0$. With increasing temperature a thermal activation of the electrons occurs. In the most basic models, it leads to a conductivity

$$\sigma = \sigma_0 \exp\left(-\frac{E_\mathrm{c} - E_\mathrm{F}}{k_\mathrm{B}T}\right),$$

with E_c characteristic for the mobility edge energy of the system, E_F the Fermi energy and σ_0 being proportional to the product of diffusion constant and relaxation time. More advanced models take into account additional processes, *e.g.*, thermally activated hopping etc.

Conversely, besides of disorder, also electronic correlation can lead to a metal-insulator transition. The Mott-insulator transition is a model in which a disorder induced insulator-to-metal transition can occur [48]. In this model, a half-filled conduction band is assumed. The electronic correlation results from a large value U of the Coulomb interaction between electrons, which prohibits movement of the electrons from site to site, *viz.*, the system is insulating. Now, by introducing disorder into the system, electrons for instance might be removed on some sites, which leads to a situation, where hopping of electrons from site to site is possible on a locale scale. As a result, a conducting (metallic) state is generated.

However, due to these localization mechanisms the resistivity cannot be described as a series of resistors ρ_0, ρ_{ph} and ρ_{mag} anymore. It has to be described in terms of different non-interacting conduction channels as expressed in the Kawabata-formula [46]

$$\sigma = \sigma_0 \exp\left(1 - \frac{C}{8lk_{\mathrm{b}}^2}(1 - \frac{l}{L_{\mathrm{i}}})\right),$$

where σ_{B} is the Boltzmann conductivity, l the mean free path, C is a constant and the inelastic diffusion length L_{i} corresponds to processes (electron-electron or electron-phonon) responsible for delocalization out of the local random potential. In moderately disordered heavy fermion systems, both, electronic correlation U and disorder are present.

3.2.2.1 Resistivity of CePt$_3$B$_{1-x}$Si$_x$

All resistivity measurements presented in this work have been performed using a conventional four probe AC method in a standard Oxford ^{4}He cryostat. Moreover, an Oxford Top loading ^{3}He insert has been employed for $T < 1.8\,\mathrm{K}$.

The parent compound CePt$_3$B was only available as a powder, hence no resistivity measurements were possible. For the alloyed material CePt$_3$B$_{1-x}$Si$_x$ polycrystalline bar-shaped samples were available. For these samples the absolute (normalized) resistivity ρ (ρ/ρ_{300}) is depicted in the Figs. 3.9 and 3.10 (3.11). In order to compare these data with pure CePt$_3$B, the resistive data of CePt$_3$B from Ref. [34] are included in the Figs. 3.9, 3.10 and 3.11.

Qualitatively, the overall shape of the resistive curves remains the same with Si alloying. However, the absolute resistivity ρ is increasing with increasing Si amount, reflecting the enhanced disorder level with alloying. As well, in the normalized resistivity ρ/ρ_{300} the low temperature resistivity ratio $(\rho_0/\rho_{300})^{-1}$ is also largest for the pure sample, consistent with least disorder in this sample.

Further, in the normalized resistivity data of the alloyed samples the antiferromagnetic transition is apparent but broadened, also reflecting the disorder induced by Silicon alloying. From the constructions in Fig. 3.10 transition temperatures of $T_{\mathrm{N}} = 6.1\,\mathrm{K}$ for the sample $x = 0.2$ and $T_{\mathrm{N}} = 4.5\,\mathrm{K}$ for

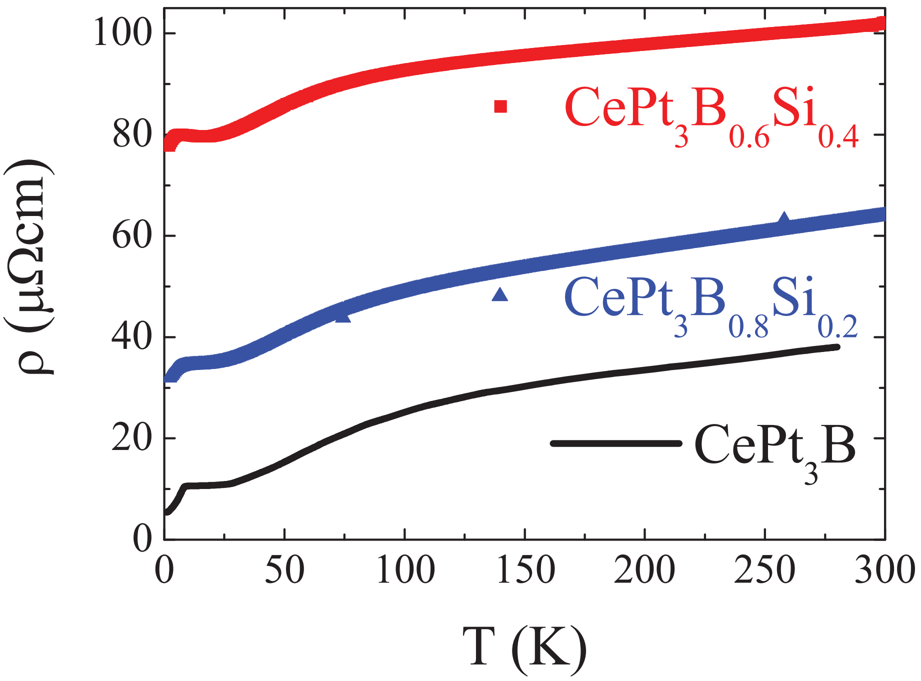

Figure 3.9: Temperature dependence of the absolute resistivity ρ of CePt$_3$B$_{1-x}$Si$_x$, $x = 0, 0.2$ and 0.4. The data for $x = 0$ are taken from Ref. [34].

$x = 0.4$ are derived. The broadening, however, results in a rather large error bar associated to the upper transition temperature.

Therefore, as a second variant to determine T_N, the minimum in the second temperature derivative $d^2(\rho/\rho_{300})/dT^2$ has also been used to determine T_N, see Fig. 3.12. While for the pure sample the transition occurs as a sharp peak, for the alloyed CePt$_3$B$_{1-x}$Si$_x$, $x = 0.2, 0.4$ the transition becomes broader due to disorder. Further, it is shifted to lower temperatures of $T_\mathrm{N} = 5.2\,\mathrm{K}$ for $x = 0.2$ and $T_\mathrm{N} = 4\,\mathrm{K}$ for $x = 0.4$, respectively.

Using the result of the susceptibility and electronic transport measurements, and by including the data for CePt$_3$Si, a preliminary phase diagram of CePt$_3$B$_{1-x}$Si$_x$ is constructed, see Fig. 3.13. The antiferromagnetic transition temperature T_N is suppressed with increasing Si alloying. By extrapolating the data, a QCP is obtained for $x \sim 0.8$. The ferromagnetic transition temperature T_C exhibits a more complicated behavior, as a linear evolution with x is not observed. However, overall a reduction of T_C with Si alloying is clearly seen.

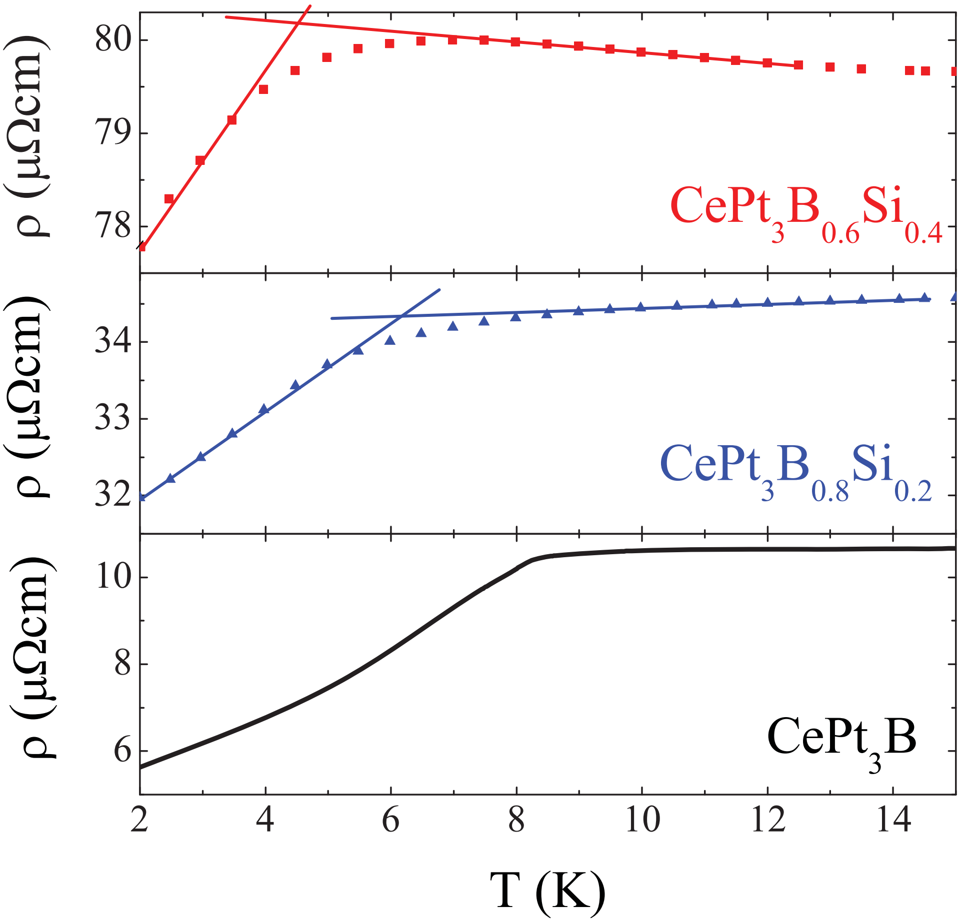

Figure 3.10: The low temperature range of the absolute resistivity ρ of $CePt_3B_{1-x}Si_x$, $x = 0, 0.2$ and 0.4. The data for $x = 0$ are taken from Ref. [34].

3.2.3 Hall effect

The Hall coefficient R_H is given by

$$R_H = \frac{V_H t}{\boldsymbol{BI}}, \tag{3.9}$$

where t is the thickness, $\boldsymbol{B}$ is the field transverse to the direction of the current $\boldsymbol{I}$, and V_H is the voltage transverse to the direction of both, the current and the field. In heavy fermions, in contrast to normal metals where the temperature dependence of the Hall coefficient is constant, a strong T dependence can

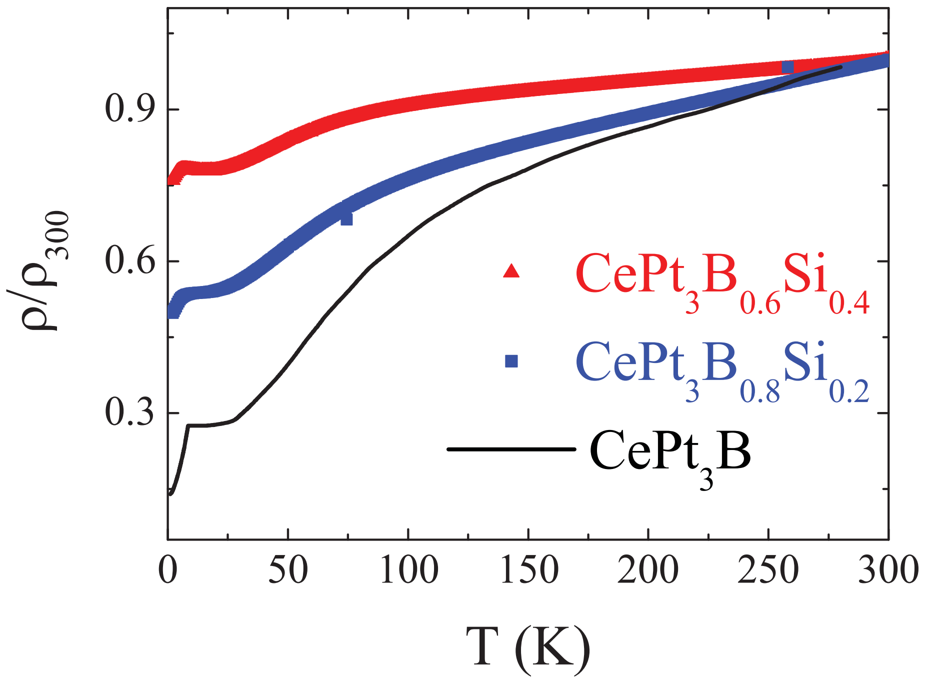

Figure 3.11: Temperature dependence of the normalized resistivity ρ/ρ_{300} of CePt$_3$B$_{1-x}$Si$_x$, $x = 0, 0.2$ and 0.4. The data for $x = 0$ are taken from Ref. [34].

be observed. Besides this, the Hall constant is much larger than in most normal metals and at low temperature drops rapidly with decreasing temperature. Hence, a maximum in $R_{\mathrm{H}}(T)$ at a temperature T_{coh} occurs, which indicates the transition into the coherent state. To analyze the Hall effect in heavy fermions, the Hall constant is separated into two terms, a normal, temperature independent term R_0 and an anomalous, temperature dependent term R_{A},

$$R_{\mathrm{H}} = R_0 + R_{\mathrm{A}}. \tag{3.10}$$

Here, R_0 represents the normal contribution to the Hall effect and measures the carrier density n. Besides this, according to Ref. [49], also skew scattering by defects contributes to R_0. Hence, in samples with similar carrier densities R_0 should act as a measure for the number of crystallographic defects.

For the anomalous term several model descriptions exist. Schoenes and Franse postulated an empirical ansatz: $R_{\mathrm{A}} \sim \chi, T \gg T_{\mathrm{C}}, \Theta_{\mathrm{CW}}$ [50]. Subsequently, Fert and Levy proposed a theoretical model which accounts for skew scattering in the anomalous Hall contribution, see Fig. 3.14 [49]. In this model the

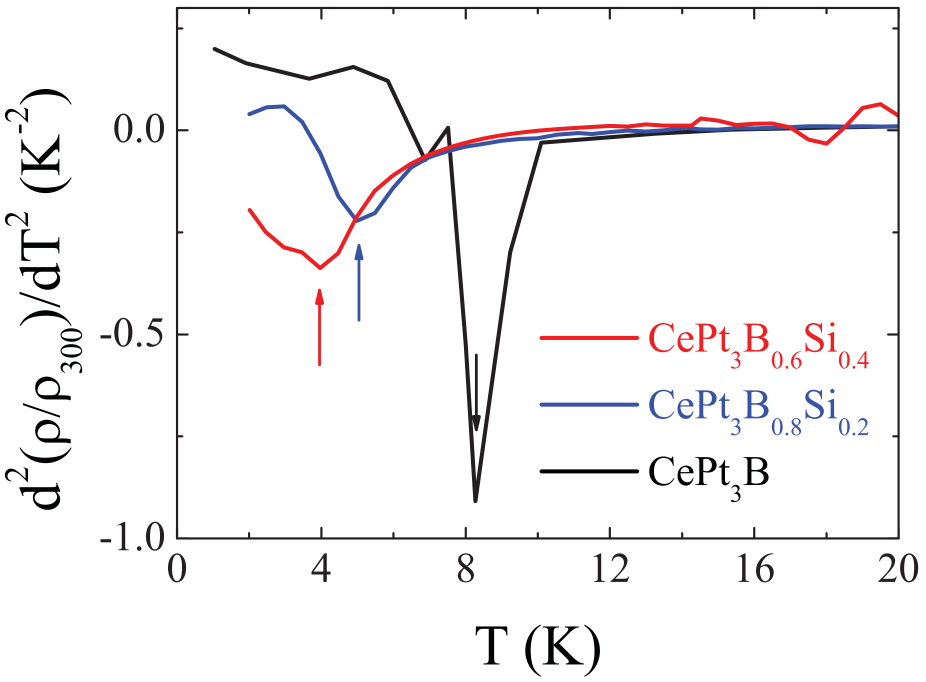

Figure 3.12: Temperature derivative $d^2(\rho/\rho_{300})/dT^2$ of CePt$_3$B$_{1-x}$Si$_x$, $x = 0, 0.2, 0.4$. The arrows indicate the transition temperature T_N for the three samples; for details see text.

anomalous contribution R_A represents intrinsic skew scattering. The temperature dependence of R_A is predicted to $R_\mathrm{A} \sim \chi\rho_\mathrm{mag}$, with χ as susceptibility and ρ_mag the magnetic scattering component of the resistivity. The intrinsic skew scattering above T_coh is given by $R_\mathrm{H}^{(T)} = \gamma\bar{\chi}(T)\rho_\mathrm{res}(T)$, with the parameter γ, which has different values above and below T_K depending on the phase shift associated with the scattering channels. $\bar{\chi}(T)$ is the reduced susceptibility and $\rho_\mathrm{res}(T)$ is the resistivity due to resonant scattering, thus the total resistivity reduced by phonon and impurity contributions.

In practice ρ_res is given by the magnetic scattering contribution ρ_mag. However, as the temperature dependence of R_H is mainly determined by the intrinsic skew scattering and the reduced susceptibility $\bar{\chi}$ does not significantly deviate from the susceptibility $\chi(T)$, the anomalous Hall constant R_A is assumed to evolve like $\propto \chi(T)\rho_\mathrm{mag}(T)$.

Fert and Levy [49] calculated their model on the basis of the periodic Anderson

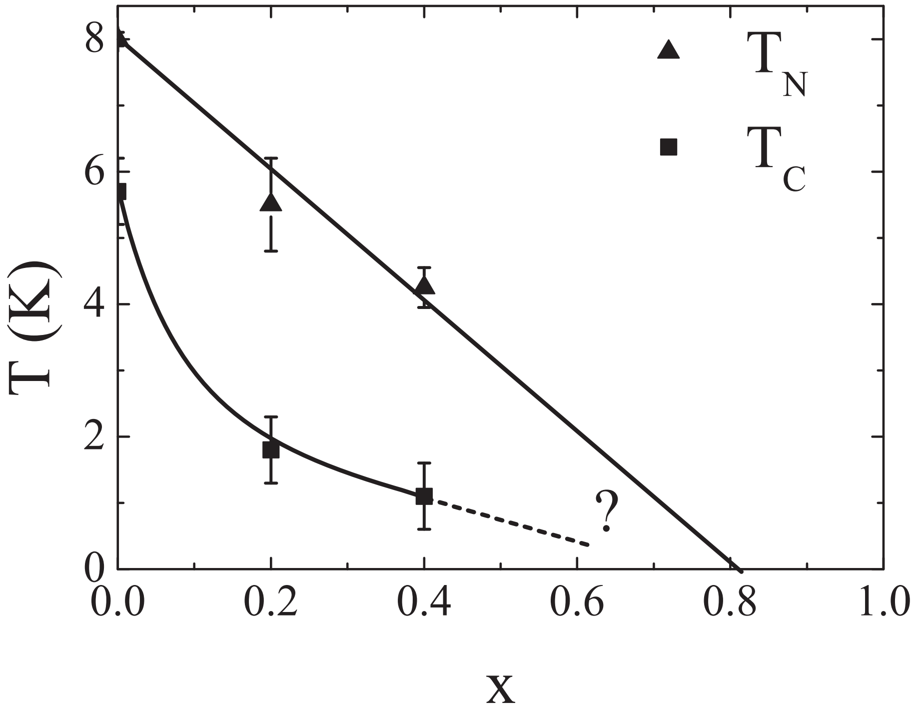

Figure 3.13: Phase diagram of CePt$_3$B$_{1-x}$Si$_x$. Black triangles indicate T_N, black squares T_C, the solid lines are guides to the eye; for details see text.

Hamiltonian, but neglected the coupling between different sites for $T > T_\mathrm{coh}$. An alternative view has been developed by Kontani and Yamada [51] on the basis of the periodic Anderson model by taking the phase factor of the mixing potential between conduction electrons and impurity ions into account. These authors describe the maximum in $R_\mathrm{H}(T)$ as a transition from a regime $T \ll T_\mathrm{coh}$ with $R_\mathrm{A} \propto \rho^2$ to one at $T \gg T_\mathrm{coh}$, with $R_\mathrm{A} = \chi$ (ρ the total resistivity).

In practice for a real system, a distinction between these models is often not unambiguous, *e.g.* in UCu$_4$Pd [52].

A fourth model to account for the anomalous Hall contribution is the side jump effect, which is usually considered only to be relevant in disordered materials [53]. Within this scenario, in the presence of disorder the scattered charge carriers are discontinuously shifted out of their original trajectory. This quantum mechanical effect is resulting in a temperature dependence $R_\mathrm{A} \propto \rho^2$, with ρ the total resistivity.

According to the model of Ref. [49] the value of the Hall constant R_H at low temperatures should be determined by structural disorder. If this prediction is

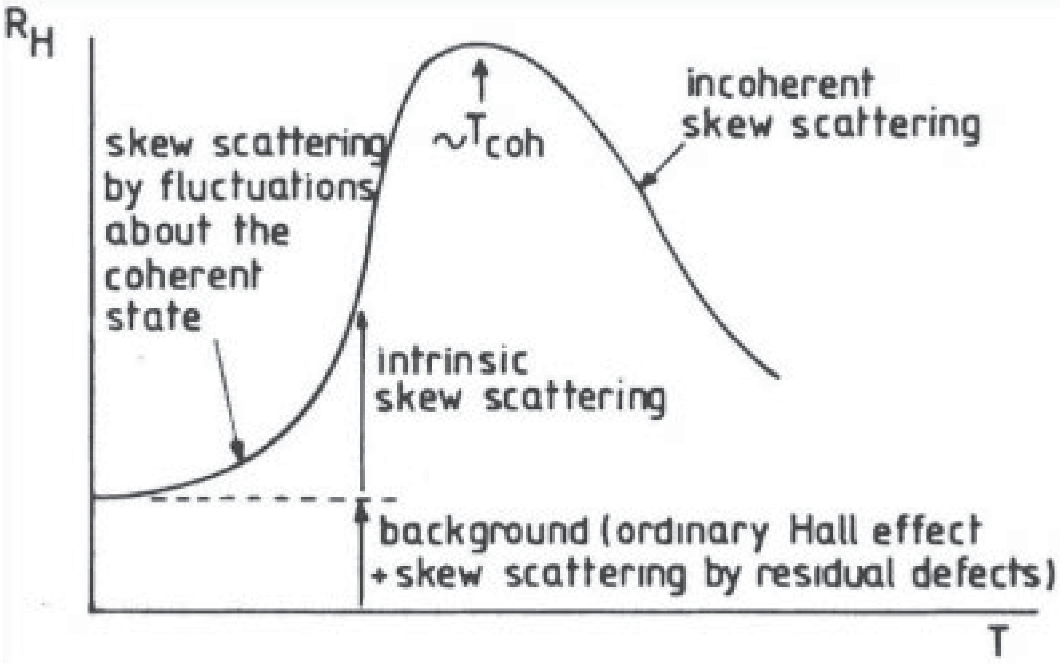

Figure 3.14: Schematic behavior of the Hall effect in heavy fermion compounds, taken from Ref. [49]; for details see text.

true, the question occurs if the general shape of the curve is affected by disorder. This would result in an influence of disorder on the coherence temperature T_{coh}, a question that will be discussed in Chapter 4.

3.2.4 Specific Heat

The specific heat represents one of the central physical quantities in the context of heavy fermion physics, as it is used to distinguish heavy fermions from "ordinary metals". Usually, the specific heat is separated into four terms:

$$c = c_{\text{el}} + c_{\text{ph}} + c_{\text{mag}} + c_{\text{nuc}}.$$

Here, c_{el} represents the electronic contribution to the specific heat, c_{ph} the specific heat of the phonons, c_{mag} the magnetic contribution and c_{nuc} the nuclear contribution to the specific heat. As the specific heat at constant volume c_{v} and that at constant pressure c_{p} are basically the same in the solid state, these two quantities are usually not distinguished here. Further, c_{nuc} is only important at very low temperatures (mK range) and therefore it is not further discussed.

Within the free electron approximation the electronic contribution to the specific heat is given by

$$c_{\mathrm{el}} = \frac{\pi^2}{3} k_{\mathrm{B}}^2 T N(E_{\mathrm{F}}), \tag{3.11}$$

with the density of states at the Fermi energy $N(E_{\mathrm{F}})$. Commonly, the linear electronic contribution to the specific heat is written as $c_{\mathrm{el}} = \gamma T$, with the Sommerfeld coefficient

$$\gamma = \frac{\pi^2}{3} k_{\mathrm{B}}^2 N(E_{\mathrm{F}}) = \frac{k_{\mathrm{B}}^2 k_{\mathrm{F}}^2 m^*}{3\hbar^2},$$

$N(E_{\mathrm{F}})$ - Fermi level density of states, k_{F} - Fermi wave vector and m^* - effective electron mass. In heavy fermion systems extraordinary large Sommerfeld parameters γ of the order of 1000 mJ/mole K^2 are observed. The Sommerfeld coefficient γ is depending linearly on the density of states at the Fermi level and thus also linearly on the effective mass of the electrons m^* (renormalisation), hence the label "heavy fermion" materials.

The phonon contribution to the specific heat c_{ph} is given by

$$c_{\mathrm{ph}} = \frac{1}{V} \sum_{ks} \frac{\partial}{\partial T} \frac{\hbar \omega_s(k)}{e^{\beta \hbar \omega_s(k)} - 1}, \tag{3.12}$$

with V the volume of the crystal, k representing the wave vector of the phonons, s denoting the branch of the phonons, $\beta = 1/k_{\mathrm{B}}T$ and $\omega_s(k)$ as the angular frequency of the phonon given by ks. As there is no analytical solution for the expression 3.12, approximation schemes are required.

For the high temperature regime the Dulong-Petit law must hold

$$c_{\mathrm{ph}} = 3nk_{\mathrm{B}},$$

with n the number of ions per unit volume, as all degrees of freedom contribute with $k_{\mathrm{B}}/2$ to the specific heat. In contrast, at low temperatures there are two models to approximate the phonon spectra. In the Debye model a linear phonon dispersion relation

$$\omega = ck$$

is assumed for the acoustic phonons, with c as a constant. It leads to

$$c_{\mathrm{ph}} = \frac{12\pi^4}{5} n k_{\mathrm{B}} \left(\frac{T}{\Theta_{\mathrm{D}}} \right)^3, \tag{3.13}$$

with the Debye temperature Θ_{D} as a measure for the stiffness of the crystal.

While the acoustic branches are usually approximated by the Debye model, the optical branches are calculated using the Einstein model. In this model the frequencies of the optical branches of the phonon spectrum are replaced by one Einstein frequency ω_{E}. However, in practice often for each optical branch p a certain Einstein frequency $\omega_{\mathrm{E,p}}$ is assigned. Assuming p optical branches leads to the optical phonon specific heat

$$c_{\mathrm{ph}}^{opt} = \sum_p nk_{\mathrm{B}} \frac{(\hbar\omega_{E,p}/k_{\mathrm{B}}T)^2 e^{\hbar\omega_{E,p}/k_{\mathrm{B}}T}}{(e^{\hbar\omega_{E,p}/k_{\mathrm{B}}T}-1)^2}. \tag{3.14}$$

At temperatures above the Einstein temperature $\Theta_{E,p} = \hbar\omega_{E,p}/k_{\mathrm{B}}$ the optical branch p contributes a constant value k_{B}/V to the specific heat, consistent with the Dulong-Petit law. At low temperatures the contribution to the specific heat evolves exponentially with temperature, reflecting that it requires a finite energy to excite optical phonons.

Additionally, another contribution to the specific heat arises in magnetically ordered materials, since the spin system also stores energy. Within mean-field theory, and ignoring fluctuations, the magnetic contribution c_{mag} of a ferromagnet per mole is given by

$$c_{\mathrm{mag}} = -\frac{3}{2} RT_{\mathrm{C}} \frac{S}{S+1} \frac{\partial}{\partial T} \left(\frac{M(T)}{M(0)} \right)^2, \tag{3.15}$$

with R as the universal gas constant. For temperatures far below the critical temperature T_{C} there is only a small contribution from the magnetic specific heat, as here the magnetization is nearly temperature independent. In the paramagnetic regime $T > T_{\mathrm{C}}$ no magnetic specific heat is observed, reflecting the fact that the spontaneous magnetization is $M(T) = 0$. Hence, only in the vicinity of the phase transition $T \to T_{\mathrm{C}}$ a substantial magnetic specific heat contribution occurs, since the derivative $\frac{\partial M^2}{\partial T}$ changes substantially, with a sharp maximum in the specific heat right at the phase transition $T = T_{\mathrm{C}}$.

While the mean-field approach reproduces the essential features of the specific heat associated to a second order magnetic phase transition, it fails to account for the T dependence of c_{mag} far below T_{C}. An improved description of c_{mag} is provided by the spin wave approximation. Consider a ferromagnetic insulator with N ordered atoms possessing spins S. Now, in a ferromagnet only acoustic (terminology analog to phonons) magnons occur with a dispersion relation

$$\hbar\omega_m(q,i) = Ja^2q^2. \tag{3.16}$$

Here, i distinguishes different magnon branches for a given wave vector q, a is the lattice parameter and J measures the strength of magnetic coupling between adjacent spins. Subsequently, the calculation is carried out as for the Debye model of the phononic specific heat, but with $\omega_m(q,i) \propto q^2$ instead of $\omega(q,i) \propto |q|$, yielding

$$c_{\mathrm{mag}}(T) = \frac{Nk_{\mathrm{B}}}{4\pi^2}\left(\frac{k_{\mathrm{B}}T}{J}\right)^{3/2}\int_0^\infty \frac{x^{5/2}exp(x)}{(exp(x)-1)^2}dx = 0.113\cdot Nk_{\mathrm{B}}(k_{\mathrm{B}}T/J)^{3/2} \tag{3.17}$$

and $V = Na^3$. To approximate above expression only next-nearest-neighbour interactions and a cubic lattice are considered, leading to a Curie temperature T_{C} given by

$$k_{\mathrm{B}}T_{\mathrm{C}} = (S+1)J. \tag{3.18}$$

Furthermore, for c_{mag} and at $T < T_{\mathrm{C}}$ it follows

$$c_{\mathrm{mag}}(T) = 0.113\cdot Nk_{\mathrm{B}}(S+1)^{3/2}(T/T_{\mathrm{C}})^{3/2}. \tag{3.19}$$

Finally, the entropy S can be calculated from the specific heat. In general, the entropy difference dS of a system is defined as

$$dS = \frac{dQ}{T},$$

with the change of heat dQ and the temperature T. The entropy can be calculated by integrating the specific heat divided by the temperature C_{p}/T

$$S = \int \frac{C_{\mathrm{p}}}{T}dT.$$

For a system with spin J, the maximum in the entropy

$$S = R\ \ln(2J+1)$$

is achieved at high temperatures.

3.2.4.1 Specific heat of $CePt_3B$

The specific heat of $CePt_3B$, as taken from Ref. [42], is plotted in Fig. 3.15 as c_P/T versus T. In addition, the specific heat for isostrucutral non-magnetic $LaPt_3B$ is included in the plot. As $LaPt_3B$ is isostrucutral and non-magnetic it is used to determine the phonon contribution to the specific heat of $CePt_3B$. Only, a correction factor $\sqrt{\frac{m_{La}}{m_{Ce}}}$ for the Debye modes has to be considered. The electronic contribution can be extracted from an extrapolation to $T = 0\,K$.

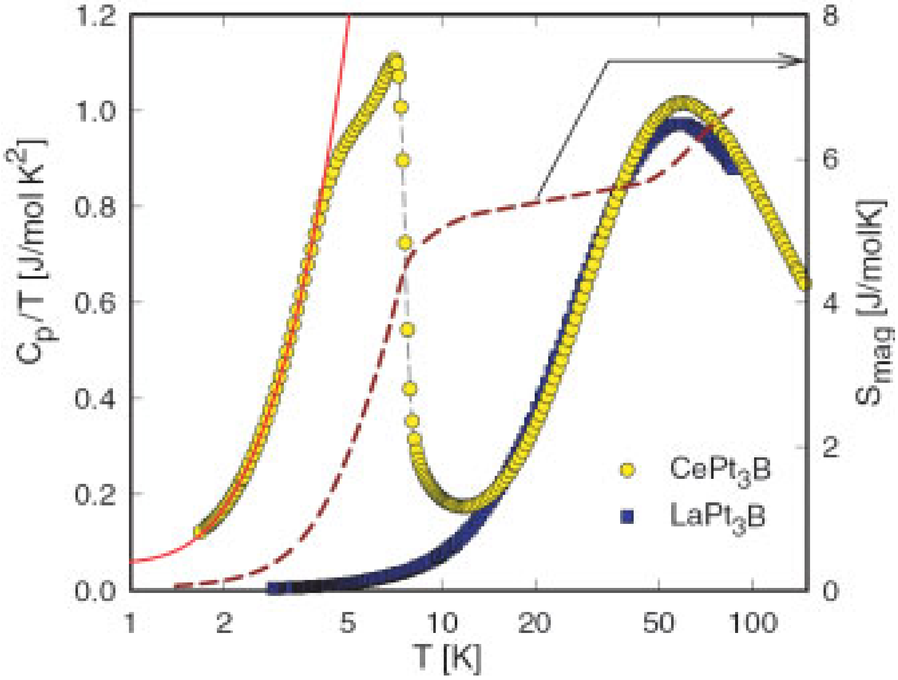

Figure 3.15: Temperature dependence of c_P/T of $CePt_3B$ (yellow dots) and $LaPt_3B$ (blue squares), taken from Ref. [42]. The red curve is a least square fit according to Eq. 3.20 plus phonon and electronic contribution. The dashed curve represents the magnetic entropy calculated from the specific heat; for details see text.

The two magnetic phase transition of $CePt_3B$ can be clearly observed as a peak in c_P for the antiferromagnetic transition at $T_N = 7.6\,K$, and as a shoulder for the ferromagnetic transition at $T_C \approx 4.5\,K$, respectively. The antiferromagnetic spin wave contribution to the specific heat is given by [54]:

$$c_{\mathrm{mag}} = \delta\Delta^{7/2}T^{1/2}\exp(-\Delta/T)\left[1+\frac{39}{20}\left(\frac{T}{\Delta}\right)+\frac{51}{32}\left(\frac{T}{\Delta}\right)^2\right], \qquad (3.20)$$

with $\delta \propto 1/D^3$. D is the spin wave velocity, Δ represents the value of the antiferromagnetic spin wave dispersion gap. Using this model Lackner *et al.* [42] obtained a gap of $\Delta \approx 7\,\mathrm{K}$ and a Sommerfeld constant $\gamma = 57\,\mathrm{mJmole^{-1}K^{-2}}$. The magnetic entropy S_{mag} is calculated after subtracting the phonon contribution by using the specific heat data of the isostructural, non-magnetic LaPt$_3$B. At T_{N} it reaches a value of about $4.5\,\mathrm{Jmol^{-1}K^{-1}}$, which is about $20\,\%$ less than the expected value of $R\ln 2$ for a spin $\frac{1}{2}$ system (Ce in a $4f_1$ state), a value only fully recovered well above T_{N}.

Besnus *et al.* [55] calculated the specific heat jump for Ce based Kondo compounds within the mean field framework. They found a close relation between the size of the specific heat jump at T_{N} and the ratio $T_{\mathrm{K}}/T_{\mathrm{N}}$. Furthermore, the entropy S_{mag}, in comparison to $12.48\,\mathrm{J/moleK}$ for a purely magnetic system [55], is suppressed. Together with the reduced peak of $c_{\mathrm{P}}(T = T_{\mathrm{N}})$, it is reflecting Kondo-type interactions. This way, a characteristic temperature $T_{\mathrm{K}} \approx 6\,\mathrm{K}$ is obtained using the calculations from Ref. [55].

Further, at higher temperatures, *i.e.*, between $20\,\mathrm{K}$ and $50\,\mathrm{K}$ the magnetic specific heat, given as the difference between c_{P} of CePt$_3$B and LaPt$_3$B is zero, resulting in a plateau in S_{mag}. This is indicating that the first excited level of the crystal electric field splitting of the ground state multiplet lies well above the ground state.

3.3 Microscopic Methods

3.3.1 Neutron scattering

Neutron scattering has become a powerful tool in solid state physics due to the physical properties of the neutron. First of all the de Broglie wavelength of a thermal neutron is of the order of interatomic distances in condensed matter. Hence, neutrons are a suitable probe to measure these distances. Apart from that, the scattering length is not a monotone function of the number of protons or nuclei in an atom, in contrast to x-ray scattering. Therefore, light elements even in the vicinity of heavy elements can be detected, with prominent examples such as deuterium in a metal or, used in this work, boron in the neighborhood of cerium.

Despite from the nuclear interaction, the neutron is a spin $\frac{1}{2}$ particle and therefore it interacts with magnetic moments. Hence, neutron scattering can be used to detect magnetic structures. As the typical energies of thermal neutrons are of the same order of magnitude as most elementary excitations in solid state physics, inelastic neutron scattering can be used to measure these excitations, *e.g.*, magnons and phonons.

The partial differential cross section $\frac{d^2\sigma}{d\Omega dE'}$ for neutrons with spin state σ, which is the number of neutrons scattered per second into a small solid angle $d\Omega$ in the direction Θ, ϕ with final energy between $E^{'}$ and $E^{'} + dE^{'}$ divided by $\Phi \; d\Omega \; dE^{'}$ is given by [56]:

$$\left(\frac{d^2\sigma}{d\Omega dE^{'}}\right)_{\sigma\lambda\rightarrow\sigma'\lambda'} = \frac{k^{'}}{k}\left(\frac{m}{2\pi\hbar^2}\right)^2 |\left\langle \boldsymbol{k'}\sigma^{'}\lambda^{'}|V|\boldsymbol{k}\sigma\lambda\right\rangle|^2\delta(E_\lambda - E_{\lambda'} + E - E^{'}). \tag{3.21}$$

Here, Φ is the flux of the incident neutrons, λ and $\lambda^{'}$ are the initial and final state of the scattering system and $\boldsymbol{k}$ and $\boldsymbol{k}^{'}$ are the initial and final state of the neutron. Correspondingly, E and $E^{'}$ are the initial and final energies of the neutron and E_λ and $E_{\lambda'}$ are the initial and final energies of the scattering system. The interaction between the neutron and the scattering system is given by V. In this work only elastic neutron scattering has been used and therefore only this topic will be discussed in further detail.

For nuclear scattering from the jth nucleus $\langle \boldsymbol{k'}|V|\boldsymbol{k}\rangle$ is given by:

$$b_j \exp(i\boldsymbol{\kappa}\cdot\boldsymbol{R_j}), \tag{3.22}$$

with the scattering vector $\boldsymbol{\kappa}$. The scattering length b_j is constant because the nuclear potential has a short range.

For magnetic scattering from the jth electron, the matrix element is [56]:

$$-\gamma r_0 \boldsymbol{\sigma}\cdot\left\{\hat{\boldsymbol{\kappa}}\times(\boldsymbol{s_i}\times\hat{\boldsymbol{\kappa}}) + \frac{i}{\hbar\kappa}(\boldsymbol{p_i}\times\hat{\boldsymbol{\kappa}})\right\}\exp\left(i\boldsymbol{\kappa}\cdot\boldsymbol{r_i}\right). \tag{3.23}$$

The factor r_0 is the classical radius of an electron $\mu_0 e^2/4\pi m_\mathrm{e}$, γ is the magnetic moment of the neutron, s_i is the spin state of the ith electron and $\boldsymbol{r_i}$ its position. $\hat{\boldsymbol{\kappa}}$ is a unit vector in the direction of $\boldsymbol{\kappa}$. The expression 3.23 is more elaborated in comparison to the corresponding nuclear counterpart. First, because the magnetic interaction is long range, and second because both, the dipole-dipole interaction for the spin and the dipole-current interaction for the orbital motion are non-central forces.

In particular for the determination of nuclear or magnetic structures the shape and the position of Bragg peaks in the diffraction pattern matters. For a ferromagnetic crystal the magnetic Bragg peaks occur at the same positions in reciprocal space as the nuclear Bragg peaks. However, there are some differences between nuclear and magnetic scattering. Nuclear scattering is weakly temperature dependent, while magnetic scattering is strongly temperature dependent as it vanishes at the Curie temperature T_{C}. More precisely, for nuclear scattering the atomic form factor is independent of the reciprocal lattice vector $\boldsymbol{\tau}$ because it is the Fourier transform of the nuclear potential which has a very short range. Hence, the only term to vary the intensity with $\boldsymbol{\tau}$ is the Debye-Waller factor. In contrast, the magnetic form factor falls rapidly with increasing $|\tau|$ as the magnetic potential has a long range.

Further, as an antiferromagnet consists of at least two interpenetrating magnetic sublattices, more complicated spin patterns are possible. For example, the most basic antiferromagnetic structure consists of oppositely aligned next nearest neighbor spins. Now, both the nuclear unit cell and the magnetic unit cell have to be considered. In this case the magnetic unit cell axes are twice as long as those of the nuclear unit cell, and therefore additional half-integer peaks in the neutron diffraction pattern are observed. As the magnetic ordering vanishes above the critical temperature T_{N} the additional peaks disappear. Moreover, aside from the information on the magnetic structure the magnitude of the magnetic moment can be estimated using neutron diffraction. Here, the nuclear peaks act as a measure for the total intensity, and by combining the knowledge of the nuclear and magnetic scattering lengths the magnetic moment can be calculated from the intensity of the magnetic peaks.

The neutron scattering experiments presented in this work have been carried out using powder diffraction (Debye-Scherrer method). In powder diffraction, the incident beam is monochromatic with wavelength λ and the sample is a powder, representing a distribution of all possible orientations of the crystallites. Hence, when illuminating the sample, Debye-Scherrer circles are observed, satisfying Bragg's law $n\lambda = 2d \sin \Theta$, d - spacing between the planes in the atomic lattice and Θ - angle between the incident beam and the scattering planes. The instruments used in this work cut out a 2D rectangle of the whole circle, resulting in diffraction lines. The intensity of these lines is integrated and detected as intensity *vs.* scattering angle.

3.3.1.1 Neutron scattering experiments on CePt$_3$B

In Ref. [34] the low temperature behavior of the bulk measurements on CePt$_3$B has been interpreted as a transition from a paramagnet to an antiferromagnet at T_N, and developing a canted antiferromagnetic structure at T_C which leads to a ferromagnetic moment [34]. As yet, a direct determination of the magnetically ordered state, and thus the fundamental information required for a verification of this scenario, is lacking.

To determine the magnetic structure of CePt$_3$B neutron scattering experiments have been carried out at the E6 spectrometer of the Berlin Neutron Scattering Center (BENSC) at the Helmholtz Zentrum Berlin in collaboration with N. Stüßer and A. Buchsteiner. A neutron wave length of $\lambda = 2.444\,\text{Å}$ has been used. Natural Boron is a very strong neutron absorber (absorption cross section $767(8)\,\mathrm{barn}$ for $2200\,\mathrm{m/s}$ neutrons), and therefore the sample examined here has been prepared using ^{11}B (absorption cross section $0.0055\,\mathrm{barn}$ for $2200\,\mathrm{m/s}$ neutrons).

The data taken at $T = 15\,\mathrm{K}$ are displayed in Fig. 3.16. These data have been fitted with the tetragonal structure model of Sologub *et al.* [41] (space group $P4mm$). Five different models have been tested, *i.e.*, occupancy of (i) B site free, (ii) Pt(1) site free, and (iii) Pt(2) site free, further (iv) leaving these parameters successively free and (v) leaving these parameters altogether free. The best result has been obtained by using model (i). Model (iv) and (v) did not yield a further reduction of $\mathrm{R}_\mathrm{Bragg}$. The occupancy of the B site has been obtained to $\sim 114\%$, reflecting a reduced occupancy of the Ce site. For model (iv) and (v) the occupancy of the Pt sites does not change significantly from stochiometric values.

The results of the refinement are summarized in Table 3.1. All parameters are in good agreement with the values obtained by Sologub *et al.* [41]. The smaller lattice parameters are reflecting a shrinking of the lattice due to the lower temperature used in our experiments, as compared to the experiments carried out by Sologub *et al.* [41].

Four Bragg peaks could not be fitted with this structure model, implying that a second phase is present in the examined sample. From the ratio of intensities between peaks associated to the $P4mm$ structure and those that could not be fitted, the volume fraction of the second phase is estimated to about $10\,\%$. Due to the small number of secondary phase peaks, the crystal structure of the second phase cannot be determined. In the refinement, by excluding the peaks associated to the second phase, a value $\mathrm{R_{Bragg}} \sim 6.2\%$ is obtained.

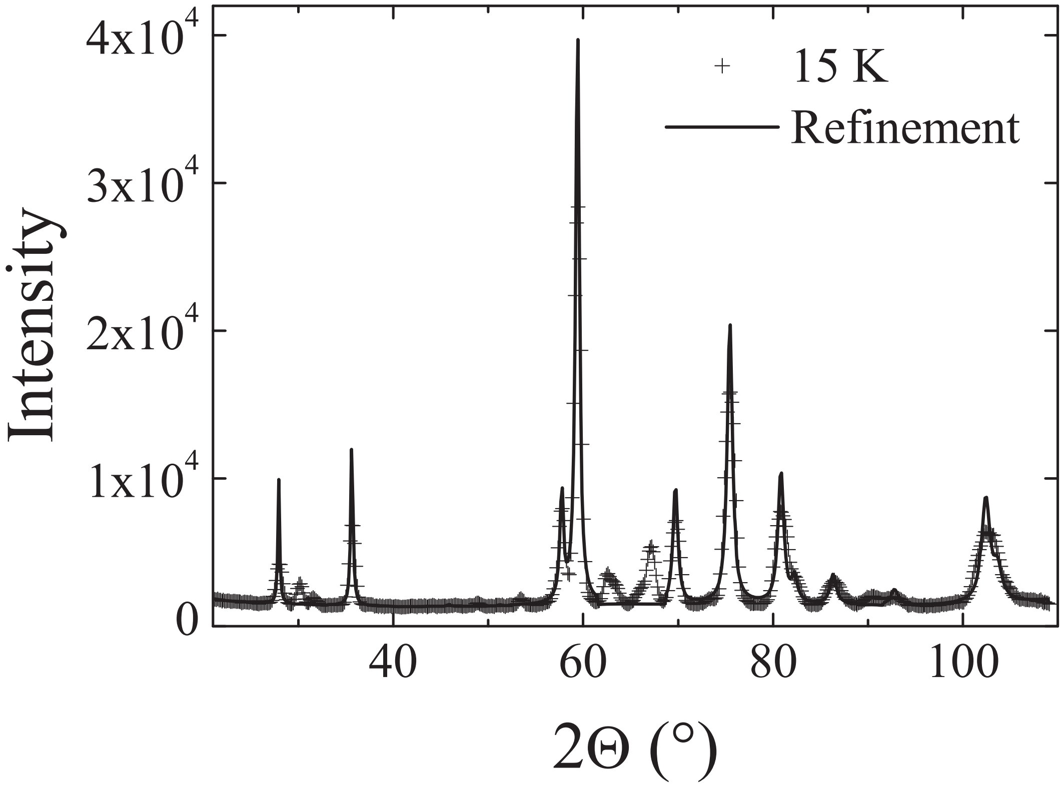

Figure 3.16: Neutron scattering pattern of CePt$_3$B (data points) and its refinement (solid line, using model (i)) at $T = 15\,\mathrm{K}$; for details see text.

In the Figs. 3.17 and 3.18 a comparison of the spectra taken at $1.6\,\mathrm{K}$ / $15\,\mathrm{K}$ and $6.55\,\mathrm{K}$ / $15\,\mathrm{K}$ are depicted. All data have been normalized to the peak at $2\Theta = 69.2\,^\circ$, which belongs to the second phase and therefore should not change upon transition into the magnetically ordered state. In addition, in the figures the difference spectra between $1.6\,\mathrm{K}$ / $15\,\mathrm{K}$ and $6.55\,\mathrm{K}$ / $15\,\mathrm{K}$ data are shown in the lower panels. In both the antiferromagnetic phase and the

	15 K	Sologub *et al.* [41]
a (Å)	3.9943(4)	4.0031(3)
b (Å)	3.9943(4)	4.0031(3)
c (Å)	5.0620(1)	5.0736(4)
R_{Bragg} (%)	6.2	4.8

15 K	x	y	z	B_{iso}
Ce	0	0	0	0.1^a
Pt(1)	0	0.5	0.522(1)	0.1^a
Pt(2)	0.5	0.5	0.131(3)	0.1^a
B	0.5	0.5	0.713(8)	0.1^a

Sologub *et al.* [41]	x	y	z	B_{iso}
Ce	0	0	0	0.587(85)
Pt(1)	0	0.5	0.5132(13)	0.429(49)
Pt(2)	0.5	0.5	0.1174(11)	0.607(75)
B	0.5	0.5	0.688(17)	1.0

Table 3.1: Results of a refinement of powder neutron diffraction data of $CePt_3B$ at $T = 15\,\mathrm{K}$, in comparison to x-ray powder diffraction refinement results of $CePt_3B$ at room temperature carried out by Sologub *et al.* [41]. In the table the lattice parameters a, b and c, the positional parameters x, y, z and the isotropic displacement factor B_{iso} for inequivalent atom sites are summarized, ^{a} is denoting a fixed parameter. The quality of the refinement is measured by R_{Bragg}; for details see text.

ferromagnetic phase additional intensity has only been found for the (1 0 0) peak at $2\Theta = 35.6\,°$. This additional integrated intensity in the difference spectrum is only ~ 2 % of the intensity of the largest peak of the CePt$_3$B lattice. No additional intensity has been found for any other examined Bragg peaks, nor have additional peaks been observed.

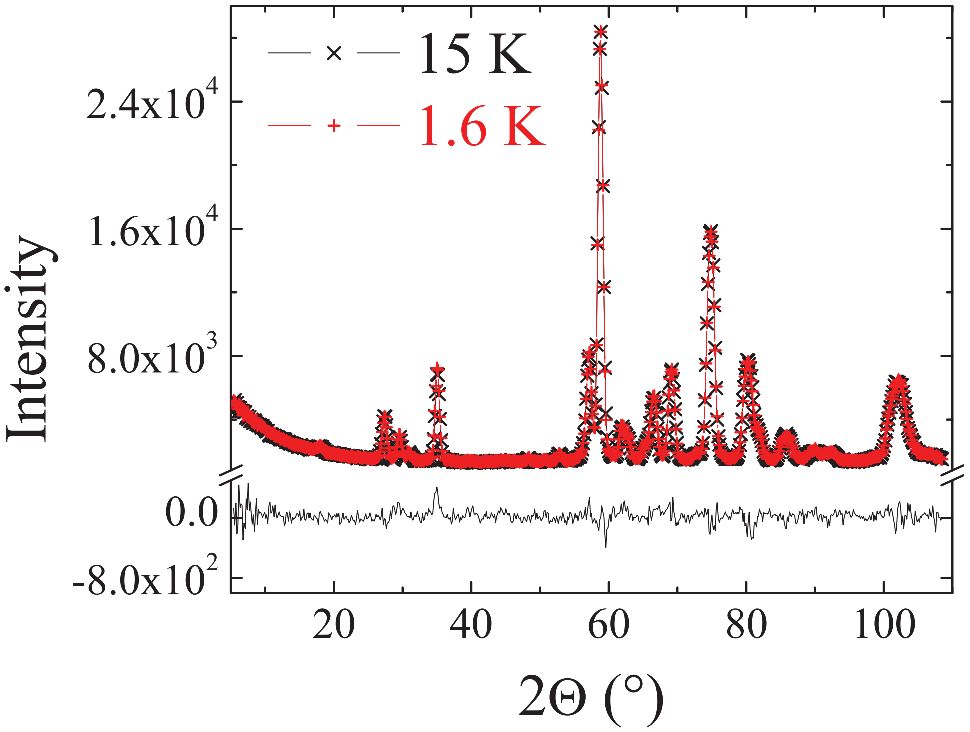

Figure 3.17: Neutron scattering pattern of CePt$_3$B, taken at 1.6 K (red) and 15 K (black). In the lower panel, the difference between the 1.6 K and 15 K data are shown; for details see text.

It implies that no information on the antiferromagnetic structure has been obtained, as no additional peaks at low temperatures are observed. As well, ferromagnetic ordering appears not be indicated by the data, despite the observation of the (1 0 0) peak intensity change, as no other peak has acquired additional intensity at low temperatures. Therefore, we believe that the additional intensity of the (1 0 0) peak is not of magnetic origin, but reflects an experimental inaccuracy of the 15 K measurement. This is supported by a detailed temperature dependence for 2Θ= 25 - 55° using a doubled counting time is depicted

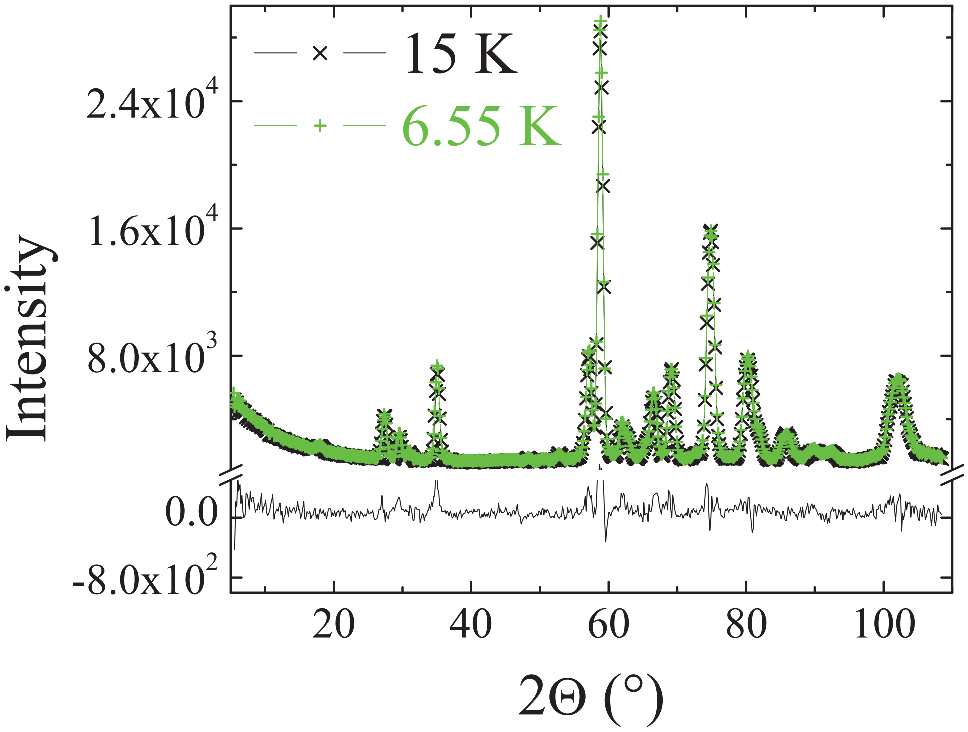

Figure 3.18: Neutron scattering pattern of $CePt_3B$, taken at $6.55\,\mathrm{K}$ (green) and $15\,\mathrm{K}$ (black). In the lower panel, the difference between the $6.55\,\mathrm{K}$ and $15\,\mathrm{K}$ data are shown; for details see text.

in Fig. 3.19. Again, no indication of magnetic ordering can be observed.

Given that no magnetic intensity is observed in our experiments, to estimate the magnetic moment that ought to be experimentally detectable, magnetic structure simulations with different magnetic moments and moment arrangements have been performed. In particular, a ferromagnetic arrangement of the magnetic moments and an antiferromagnetic arrangement with a doubling of the unit cell in a direction have been assumed, see Figs. 3.20 and 3.21.

These simulations indicate that a magnetic moment of $0.5\,\mu_\mathrm{B}$ in the ferromagnetic and $0.2\,\mu_\mathrm{B}$ in the antiferromagnetic case should be detectable in our experiments. The absence of a magnetic signature in the E6 measurements could either indicate that the actual sample used here does not exhibit magnetic order and the susceptibility signal stems from the second phase, or that the ordered moment is below the detection limit of the E6 instrument. Thus, in order to

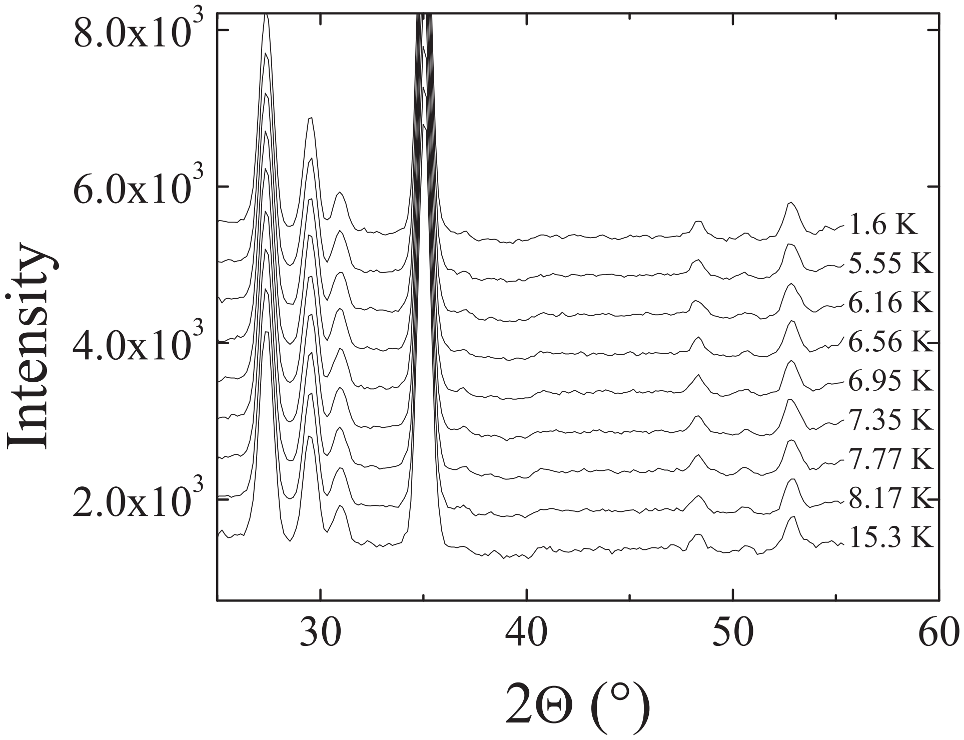

Figure 3.19: Neutron scattering pattern of CePt$_3$B at various temperatures; for details see text.

decide between these two scenarios, μSR measurements have been performed.

3.3.2 μSR measurements

In contrast to neutron scattering measurements, μSR is a local probe technique, *i.e.*, information on the magnetic behavior stems from the direct vicinity of the probing object, *viz.*, the muon. Due to the large magnetic moment of the muon (3.18 times larger than a proton), μSR is able to detect very small internal magnetic fields of the order of 10^{-5} T. Furthermore, μSR experiments can distinguish magnetic and non-magnetic phases co-existing in the same sample. The amplitudes of the μSR signals from ordered/non-ordered phases are proportional to the volume of the sample occupied by those particular phases.

The muon is an elementary particle with spin $\frac{1}{2}$, a mass of roughly 200 electron masses and a charge that could be either positive or negative with an absolute

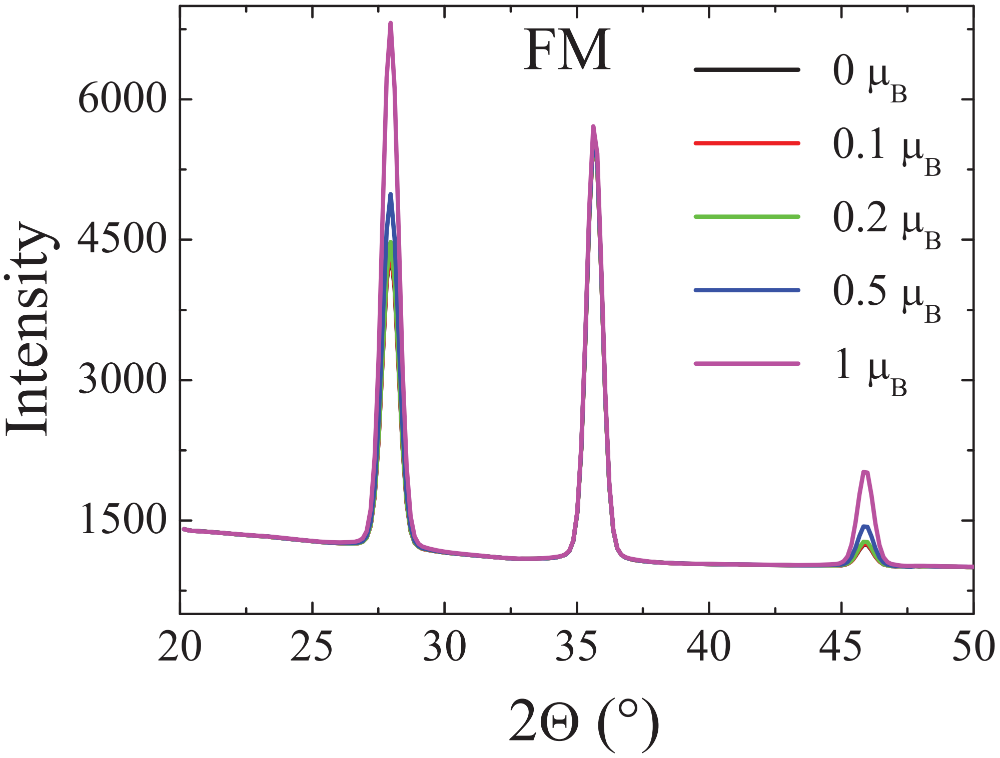

Figure 3.20: Simulated neutron scattering pattern of $\mathrm{CePt_3B}$ assuming a ferromagnetic alignment of the moments of size as given in the figure; for details see text.

value of $|e|$. For μSR spectroscopy the positive muon μ^+ is commonly used instead of the negative muon μ^-, because the μ^- will be localized close to an atom nucleus while the μ^+ will go to interstitial sites of the lattice.

In μSR facilities muons are produced by directing a beam of medium energy protons ($E \geq 500$ MeV) on a target which consists usually of light elements like beryllium or carbon. In this subsequent decay process positive pions (π^+) are produced which decay with $\tau_\pi = 26\,\mathrm{ns}$:

$$\pi^+ \longrightarrow \mu^+ + \nu_\mu. \tag{3.24}$$

The muon beam resulting from this decay process is completely spin polarized, as the pion (π^+) is a $S = 0$ particle (in the inertial frame of the pion) and the neutrino ν_μ has a spin antiparallel to its momentum. Hence the muon μ^+ also has a spin antiparallel to its momentum.

A typical experimental setup for a zero field μSR experiment is depicted in

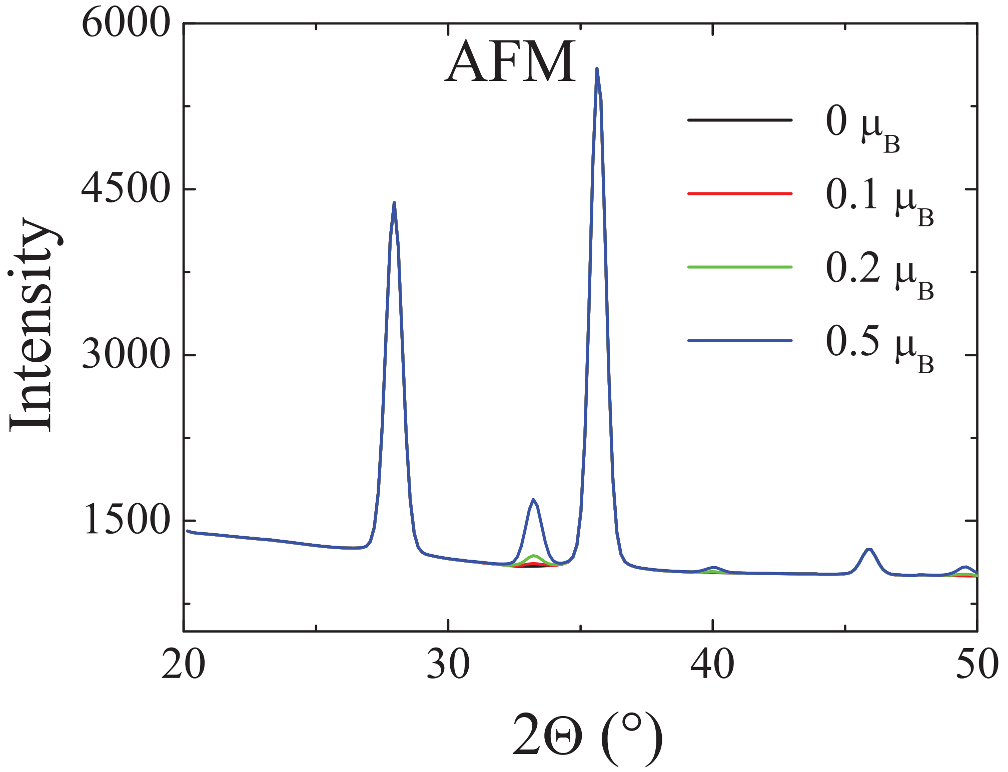

Figure 3.21: Simulated neutron scattering pattern of CePt$_3$B assuming an antiferromagnetic alignment of the moments of size as given in the figure; for details see text.

Fig. 3.22. After implanting the muon in the sample it loses its energy by Coulomb interaction mediated scattering processes which do not influence its spin polarization. Finally, the muon rests on an interstitial site. In a magnetic field B the muon-spin precesses with the Larmor frequency $\omega_\mu = \gamma_\mu B$, where $\gamma_\mu = ge/2m_\mu$ is the gyromagnetic ratio for the muon. It decays with a lifetime $\tau_\mu = 2.2\,\mu$s in a three particle process:

$$\mu^+ \longrightarrow e^+ + \nu_\mathrm{e} + \bar{\nu_\mu}. \tag{3.25}$$

The energy of the positrons vary, based on the momentum distribution between the three particles. The μ decay, as a weak decay, violates the parity symmetry, *viz.*, more positrons e^+ are emitted in the direction of the μ^+ spin than in the opposite direction. The positrons are counted by detectors which are positioned in front and behind the sample. As an example, the angular dependence displayed for emitted positrons with highest energy is depicted in Fig. 3.23.

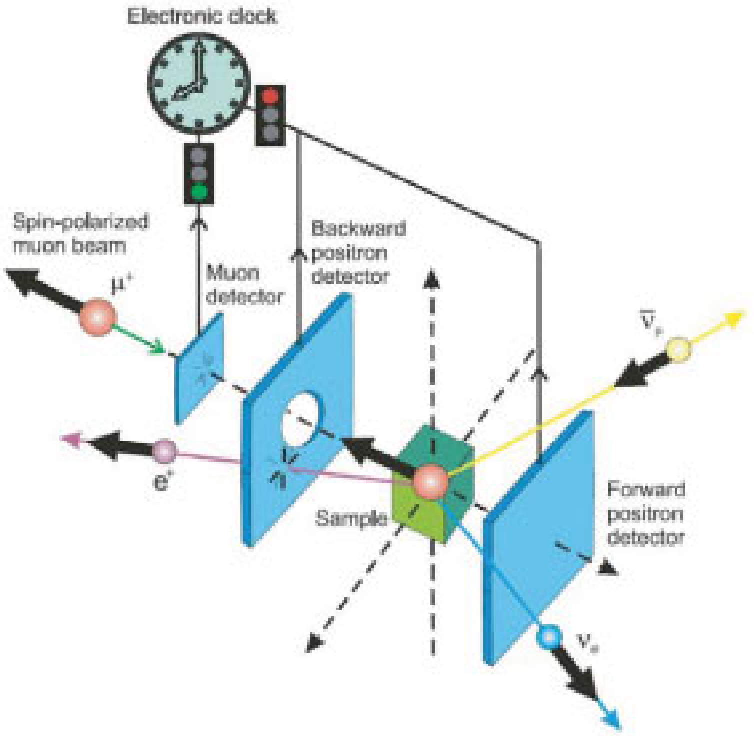

Figure 3.22: Typical experimental setup for a zero field μSR experiment, taken from Ref. [57]; for details see text.

However, in a μSR experiment an integration over all energies is measured. In this case, the angular dependence is not as pronounced as in Fig. 3.23, but a substantial asymmetry also in the direction of the spin is observed. From the precession of the muon spin the internal magnetic field at the local muon site can be estimated.

3.3.2.1 μSR measurements on CePt$_3$B

To decide whether the discrepancy between susceptibility data and neutron scattering experiments stems from a second phase, or if the magnetic moment is too small to be detected in our neutron scattering experiment, μSR experiments on CePt$_3$B have been carried out at the Paul Scherrer Institut in collaboration with H.-H. Klauß and H. Luetkens. In these zero field μSR experiments

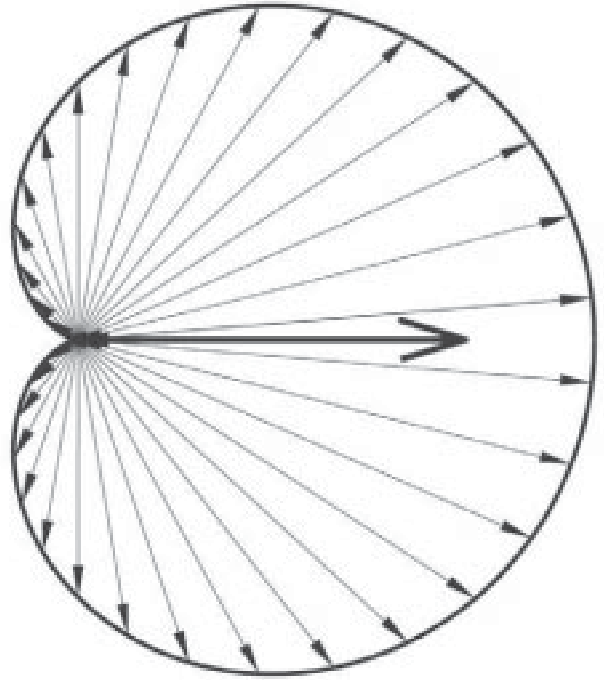

Figure 3.23: Angular dependence of μ^+ decay for emitted positrons with highest energy [58]. The big arrow is indicating the direction of the muon spin; for details see text.

a distinct μSR oscillatory signal is observed below T_{N} (see Fig. 3.24), implying an ordered local moment below T_{N}.

From the time dependence of the muon signal the oscillation frequency is determined as function of temperature. The frequency of these oscillations together with the inverse susceptibility χ^{-1} are depicted in Fig. 3.25. Both transition temperatures T_{N} and T_{C} are observed in the muon oscillation frequency and in the susceptibility data indicating the presence of an ordered magnetic moment of the order of $1\,\mu_{\mathrm{B}}$ at the Ce site. An ordered moment of this size ought to be detectable in neutron scattering experiments.

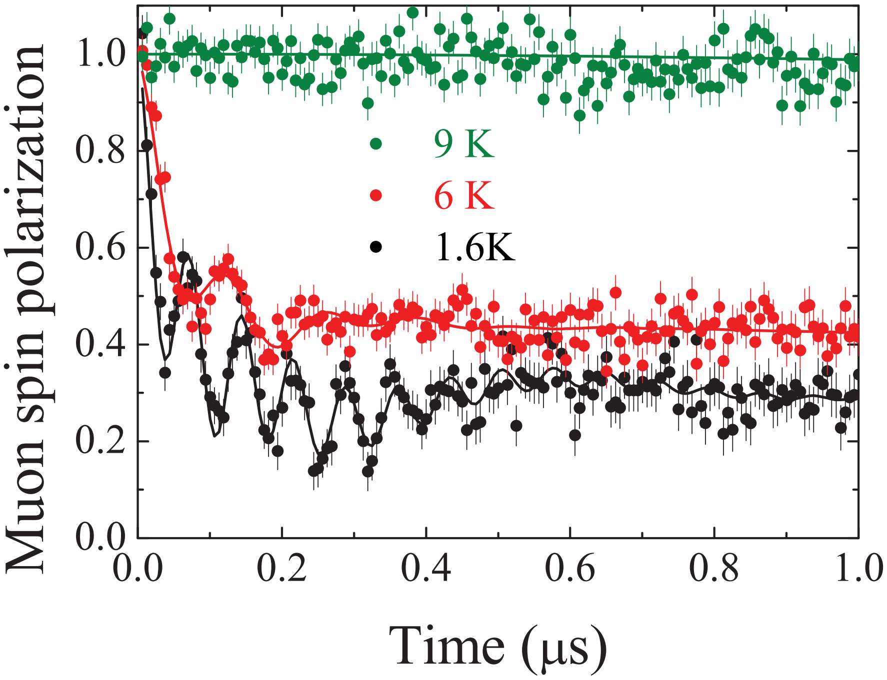

Figure 3.24: Time dependence of the μ^+ spin polarization of CePt$_3$B. Fro clarity, only selected temperatures of $T = 1.6\,\mathrm{K}$; $6\,\mathrm{K}$ and $9\,\mathrm{K}$ are plotted; for details see text.

3.4 Conclusion of the investigation of CePt$_3$B$_{1-x}$Si$_x$

In conclusion, the investigations on the alloying series CePt$_3$B$_{1-x}$Si$_x$ confirmed the bulk properties of CePt$_3$B as reported by Ref. [34]. The alloyed samples CePt$_3$B$_{1-x}$Si$_x$, $x = 0.2, 0.4$ exhibited lower transition temperatures T_N and T_C. The structural properties, investigated by neutron scattering experiments, are in good agreement with those reported in Ref. [41], with evidence for a small amount of a secondary phase ($\sim 10\%$ volume). The μSR experiments show unambiguously the existence of an ordered moment of the order of $1\,\mu_\mathrm{B}$. Taking the susceptibility and μSR measurements together, we can conclude that the magnetism is a bulk property of CePt$_3$B. So far, the reason for the difference in observations between neutrons and μSR/susceptibility measurements is not clear and will require further investigations.

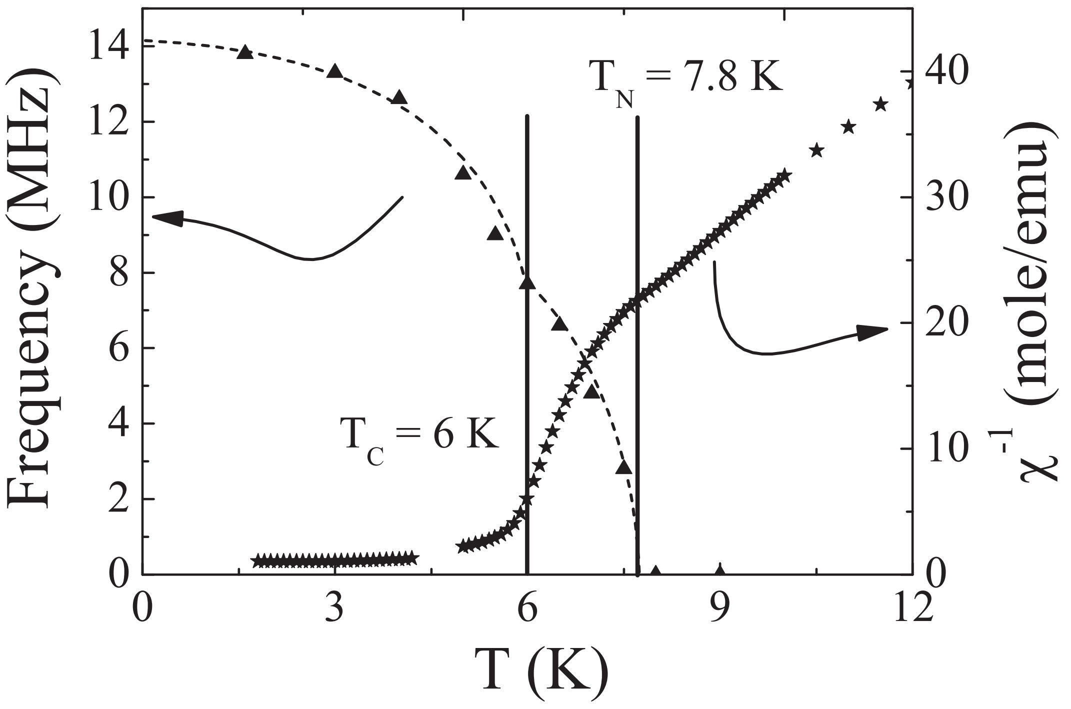

Figure 3.25: Oscillation frequency of the muon signal obtained from μSR experiments, together with the inverse susceptibility χ^{-1} of CePt$_3$B. The dashed line is an extrapolation; for details see text.

3.4.1 X-ray resonant scattering

X-ray diffraction is a standard experimental tool to investigate ordered structures, *i.e.*, structures of crystals or molecules like DNA. Now, x-rays do not only couple to the electron shell of an atom but also to a magnetic moment. However, using a common laboratory x-ray tube magnetic diffraction is rather difficult to observe, as the magnetic scattering contribution is only a relativistic correction to the total scattering cross section and therefore its intensity is six orders of magnitude smaller than charge scattering. Hence, using standard x-ray tubes it took until 1972 for the first successful x-ray magnetic diffraction experiment [59].

In recent years, with the availability of synchrotron radiation sources it has become much more convenient to perform magnetic scattering experiments. In consequence, nowadays magnetic scattering experiments provide various informations on magnetic correlation lengths, the local magnetic moments, the magnetic structure and phase transitions.

However, even using synchrotrons the intensity of magnetic diffraction is still several orders of magnitude weaker than charge scattering. Therefore, magnetic scattering is still difficult, and only the discovery of resonant scattering changed the situation. Resonant scattering leads to a significant resonant enhancement for the magnetic cross section. It occurs at an absorption edge, where a core level electron is promoted to an unoccupied state above the Fermi energy. Afterwards the unoccupied core electron state is filled again, which is associated by a reemission of a photon.

Theoretically, these transitions can be described in terms of magnetic and electric multipole expansions. In the x-ray energy regime it turns out that predominantly the electric dipole and electric quadrupole transitions contribute, hence only these contributions are considered. In the $4f$-elements mainly the L_{II} ($2p \rightarrow 5d$, dipolar) and L_{III} ($2p \rightarrow 4f$, quadrupolar) as well as the M_{II} ($3p \rightarrow 5d$, dipolar) and M_{III} ($3p \rightarrow 4f$, quadrupolar) edges are of interest. In the case of $5f$-elements, the M_{IV} edge is of particular interest as it directly provides a dipolar connection between the $3d_{3/2}$ states and the $5f$-states. By convention, electric dipolar transition are labeled E1, electric quadrupolar transitions are labeled E2.

For the following considerations it is important to perform polarization analysis of the scattered x-rays. Radiation, as provided by a synchrotron, is mainly linear polarized, making polarization dependent experiments possible. The radiation is linearly polarized in the plane of the synchrotron, while above and below this plane it is circular polarized to some extend. The polarization plane is defined with respect to the scattering plane, by convention σ-polarisation is perpendicular and π-polarisation is parallel to the scattering plane. Hence, in an experiment in vertical geometry the incident radiation is σ-polarized. In Fig. 3.26 a typical vertical scattering geometry is depicted.

Hence, a study of polarization changes for the scattered beam is very convenient. The unrotated $\sigma - \sigma$ and rotated $\sigma - \pi$ components of the scattered beam are separated by an analyzer crystal. For the polarization analysis we take advantage of the fact that for pure charge scattering in a dipole transition only $\sigma - \sigma$ scattering is allowed. Therefore, for analyzing the polarization of the scattered beam the analyzer crystal is aligned to scatter only the $\sigma - \sigma$ component. After rotating the analyzer crystal by 90° around the scattered

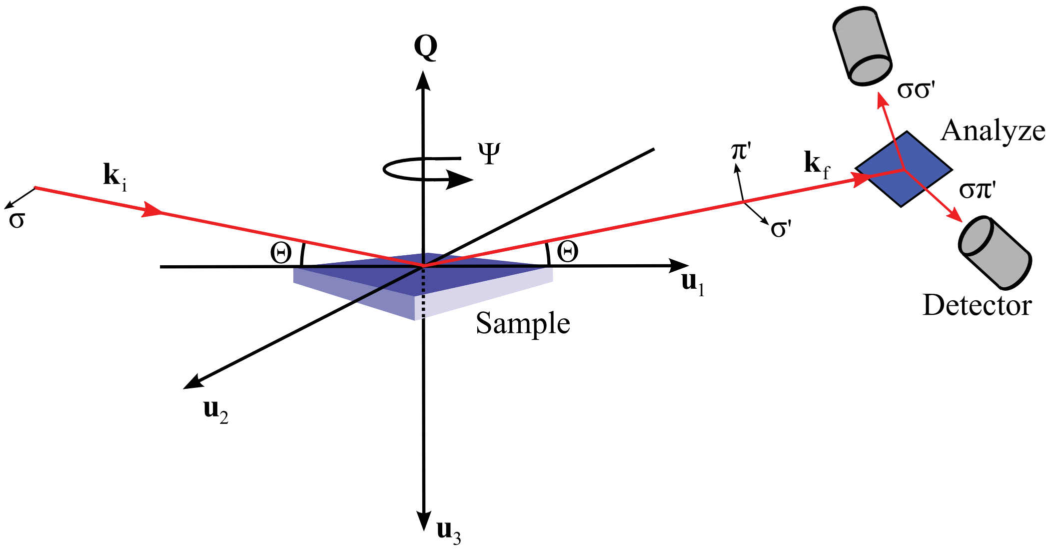

Figure 3.26: Vertical scattering geometry for an x-ray scattering experiment. For clarity, only the σ component of the incident beam is depicted. Polarization analysis can be performed by rotating the detector. Azimuthal dependent experiments can be performed by rotating Ψ; for details see text.

beam, only the $\sigma - \pi$ component is scattered by the analyzer crystal. Hence, by rotating the analyzer around the scattered beam the unrotated $\sigma - \sigma$ and the rotated $\sigma - \pi$ components of the scattering can be determined.

Furthermore, by varying Ψ, an azimuthal dependence of the scattering can be measured, which reflects the shape of the electron distribution on the scattering atoms. A detailed theory of the polarization dependence for resonant x-ray scattering is given by Hill and McMorrow [60]. The resonant dipole scattering amplitude for an incommensurate antiferromagnet is given by

$$\begin{aligned} f_{nE1}^{XRES} &= F^{(0)} \begin{pmatrix} 1 & 0 \\ 0 & \cos 2\Theta \end{pmatrix} \qquad (3.26) \\ &- iF^{(1)} \begin{pmatrix} 0 & z_1 \cos\Theta + z_3 \sin\Theta \\ z_3 \sin\Theta - z_1 \cos\Theta & -z_2 \sin 2\Theta \end{pmatrix} \\ &+ iF^{(2)} \begin{pmatrix} z_2^2 & -z_2(z_1 \sin\Theta - z_3 \cos\Theta) \\ +z_2(z_1 \sin\Theta + z_3 \cos\Theta) & -\cos^2\Theta(z_1^2 \tan^2\Theta + z_3^2) \end{pmatrix}, \end{aligned}$$

where Θ is the Bragg angle. The first term describes the charge scattering, the second term produces first harmonic magnetic satellites and the last term stems from second harmonic satellites.

Even though the intensity of the quadrupolar transition is typically weaker than the intensity of the dipolar transition, it still can be significant in experiments. The quadrupolar scattering amplitude can also be found in Hill and McMorrow [60], but will not be further considered here.

In principle, with the two expressions for the dipolar and quadrupolar contribution to the resonant process, in an azimuthal angle dependence experiment we can determine if the origin of the scattering is due to charge or magnetic ordering. Furthermore, the orientation of the magnetic moments are accessible.

Altogether, the scattering amplitude is given by

$$A = \epsilon' \cdot f \cdot \epsilon, \tag{3.27}$$

with ϵ (ϵ') the polarization of the incident (scattered) beam. f is the resonant scattering length of the unit cell, given by

$$f = \sum_n D_n \exp(i\boldsymbol{Q} \cdot \boldsymbol{r_n}), \tag{3.28}$$

with $\boldsymbol{Q}$ the scattering vector and $\boldsymbol{r_n}$ the position of the n-th atom. D_n represents the resonant scattering length of the n-th atom.

With this brief overview of x-ray resonant scattering the basic principles to discuss the experiments on PrB_6 in Chapter 7 are provided. Furthermore, the background to understand the experiments to determine the ordering parameter in UPd_3 is given.

4 Disorder effects in UPd_2X, X=Sb, Sn

4.1 Introduction

UPd_2X, X = Sb and Sn, belong to the class of UT_2M compounds, where T is a d-electron metal and M a heavier metal such as In, Sn, Sb or Pb. Many of these systems are moderately mass enhanced to heavy fermion like f-electron intermetallics. Altogether, the class of compounds UT_2M displays a rich variety of different physical properties, such as:

- structural instabilities like in UPd_2In [61] and UNi_2Sn [62];
- antiferromagnetic ordering, *e.g.*, in UPd_2In [61], UCu_2Sn [63] or UPd_2Pb [64];
- Pauli paramagnetism like in UNi_2Sn [62, 63] and UNi_2In [65];
- multiple magnetic transitions, *e.g.*, in UPt_2In from Pauli paramagnetism to antiferromagnetism, and subsequently at low temperatures ferrimagnetic ordering. [66]

The compounds UT_2M have been subject to a very extensive set of studies for more than two decades by now. Most of these compounds crystallize in the cubic Heusler structure or in a structure derived from the Heusler lattice but with lower symmetry. For example, the related structures with lower symmetries have been found in UCu_2Sn ($P6_3/mmc$) [63] and UAu_2Al ($Pnma$) [65]. In Fig. 4.1 the Heusler lattice and the orthorhombic $Pnma$ structure are displayed to visualize the affinity between these two crystal structures. These observations reflect the tendency towards structural instabilities for the class of UT_2M materials, a tendency found for Heusler compounds in general, *e.g.*, in the archetypical ferromagnetic shape memory alloy Ni_2MnGa [67] or the related system Co_2NbSn [68]. Both compounds show a structural transition at $T_S \sim 200 - 400\,K$ for Ni_2MnGa and $200 - 250\,K$ for Co_2NbSn, respectively

[67, 68]. The temperature at which the transition takes place strongly depends on the actual stoichiometry of the sample.

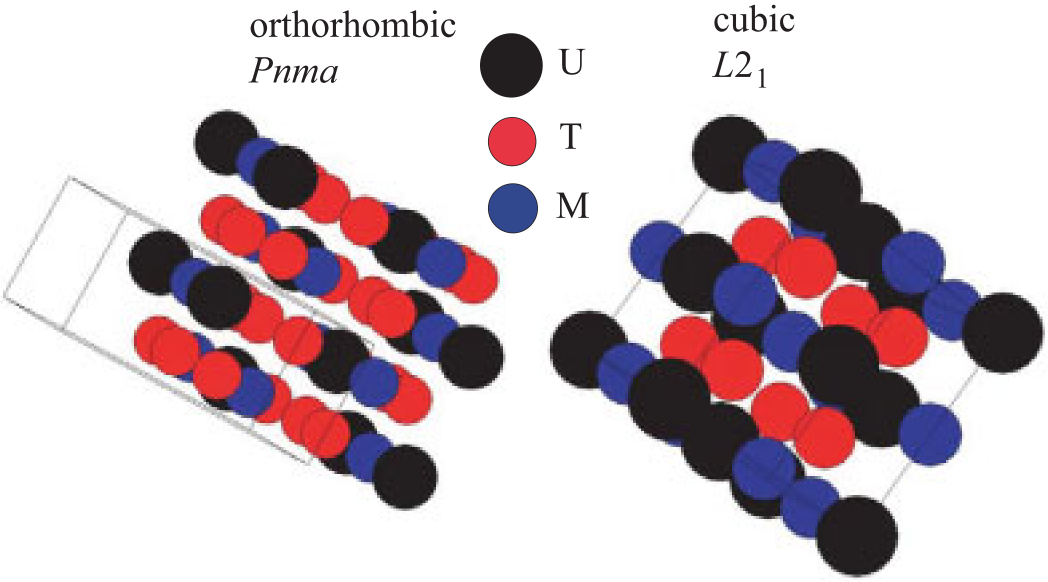

Figure 4.1: Cubic Heusler $L2_1$ in comparison to the orthorhombic $Pnma$ structure. The unit cell is indicated by black lines, for details see text.

Structural disorder is an important topic in heavy fermion systems, *e.g.*, even moderate disorder in the vicinity to a quantum critical point can lead to non-Fermi liquid behavior [69], extraordinary large residual resistivity values for such intermetallic Uranium compounds or even a non-metallic behavior of the temperature dependence of the resistivity.

4.1.1 Review of the class of compounds: UT$_2$M

In the following, an overview of UT$_2$M compounds investigated in recent years is given. In particular, the structural properties and those physical properties related to the level of disorder have been summarized.

For the compounds UT$_2$In, as it can be seen in Table 4.1, that with the lightest transition element T (Ni) crystallizes in a stable Heusler structure. With increasing the atomic mass number to Pd, and thus the atomic diameter of the transition metal element, a structural phase transition at $T_{\mathrm{S}} = 180\,\mathrm{K}$ occurs (for atomic radii, see Table 4.2). Takabatake *et al.* [61] performed x-ray diffraction experiments on the low temperature phase of UPd_2In, but they were not able to index the diffraction peaks, hence the low temperature structure of UPd_2In is still not resolved. In case of the $5d$ element Pt [66] the crystal lattice is not even the cubic $L2_1$ Heusler structure anymore, but of hexagonal $P6_3/mmc$ symmetry. Hence, for this group of materials there is a structural instability, possibly as result of the ionic diameter or atomic mass of the transition metal.

This trend is not followed by UAu_2In, as this compound crystallizes in the cubic Heusler structure as reported for the compounds with lighter transition elements. However, for both UPd_2In and UAu_2In the residual resistivity is large and the ratio of the resistivity between room temperature and low temperature (ρ_{300}/ρ_0) is small, indicating the presence of structural disorder in these materials. In contrast, the other two samples UNi_2In and UPt_2In show a small residual resistivity and a resistivity ratio of the same order of magnitude as for common metallic heavy fermion systems, reflecting a well ordered crystal structure.

In the family of compounds UT_2Sn the issue concerning the structural properties is more complicated and no clear trend is detectable. However, the existence of three different crystal structures and the presence of a structural transition in UNi_2Sn and UAu_2Sn again indicates structural instabilities in this family of compounds. Moreover, some of the samples show a large residual resistivity, *e.g.*, UNi_2Sn: $\rho_0 = 206\,\mu\Omega\mathrm{cm}$ and UAu_2Sn: $\rho_0 = 125\,\mu\Omega\mathrm{cm}$, and a small resistivity ratio ρ_{300}/ρ_0 of 0.74 and 1.08, respectively. All the compounds listed in Table 4.3 are characterized by comparatively small resistivity ratios, with the highest value of ~ 13 for UPd_2Sn, reflecting a stronger tendency for UT_2Sn towards structural instabilities than for the family UT_2In.

In Fig. 4.2 the different crystal structures as function of temperature of the compounds UT_2Sn and UT_2In are summarized. The compounds in the upper left corner, UNi_2Sn to UPd_2In, feature cubic Heusler structure at room temperature. At lower temperatures UNi_2Sn shows a phase transition at $\sim 220\,\mathrm{K}$, whereas, in the family UT_2In two members, UPd_2In and UNi_2In, crystallize in the cubic Heusler structure with an additional structural transition of UPd_2In at $180\,\mathrm{K}$. Hence, there is the tendency to build stable Heusler structures for the family UT_2In, whereas the tendency to structural instabilities is more pro-

UT$_2$In	**Ni** (*3d*)	**Pd** (*4d*)	**Pt** (*5d*)	**Au** (*5d*)
Crystal structure	cubic	cubic	hexagonal	cubic
Space group	$L2_1$	$L2_1$	$P6_3/mmc$	$L2_1$
a (Å)	6.501	6.804	4.569	6.969
c (Å)	-	-	8.920	-
Type of magnetism	PP	AFM	Multi	AFM
T_N (K)	-	20	35	70
Θ_CW (K)	31	-307 (-111)	-178	n.r.
μ_eff (μ_B)	n.r.	3.78 (3.16)	3.25	3.50
γ (mJ/mole K^2)	45	200	100	n.r.
$\rho_0(\mu\Omega cm)$	~4	~150	~3	~ 75
ρ_{300}/ρ_0	25.5	~0.9	~41	~1.7
specials		structural transition at 180K		
Ref.	[63]	[61]	[66]	[70]

Table 4.1: Physical properties of UT$_2$In. Abbreviations: AFM denotes antiferromagnetism with the Néel temperature T_N, PP indicates Pauli paramagnetism and Multi that multiple magnetic transitions were found at different temperatures (with the highest transition temperature listed in the table). "n.r." indicates that the corresponding parameter has not been reported, the parameter values for UPd$_2$In given in brackets are measured below the structural transition occurring at $180\,\mathrm{K}$.

element	**Ni** (*3d*)	**Cu** (*3d*)	**Pd** (*4d*)	**Pt** (*5d*)	**Au** (*5d*)
empirical atomic radius	135	135	140	135	135

Table 4.2: Empirical atomic radii of Ni, Cu, Pd, Pt and Au, from Ref. [71].

UT$_2$Sn	**Ni** (*3d*)	**Cu** (*3d*)	**Pd** (*4d*)	**Pt** (*5d*)	**Au** (*5d*)
Crystal structure	cubic	hexagonal	orthorhombic	hexagonal	hexagonal
space group	$L2_1$	$P6_3/mmc$	$Pnma$	$P6_3/mmc$	$P6_3/mmc$
a (Å)	6.459	4.459	9.9787	4.550	4.704
b (Å)	-	-	4.58843	-	-
c (Å)	-	8.712	6.89166	9.021	9.208
Type of magnetic order	PP	AFM	PP	AFM	PP
T_{N} (K)	-	16.6	-	60	-
Θ_{CW} (K)	n.r.	-89	-77	-220	n.r.
μ_{eff} (μ_{B})	n.r.	3.36	3.18	3.61	n.r.
γ (mJ/mole K^2)	45	60	70	17	n.r.
$\rho_0(\mu\Omega cm)$	206	105	14	35	125
ρ_{300}/ρ_0	0.74	4.1	13	9.2	1.08
specials	structural transition $\sim 220\,\mathrm{K}$	Ferroquadrupolar ordering at $16\,\mathrm{K}$			structural transition $\sim 1090\,\mathrm{K}$ from $L2_1$ to $P6_3/mmc$
Ref.	[62, 63, 72]	[65, 73]	[74, 75]	[65]	[70, 76]

Table 4.3: Physical properties of UT$_2$Sn, with abbreviations as in Table 4.1.

nounced in the class UT$_2$Sn.

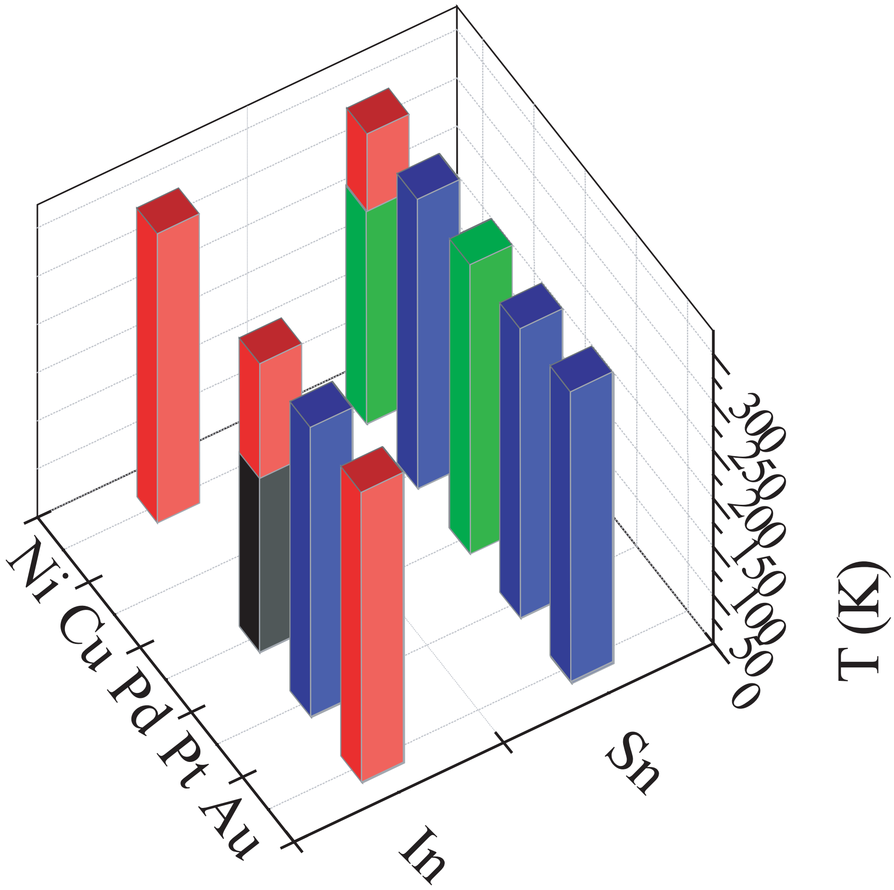

Figure 4.2: Crystal structure as function of temperature and transition metal ion T in UT$_2$Sn and UT$_2$In. Green denotes orthorhombic $Pnma$, blue hexagonal $P6_3/mmc$, red cubic $L2_1$ and black implies that the structure has not been resolved so far.

Beside the two above mentioned families of Uranium compounds, two other compounds, UAu$_2$Al and UPd$_2$Pb, have been investigated in the literature, see Table 4.4. Also these compounds have a rather small resistivity ratio ρ_{300}/ρ_0 of 1.7 and 9.5, suggesting some level of crystallographic disorder.

Altogether, this summary reflects that a tendency towards a structural instability is inherent to U based Heusler compounds. Insofar this instability does not lead to a structurally fully relaxed lattice, it appears that it causes strain and structural disorder in the compounds. Combining this observation with the presence of strong electronic correlations, the physical properties of U based Heusler compounds depend sensitively on the actual sample quality.

compound	**UAu_2Al**	**UPd_2Pb**
Crystal structure	orthorombic	cubic
space group	*Pnma*	$L2_1$
a (Å)	7.683	6.85
b (Å)	7.239	-
c (Å)	5.730	-
Type of magnetic order	AFM	AFM
T_N (K)	25	35
Θ_CW (K)	-97	-51
μ_eff (μ_B)	2.96	2.8
γ (mJ/mole K^2)	102	98
$\rho_0(\mu\Omega cm)$	$\sim$35	n.r.
ρ_{300}/ρ_0	9.5	1.7
Ref.	[65]	[64]

Table 4.4: Properties of uranium based Heusler compounds, abbreviations as in Tab. 4.1.

In this context, one additional difficulty is associated with the preparation of the samples, *i.e.*, the low melting point of some of the constituents, *e.g.*, for Sn and In (T_m = 232°C and 156.2°C, respectively). Together with the high melting point of 1132.4°C for uranium and the different transition metals, the vapor pressure of the low melting constituents is already comparatively large before all elements are melted and mixed during the synthesis procedure. In this situation, preferential evaporation of some elements might occur during sample preparation, resulting in off-stoichiometric material.

However, structural investigations by means of microscopic methods have been performed on $UPd_{2-x}Sn$ [77]. Therefore, the question arises if the structural disorder properties found for $UPd_{2-x}Sn$ also exists in other members of the class of compounds UT_2M.

4.2 Structural and magnetic properties of UPd_2Sb

In order to further understand the relevance of structural instabilities and the types of structural disorder a case study material from the class of compounds UT_2M is needed. UPd_2Sb is a suitable candidate as this compound has a small resistivity ratio indicating the presence of disorder. Therefore, UPd_2Sb was selected to investigate the structural properties by means of neutron scattering.

4.2.1 Crystal structure

The uranium based heavy fermion compound UPd_2Sb has been synthesized and characterized for the first time by Gofryk *et al.* [78]. The samples which have been examined in this work were synthesized by arc-melting the constituents in stoichiometric ratio (U: 2N8, Pd: 5N, Sb: 5N) under titanium-gettered argon atmosphere. The buttons were remelted several times to ensure good homogeneity. No further heat treatment was applied [78].

Subsequently, in Ref. [78], the crystal structure was checked at room temperature using a Siemens D5000 x-ray powder diffractometer with Cu K_α radiation. From the x-ray measurements the sample appears to be single phase with cubic symmetry and a lattice parameter of $a = 6.766(2)$ Å at room temperature [78]. Based on the x-ray diffraction pattern Gofryk *et al.* [78] suggested that the material crystallizes in a Heusler lattice.

4.2.2 Transport properties

The temperature dependence of the electrical resistivity ρ of UPd_2Sb, as measured in Ref. [78], is depicted in Fig. 4.3. At room temperature the resistivity is about $210\,\mu\Omega\mathrm{cm}$. Such an order of magnitude is large, but not absolutely uncommon for uranium intermetallics. However, quite uncommonly, with decreasing temperature the resistivity is continuously increasing and reaches a value of $262\,\mu\Omega\mathrm{cm}$ at lowest temperature. The antiferromagnetic phase transition can be seen as an additional, but rather smooth upturn of $\rho(T)$. Its signature is more pronounced in the temperature dependence of the derivative of the resistivity $\frac{d\rho}{dT}(T)$, see inset Fig. 4.3.

Above the phase transition the data have been fitted assuming Kondo behavior [78]

$$\rho(T) = \rho_0 + \rho_0^\infty + c_\mathrm{K} \ln T,$$

where ρ_0 describes the scattering of conduction electrons on defects, ρ_0^∞ on disordered spins and $c_\mathrm{K} \ln T$ on Kondo impurities. Employing a least square

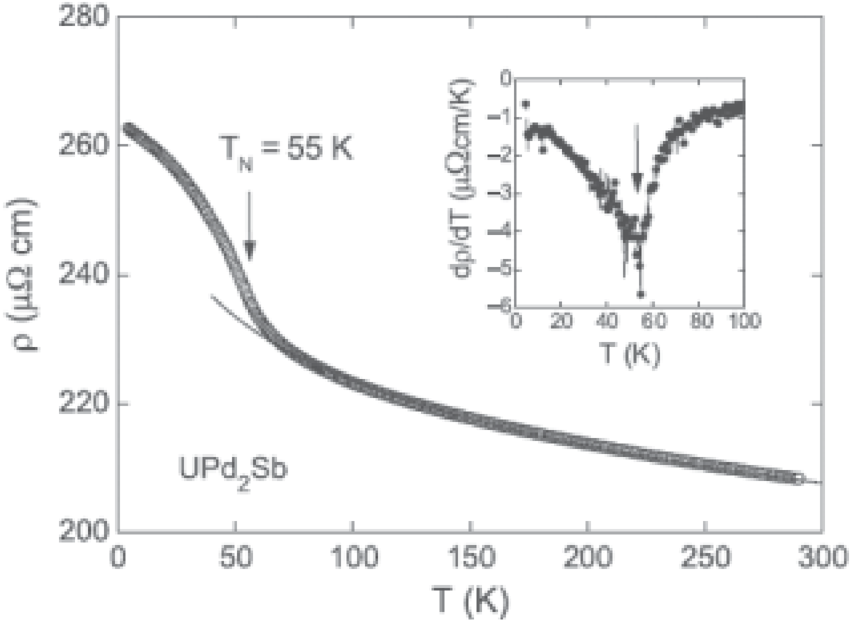

Figure 4.3: Temperature dependence of the electrical resistivity of UPd$_2$Sb in zero magnetic field. The solid line is indicating a fit to the data assuming a Kondo like behavior. The antiferromagnetic transition temperature T_N is marked. In the inset the derivative of the resistivity $d\rho/dT$ is displayed. The phase transition at T_N is marked by an arrow, for details see text (figure taken from [78]).

fit to the data the following parameters could be determined: $\rho_0 + \rho_0^\infty = 278\,\mu\Omega\mathrm{cm}$ and $c_\mathrm{K} = -14\,\mu\Omega\mathrm{cm}$.

However, the overall semiconductor-like behavior of the resistivity of UPd$_2$Sb in combination with the large residual resistivity is hinting towards an alternative scenario. As heavy fermion systems are very sensitive to structural disorder regarding their electronic transport properties, possibly this behavior might reflect crystallographic disorder. The strong influence of even moderate levels of disorder in strongly correlated electron systems has been shown by Maksimov *et al.* [77] and is discussed in chapter 3.

4.2.3 Thermodynamic properties

Furthermore, in Ref. [78] the magnetic susceptibility χ of UPd$_2$Sb has been measured in an applied field of 0.1 T, with χ^{-1} shown in Fig. 4.4. At low temperatures a distinct minimum in χ^{-1} manifests the onset of antiferromagnetic ordering below the Néel temperature $T_{\mathrm{N}} = 55\,\mathrm{K}$. Above T_{N} the susceptibility exhibits a modified Curie-Weiss behavior in the form of

$$\chi(T) = \frac{N\mu_{\mathrm{eff}}^2}{3k_{\mathrm{B}}(T - \Theta_{\mathrm{CW}})} + \chi_0,$$

with an effective moment $\mu_{\mathrm{eff}} = 2.7\,\mu_{\mathrm{B}}$, the Curie-Weiss temperature $\Theta_{\mathrm{CW}} = -86\,\mathrm{K}$ and $\chi_0 = 3 \cdot 10^{-4}\,\mathrm{emu/mole}$. The fit is included as a solid line in Fig. 4.4.

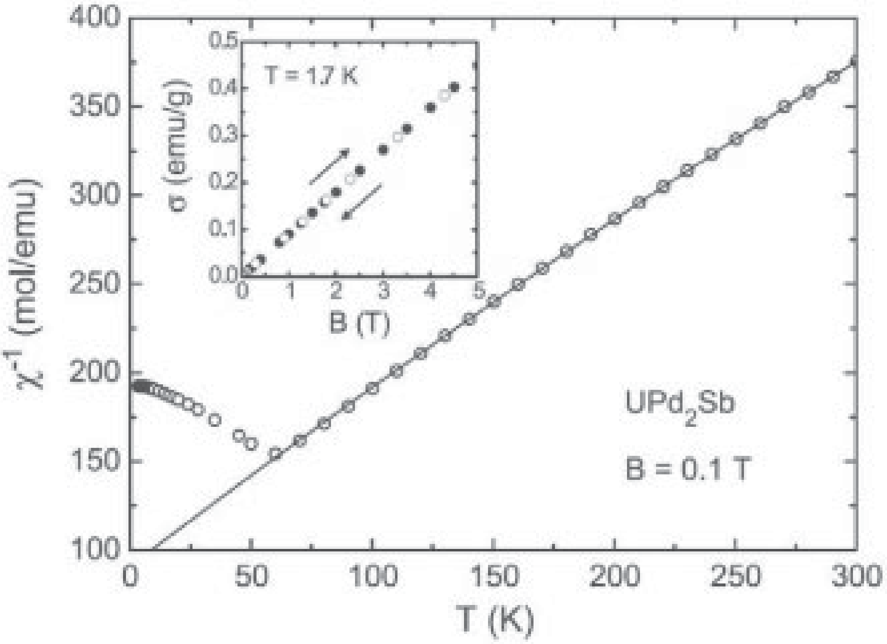

Figure 4.4: Temperature dependence of the inverse magnetic susceptibility of UPd$_2$Sb in a magnetic field $B = 0.1\,\mathrm{T}$. In the inset the magnetization versus magnetic field at $T = 1.7\,\mathrm{K}$ is depicted (full circles are indicating an increasing field, open circles a decreasing field), taken from Ref. [78].

The negative Curie-Weiss temperature Θ_{CW} is consistent with the antiferromagnetic ordering at lower temperatures. The effective moment μ_{eff} is reduced, compared to the expected magnetic moment of a free U^{3+} or U^{4+} ion

($3.62\mu_{\mathrm{B}}$ and $3.58\mu_{\mathrm{B}}$, respectively). The antiferromagnetic transition temperature T_{N} is reduced as compared to the absolute value of the Curie-Weiss temperature. The reduced value of T_{N} is typical for strong Kondo interactions [78]. In addition, in the inset of Fig. 4.4 the magnetization of UPd$_2$Sb versus the applied field is depicted, no hysteresis nor metamagnetic transition is observed.

The specific heat has been measured in Ref. [78] between 3 K and 70 K employing a standard adiabatic method. The result is depicted in Fig. 4.5. The antiferromagnetic phase transition at $T_{\mathrm{N}} = 55\,\mathrm{K}$ is not reflected as a well defined peak, but only seen as a small shoulder in the specific heat data (marked by an arrow). The transition is more pronounced in c_{p}/T versus T, as can be seen in the upper left inset of Fig. 4.5 where it is marked by an arrow.

Thus, the feature, which indicates the antiferromagnetic transition in the specific heat is rather broad and small, compared to a textbook specific heat anomaly indicating a second order magnetic phase transition. Again, this smoothing of the transition indicates that crystallographic disorder affects the physical properties in the sample studied here.

In the lower right inset of Fig. 4.5 c_{P}/T versus T^2 is displayed to verify a linear behavior in this type of representation and to allow an extrapolation of the data to low temperatures. The solid line in the lower right inset of Fig. 4.5 is a fit using the standard equation for specific heat in metallic samples:

$$c_{\mathrm{P}}(T) = \gamma T + \beta T^3,$$

where γT represents the electronic contribution and βT^3 the phonon contribution to the specific heat. From the fit parameters $\gamma = 81\,\mathrm{mJ/moleK}^2$ and $\beta = 4.1\,\mathrm{mJ/moleK}^4$ are obtained. Thus, in comparison to normal metals the value of the Sommerfeld coefficient γ is enhanced by one order of magnitude. Such behavior reflects moderately strong electronic correlations in this system, implying that it belongs to the class of moderately mass enhanced f-electron materials.

To determine the Debye temperature from the value β the formula $\Theta_{\mathrm{D}} = \sqrt[3]{12R\pi^4/5\beta}$ is employed [79]. This way, a Debye temperature Θ_{D} of $124\,\mathrm{K}$ is calculated. While this value is rather low, compared to normal metals, it is of the same order of magnitude as for related materials, *e.g.*, $\Theta_{\mathrm{D}} = 127\,\mathrm{K}$ for UPd$_2$Pb [61] and $180\,\mathrm{K}$ for UPd$_2$In [64].

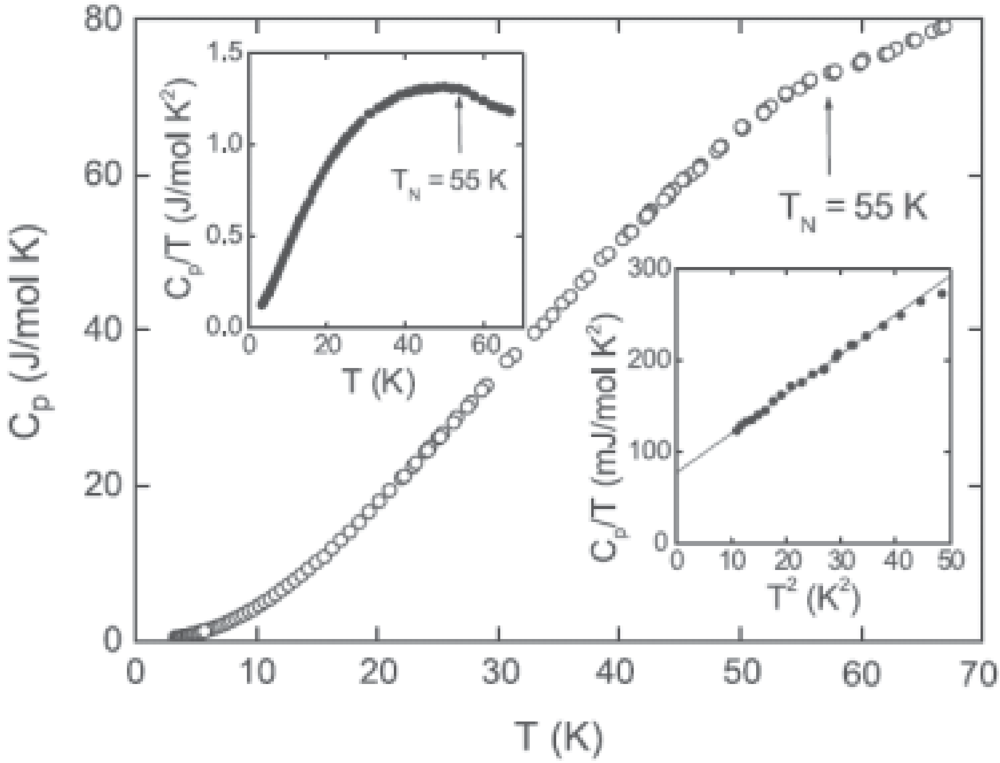

Figure 4.5: Temperature dependence of the specific heat of UPd_2Sb in zero magnetic field taken from Ref. [78]. The antiferromagnetic transition temperature T_{N} is marked by an arrow. In the upper inset c_{p}/T versus temperature is displayed. The phase transition is again marked by an arrow. In the lower inset c_{p}/T is plotted as a function of T^2. The solid line represents a fit to the data, for details see text.

4.2.4 Neutron scattering experiments

In Ref. [78] the semiconductor-like resistivity is attributed to a Kondo-like behavior. An alternative scenario accounting for the negative $d\rho/dT$ over the whole temperature range investigated in Ref. [78] would consider structural disorder induced localization effects [46, 77]. Such an approach might also explain the rather broad antiferromagnetic transition seen in the specific heat data of the sample UPd_2Sb examined in this work. In this situation, UPd_2Sb needs to be examined extensively with respect to the presence of structural disorder in order to distinguish between the two scenarios proposed to explain the unusual behavior of the resistivity.

Now, in x-ray diffraction experiments it is often difficult to detect small amounts of disorder (*e.g.* $\sim 10\,\%$ of crystallographic randomness). The reason is that the x-ray cross section is proportional to Z^2, with Z the atomic number of the corresponding element. Hence, it is very difficult to detect atoms with a small atomic number, when there are atoms with a much larger Z present in the material. Furthermore, it is difficult to detect site exchange between atoms with similar atomic numbers, as the cross section does not differ significantly. Therefore, comparing U (atomic number 92) with Pd (atomic number 46) and Sb (atomic number 51) x-ray scattering is not the optimum tool to detect small amounts of disorder in this compound, and the x-ray experiments from Ref. [78] have to be considered as being inconclusive regarding this issue. As a consequence, we have carried out neutron scattering experiments to study the structural and magnetic properties of UPd$_2$Sb.

4.2.4.1 Structural properties

In order to figure out if the physical properties of UPd$_2$Sb are induced by disorder, high resolution neutron scattering using the Fine Resolution Powder Diffractometer E9 at the Berlin Neutron Scattering Center (BENSC) at the Helmholtz Zentrum Berlin have been performed. Neutron scattering is a very suitable method to resolve disorder in UPd$_2$Sb, because the constituents of the material have a fairly bright elemental contrast, as is evidenced by the different scattering cross sections (U: $8.87\,\mathrm{barn}$, Sb: $3.64\,\mathrm{barn}$, Pd: $4.48\,\mathrm{barn}$). Thus, in order to examine the crystallographic structure and to search for the presence of disorder a neutron powder diffraction study at room temperature and $60\,\mathrm{K}$ has been performed, using a neutron wavelength of $\lambda = 1.797\,\text{Å}$.

The total diffraction pattern measured at $60\,\mathrm{K}$ is depicted in Fig. 4.6. A result of a full Rietveld refinement using a derivative of the fully ordered Heusler lattice is included in Fig. 4.6. Using a lattice parameter $a = 6.7407(3)\,\text{Å}$ ($a = 6.7625(3)\,\text{Å}$) for the $60\,\mathrm{K}$ ($300\,\mathrm{K}$) data, most experimentally observed peaks could be reproduced. Only three very small peaks with a relative integrated intensity of $\sim 2\,\%$ could not be reproduced.

In order to better understand the nature of the disorder different structure models, including different site exchange models for the atomic positions, have

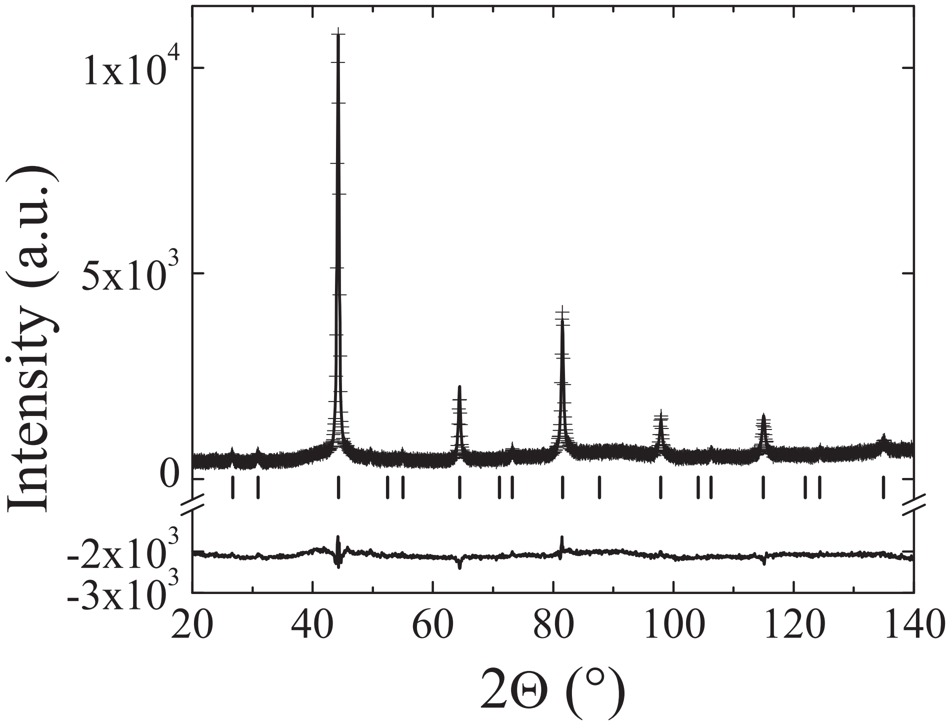

Figure 4.6: Neutron powder diffraction spectrum of UPd$_2$Sb at $60\,\mathrm{K}$. The solid line represents a fit which allows $20\,\%$ U and Sb site exchange, using a full Rietveld refinement, the tics indicate Bragg peak positions. The solid line in the lower panel shows the difference between the experimental data and the fit, for details see text.

been tested. The fitted models are (a) a Heusler structure without site exchange, (b) a U-Pd site exchange model with the amount of U atoms located on Pd sites and vice versa as fitting parameters, (c) a U-Sb site exchange model with the number of U atoms located on Sb sites and vice versa as fitting parameters. All these models have been tested with I.) the thermal displacement parameter B_{iso} equal for all atoms and II.) different B_{iso} parameters for different atoms.

However, for all models the residual value for the Bragg factor R_{Bragg} is rather poor. R_{Bragg} is a parameter to describe the quality of the fit, defined by:

$$R_{\mathrm{Bragg}} = 100\frac{\sum_h |{}'I'_{\mathrm{obs},h} - I_{\mathrm{calc},h}|}{\sum_h |{}'I'_{\mathrm{obs},h}|}, \tag{4.1}$$

with $I_{\mathrm{calc},h}$ the calculated integrated intensity of the fit. $'I'_{\mathrm{obs},h}$ is a modified observed integrated intensity

$$'I'_{\mathrm{obs},h} = I_{\mathrm{calc},h} \sum_i \left\{ \frac{\Omega(T_i - T_h)(y_i - b_i)}{(y_{\mathrm{c},i} - b_i)} \right\}, \tag{4.2}$$

with T - scattering variable (*e.g.* 2Θ in powder diffraction experiments), y_i ($y_{\mathrm{c},i}$) - observed (calculated) profile intensity and b_i observed background [80].

With the fully ordered Heusler lattice a value R_{Bragg} of $\sim 21\,\%$ has been obtained for the $60\,\mathrm{K}$ data. Overall, the best value R_{Bragg} has been found using a model which allows about $20\,\%$ site exchange between U and Sb ions, yielding $R_{\mathrm{Bragg}} \sim 18\,\%$, see Fig. 4.6. For the $300\,\mathrm{K}$ data a value $R_{\mathrm{Bragg}} \sim 19\,\%$ for the fully ordered Heusler lattice has been found, see Fig. 4.7. Using a site exchange model leads to no further reduction of R_{Bragg}.

Moreover, for all these different structure models unusually large isotropic thermal displacement factors $B_{\mathrm{iso}} = 4.8\,\text{Å}^2$ for U and Pd atoms and $B_{\mathrm{iso}} = 1.8\,\text{Å}^2$ for the Sb atoms at low temperatures of $T = 60\,\mathrm{K}$ are obtained. At $T = 300\,\mathrm{K}$ the thermal displacement factor is even larger being $B_{\mathrm{iso}} = 5.1\,\text{Å}^2$ for U and Pd atoms and $B_{\mathrm{iso}} = 2.0\,\text{Å}^2$ for the Sb atoms, which is consistent with the higher temperature of the experiment. The extraordinary large thermal displacement factors B_{iso} for both temperatures possibly reflect structural disorder, which is characterized by a small static displacement of the atoms out of their high symmetry positions. Moreover, even with the optimized models, the large R_{Bragg} values indicate a fundamental problem of the fits.

A closer inspection of the results of the Rietveld refinement reveals the shortcomings of the Rietveld refinements. In Fig. 4.8 a detailed view of the (2 2 0) peak, which is located at $2\Theta = 44\,°$, is displayed. The solid line in Fig. 4.8 represents the result of the fit with the site exchange model, allowing $20\,\%$ U-Pd site exchange. As can be seen from the figure, the peak consists of a central main area, adjacent to which there are broad tails. These broad tails are not adequately described by the refinements carried out here, and account for the large R_{Bragg} values. [1]

The broad tails of the Bragg peaks clearly indicate that there are structurally short-range ordered regions in the sample. A picture, that most of the ma-

---

[1] The step in the fit function at the bottom of the main peak is a fit artifact. The peak has a FWHM of $0.5\,°$, but this cannot be adapted to the broad tails, resulting in the small step of the fit function.

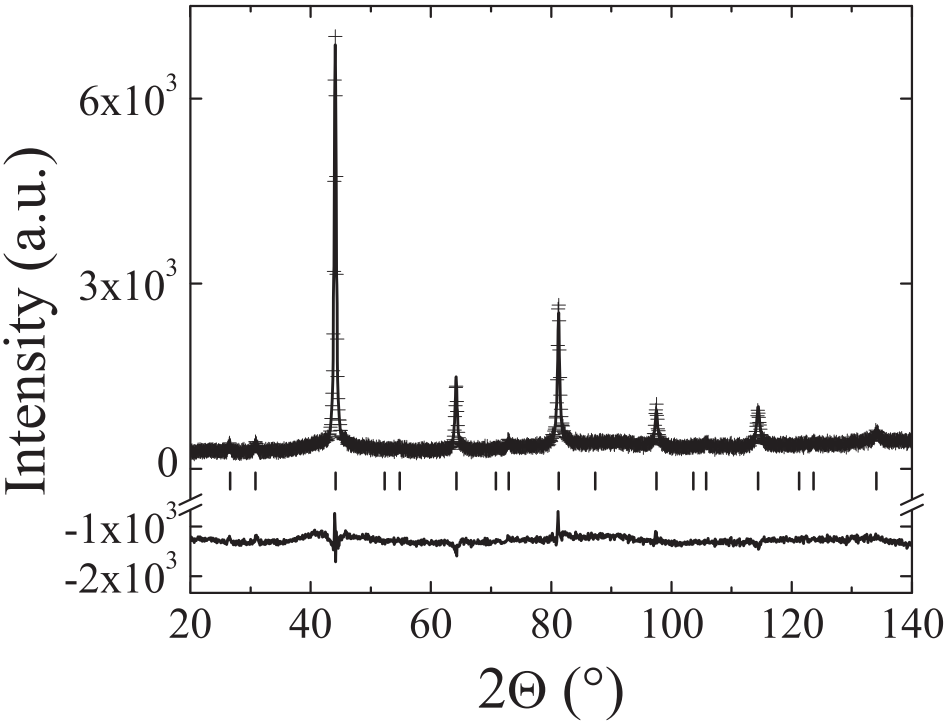

Figure 4.7: Neutron powder diffraction spectrum of UPd_2Sb at 300 K. The solid line represents a fit with the fully ordered Heusler lattice, using a full Rietveld refinement, the tics indicate Bragg peak positions. The solid line in the lower panel shows the difference between the experimental data and the fit, for details see text.

terial orders in a (derivative of the) Heusler lattice, and only a small amount of the material in between these crystalline grains is disordered, seems to be appropriate. The model would consist of crystalline grains with the Heusler structure, and between these grains there are strongly disordered regions giving rise to the quasi-amorphous signal in the neutron scattering experiment, *viz.*, the broad tails.

Regarding the origin of the physical mechanisms leading to the structural disorder in UPd_2Sb, one can think of two different scenarios. First, a static model is possible in which one of the constituents of the compound is either too small or too large to fit into the crystal structure. While preparing the samples, this would cause stress in the sample, with only small grains crystallizing, and the remaining sample containing heavily stressed areas. The second sce-

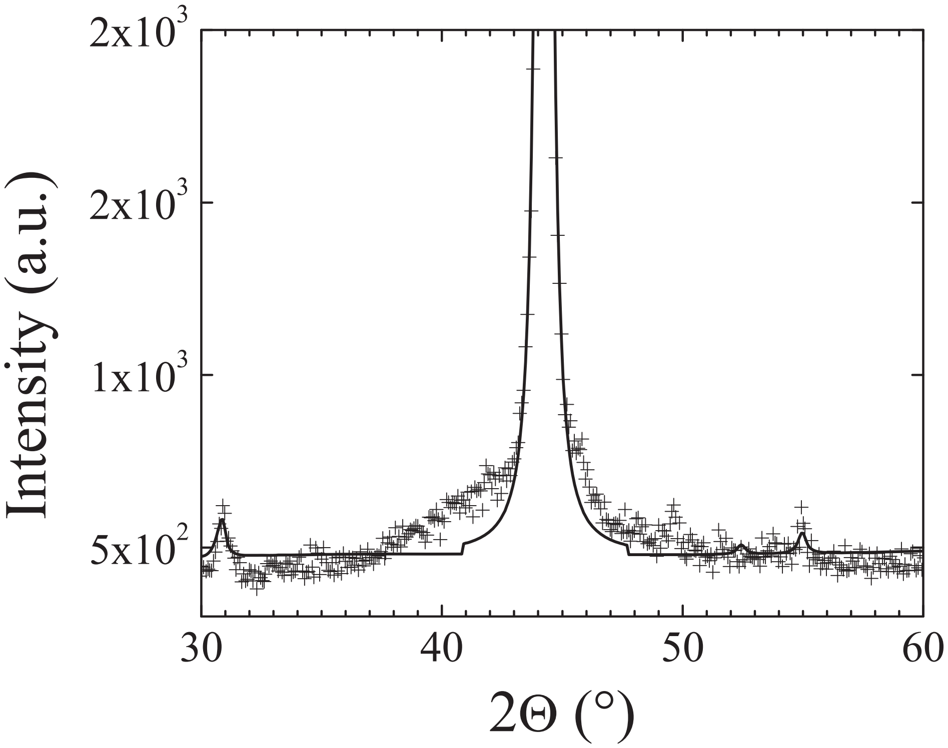

Figure 4.8: Enlarged region of the neutron powder diffraction spectrum of UPd$_2$Sb. The step in the fit function at the bottom of the main peak is only a fit artifact.

nario would consider phonon softening, in which the dispersion relation of the phonons has a second local minimum. In this case, the material would show a tendency towards a structural instability. To distinguish between these scenarios further measurements would be required.

4.2.4.2 Magnetic structure

The detected structural disorder in UPd$_2$Sb strongly influences the transport properties, resulting in a semiconductor-like behavior from room temperature to low temperatures of 2 K. Furthermore, the antiferromagnetic transition is broadened, as detected in specific heat measurements. Then, the question occurs, if the magnetic structure of UPd$_2$Sb is also influenced by structural disorder.

In order to determine the antiferromagnetic structure of UPd$_2$Sb powder neutron scattering experiments have been carried out at $T = 60\,\mathrm{K}$ and $1.6\,\mathrm{K}$ using the Focussing Diffractometer E6 at the Berlin Neutron Scattering Center BENSC (neutron wavelength of $\lambda = 2.444\,\text{Å}$). In the data taken with the E6 diffractometer, the previously observed broadening of the tails of the Bragg peaks is reproduced. These tails reflect the structural disorder in UPd$_2$Sb and have prohibited a full Rietveld refinement of the data. Now, in order to parameterize these tail structures for the refinement of the E6 data an ad-hoc non-linear background function has been used. Then, a full Rietveld refinement of the neutron diffraction data, using the known crystal structure of the Heusler lattice, can be performed for the high temperature measurement, see Fig. 4.9. Using this method a residual value $R_{\mathrm{Bragg}} = 8.3\,\%$ is obtained for the $60\,\mathrm{K}$ data.

Including an additional magnetic phase for the antiferromagnetic state yields a refinement of the data taken at $1.6\,\mathrm{K}$ with a residual value R_{Bragg} of $5.8\,\%$. The used antiferromagnetic structure of UPd$_2$Sb refinement consists of uranium magnetic moments ferromagnetically coupled within a plane aligned along two cubic axes of the Heusler lattice, and which are antiferromagnetically staggered along the third cubic axis. This magnetic structure has also been obtained for the related system UPd$_{1.85}$Sn (see Refs. [77, 81]). From the intensity ratio between the nuclear and the magnetic Bragg peaks the ordered moment of UPd$_2$Sb was determined to $\mu_{\mathrm{ord}} = 1.3\,\mu_{\mathrm{B}}$ at zero temperature. This value as well nicely compares to that of UPd$_{1.85}$Sn ($\mu_{\mathrm{ord}} \simeq 1\,\mu_{\mathrm{B}}$ at zero temperature).

For a more detailed investigation of the antiferromagnetic phase a temperature dependent study of a magnetic peak (1 1 0) has been performed. Although all measurements have been performed with the same number of incident neutrons, to check for a constant intensity a structural peak (1 1 1) has also been measured. In Fig. 4.10 the temperature dependence of these peaks is displayed. At $T = 3\,\mathrm{K}$, $6\,\mathrm{K}$, $10\,\mathrm{K}$ and $20\,\mathrm{K}$ no reduction of the magnetic peak intensity is observed, hence for clarity these data are not shown. Consistent with the bulk properties a reduction of the sublattice magnetization is observed above $20\,\mathrm{K}$, with the ordered magnetic moment having disappeared for $T \geq 60\,\mathrm{K}$.

The development of the antiferromagnetic moment as function of temperature

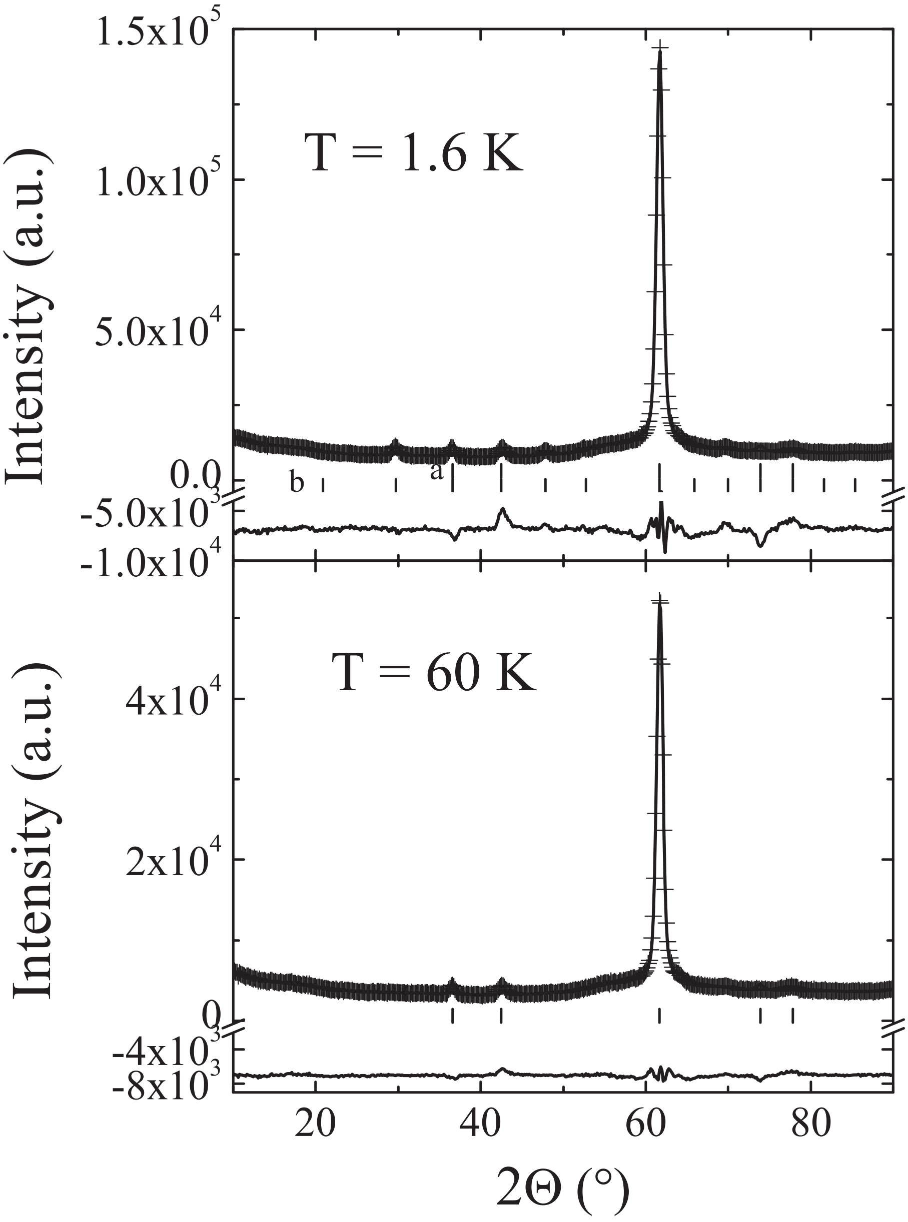

Figure 4.9: Powder neutron diffraction pattern of UPd_2Sb at 1.6 K (top) and 60 K (bottom). The solid line represents a Rietveld refinement, the tics (a) indicate structural Bragg peaks, the tics (b) in the 1.6 K graph indicate the Bragg peaks from the antiferromagnetically ordered phase. The solid lines at the bottom of the figures show the difference between the experimental data and the fit, for details see text.

for the (1 1 0) peak is depicted in Fig. 4.11. Aside from experimental scatter, the overall behavior of the ordered magnetic moment is that expected for the sublattice magnetization of a standard local moment antiferromagnet with a

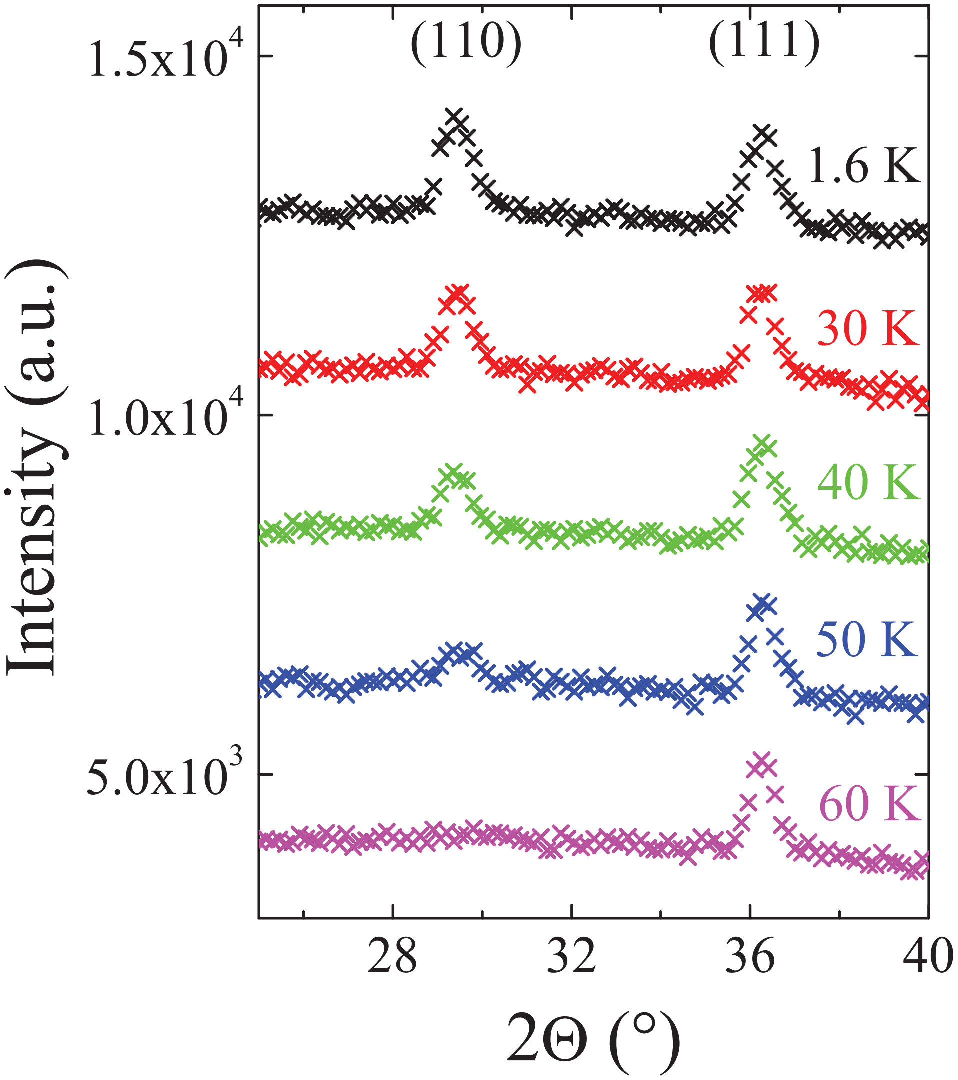

Figure 4.10: Temperature dependence of the magnetic (1 1 0) and structural (1 1 1) peak of UPd_2Sb. Data shifted against each other for clarity, for details see text.

critical behavior $\mu_{\mathrm{ord}} \propto (T_{\mathrm{N}} - T)^{2\beta}$, $\beta = 0.3 \pm 0.1$.

A closer inspection of the (1 1 0) and (1 1 1) peaks reveals, that the width of the structural peak is smaller than that of the magnetic peak, see Fig. 4.12. Fits of the data using gaussian peak functions yield a FWHM of $0.655°$ for

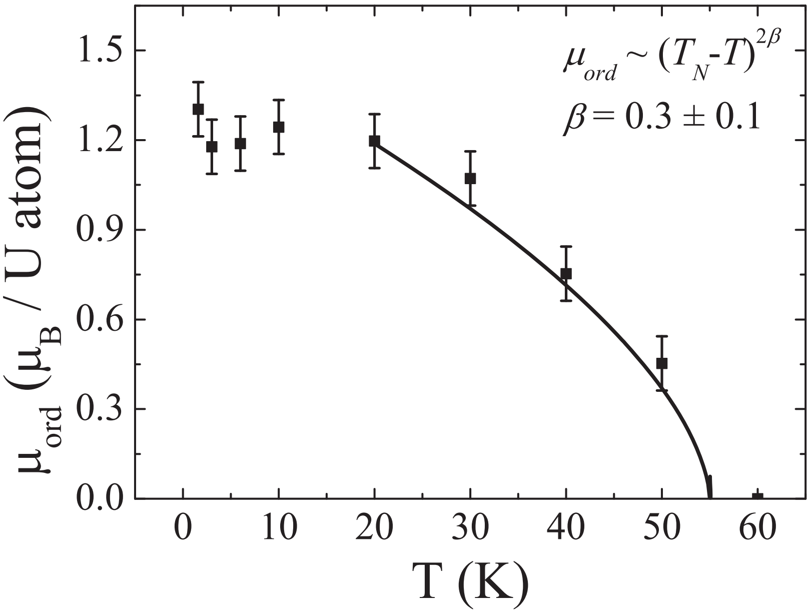

Figure 4.11: Temperature dependence of the ordered magnetic moment of UPd_2Sb from neutron diffraction, obtained from the intensity evolution of the (1 1 0) peak. The solid line is a fit $\mu_{\mathrm{ord}} \propto (T_{\mathrm{N}} - T)^{\beta}$, for details see text.

the structural (1 1 1) peak, a value which corresponds to the resolution limit of the E6 spectrometer in this 2Θ range. In contrast, for the (1 1 0) peak a FWHM $0.818°$ is obtained, which is significantly larger than the experimental resolution limit.

Thus, the structural Bragg peak is resolution limited in our experiment, whereas the magnetic peak appears broadened, reflecting a comparatively small correlation length (order of magnitude hundred Å) in the antiferromagnetic phase. This behavior is similar to that observed in related compounds such as UPd$_{2-x}$Sn or U$_2$PdGa$_3$ and U$_2$PtGa$_3$ [77, 82]. It implies that the structural disorder affects the magnetic behavior in this respect, in a quite similar fashion as observed in previous investigations.

4.2.5 Conclusion

The crystallographic disorder in UPd$_2$Sb has been determined to result from a kind of phase separation with small, structurally well ordered grains embedded in "quasi amorphous" regions. The transport properties are influenced by the structural disorder, resulting in a semiconductor-like behavior over the whole temperature range. The magnetic structure has been determined to consist of ferromagnetically coupled magnetic moments within a plane aligned along two cubic axes, and which are antiferromagnetically staggered along the third cubic axis. A non resolution limited magnetic Bragg peak reflects a magnetic correlation length of the order of hundred Å, mirroring an influence of the structural properties on the magnetism in UPd$_2$Sb.

4.3 Fermi liquid state in UPd$_2$Sn

4.3.1 Introduction

The transport properties of heavy fermions are strongly influenced by structural disorder, *e.g.*, disorder induced localization effects or disorder induced non-Fermi liquid behavior in the vicinity of a quantum critical point as discussed in Chapter 3 may occur. Furthermore, Fert and Levy [49] predicted a disorder dependency of the Hall effect. As yet, a verification of the latter

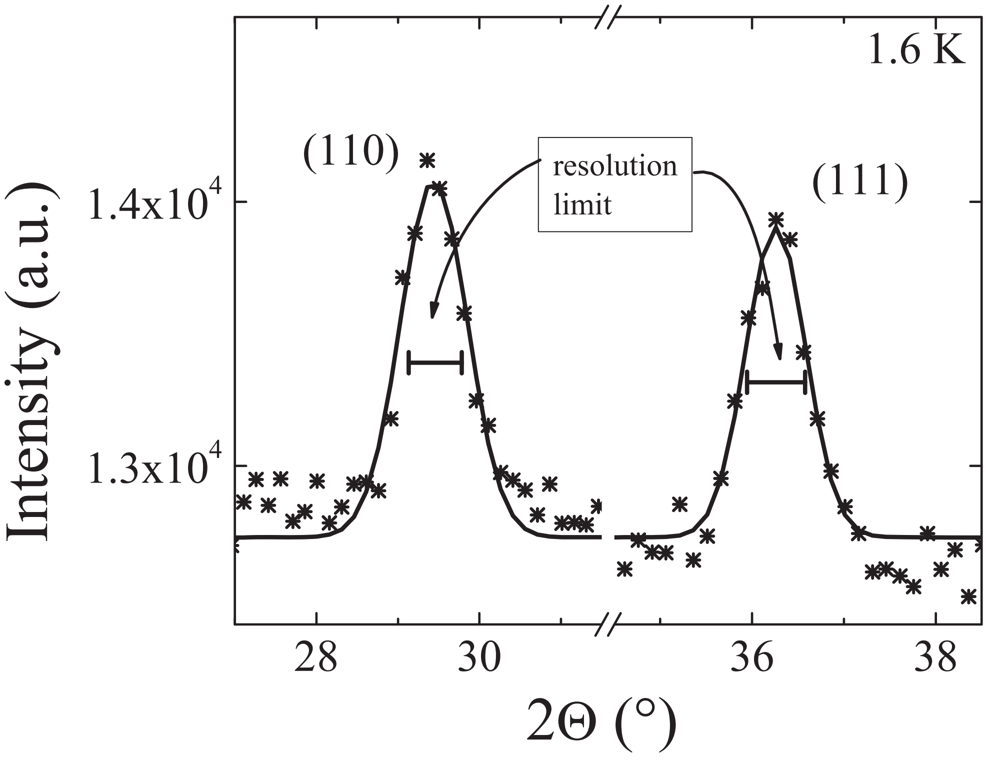

Figure 4.12: Comparison of the peak width of the magnetic (1 1 0) and structural (1 1 1) peaks of UPd$_2$Sb. The solid lines represent fits to the data using gaussian peak functions. The two horizontal bars indicate the experimental resolution limit of the E6 spectrometer at BENSC.

prediction is lacking. In this situation, an investigation of an extended set of samples with a controlled and well known level of structural disorder is required. In this context the work of Maksimov *et al.* [77] indicated that a class of compounds UPd$_{2-x}$Sn; $x = 0.02, 0.04$, with different heat treatments might be a suitable candidate for such an investigation.

UPd$_{2-x}$Sn, $x = 0$, crystallizes in an orthorhombic $Pnma$ lattice and shows no magnetic ordering. However, off-stoichiometric samples, and thus moderately disordered material, form a cubic $Fm3m$ structure [74, 77]. Experimentally, it has been observed that for $x \leq 0.04$ UPd$_{2-x}$Sn crystallizes in the orthorhombic $Pnma$ structure, while for $x \geq 0.05$ it forms in the cubic $Fm3m$ lattice [77].

This structural transition suggests that UPd$_{2-x}$Sn shows an affinity to structural disorder. Maksimov *et al.* [77] investigated the influence of structural disorder on the physical properties. Based on the work by Maksimov, the question occurs in which way the transport properties of UPd$_{2-x}$Sn on the nonmagnetic side of the phase diagram are influenced by the interplay of electronic correlations and structural disorder. To answer these questions, a detailed investigation for several samples in the orthorhombic phase with $0 \leq x \leq 0.04$ and different heat treatments is presented here.

Therefore, the electronic transport properties of a set of samples UPd$_{2-x}$Sn with different stochiometry $x < 0.05$ and various heat treatments have been examined. In particular, the following samples have been examined in this work: UPd$_{2-x}$Sn with $x = 0$ in as-cast form, annealed at 700°C, and 800°C for one week, $x = 0.02$ in as-cast form and annealed at 800°C for one week, and $x = 0.04$ in as-cast form and annealed at 800°C for one week.

4.3.2 Specific resistivity of UPd$_{2-x}$Sn

Previously, Maksimov *et al.* [77] observed a metallic behavior of the resistivity for orthorhombic UPd$_{2-x}$Sn, $x < 0.05$. At high temperatures, a large temperature independent specific resistivity ($\sim 150\,\mu\Omega\mathrm{cm}$) has been found, which in such intermetallic uranium compounds is generally associated with scattering from crystal electric field excitations and Kondo-like interactions, as well as with magnetic scattering and scattering from phonons. With decreasing temperature, at about $100\,\mathrm{K}$, a substantial reduction of the resistivity is observed, which denotes the transition into a coherent state. Finally, at sufficiently low temperatures $T < T^*$, the resistive behavior can be described within Fermi liquid theory with $\rho = \rho_0 + AT^2$. T^* denotes the Fermi liquid temperature, *i.e.*, Fermi liquid behavior is observed below T^*.

Surprisingly, Maksimov *et al.* [77] found an extraordinary strong sample dependence of the residual resistivity of their samples UPd$_{2-x}$Sn, ranging from $1\,\mu\Omega\mathrm{cm}$ for annealed UPd$_2$Sn to $98\,\mu\Omega\mathrm{cm}$ in as-cast UPd$_{1.96}$Sn. Moreover, these experiments indicated possible deviations from Fermi liquid behavior for some of the high resistive samples. Hence, from the studies in Ref. [77] the question arises, if in a Fermi liquid system a non-Fermi liquid behavior can be induced through disorder, possibly in a way as proposed by Rosch [23].

Even if such a scenario is not realized for UPd$_{2-x}$Sn a study of the resistive properties of a set of samples UPd$_{2-x}$Sn with varying residual resistivities as result of varying disorder levels allows to investigate if the Fermi liquid parameters A and T^* are disorder dependent.

For the samples UPd$_{2-x}$Sn studied here ρ has been measured in the range from $T = 0.5$ to $300\,\mathrm{K}$. The overall behavior is shown in the Figs. 4.13, 4.14 and 4.15. Qualitatively, the same behavior as by Maksimov *et al.* [77] is observed.

For all samples UPd$_{2-x}$Sn; $x = 0$ (Fig. 4.13) no phase transition is observed, *i.e.*, the material is a "heavy fermion vegetable". At low temperatures, the transition into the coherent state occurs. The same behavior is observed for the other non-stoichiometric samples UPd$_{2-x}$Sn; $x = 0.02$ and UPd$_{2-x}$Sn; $x = 0.04$, see Figs. 4.14 and 4.15, respectively.

The values of the resistivity at lowest temperature ρ_0, at room temperature ρ_{300}, and the ratio ρ_{300}/ρ_0 are summarized in Table 4.5. From this table, a range of resistivity ratios ρ_{300}/ρ_0 between about 2 and 16 is observed for the samples UPd$_{2-x}$Sn. For the as-cast samples the ratio is between 2.2 and 2.8, while for the annealed samples the ratio is larger ranging from 4.6 to 15.8, as expected because of less disorder. As well, with decreasing concentration of Pd the resistivity ratio is decreasing for the as-cast as well as for the annealed samples, again reflecting less disorder for the samples closer to stochiometry 1:2:1.

On the other hand, the absolute values of the resistivity show some irregularities, see Table 4.5 and Fig. 4.16. Especially the values for the two an-

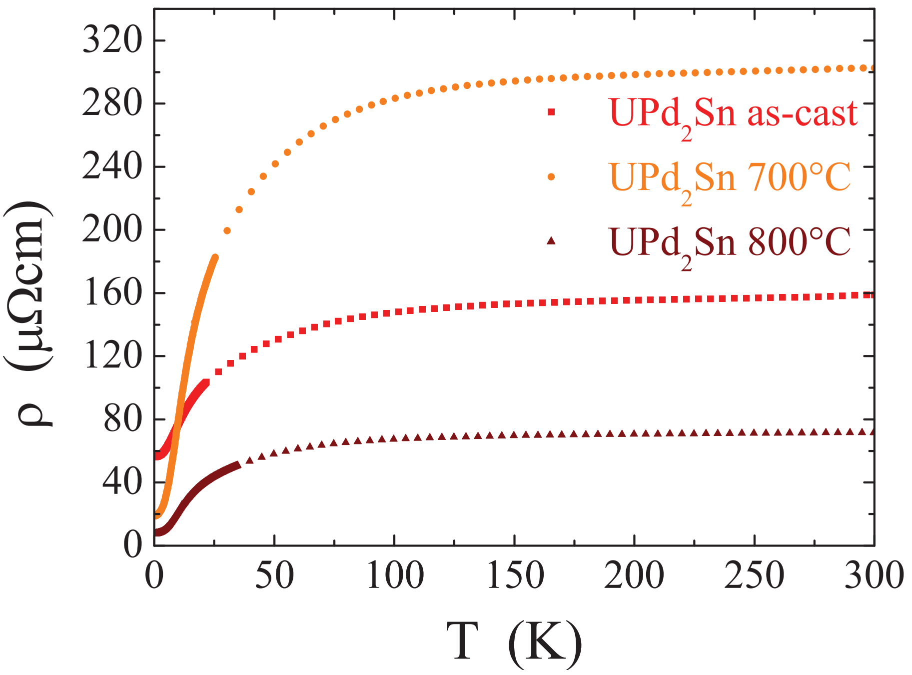

Figure 4.13: Temperature dependence of the resistivity of UPd_2Sn for the as-cast sample (red squares) and the annealed ones (700°C - orange dots), (800°C - bordeaux triangles), for details see text.

nealed samples $UPd_{2-x}Sn$; $x = 0$, show different absolute resistivity values, compared to those examined in the Refs. [74, 77]. In particular, $UPd_{2-x}Sn$; $x = 0$ annealed at 700° C has a room temperature resistivity value, which is larger by about a factor 2 than the other samples examined here or reported in Refs. [74, 77], while $UPd_{2-x}Sn$; $x = 0$, annealed at 800°C has a room temperature resistivity value, which is smaller by a factor 2 compared to those other samples.

One explanation for this variance in absolute ρ values might be the presence of microcracks in the sample annealed at 700°C, that is the true current path in the sample would be longer resulting in a larger resistivity. In contrast, microcracks cannot explain the reduction of ρ for the sample annealed at 800°C. Here, one might speculate that during the annealing process a second grain boundary phase forms, causing a short circuit in the sample. For instance, this could be due to the low melting point of Sn and the resulting high vapour pres-

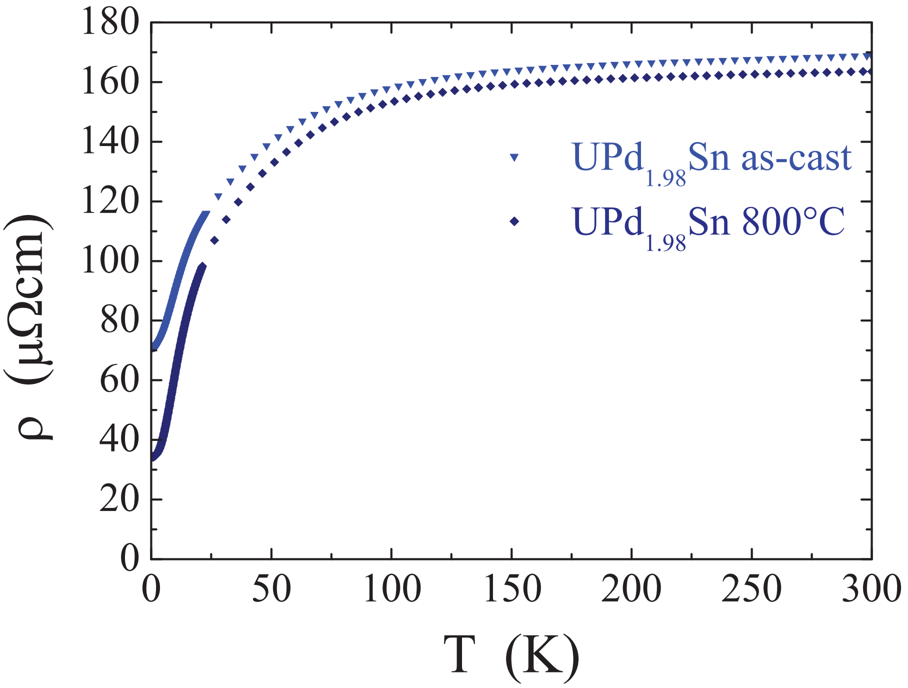

Figure 4.14: Temperature dependence of the resistivity of as-cast (light blue triangles) and annealed (800°C - dark blue diamonds) UPd$_{1.98}$Sn, for details see text.

sure. This way, it may lead to a Sn rich phase in the grain boundaries or on the surface of the sample, a behavior often observed for Sn containing samples.

With these irregularities in ρ_{300} it is more useful to compare the resistivity data normalized to $300\,\mathrm{K}$. With such a normalization, as plotted in Fig. 4.17, it is easy to see that the qualitative behavior of all samples is the same. Only the resistivity ratios are different, which thus is a measure for the disorder level in the different samples. Altogether it is ensured that all samples show the generic behavior of orthorhombic UPd$_{2-x}$Sn [77]. Furthermore, with the present set of samples a large range in terms of the experimental parameter "crystallographic disorder" is covered.

Therefore, with our set of samples we are able to address the question if the system UPd$_{2-x}$Sn is driven into non-Fermi liquid behavior, *i.e.*, $\rho = \rho_0 + AT^y$, $y < 2$, by disorder. Even if this should not happen, that is if Fermi liquid behavior with $\rho = \rho_0 + AT^2$ remains prevalent, the question can be investigated if the temperature range $0 < T < T^*$ within which Fermi liquid behavior is

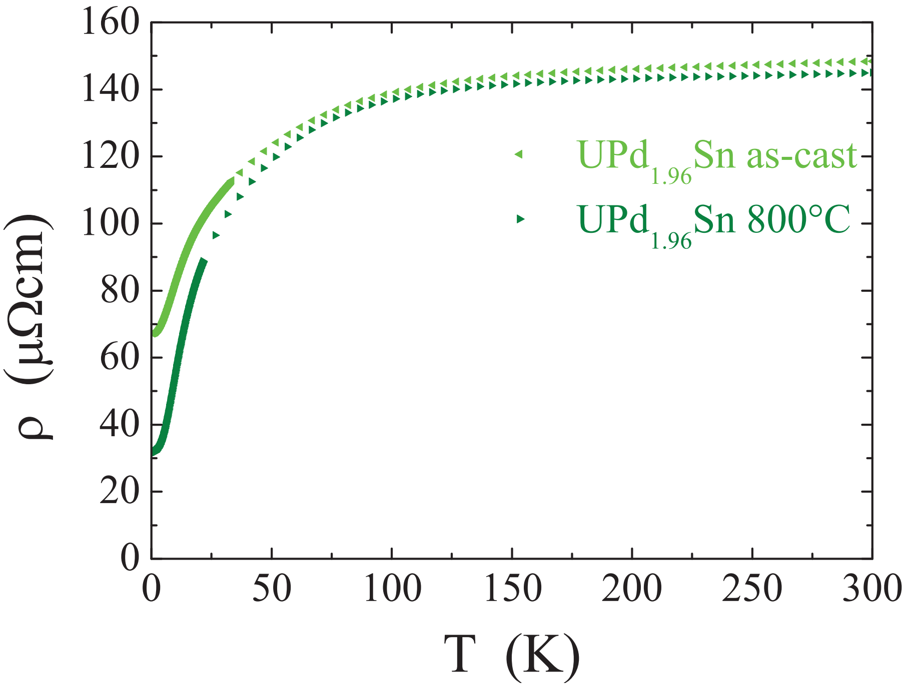

Figure 4.15: Temperature dependence of the resistivity of $UPd_{1.96}Sn$ for the as-cast (light green triangles) and the annealed sample (800°C - dark green triangles), for details see text.

observed depends on the level of disorder.

In order to test these scenarios, the data have to be fitted using $\rho = \rho_0 + AT^y$. Since, fitting the data with free parameters ρ_0, A, y yields no significant deviation of y from the Fermi liquid prediction $y = 2$ for any of the samples. In consequence, for a detailed analysis of the Fermi liquid behavior, in the following the data are analyzed using $\rho = \rho_0 + AT^2$. In this analysis, due to correlation of the fitting parameters ρ_0 and A, these two parameters are very sensitive to the fitting interval. Therefore, in order to verify the prediction from Fermi liquid theory and to determine the Fermi liquid temperature T^*, in which the coherent state is developed, the data have been fitted in different temperature intervals $T(1)$ to $T(N)$. Here, $T(1)$ is representing the lowest measured temperature and $T(N)$ is varied. As the fit is sensitive to the fitting range, a quantitative measure for the fit quality, *i.e.*, for the deviation between measured data and fit in the fitted area is needed. One such measure would be

	$\rho_{300}(\mu\Omega cm)$	$\rho_0(\mu\Omega cm)$	ρ_{300}/ρ_0
$UPd_{1.96}Sn$ as-cast	148	67	2.2
$UPd_{1.96}Sn$ 800°C	145	32	4.5
$UPd_{1.98}Sn$ as-cast	169	71	2.4
$UPd_{1.98}Sn$ 800°C	164	34	4.8
UPd_2Sn as-cast	159	56	2.8
UPd_2Sn 700°C	303	19	15.9
UPd_2Sn 800°C	72	8	9

Table 4.5: Room temperature resistivity ρ_{300}, low temperature resistivity ρ_0 and resistivity ratio ρ_{300}/ρ_0 of $UPd_{2-x}Sn$.

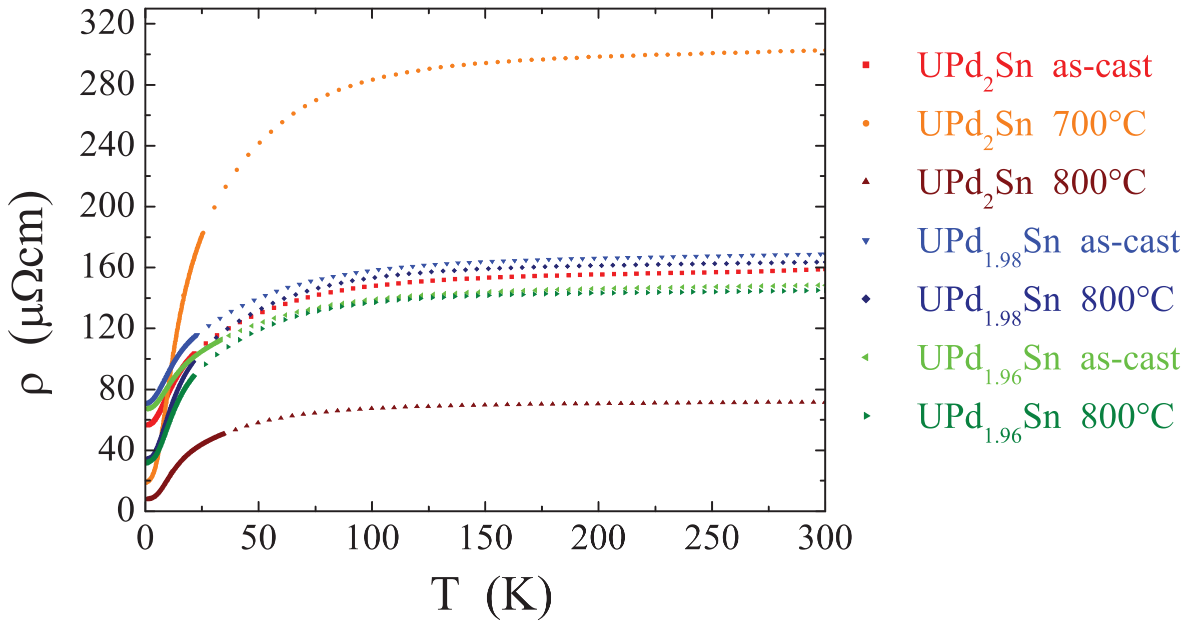

Figure 4.16: Temperature dependence of the resistivity of $UPd_{2-x}Sn$, $x = 0$, 0.02 and 0.04; for details see text.

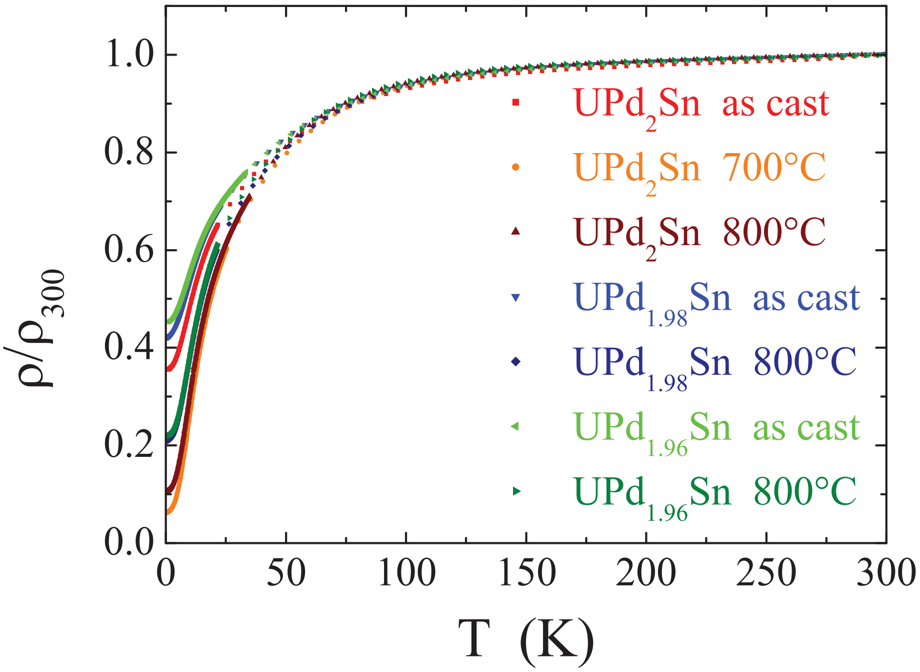

Figure 4.17: Normalized temperature dependence of the resistivity of UPd$_{2-x}$Sn, $x = 0$, 0.02 and 0.04; for details see text.

a relative deviation between fit and data per number of data points [83],

$$\zeta(T(N)) = \frac{\sum_{i=1}^{N} \frac{|\rho_{\mathrm{exp},i}(T)-\rho_{\mathrm{fit},i}(T)|}{\rho_{\mathrm{exp},i}(T)}}{N}. \tag{4.3}$$

$\Delta T(N) = [T(1), \ldots, T(N)]$ starts at the lowest measured temperature $T(1) = T_{\mathrm{low}}$ up to the highest fitted one $T(N) = T_{\mathrm{max}}$. N is the number of data points in the corresponding temperature range $\Delta T(N)$. $\rho_{\mathrm{exp},i}$ is the ith data point in the temperature interval $\Delta T(N)$ and $\rho_{\mathrm{fit},i}$ the corresponding fitted point in $\Delta T(N)$. For each range $\Delta T(N)$, a set of fit parameters is determined and ρ_{fit} is calculated. The argument of the sum represents the relative deviation between fit and data at temperature T_i. The sum is giving a measure for the overall mismatch between fit and data in the whole range $\Delta T(N)$, *viz.*, the fit quality. Division by N yields the average mismatch per point. With this notation, $\zeta(T_{\mathrm{max}})$ represents a measure for the fit quality in the temperature range $\Delta T(N) = [T_{\mathrm{low}}, \ldots T_{\mathrm{max}}]$, provided that N is not too small. For small values N (for narrow temperature ranges fitted), ζ will tend to zero. This is strictly true for $N = 1$, as for a single point it can be ensured that $\rho_{\text{exp}} - \rho_{\text{fit}} = 0$.

If a fit adequately describes the data, then $\zeta(T_{\text{max}})$ is constant, its absolute value being controlled by the scatter of the data. Conversely, an inappropriate fit leads to a continuously increasing $\zeta(T_{\text{max}})$ with T_{max} since with a larger range $\Delta T(N)$ the mismatch will become worse. With the ζ function a tool is provided which gives a measure for the quality of the fit. For the determination of the characteristic temperature T^* a plot ζ versus $T(N)$ is used, see as an example Fig. 4.18. In this figure, in principle the expected behavior has been found. Only in the intermediate range of $T(N)$ a decrease of ζ instead of a constant behavior is observed.

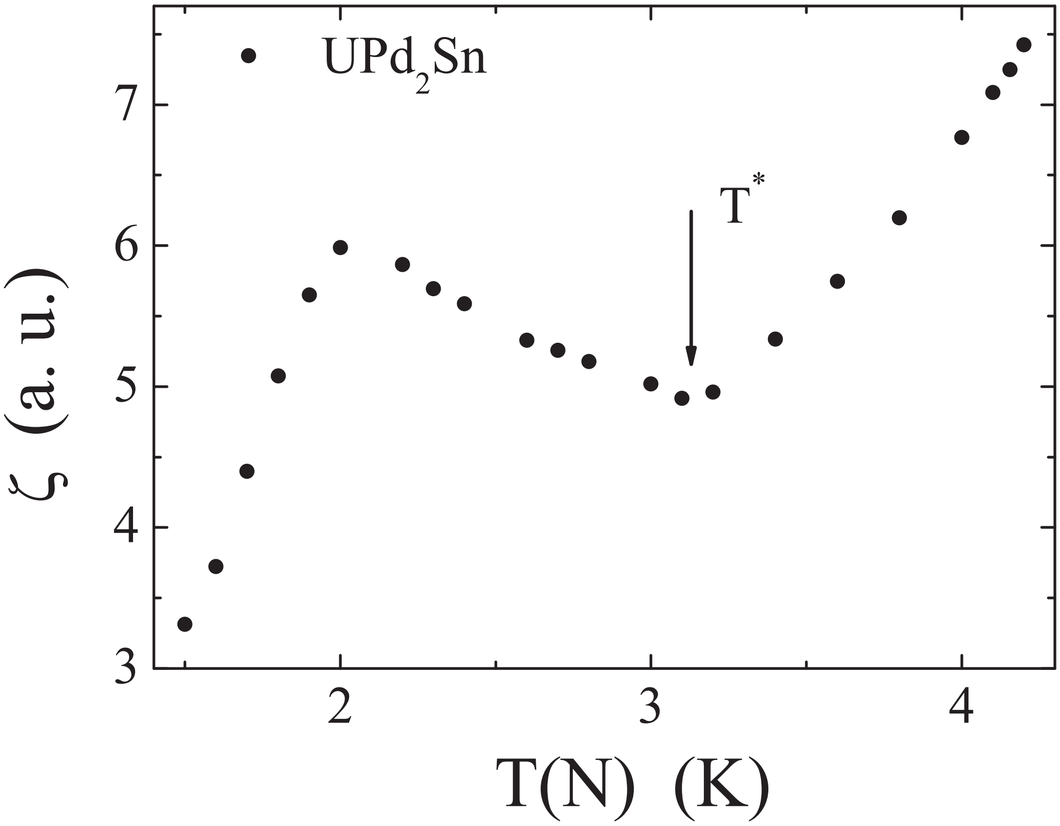

Figure 4.18: The quality of the fit for as-cast UPd$_2$Sn using the ζ function, for details see text.

The decrease of ζ for $2\,\text{K} \lesssim T(N) \lesssim 3\,\text{K}$ is explained with a higher scattering of ρ_{exp} at low temperatures $T < 2$ K. With increasing $T(N)$ the relative deviation between ρ_{exp} and ρ_{fit} is reduced as the scattering of the data is reduced for $T > 2$ K. Thus, the temperature T^* is given by the temperature at which a change from decreasing ζ to increasing ζ occurs.

Having thus established T^*, it is possible to obtain the optimum values for ρ_0 and A. The values T^*, ρ_0 and A of all samples UPd$_{2-x}$Sn have been determined using this method and are summarized together with ρ_{300}/ρ_0 in Table 4.6.

Here, the resistivity ratio ρ_{300}/ρ_0 serves as a measure of the level of disorder. In Fig. 4.19 the characteristic temperature T^* *vs.* resistivity ratio ρ_{300}/ρ_0 for orthorhombic UPd$_{2-x}$Sn is depicted. From the figure no clear dependency of the two quantities is derived, implying that structural disorder in orthorhombic UPd$_{2-x}$Sn has no detectable influence on the onset of the coherent state, as determined by T^*. Furthermore, a non-Fermi liquid behavior induced by structural disorder, as discussed by Rosch [23], cannot be observed. Possibly, UPd$_{2-x}$Sn is too far away from the quantum critical point to develop disorder induced non-Fermi liquid behavior, which means that the theory from Ref. [23] is not applicable here.

4.3.3 Hall effect in UPd$_2$Sn

According to Fert and Levy [49] the Hall constant R_H is influenced by disorder. Skew scattering on impurities results in a constant background in $R_\mathrm{H}(T)$, leading to a dependence of R_H on the level of structural disorder in particular at low temperatures. Furthermore, the question occurs, if the overall shape of

	T^* (K)	A	ρ_0 ($\mu\Omega cm$)	ρ_{300}/ρ_0	T_coh (K)
UPd$_{1.96}$Sn as cast	3.2	$1.41 \cdot 10^{-7}$	67	2.2	35
UPd$_{1.96}$Sn 800°C	3.4	$1.9 \cdot 10^{-7}$	32	4.5	70
UPd$_{1.98}$Sn as cast	3.4	$1.88 \cdot 10^{-7}$	71	2.4	42
UPd$_{1.98}$Sn 800°C	2.4	$1.96 \cdot 10^{-7}$	34	4.8	77
UPd$_2$Sn as cast	3.1	$1.92 \cdot 10^{-7}$	56	2.8	52
UPd$_2$Sn 700°C	2.7	$4.19 \cdot 10^{-7}$	19	16.0	75
UPd$_2$Sn 800°C	3.8	$1.22 \cdot 10^{-7}$	8	9.5	70

Table 4.6: Fermi liquid temperature T^*, resistive prefactor A, low temperature resistivity ρ_0, resistivity ratio ρ_{300}/ρ_0, and coherence temperature $T_\mathrm{coh}$of UPd$_{2-x}$Sn.

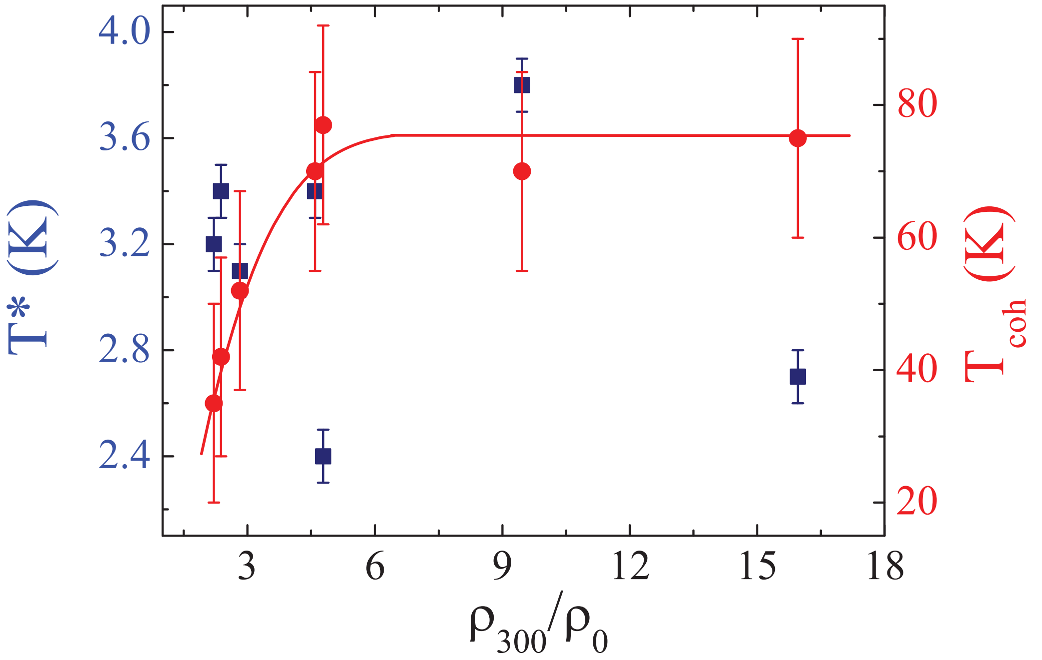

Figure 4.19: Fermi liquid temperature T^* derived from the fits *vs.* resistivity ratio ρ_{300}/ρ_0 for orthorhombic UPd$_{2-x}$Sn. In the figure, T_{coh} as discussed below is included, for details see text.

$R_{\mathrm{H}}(T)$ is modified by a large value of $R_{\mathrm{H,imp}}$, effectively resulting in a disorder dependent coherence temperature T_{coh}.

In Fig. 4.20 the Hall coefficient R_{H} is plotted against the temperature T for all samples. For comparison, the data for as-cast UPd$_{2-x}$Sn, $x = 0$, investigated by Maksimov *et al.* [77], are included. The overall shape of $R_{\mathrm{H}}(T)$ is the same for all samples, with a maximum around $\sim 50\,\mathrm{K}$. On the other hand the absolute values of $R_{\mathrm{H}}(T)$ show big differences up to a factor 5.

Regarding the origin of the large differences in the absolute values R_{H} is unclear. One possible scenario is that in the polycrystalline samples the actual measured thickness d of the polycrystalline resistive bar is not the adequate value to determine the Hall coefficient R_{H}. There might be cracks in the samples which would lead to a reduction of the effective thickness, and thus one would have to use an effective value d_{eff} instead of d.

In order to test this assumption, R_{H} has been normalized to a value at $\sim 200\,\mathrm{K}$.

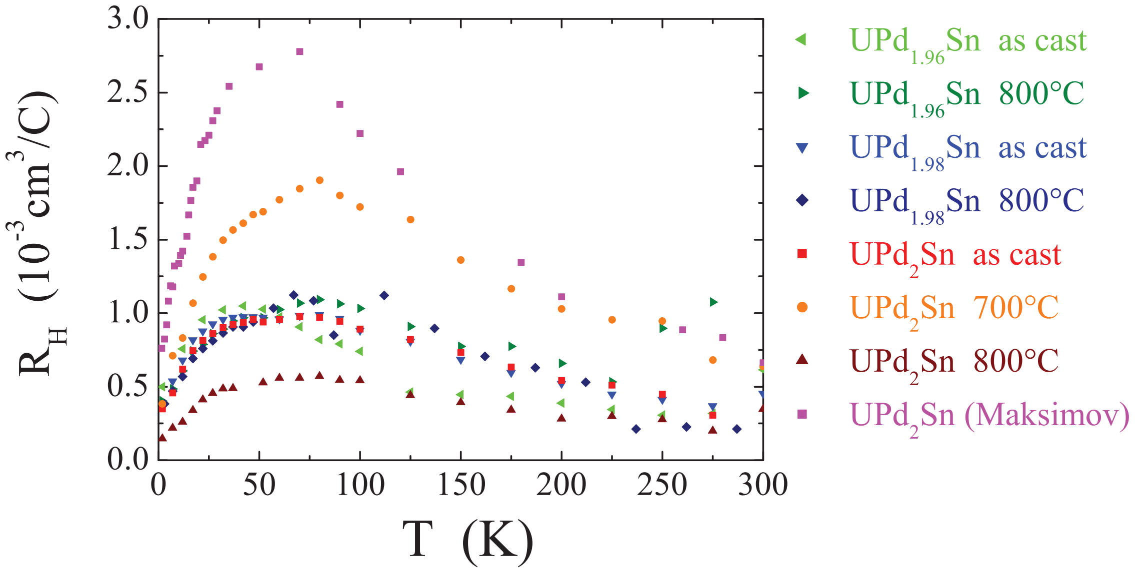

Figure 4.20: Temperature dependence of the Hall coefficient of $UPd_{2-x}Sn$, the magenta data are measured by Maksimov [77] on as-cast UPd_2Sn, for details see text.

As shown in Fig. 4.21, using the normalized Hall constant $R_{\mathrm{H,eff}}$ a much better agreement between the different data sets is observed. This supports the notion of cracks, prohibiting the establishment of the correct thickness of the sample. However, using this assumption, the similar temperature dependencies of $R_{\mathrm{H,eff}}$ reveal no significant correlation between disorder and Hall effect.

Further, the principle behavior predicted by Fert and Levy can be seen in Fig. 4.21. At high temperatures a Curie-Weiss-like behavior is observed and all samples show a pronounced maximum in R_{H} with a coherence temperature T_{coh} in the regime of $\sim$ 40 K to 70 K. The dependence of T_{coh} on the level of disorder, given by the resistivity ratio ρ_{300}/ρ_0, is displayed in Fig. 4.19. The coherence temperature increases with disorder up to saturation for low disorder values, *i.e.*, large ρ_{300}/ρ_0. Below the coherence temperature the Hall coefficient R_{H} is reduced, which is consistent with this theory. The differences

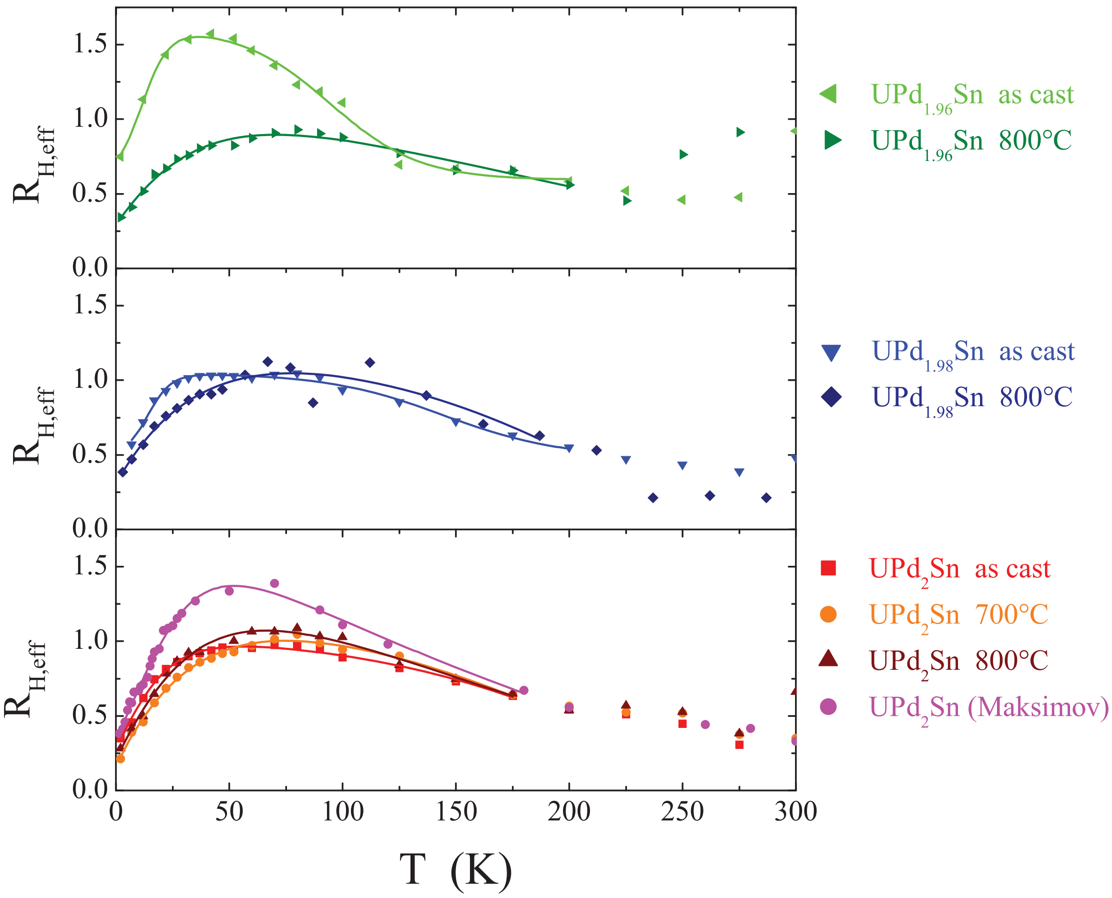

Figure 4.21: Temperature dependence of the normalized Hall coefficient of $UPd_{2-x}Sn$, the magenta data are measured by Maksimov [77] on as-cast UPd_2Sn. The solid lines are guides to the eye, for details see text.

in the normalized values $R_{\mathrm{H,eff}}$ for the samples $UPd_{2-x}Sn$ are rather small, and no correlation between structural disorder and residual R_{H} is observed.

Therefore, the similarity in the T dependence of the normalized Hall coefficient, compared to the differences in the absolute values, reflects a problem in the determination of the effective thickness rather than differences in the carrier density.

4.3.4 Conclusion

In conclusion, a detailed study of the transport properties of orthorhombic UPd$_{2-x}$Sn has been carried out. In this study a detailed analysis of the Fermi liquid behavior, as observed in the resistivity, and the signatures of the coherent state appearing in the Hall effect have been performed. The predictions of Rosch [23] regarding a disorder induced non-Fermi liquid behavior do not apply to the materials studied here. Rosch predicted a non-Fermi liquid behavior in the vicinity of a QCP, therefore one might speculate, that UPd$_2$Sn is not close enough to a QCP. Of course, here the question occurs of a quantitative measure of the "distance" to the QCP. Furthermore, no characteristic dependency of the Fermi liquid temperature T^* on disorder could be established, implying that this quantity is a rather robust characteristic parameter of the Fermi liquid state.

In addition, no disorder dependency of the residual value of the Hall constant R_H has been observed in this study, together with an increase of the coherence temperature T_coh, as it appears in the Hall effect, with decreasing disorder level. Both findings are at odds with the theory of Fert and Levy [49], casting doubt on the adequacy of this model. Here, additional theoretical studies on the anomalous Hall effect in heavy fermion systems would be desirable.

5 UPt_2Si_2: Field induced phases in an antiferromagnet

5.1 Introduction

In the context of electronic transport properties influenced by moderate structural disorder in heavy fermion systems, UPt_2Si_2 has been studied intensively as a model system [84]. For this material, the type of structural disorder has been determined and based on these findings, Otop [84] explained the main characteristics of the electronic transport properties of moderately disordered UPt_2Si_2. Further, additional analysis of the experimental data in Ref. [85] has provided evidence that the antiferromagnetic heavy fermion compound UPt_2Si_2 should be discussed as an itinerant rather than a localized $5f$ electron system, this in contrast to a crystalline electric field scheme view previously put forth by Nieuwenhuys [86].

In order to further elucidate the question of itinerancy, in the following high field magnetization and resistivity measurements are presented and the magnetic phase diagrams are derived. The experimental data are compared to the calculations carried out by Nieuwenhuys [86], this way giving additional evidence for an itinerant picture of UPt_2Si_2. Moreover, the magnetic phase diagrams of UPt_2Si_2 resemble those of URu_2Si_2, bringing up the issue of exotic high field phases in UPt_2Si_2 analogous to URu_2Si_2.

5.2 Crystallographic structure

As the physical ground state properties of heavy fermion systems are very sensitive to even a moderate level of structural disorder, to gain a full understanding of the exotic ground state properties of these strongly correlated electron systems the relationship between disorder and ground state properties must be understood. It is very difficult to prepare or obtain samples with a well defined amount of moderate (*i.e.*, $\sim 10\,\%$ of crystallographic randomness) disorder. As well, it is very hard to experimentally detect such moderate levels of disorder. In this situation, a model substance is required which allows to study both, the crystallographic disorder and its effect on the physical properties.

In this context, UT_2M_2 materials (with T representing a transition metal and M elements of the periodic table groups III or IV, most commonly Si or Ge) turn out to be of special value. These systems usually crystallize in one of two tetragonal structures: either the $CaBe_2Ge_2$ ($P4/nmm$) or the $ThCr_2Si_2$ ($I4/mmm$) lattice (Fig. 5.1). Both are derivatives of the $BaAl_4$ structure, the $CaBe_2Ge_2$ lattice possessing a lower symmetry of the unit cell than the $ThCr_2Si_2$ lattice. The close relation between the two structures can lead to structural instabilities. For instance, in UCo_2Ge_2 a structural transition between the two structures has been found [87].

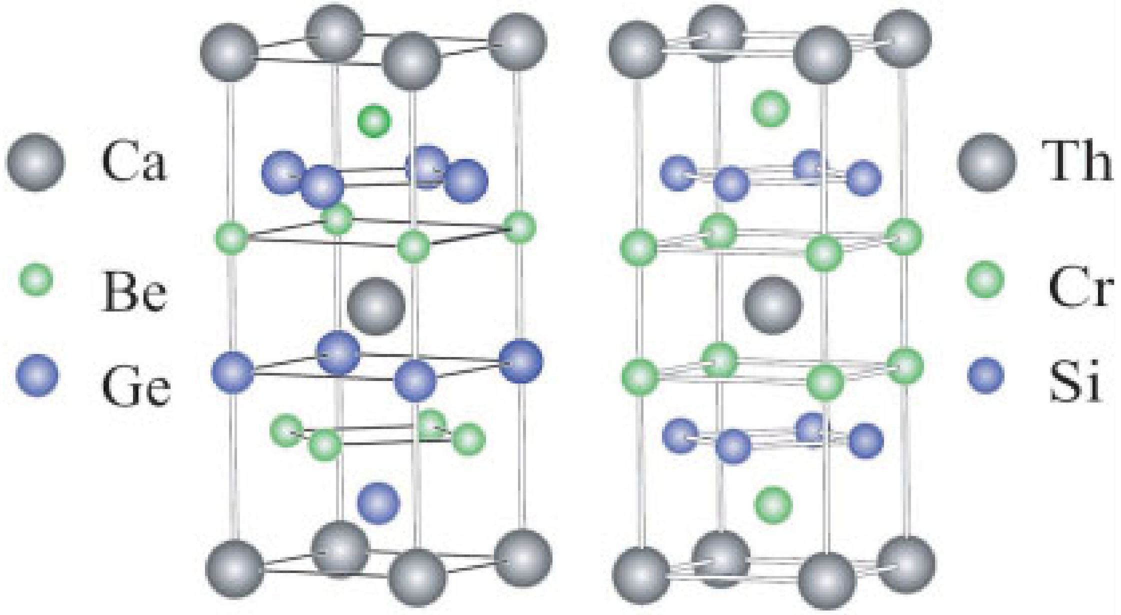

Figure 5.1: The tetragonal structure of the $CaBe_2Ge_2$ (left) and the $ThCr_2Si_2$ (right) lattices.

Even if no structural transition occurs, the close relation between the two structures can lead to crystallographic disorder as observed in a recent study of

URh_2Ge_2. In this compound, $\sim 5 - 10\,\%$ of Rh/Ge site exchange generates moderate bond length disorder, as it has been established for an as-grown crystal by x-ray absorption fine structure experiments [88]. This type of disorder is the origin of a spin glass ground state below $\sim 9\,\mathrm{K}$ and it controls the electronic transport properties [89].

In this situation, to go a step beyond the studies carried out so far concerning the influence of disorder on the physical properties of correlated electron systems, a material would be needed which fulfills various requirements. First, the material has an inherent tendency towards a structural instability, resulting in a moderate level of crystallographic disorder. Second, it must be possible to detect the disorder and to quantify its level. Regarding this point, it is difficult to detect disorder in U intermetallics by means of x-ray diffraction with the scattering cross section for U being extremely large, compared to other constituents, and hence most of the disorder signatures of the other elements being hidden. In this situation, the complementarity of neutron scattering might possibly be used to detect disorder. At last, it would be desirable if single crystalline samples with different heat treatments are available in order to study the influence of an annealing process on the structural and physical properties.

Given these requirements, UPt_2Si_2 has been demonstrated to be a very suitable candidate to study disorder effects in heavy fermions [85]. Regarding the issue of determining type and level of disorder, the containing elements U, Pt and Si have a very bright elemental contrast in neutron scattering due to their different neutron scattering cross sections (U: $8.9\,\mathrm{barn}$, Pt: $11.7\,\mathrm{barn}$ and Si: $2.2\,\mathrm{barn}$). We will review the properties of this material in order to set the ground for the ensuing discussion of the physical properties.

In the following brief summary of the physical properties we will in particular pay attention to the structural disorder and electronic transport properties of UPt_2Si_2. Afterwards, magnetization and electronic transport measurements in high magnetic fields will be presented. Based on these data the magnetic phase diagram will be generated and compared with the phase diagram of URu_2Si_2 [90]. Using the high magnetic field measurements the validity of calculations based on the crystal electric field model will be discussed [86].

If not noted otherwise ,the measurements discussed in this work have been carried out on as-cast single crystalline material grown by a modified Czochralski method in Leiden as described in Ref. [91]. For the samples studied here, single crystal neutron scattering experiments have been performed using the E5 spectrometer at BENSC, with a wavelength $\lambda = 2.4307\,\text{Å}$ at a temperature $T = 50\,\text{K}$. For the refinement of the data a $CaBe_2Ge_2$ lattice (space group $P4/nmm$) has been used. Within experimental resolution an optimum refinement has been found for a fully ordered lattice of stoichiometry 1 : 2 : 2. The results are summarized in Tab. 5.1. The lattice parameters and the atomic sites x, y, z match well the results reported for polycrystalline [92] and single crystalline [93] samples. The displacement parameters U_{11} and U_{22} on the Pt(2)/Si(2) sites have been observed to be extraordinary large, see Tab. 5.1. Since the experiments have been carried out at low temperatures of $50\,\text{K}$, this displacement cannot be thermally induced.

For further illustration these findings are depicted schematically in Fig. 5.2. A structure is observed which consists of ordered and disordered layers. The displacement on the Pt(2)/Si(2) ligand sites is within the tetragonal $a-b$ plane. This type of disorder is reflected in an unusual behavior of the thermal expansion.

In Fig. 5.3 the lattice parameters along the a and c axis of UPt_2Si_2 are displayed as function of temperature. These data have been derived from powder neutron diffraction using the E9 spectrometer at BENSC (neutron wave lengths $\lambda = 1.797429\,\text{Å}$ and $1.308\,\text{Å}$; refinement values $R_{\text{Bragg}} \sim 6-8\,\%$). The c axis lattice constant shows a normal behavior as it shrinks with decreasing temperature in contrast to the a axis behavior. For the a axis a minimum at around $100\,\text{K}$ has been found, apparently reflecting a tendency towards a structural

	x	y	z	U_{11} ($\text{Å}^2/8\pi^2$)	U_{22} ($\text{Å}^2/8\pi^2$)	U_{33} ($\text{Å}^2/8\pi^2$)
U	1/4	1/4	0.8484(2)	0.45(4)	0.45(4)	0.08(4)
Pt(1)	1/4	1/4	0.3785(2)	0.10(3)	0.10(3)	0.28(4)
Pt(2)	3/4	1/4	0	1.86(5)	1.86(5)	0.14(4)
Si(1)	3/4	1/4	1/2	0.10(6)	0.10(6)	0.18(7)
Si(2)	1/4	1/4	0.1330(3)	0.94(8)	0.94(8)	0.29(8)

Lattice parameters: $a = 4.186\,\text{Å}$, $c = 9.630\,\text{Å}$

Table 5.1: Single crystal neutron scattering refinement from Ref. [85], for details see text.

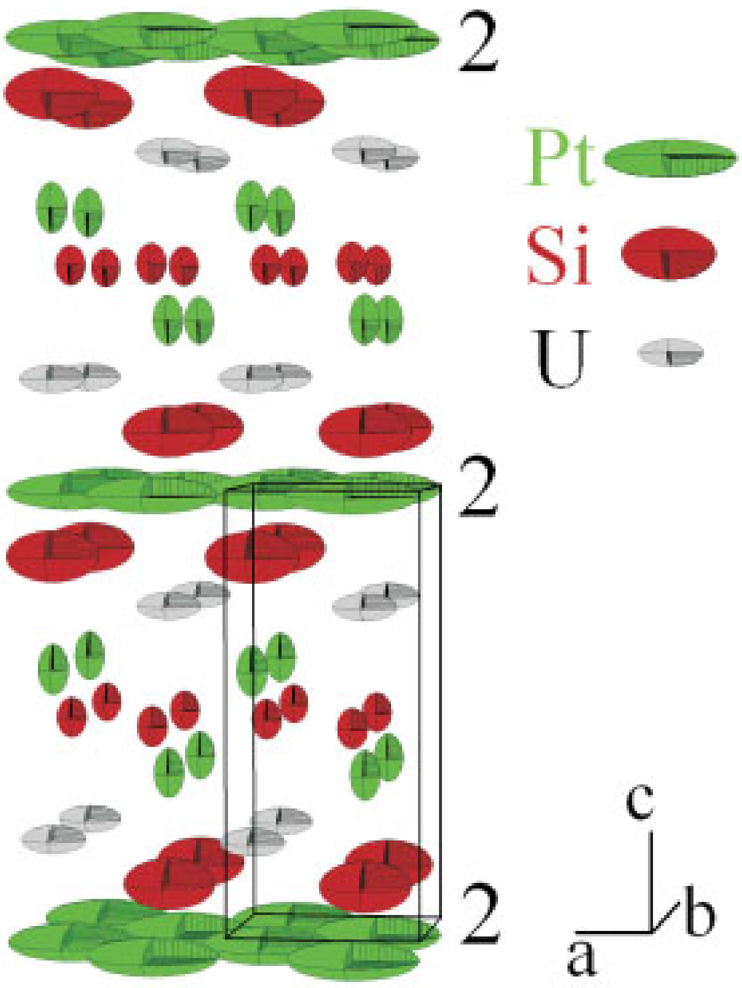

Figure 5.2: Crystal structure of UPt_2Si_2 in a thermal displacement ellipsoidal representation; for details see text.

distortion in UPt_2Si_2 [85] as a result of the compression of the lattice.

5.3 Magnetic properties

The susceptibility χ of UPt_2Si_2 for $B//a$ and $B//c$ is depicted in Fig. 5.4. The high temperature range ($\sim 40 - 400\,\mathrm{K}$) of the susceptibility data cannot be fitted using a Curie-Weiss law. The data has to be separated into two regimes, *i.e.*, above and below $250\,\mathrm{K}$. In Ref. [84] it is suggested that this separation might be associated to a previously reported phase transition at $305\,\mathrm{K}$ [94].

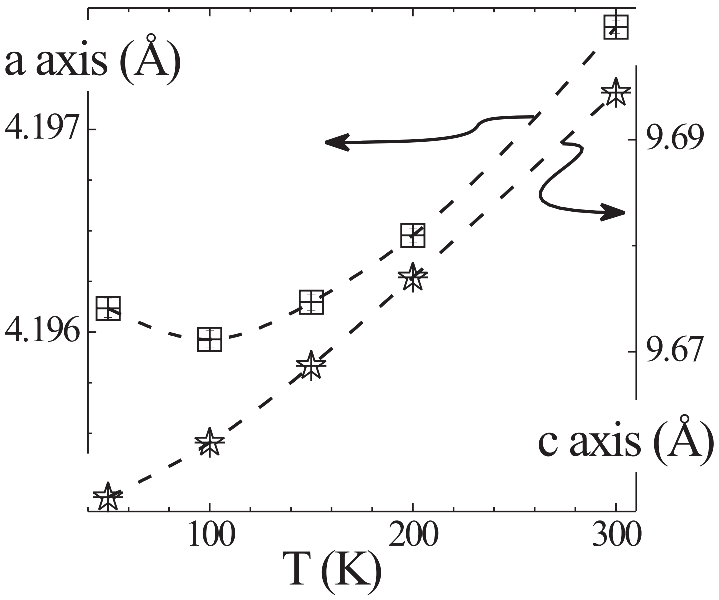

Figure 5.3: Temperature dependence of the a and c axis lattice parameters in UPt$_2$Si$_2$, for details see text [85].

However, fitting the data below $250\,\mathrm{K}$ using a Curie-Weiss fit

$$\chi = \frac{C}{T - \Theta_{\mathrm{CW}}} \tag{5.1}$$

with $C = N_{\mathrm{A}}\mu_{\mathrm{eff}}^2/3k_B$, Θ_{CW}: Curie-Weiss temperature and μ_{eff}: effective moment in Bohr magnetons, yields an effective moment of $4.17\,\mu_{\mathrm{B}}$ ($3.09\,\mu_{\mathrm{B}}$) and a Θ_{CW} of $-116\,\mathrm{K}$ ($-35\,\mathrm{K}$) for the a (c) axis. The effective moment for the a axis is much to large to stem from U ions as those values are much smaller for the different ionization states. The large value of the magnetic moment previously was attributed to crystal electric field effects influencing the susceptibility [86].

The difference between field cooled (FC) and zero field cooled (ZFC) measurements in the susceptibility data at low temperatures reflects structural disorder, see Fig. 5.5. For an accurate determination of the deviation between FC and ZFC measurements the difference $\Delta\chi = \chi_{\mathrm{FC}} - \chi_{\mathrm{ZFC}}$ is plotted in the lower panel of Fig. 5.5. The temperature where the ZFC measurements is different from the FC data, *i.e.*, $\Delta\chi \neq 0$, is introduced as a new characteristic temperature T_{irr} as indicated in Fig. 5.5.

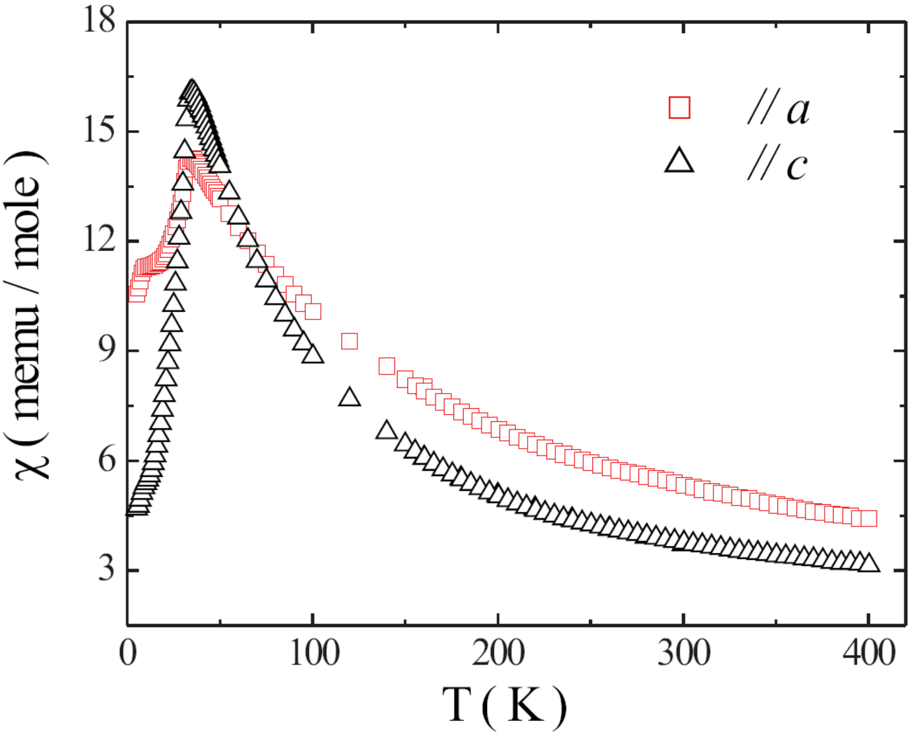

Figure 5.4: Temperature dependence of the susceptibility χ of UPt_2Si_2 for $B//a$ and $B//c$, for details see text [84].

For an exact determination of the magnetic transition temperature specific heat measurements between 10 K and 50 K in zero field using a standard adiabatic method have been performed, see Fig. 5.6. In order to determine T_N more accurately the electronic and phononic contribution to the specific heat (solid lines in Figs. 5.6) have been subtracted, with $c_\mathrm{p,mag}$ depicted in Fig. 5.7.

As a nonmagnetic isostructural sample (*e.g.*, $ThPt_2Si_2$) was not available to perform a phonon correction, a fitting model using the full Debye integral and including an optical mode has been employed. For the phonon contribution two Debye modes ($\Theta_\mathrm{D1}(\mathrm{U}) = 122\,\mathrm{K}$ and $\Theta_\mathrm{D2}(\mathrm{Pt}) = 218\,\mathrm{K}$) and one Einstein mode ($\Theta_\mathrm{E}(\mathrm{Si}) = 491\,\mathrm{K}$) have been assumed. The electronic contribution to the specific heat was reported to $\gamma = 32\,\mathrm{mJ}/(\mathrm{moleK}^2)$ and is included in the specific heat background (solid lines) depicted in Fig. 5.6.

This way the magnetic contribution $c_\mathrm{p,mag}$ to the specific heat has been obtained, see Fig. 5.7. Using a linear extrapolation scheme the transition temperature T_N was determined to 32.1 K. Furthermore, from $c_\mathrm{p,mag}/T$ using an

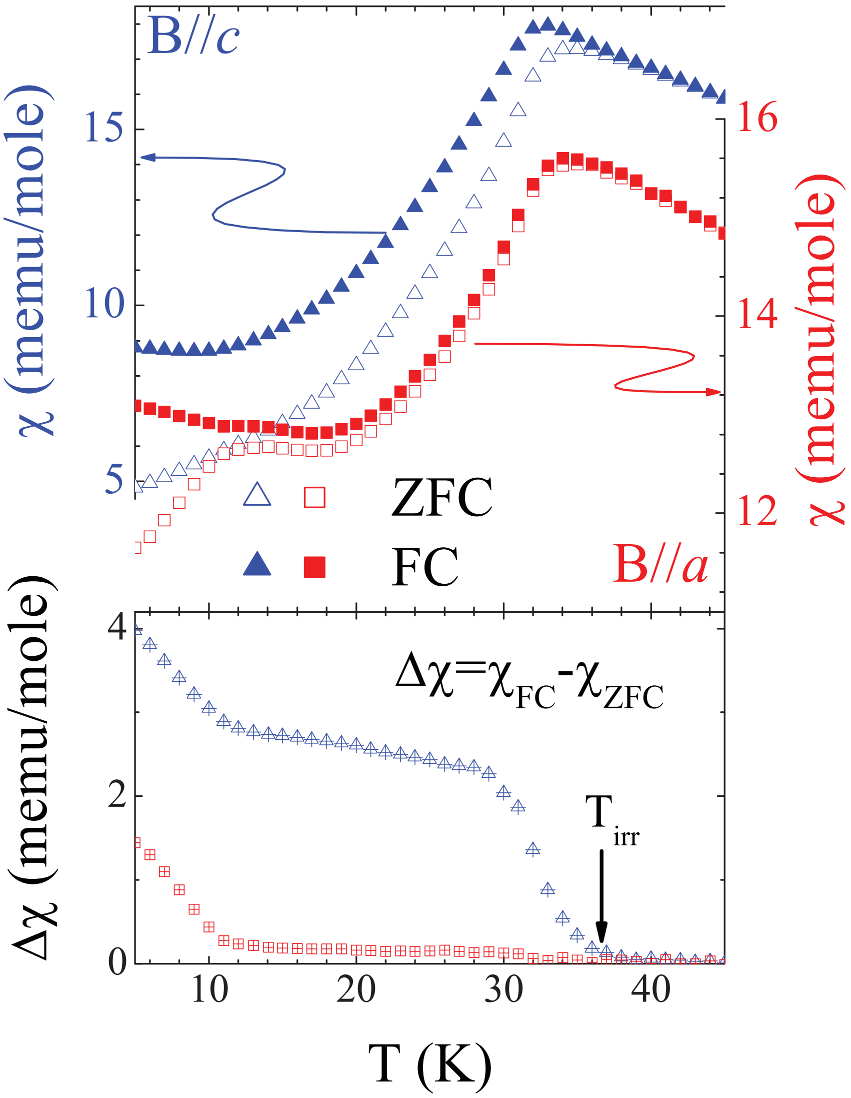

Figure 5.5: Temperature dependence of the susceptibility χ (upper pannel) and $\Delta\chi = \chi_{\mathrm{ZFC}} - \chi_{\mathrm{FC}}$ (lower pannel) of UPt_2Si_2, for details see text [84].

entropy balance model T_{N} was determined to 32.9 K. However, the peaks

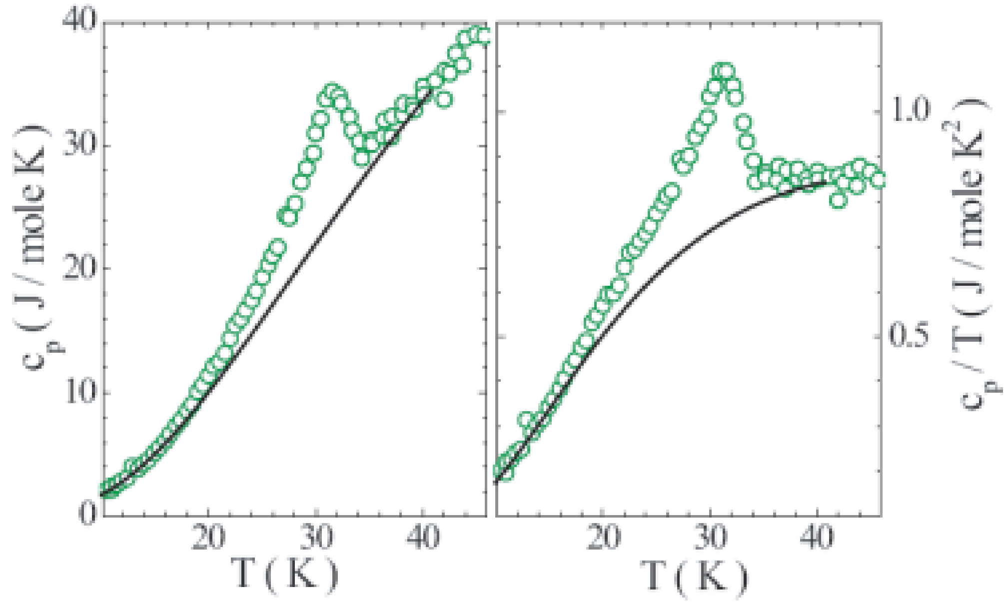

Figure 5.6: Temperature dependence of the specific heat c_p and c_p/T of UPt$_2$Si$_2$. The black solid line is representing the non-magnetic contribution, for details see text [84].

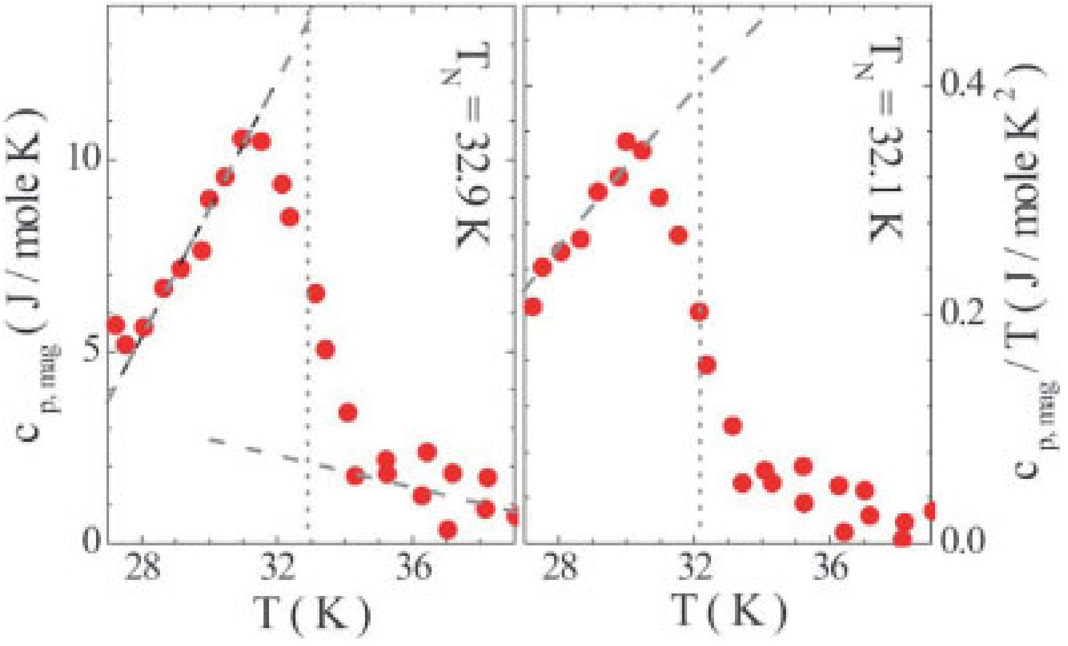

Figure 5.7: Temperature dependence of the magnetic specific heat $c_\mathrm{p,mag}$ and $c_\mathrm{p,mag}/T$ of UPt$_2$Si$_2$, for details see text [84].

which are indicating the transition are rather broad ($\sim 3\,\mathrm{K}$) again reflecting structural disorder in this sample UPt_2Si_2.

The magnetic structure of UPt_2Si_2 has been derived from single crystal neutron scattering experiments using the E1 spectrometer at BENSC (neutron wave length $\lambda = 2.42757\,\text{Å}$). The magnetic structure of Ref. [93] (moments are pointing along the c axis and building up ferromagnetic sheets within the a-b plane which are antiferromagnetically coupled on adjacent planes along the c axis) could be confirmed. The magnetic moment is $\sim 2.5\,\mu_\mathrm{B}/\mathrm{U\,atom}$, and thus somewhat larger than in Ref. [93].

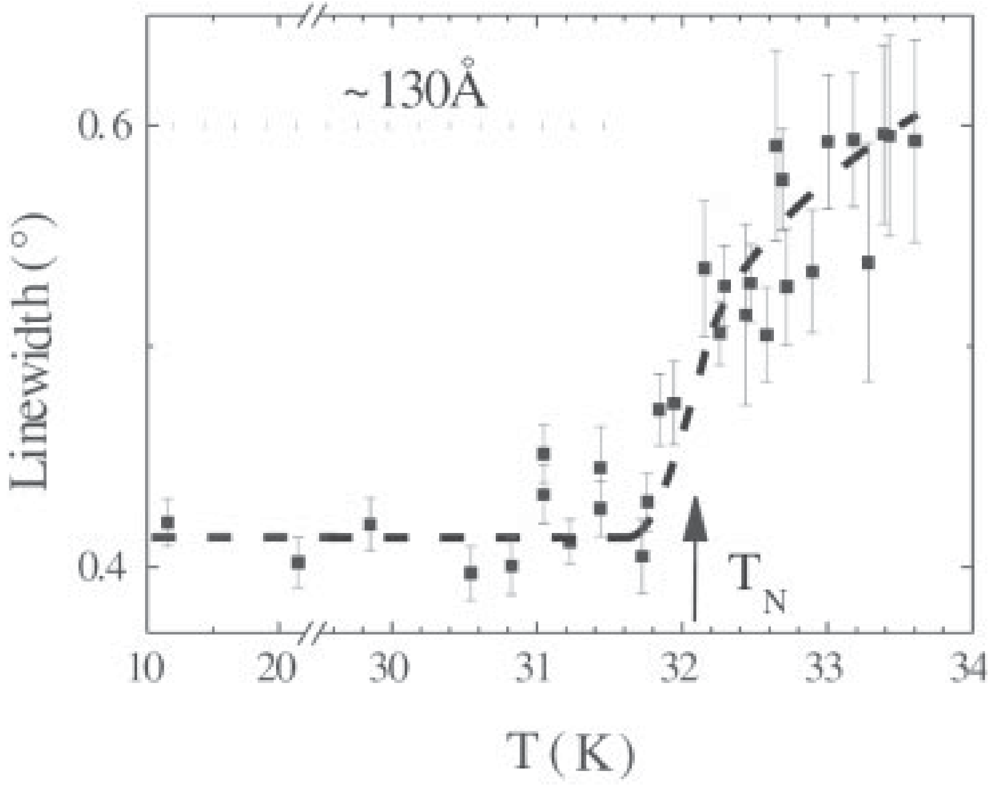

Figure 5.8: Temperature dependence of the linewidth of (1 0 0) Bragg peak of UPt_2Si_2, for details see text [84].

The linewidth of the magnetic (1 0 0) Bragg peaks is depicted in Fig. 5.8 [84]. Below T_N the peak is resolution limited, reflecting a magnetic correlation length larger than the experimental resolution limit. Above T_N the Bragg peaks are broadened reflecting a limited magnetic correlation length. At $T = 34\,\mathrm{K}$ a correlation length of $\sim 130\,\text{Å}$ is obtained, again reflecting structural disorder in good agreement with the broadening seen in specific heat data.

5.4 Electronic transport properties

Aside from the anisotropy in the magnetic properties, UPt_2Si_2 exhibits also an extraordinary strong anisotropy in the electrical resistivity. Single crystals of UPt_2Si_2 grown in Leiden (black, closed symbols) and in Sapporo (green, open symbols) have been measured along the a and c axis, see Fig. 5.9. The crystal grown in Sapporo has smaller residual resistivities ($213\,\mu\Omega\mathrm{cm}\ //c$ and $38.5\,\mu\Omega\mathrm{cm}\ //a$) in contrast to the crystal grown in Leiden ($335\,\mu\Omega\mathrm{cm}\ //c$ and $43\,\mu\Omega\mathrm{cm}\ //a$). Further, the resistivity ratio is smaller for the latter one, being 0.96 and 3.5 for $//c$ and $//a$, respectively, in contrast to 1.5 for $//c$ and 5.3 for $//a$ for the Sapporo crystal. The stark sample dependence of the resistivity reflects the strong influence on the level of crystallographic disorder. In the discussion below only the crystal from Leiden will be considered.

The resistivity along the a axis shows heavy fermion metallic behavior with an antiferromagnetic ground state. The broad maximum around $180\,\mathrm{K}$ indicates the transition into the coherent state. The AFM transition appears as a kink in the resistivity at low temperatures, see Fig. 5.10. Altogether the behavior along the a axis is that of a Kondo type heavy fermion antiferromagnet.

The antiferromagnetic transition appears in the resistivity derivative $d\rho/dT$ as a maximum (Fig. 5.11). This way T_{N} is determined to $32\,\mathrm{K}$, in good agreement with the thermodynamic measurements discussed above. The resistivity reduction below the antiferromagnetic transition can be described with a fit assuming a freezing out of magnons caused by the opening of a spin wave excitation gap:

$$\rho(T) = \rho_0 + AT^2 + \frac{DT}{\Delta}\left[1 + \frac{2T}{\Delta}\right] \exp\left(-\frac{\Delta}{T}\right). \tag{5.2}$$

A fit below $20\,\mathrm{K}$ yields gap values $\Delta = 44\,\mathrm{K}$ and $47\,\mathrm{K}$ for the crystals from Leiden and Sapporo, respectively, see Fig. 5.10.

The resistivity along the c axis is completely different from the behavior observed along the a axis. At high temperatures a non-metallic behavior with a negative $d\rho/dT$ is observed (Fig. 5.9). Matthiesen‘s rule is not valid as the

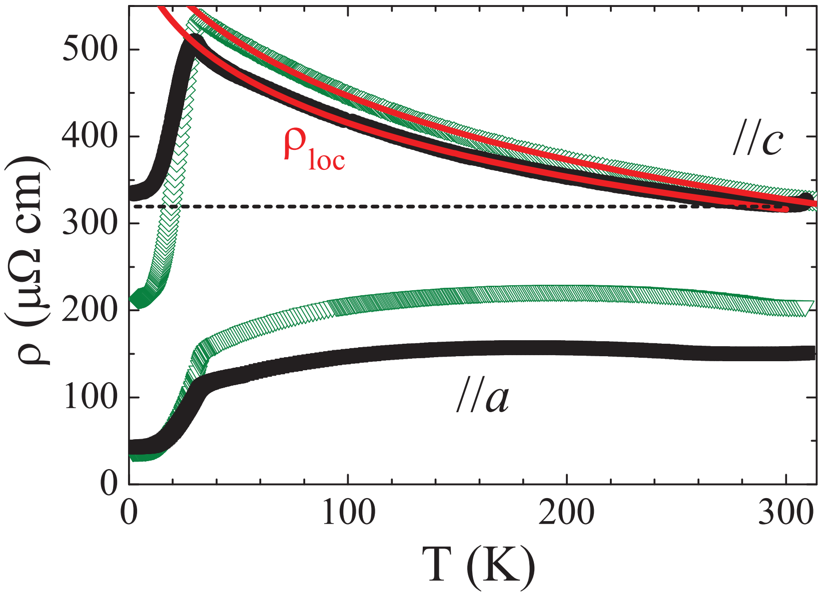

Figure 5.9: Temperature dependence of the resistivity of UPt$_2$Si$_2$ measured along the a and the c axis. The black, closed (green, open) data points are measured on a single crystal grown in Leiden (Sapporo). The red curve indicates a fit assuming disorder induced localization behavior [85].

residual resistivity is larger than the room temperature value (Leiden crystal). The extraordinary behavior above T_{N} is associated to the ligand disorder on the Pt(2)/Si(2) sites. The idea is that the wave functions of the electrons are localized in between disordered Pt(2)/Si(2) planes, that is electronic localization on a length scale of a few Å.

The electronic transport properties in disordered heavy fermion systems can be parameterized by localization theory [89]. In this situation the conductivity is given by $\sigma_0 + \sigma(T)$, with the conductivity correction $\sigma(T)$ given by

$$\Delta\sigma(T) = \frac{e^2}{2\pi^2\hbar}\left(3\sqrt{b + c^2T^2} - cT - 3\sqrt{b} + d\sqrt{T}\right), \tag{5.3}$$

with $b = 1/D\tau_{\mathrm{so}}$, $c = \sqrt{1/4D\tau_i T^2}$, $d = 0.7367\sqrt{k_{\mathrm{B}}/D\hbar}$ (diffusion coefficient D, spin-orbit τ_{so}, and inelastic τ_i scattering times) [95, 96]. The full resistivity is then given by $\rho_{\mathrm{loc}} = (\sigma_0 + \Delta\sigma)^{-1}$. Using this model an excellent description

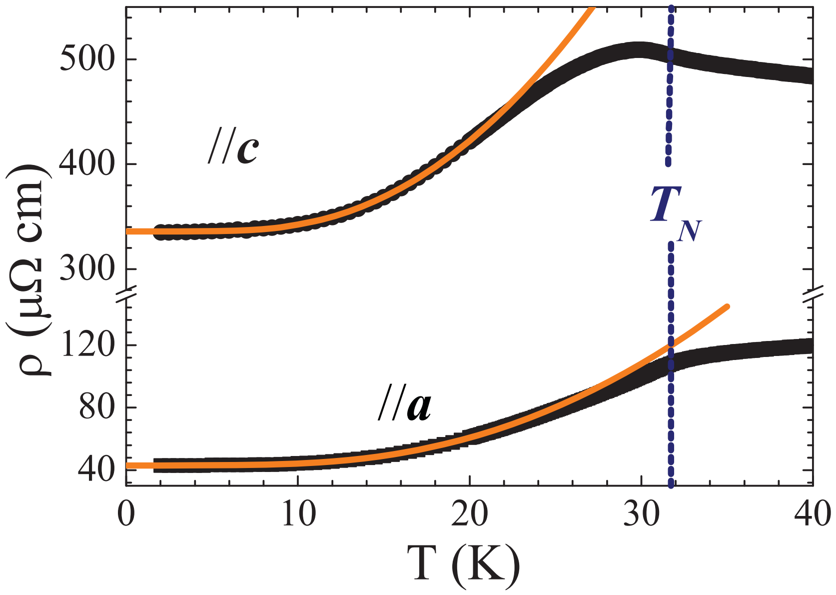

Figure 5.10: Temperature dependency of the resistivity ρ along a and c axis of UPt_2Si_2 for the Leiden crystal. The orange curve indicates a fit assuming a freezing out of magnons caused by the opening of a spin wave excitation gap. The antiferromagnetic transition temperature is indicated [85].

of the data above T_N can be achieved (solid red line in Fig. 5.9).

Upon lowering the temperature just below T_N, initially a stronger increase followed by a reduction of the resistivity is observed (Fig. 5.10). This "overshoot" is difficult to see in the temperature dependence of the resistivity, but more clearly it is observed in the derivative of the resistivity $\mathrm{d}\rho/\mathrm{d}T$ as a minimum at T_N subsequently followed by a maximum, see Fig. 5.11. This behavior is reflecting a superzone formation on the Fermi surface and implies that a Fermi surface reconstruction occurs at T_N.

The anomaly in the resistivity reflects band gaps introduced by superzone formation upon onset of long range magnetic ordering. This notion is supported by band structure calculations carried out by P. Oppeneer, University Uppsala [97]. These calculations indicate that a pseudo gap appears at the Fermi surface upon entering the magnetically ordered state. It implies that the essential

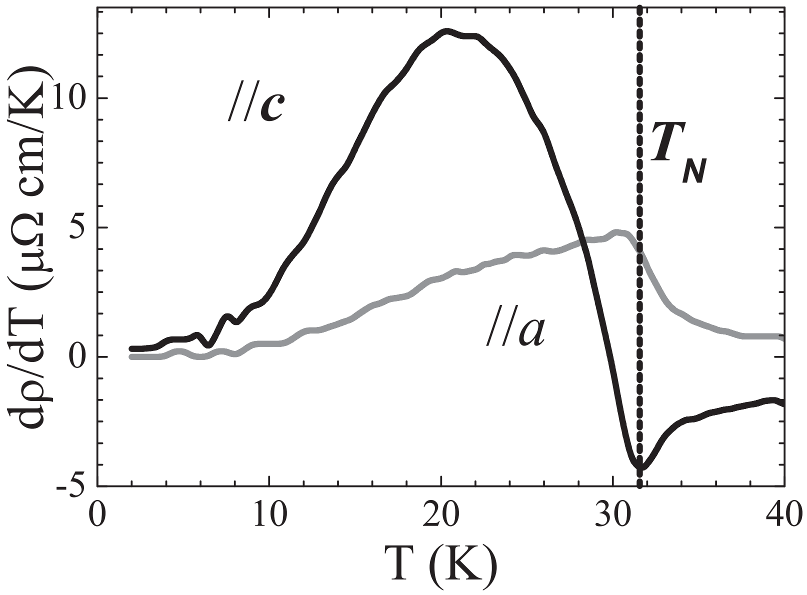

Figure 5.11: Temperature dependency of the resistivity derivative $d\rho/dT$ along a and c axis of UPt$_2$Si$_2$ for the Leiden crystal. The antiferromagnetic transition temperature is indicated [85].

behavior of UPt$_2$Si$_2$ is explained in a band structure model, and that the crystal electric field model is not valid.

The low temperature data of the c axis resistivity can be described with the same model as along the a axis (Eq. 5.2), but this time without the AT^2 term as along the c axis no transition into the coherent state occurs. From the fit, the value of the gap has been obtained to $\Delta = 44\,\mathrm{K}$ for $I//a$ and $\Delta = 32\,\mathrm{K}$ for $I//c$ axis, respectively.

To elucidate the magnetic field dependence of the spin excitation gap Δ, resistivity measurements in fields up to $9\,\mathrm{T}$ at temperatures between $2\,\mathrm{K}$ and $40\,\mathrm{K}$ along the c axis have been carried out. These measurements have been performed on an annealed sample (900° C/1 week). In Ref. [84] it is shown that the annealing process does not alter the physical properties significantly. Thus, it is ensured that the data from annealed samples can be used to determine the in-field behavior of UPt$_2$Si$_2$. The value of the spin wave gap has been obtained by fitting these measurements with Eq. 5.2. As well, the transition temperature $T_{\rm N}$ has been determined from the minimum in $d\rho/dT$. Both quantities are summarized in the phase diagram depicted in Fig. 5.12.

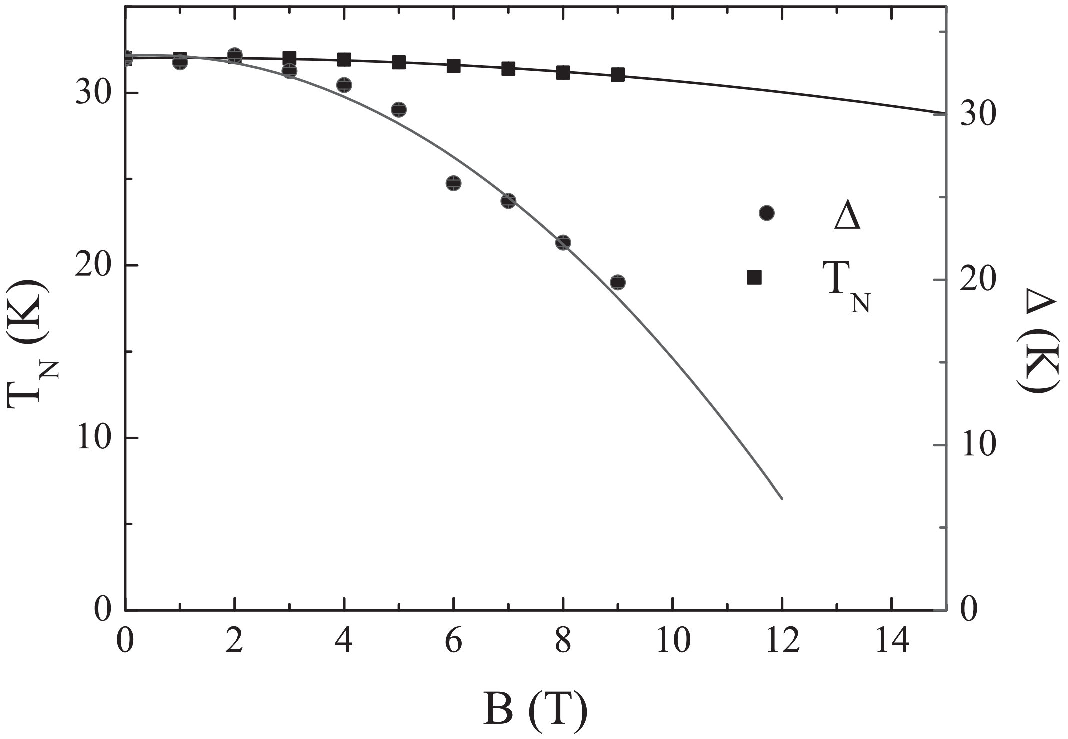

Figure 5.12: Spin excitation gap Δ and antiferromagnetic transition temperature $T_{\rm N}$ of $\rm UPt_2Si_2$. The magnetic field B has been applied along the c axis. $T_{\rm N}$ is indicated by black squares, values of the gap Δ are indicated by dark gray dots. The solid lines are fits to the data, for details see text.

The value of the spin wave gap Δ exhibits a larger reduction in an applied magnetic field than the antiferromagnetic transition temperature $T_{\rm N}$. The field dependence of the spin excitation gap has been fitted in the same way as for $\rm URu_2Si_2$ [98], using

$$\Delta(B) = \Delta(0)\left[1 - (B/B_{\rm gap,c})^2\right],$$

with $B_{\rm gap,c} = 13.8\,\rm T$ - critical field of the spin gap and $\Delta(0) = 33.8\,\rm K$. Analogous to the field dependence of the spin excitation gap, the antiferromagnetic transition has been fitted using the corresponding expression:

$$T_{\rm N}(B) = T_{\rm N}(0)\left[1 - (B/B_{\rm afm,c})^2\right],$$

with $B_{\mathrm{afm,c}} = 50\,\mathrm{T}$ - critical antiferromagnetic field and $T_{\mathrm{N}}(0) = 32\,\mathrm{K}$.

The different field dependencies of the spin excitation gap and the antiferromagnetic transition temperature are rather puzzling, as the gap Δ can be closed with a rather small magnetic field of $13.8\,\mathrm{T}$, whereas a field of $50\,\mathrm{T}$ is needed to suppress antiferromagnetic ordering.

We speculate that the observed different behavior of the gap Δ and the antiferromagnetic transition temperature T_{N} is due to two different energy scales in UPt_2Si_2. It might be a hint, that UPt_2Si_2 exhibits a mixed localized/itinerant behavior, with a dominant itinerant contribution, in a similar fashion as suggested for related systems like UPt_3 and UPd_2Al_3 [99, 100].

Altogether, from these studies it appears that the crystal electric field description put forth in Ref. [86] is not suitable to account for the transport properties of UPt_2Si_2. Hence, UPt_2Si_2 is not a localized f electron system in the way as thought previously. Instead, these new insights indicate that a band structure model ought to be more adequate to describe UPt_2Si_2. In the following, measurements have been carried out to lend more support to the notion that a crystal electric field model is not applicable to UPt_2Si_2.

5.5 High magnetic field measurements

Hitherto, high field experiments have only been discussed within the crystal field model [86]. Here, with the band structure approach to understand the properties of UPt_2Si_2 a re-investigation of the high field behavior is presented.

High field magnetization measurements have been carried out at the Laboratoire National des Champs Magnétiques Pulsés (LNCMP) in Toulouse in collaboration with H. Rakoto in a $60\,\mathrm{T}$ pulsed field magnet (for the experimental setup see Ref. [101]). The magnetization as function of the external field for different temperatures along the a and the c axes is depicted in the Figs. 5.13 and 5.14, respectively.

In good agreement with Amitsuka *et al.* [102] a metamagnetic transition, which occurs as an inflection point in the magnetization, is observed at low temperatures. The transition along the c axis occurs in two steps at $25\,\mathrm{T}$ and $32.2\,\mathrm{T}$ at $1.7\,\mathrm{K}$ and $4\,\mathrm{K}$. At $10\,\mathrm{K}$ only the lower transition persists, at $20\,\mathrm{K}$ also

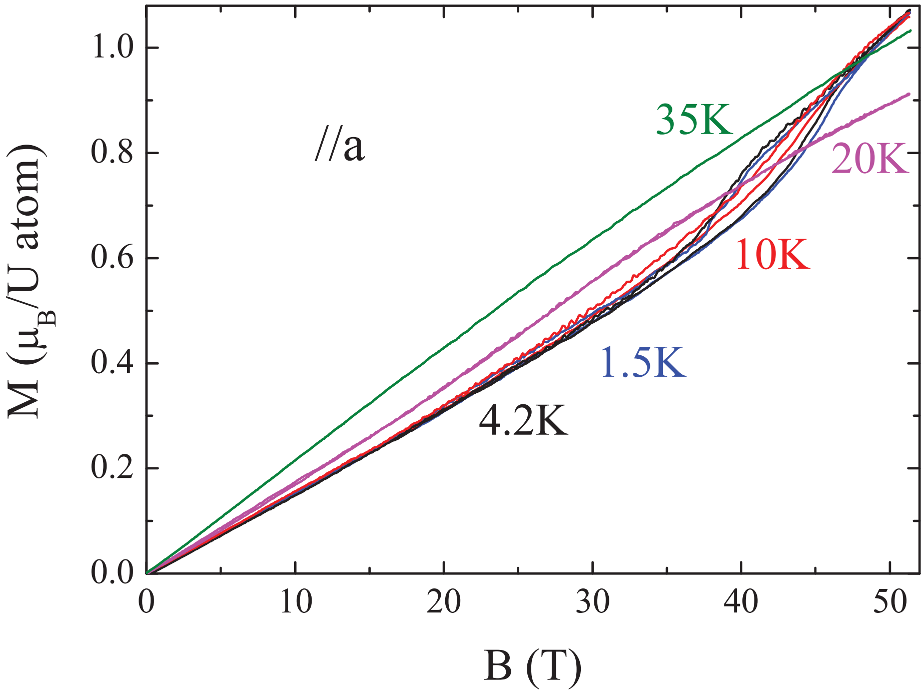

Figure 5.13: High field magnetization curves of UPt_2Si_2 for temperatures of $1.5\,K$, $4.2\,K$, $10\,K$, $20\,K$ and $35\,K$ with the magnetic field applied parallel to the a axis.

this transition has vanished. Along the a axis a dominant one-step transition is observed. The transition field is $46\,T$ at $1.7\,K$, decreases to $43.8\,T$ at $10\,K$, and is not observable anymore at $20\,K$. Also, a multistep-like fine structure with small hysteresis, as in previous works, is verified.

In Fig. 5.15 the low temperature magnetization at $T = 1.5\,K$ (solid line), in comparison with calculated magnetization based on the crystal electric field model by Nieuwenhuys [86], is depicted.

Along the a axis, a metamagnetic transition is seen in the calculated curve at $\sim 67\,T$, in contrast to $46\,T$ in the measured data. For the c axis, above $\sim 20\,T$ the calculations strongly deviate from the measured values, with only one transition predicted in the calculated curve in contrast to two transitions in the measured curve. Altogether this is indicating that a crystal electric field model is not appropriately describing the physical properties of UPt_2Si_2.

To more clearly visualize the hysteresis the difference between averaged mag-

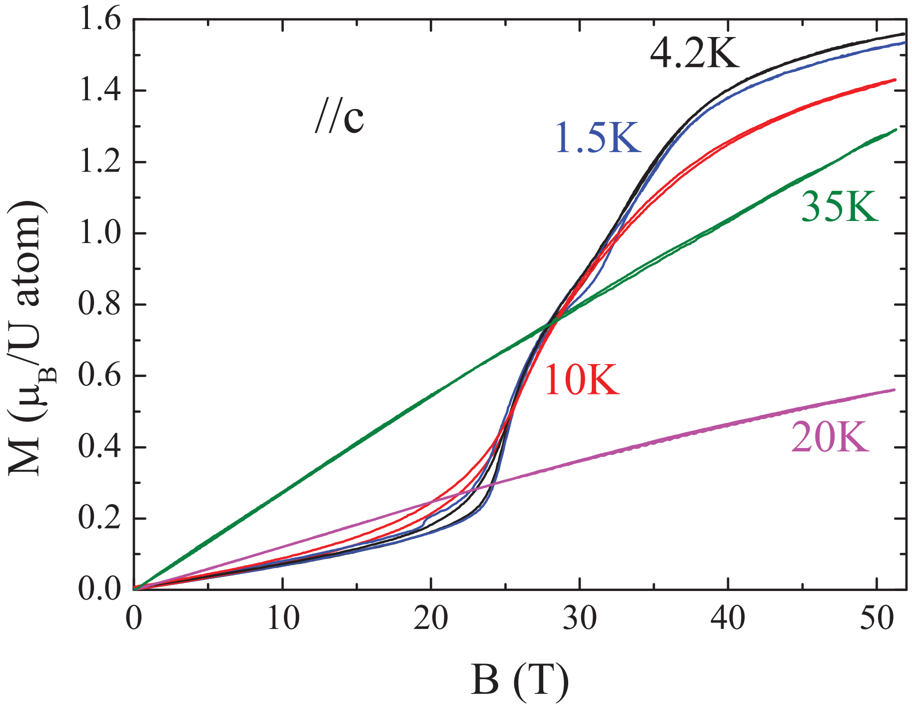

Figure 5.14: High field magnetization curves of UPt_2Si_2 for temperatures of $1.5\,\mathrm{K}$, $4.2\,\mathrm{K}$, $10\,\mathrm{K}$, $20\,\mathrm{K}$ and $35\,\mathrm{K}$ with the magnetic field applied parallel to the c axis.

netizations and field-sweep up (field-sweep down) values for $B//a$ and $B//c$ are depicted in the Figs. 5.16 and 5.17, respectively. For $B//a$, at $1.7\,\mathrm{K}$ the hysteresis sets in at $\sim 15\,\mathrm{T}$, the hysteretic behavior up to around $37\,\mathrm{T}$ probably is an experimental artifact, with only $0.02\,\mu_{\mathrm{B}}/\mathrm{Uatom}$ difference between field-sweep up and down at an absolute magnetization of $0.6\,\mu_{\mathrm{B}}/\mathrm{U\,atom}$. However, between $\sim 37\,\mathrm{T}$ and $\sim 48\,\mathrm{T}$ there is additional structure in the hysteresis, with a maximum difference between upper and lower curve of $0.08\,\mu_{\mathrm{B}}/\mathrm{Uatom}$, which clearly is intrinsic to UPt_2Si_2.

Similar as for $B//a$, for $B//c$ there is a low field hysteretic region resulting from experimental inaccuracies in these pulsed magnetic field experiments. Further, two hysteretic regions are observed, from $\sim 19\,\mathrm{T}$ up to $\sim 27\,\mathrm{T}$ (with a difference of $0.1\,\mu_{\mathrm{B}}/\mathrm{U\,atom}$) and subsequently one up to $\sim 33\,\mathrm{T}$ (with a difference of $0.06\,\mu_{\mathrm{B}}/\mathrm{U\,atom}$), which are intrinsic. With increasing temperature the hysteresis becomes smaller and vanishes at $20\,\mathrm{K}$ for both directions.

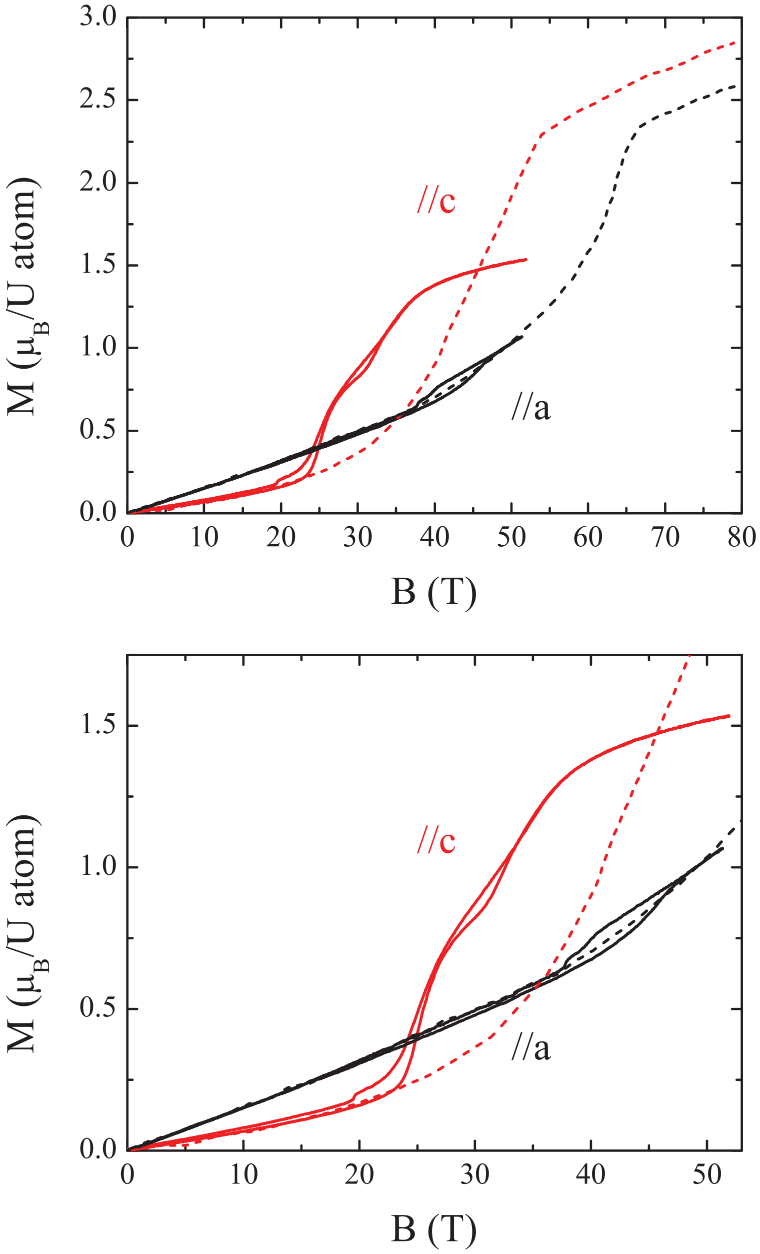

Figure 5.15: Measured (solid lines) and calculated (dashed lines) high field magnetization curves of UPt_2Si_2 at $1.5\,K$ with the magnetic field applied parallel to the a and c axes. In the lower panel a smaller section is depicted. The calculated curves are taken from Ref. [86].

A metamagnetic transition is defined as an inflection point in the magnetization curve. Therefore, it can be seen as a maximum in the field dependent susceptibility. This quantity has been obtained by differentiation of the magne-

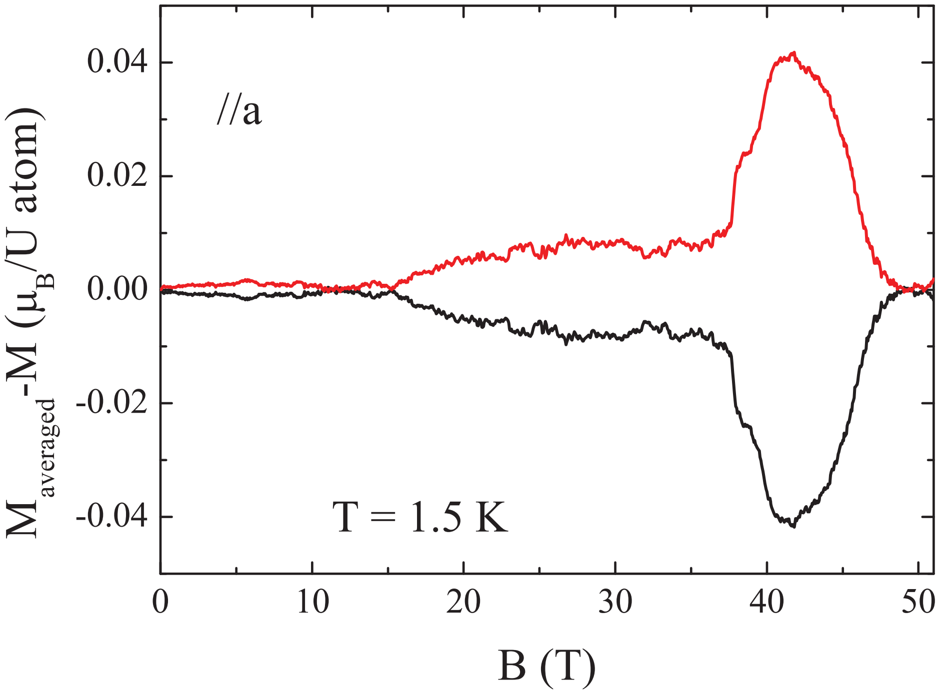

Figure 5.16: Difference between averaged magnetization and field-sweep up (red) (field-sweep down (black)) values of UPt$_2$Si$_2$ for $T = 1.5\,\mathrm{K}$ with the magnetic field applied parallel to the a axis.

tization curves. For this analysis the point density of the magnetization curves has been reduced by smoothing to 100 points for the whole magnetic field range. Afterwards, the average value of field-sweep up and down values have been calculated. These averaged curves are then differentiated and shown in Figs. 5.18 and 5.19 for $B//a$ and $B//c$, respectively. This way the metamagnetic transition field can be determined more accurately.

For $B//a$, at low temperatures of $1.5\,\mathrm{K}$ and $4.2\,\mathrm{K}$ the transitions appear at $38\,\mathrm{T}$ and $45\,\mathrm{T}$. At $10\,\mathrm{K}$ only one maximum is clearly observable at $43\,\mathrm{T}$. For $B//c$, at low temperatures ($1.5\,\mathrm{K}$ and $4.2\,\mathrm{K}$), again two maxima in the susceptibility at $25\,\mathrm{T}$ and $32\,\mathrm{T}$ occur, at $10\,\mathrm{K}$ only one transition at $26\,\mathrm{T}$ is observable. Above $10\,\mathrm{K}$ no transition is visible anymore.

Further, high magnetic field longitudinal resistivity measurements using a standard four point technique have been carried out at the Hochfeld-

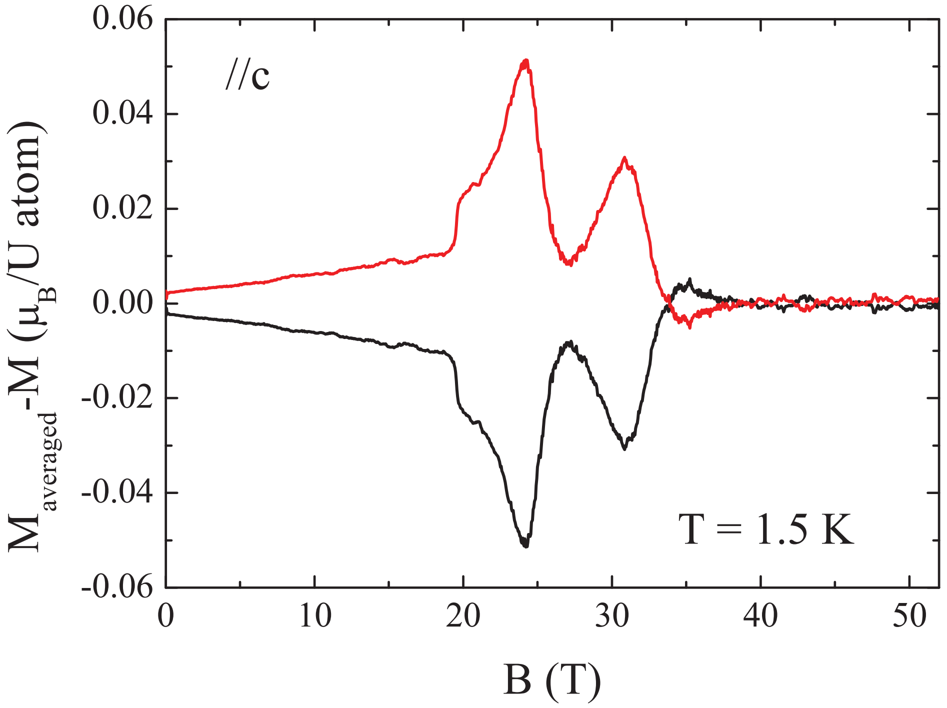

Figure 5.17: Difference between averaged magnetization and field-sweep up (red) (field-sweep down (black)) values of UPt_2Si_2 for $T = 1.5\,\mathrm{K}$ with the magnetic field applied parallel to the c axis.

Magnetlabor Dresden, Forschungszentrum Rossendorf, in collaboration with M. Bartkowiak. The measurement of the resistivity of metallic samples in a high magnetic field is a sophisticated experimental technique. Due to the short duration of a pulse (typical $\sim\ 150\,\mathrm{ms}$) the electronics for data acquisition have to work very fast. Therefore, a digital storage oscilloscope has been used for data acquisition which, in comparison to a lock-in amplifier, has a reduced signal-to-noise ratio. For each field sweep (up and down) 1024 data points have been recorded. The data point density for the field sweep down is somewhat higher than for field sweep up because of the longer duration of the down sweep. Therefore, in this work only the field sweep down data are shown and analyzed. Due to the larger absolute resistance values, the signal-to-noise ratio is larger for $B//c$ than for $B//a$.

The data interpretation of the pulsed field resistivity experiments for both crys-

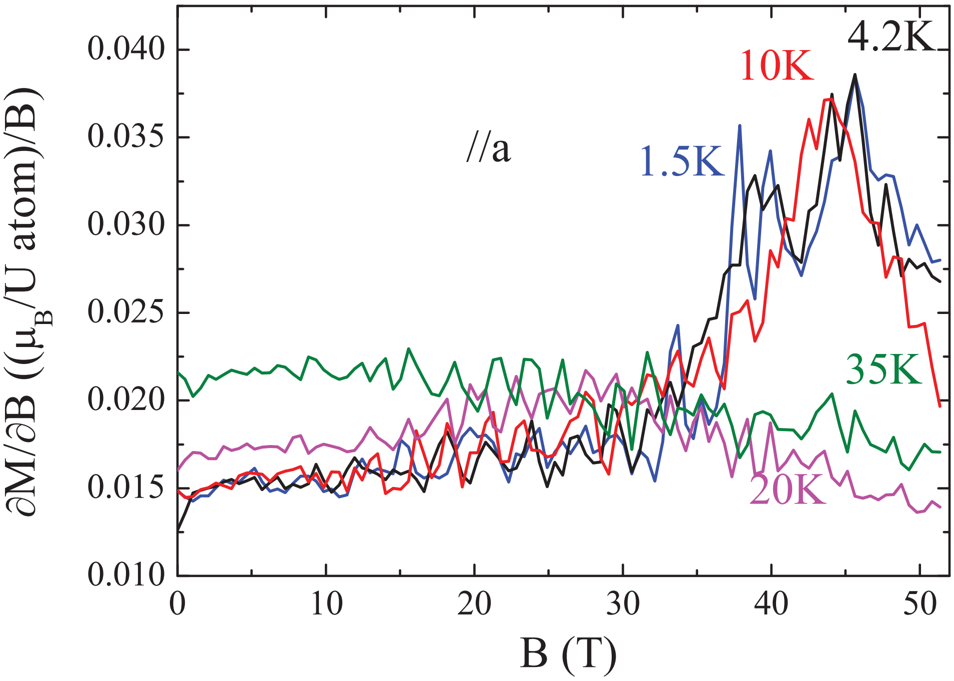

Figure 5.18: Field dependence of the susceptibility $\partial M/\partial B$ of UPt$_2$Si$_2$ at various temperatures with the magnetic field applied parallel to the a axis.

tallographic directions is in part still affected by the comparatively low signal-to-noise ratio. Therefore, in order to ensure that the pulsed field data reflect the intrinsic behavior of UPt$_2$Si$_2$, additional field dependent resistivity measurements for both crystallographic directions in static magnetic fields up to $18\,\mathrm{T}$ have been carried out by M. Bartowiak in Dresden. For comparison, in Figs. 5.20 and 5.21 high magnetic field measurements in static and pulsed fields for $B//a$ and $B//c$, respectively, are depicted. These data verify that the pulsed field measurements show the same principal behavior as measurements in static fields, even though it is with a smaller signal-to-noise ratio.

Further, in the Figs. 5.22 and 5.23 the normalized magnetoresistivity $\frac{\rho-\rho(B=0)}{\rho(B=0)}$ in magnetic fields up to $\sim 50\,\mathrm{T}$ for $B//a$ and $B//c$ are depicted. In general, for $B//a$ below $35\,\mathrm{K}$ the normalized magnetoresistivity is increasing with field, up to a maximum value of 0.9 for $4.2\,\mathrm{K}$. At $1.4\,\mathrm{K}$ a saturation at about $40\,\mathrm{T}$ is found, which is shifted to $50\,\mathrm{T}$ at $4.2\,\mathrm{K}$. At $12\,\mathrm{K}$ only data up to $45\,\mathrm{T}$

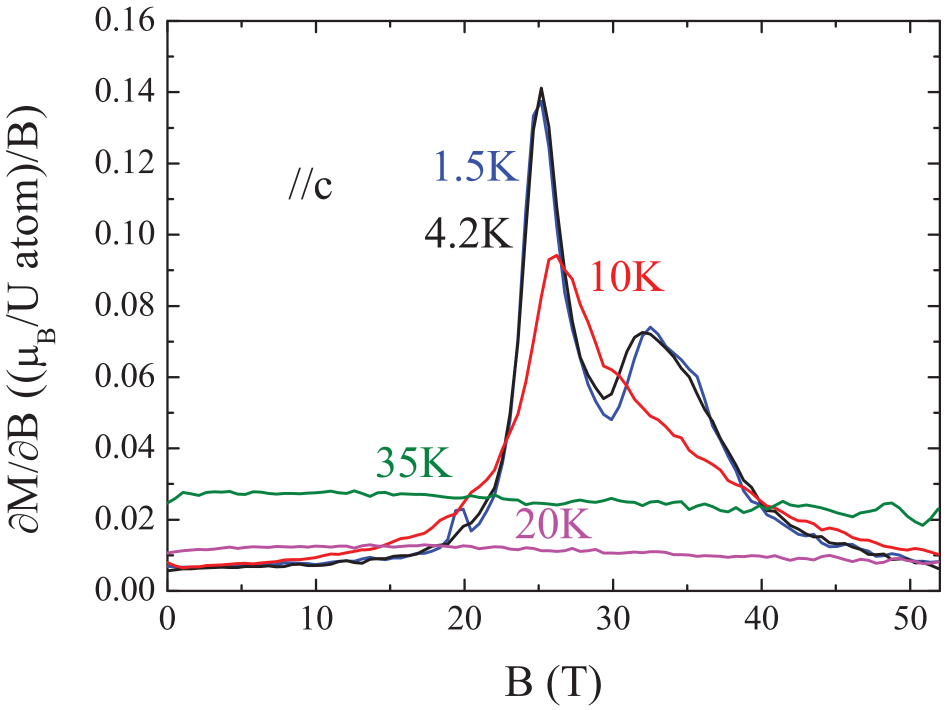

Figure 5.19: Field dependence of the susceptibility $\partial M/\partial B$ of UPt_2Si_2 at various temperatures with the magnetic field applied parallel to the c axis.

are available, hence if a plateau is present in the normalized magnetoresistivity it possibly is not seen in this limited field range.

For the c axis measurements, at low temperatures a distinct maximum at $\sim 25\,\mathrm{T}$, which is slightly shifted to lower fields ($\sim 22\,\mathrm{T}$) at $20.3\,\mathrm{K}$ is observable in the normalized resistivity. Beyond the resistive maximum $\frac{\rho-\rho(B=0)}{\rho(B=0)}$ strongly decreases and saturates at a negative normalized magnetoresistivity of ~ -0.35 at $1.6\,\mathrm{K}$. For temperatures above $20.3\,\mathrm{K}$ the maximum has vanished, and instead the normalized magnetoresistivity is always negative.

Qualitatively, the field dependence of the magnetoresistivity can be explained by a combination of (a) a reduction of spin disorder scattering, and possibly both, (b) Fermi surface effects and (c) crystallographic disorder. In (a), the spins are polarized in the direction of the magnetic field, and with the reduced level of structural disorder in the spin system the electrons can move more easily. In (b), the antiferromagnetic order is associated to Fermi surface effects

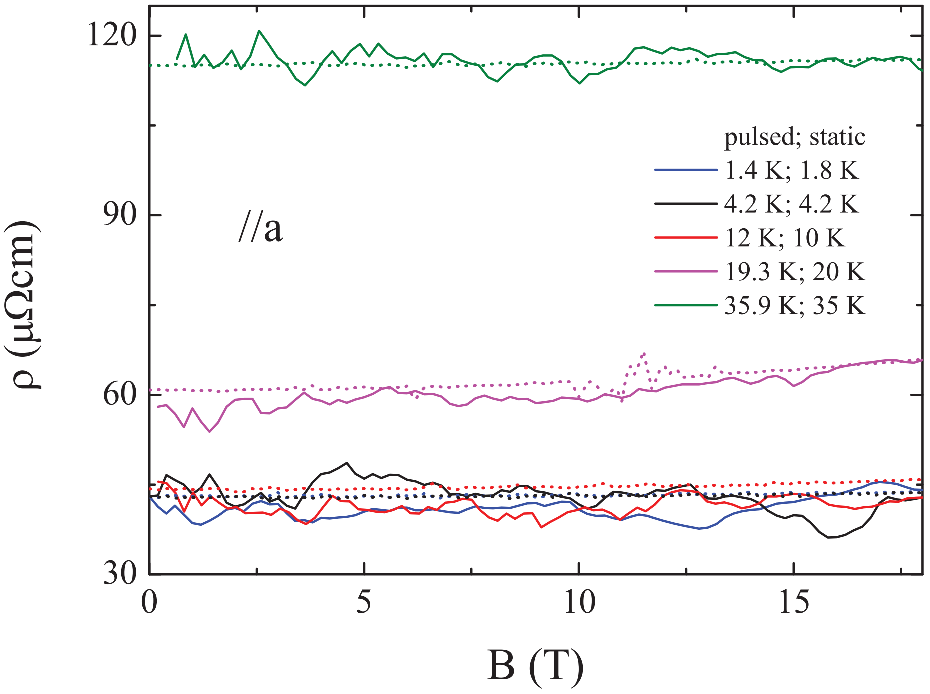

Figure 5.20: Comparison of static and pulsed high magnetic field resistivity measurements of UPt$_2$Si$_2$ at various temperatures with the magnetic field applied parallel to the a axis. Solid lines indicate pulsed field measurements, dotted lines represent measurements in static fields.

which might be affected in high magnetic fields. Compared to the other effects, (c) changes of the level of electronic localization in magnetic fields generally are considered to be relatively small and probably are only of secondary order in the present case.

In the following it will be tested to what extent the normalized magnetoresistivity $\frac{\rho-\rho(B=0)}{\rho(B=0)}$ displays the same principal behavior as the differential susceptibility. Based on this analysis, using normalized resistivity and differential susceptibility data, the magnetic field phase diagram will be generated.

In the Figs. 5.24 and 5.25 the normalized magnetoresistivity $\frac{\rho-\rho(B=0)}{\rho(B=0)}$ and the susceptibility of UPt$_2$Si$_2$ as function of the magnetic field applied parallel to the a axis for various temperatures are depicted. Each plot displays the resistivity and susceptibility data taken at the same temperature or the ones most

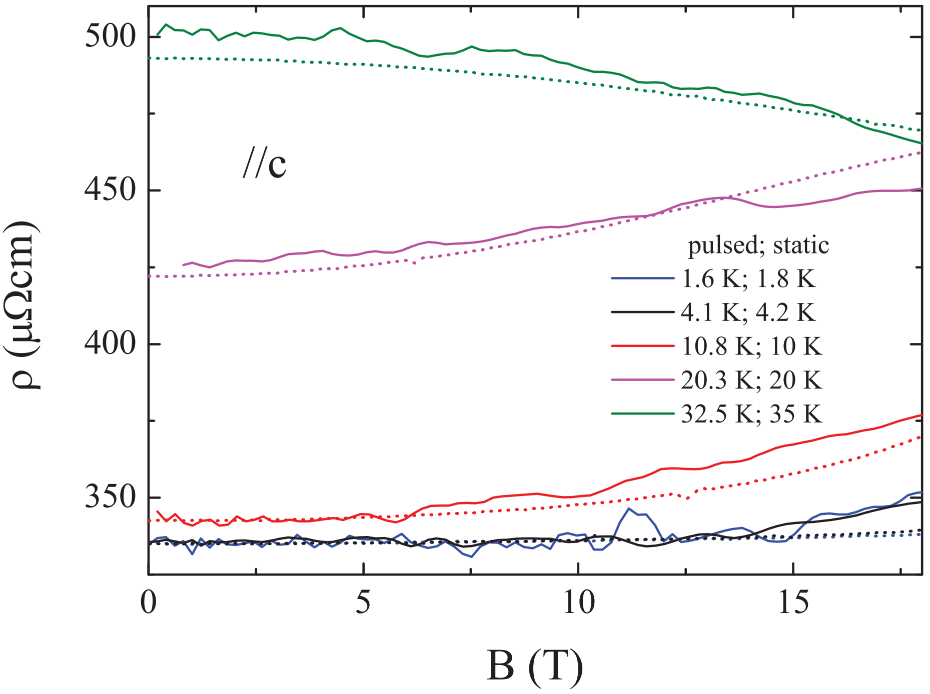

Figure 5.21: Comparison of static and pulsed high magnetic field resistivity measurements of UPt_2Si_2 at various temperatures with the magnetic field applied parallel to the c axis. Solid lines indicate pulsed field measurements, dotted lines represent measurements in static fields.

closely to each other.

For $B//a$, at $35\,\mathrm{K}$ both, susceptibility and magnetoresistivity, are featureless, consistent with the paramagnetic state of UPt_2Si_2. Surprisingly, at $20\,\mathrm{K}$ there is a clear mismatch between susceptibility and magnetoresistivity above $30\,\mathrm{T}$, which needs to be verified in future experiments. In contrast, at $12\,\mathrm{K}$ and below, both, susceptibility and magnetoresistivity, behave in a similar fashion, with maxima in high fields of about $45\,\mathrm{T}$, although the noise level prohibits a very accurate determination of transition fields.

Further, in the Figs. 5.26 and 5.27 the normalized magnetoresistivity $\frac{\rho-\rho(B=0)}{\rho(B=0)}$ and the susceptibility of UPt_2Si_2 as function of the magnetic field applied parallel to the c axis for various temperatures are depicted. At $10\,\mathrm{K}$ and above both, susceptibility and magnetoresistivity, display a similar behavior. In con-

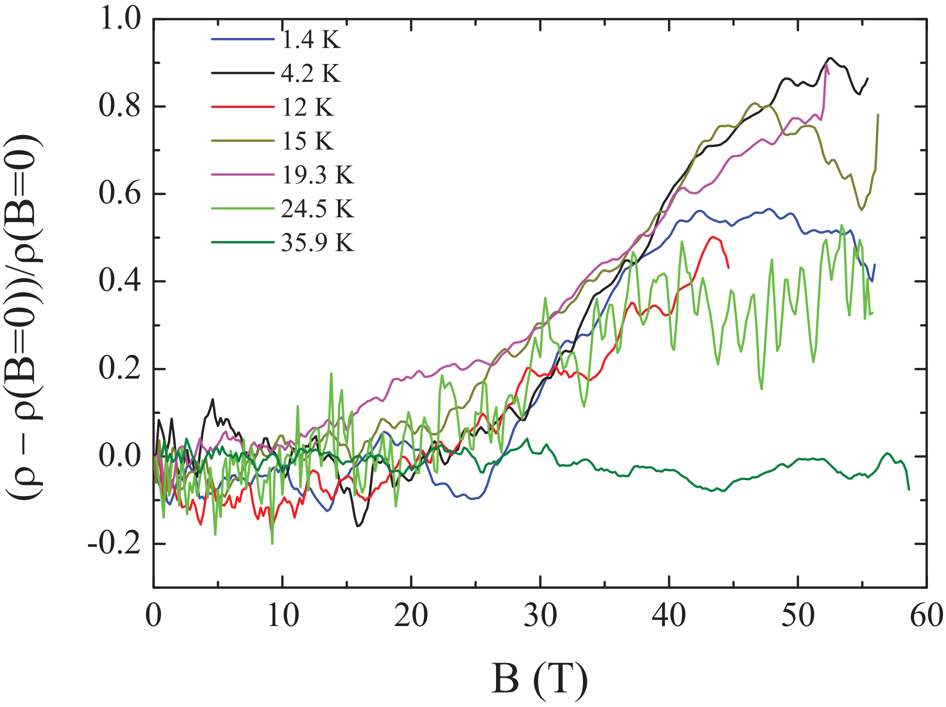

Figure 5.22: Field dependence of the normalized magnetoresistivity $\frac{\rho-\rho(B=0)}{\rho[B=0)}$ of UPt$_2$Si$_2$ at various temperatures with the magnetic field applied parallel to the a axis.

trast, at $4.2\,\mathrm{K}$ and below in the magnetoresistivity only one maximum appears, while in the susceptibility there are two. However, from magnetoresistivity data it appears as if there is a discontinuous change of the field evolution approximately at the field of the second susceptibility maximum. Additional experiments will have to verify this point.

From the maxima in $\partial M/\partial B$ the phase diagrams for $B//a$ and $B//c$ are obtained, see Figs. 5.28 and 5.29, respectively. In the phase diagram for $B//c$, in addition the values obtained from the maxima in $\partial\rho/\partial B$ and $\partial\rho/\partial T$ are included. The possible phase boundaries are indicated by dashed lines. Due to the higher noise level in the resistivity measurements for $B//a$ an analysis as performed for $B//c$ was not possible. Even a smoothing of the curve prior to the differentiation does not yield a sufficient reduction of the noise level, leading to unreasonably large error bars in the phase diagram. Therefore, these data points are not included in the phase diagram.

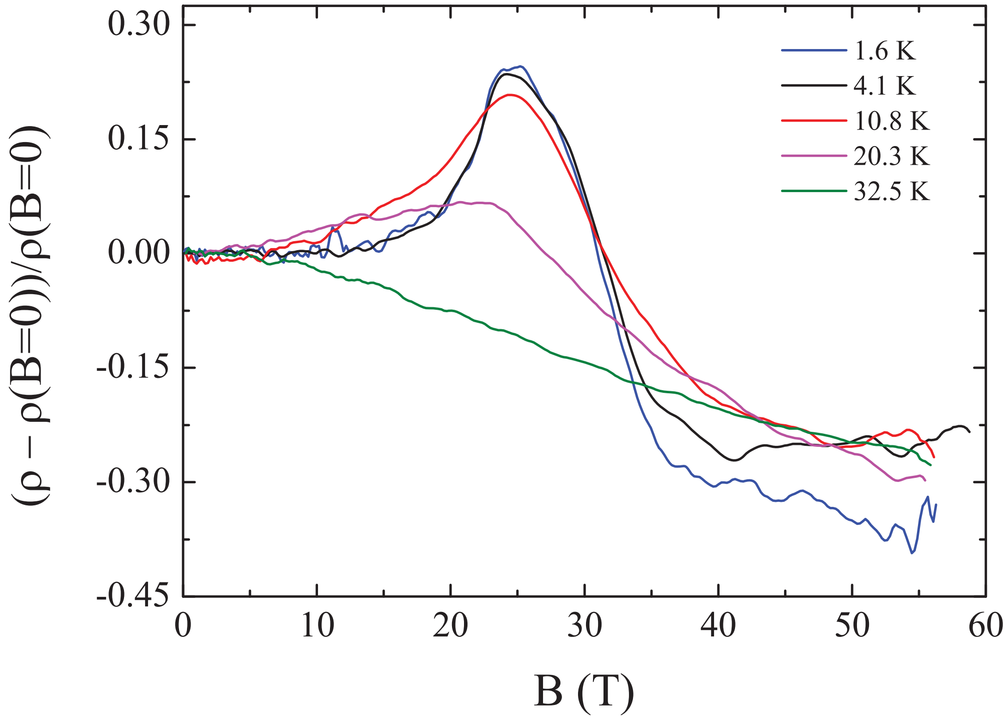

Figure 5.23: Field dependence of the normalized magnetoresistivity $\frac{\rho-\rho(B=0)}{\rho[B=0)}$ of UPt_2Si_2 at various temperatures with the magnetic field applied parallel to the c axis.

Surprisingly, and in contrast to previous high field studies on UPt_2Si_2, the phase diagrams are quite complex, with two phases for $B//a$ and two or three phases for $B//c$ which are probably magnetically ordered.

The phase diagram of UPt_2Si_2 reveals close similarities to the phase diagram of URu_2Si_2, which is depicted in Fig. 5.30 (from Ref. [90]). URu_2Si_2 is a heavy fermion material in which the f electrons have an itinerant character, rather than being localized. At low temperatures ($T < 17.5\,\mathrm{K}$), URu_2Si_2 is characterized by a hidden order phase. In magnetic fields, this phase is first destroyed by a critical field of $\sim 35\,\mathrm{T}$, and at $\sim 36\,\mathrm{T}$ a field induced reentrant phase is created. In contrast to URu_2Si_2, UPt_2Si_2 is not a hidden order material but orders antiferromagnetically at low fields. We speculate, that the existence of the high field phases in both materials reflects Fermi surface effects. Hence, these similarities would indicate that UPt_2Si_2 cannot be described in terms

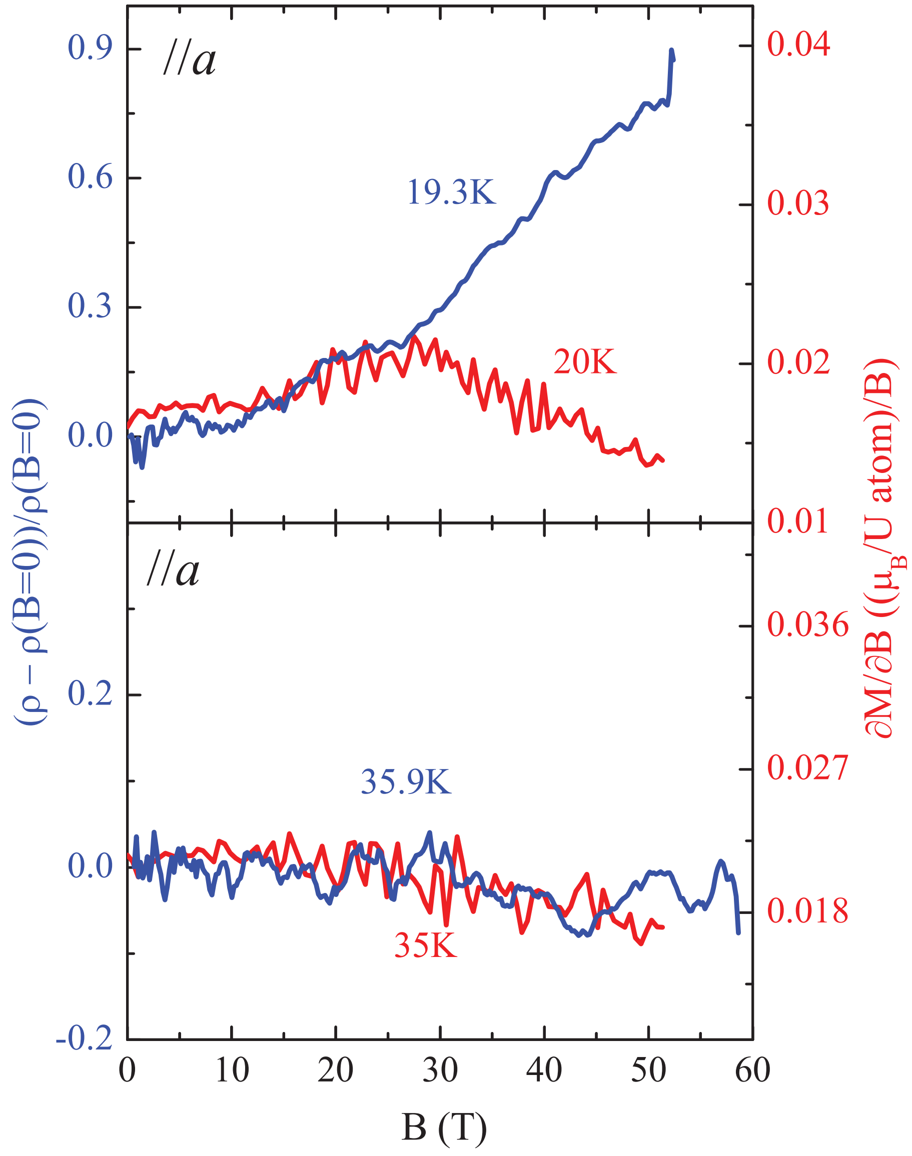

Figure 5.24: Field dependence of the normalized magnetoresistivity $\frac{\rho-\rho(B=0)}{\rho(B=0)}$ and the susceptibility of UPt_2Si_2 with the magnetic field applied parallel to the a axis.

of a crystal electric field model, and that UPt_2Si_2 is another typical Uranium compound for which itinerant effects have to be considered.

In order to further clarify the high field behavior of UPt_2Si_2 and reveal the na-

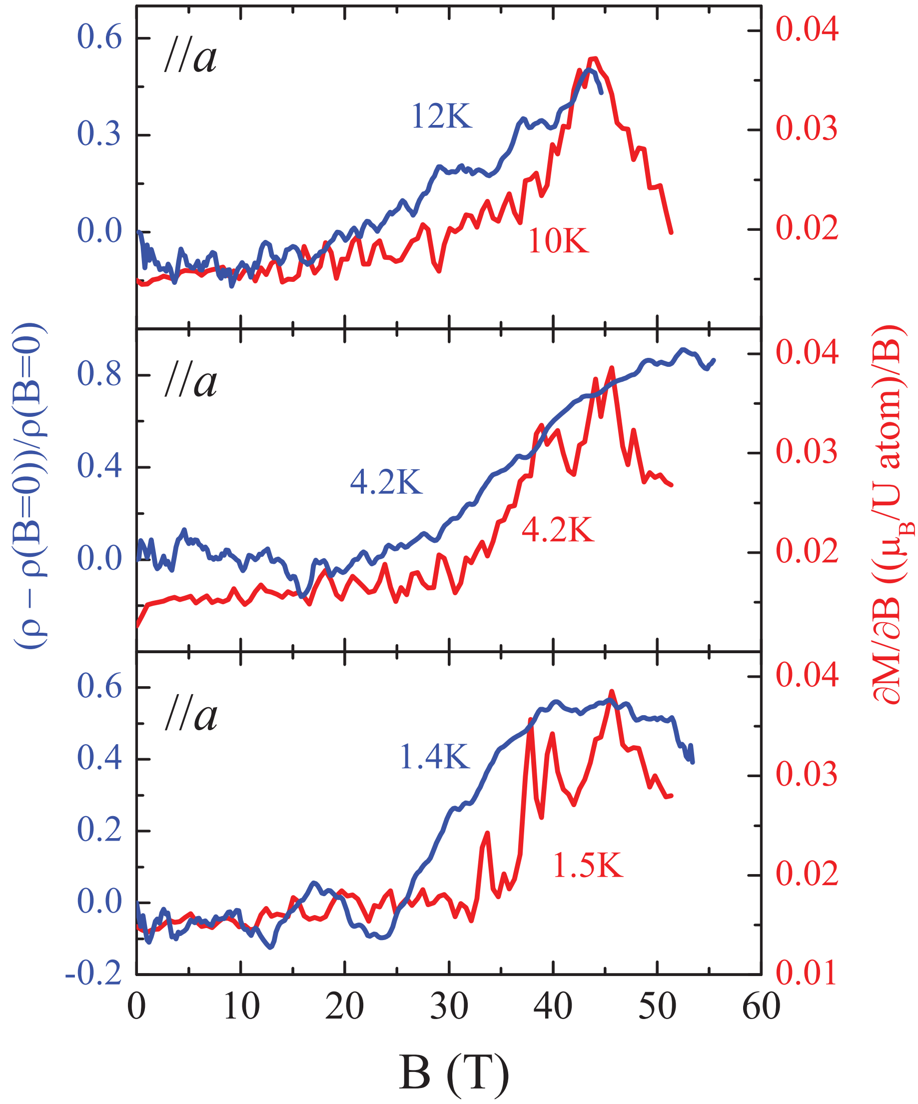

Figure 5.25: Field dependence of the normalized magnetoresistivity $\frac{\rho-\rho(B=0)}{\rho(B=0)}$ and the susceptibility of UPt_2Si_2 with the magnetic field applied parallel to the a axis.

ture of these different phases a detailed investigation including additional high field magnetization and high field resistivity will be necessary. In particular, magnetoresistivity measurements for $B//a$ with a higher signal-to-noise ratio would be very helpful to complete the exciting phase diagram of UPt_2Si_2.

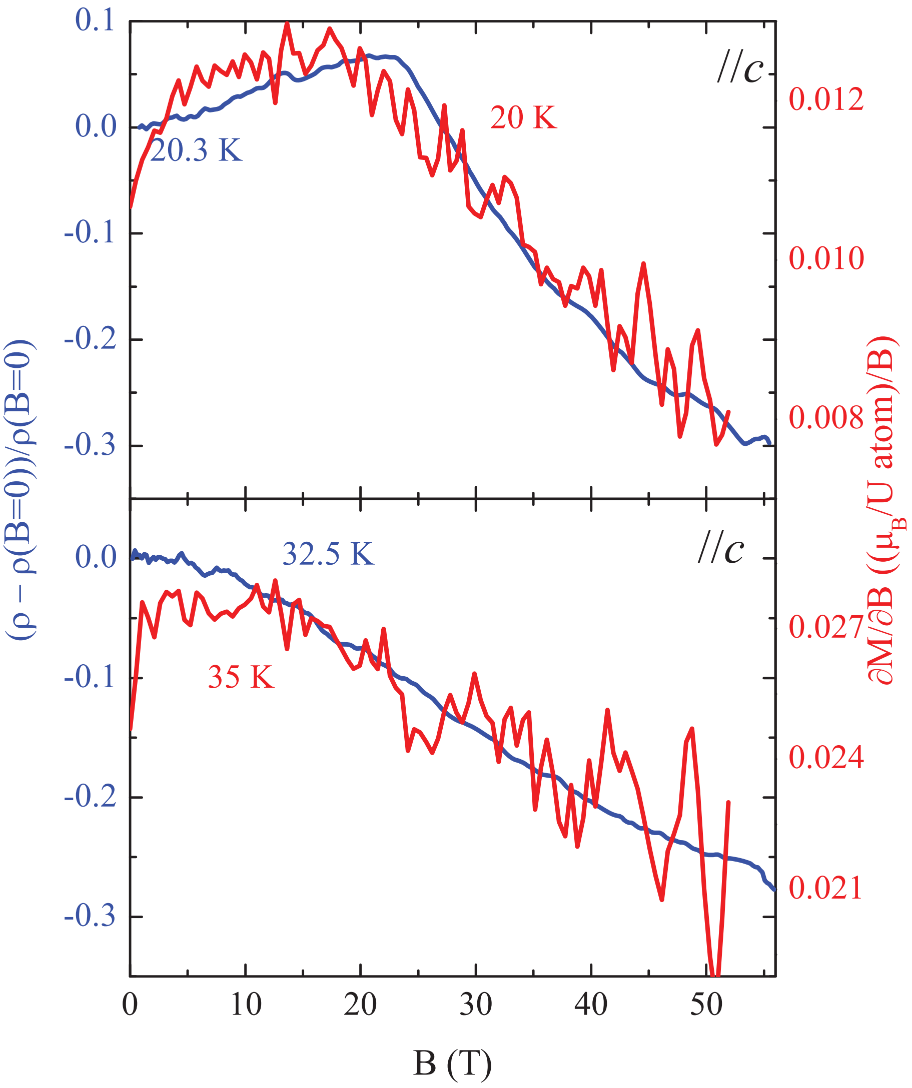

Figure 5.26: Field dependence of the normalized magnetoresistivity $\frac{\rho-\rho(B=0)}{\rho(B=0)}$ and the susceptibility of UPt$_2$Si$_2$ with the magnetic field applied parallel to the c axis.

5.6 Conclusion

In conclusion, the reinvestigation of UPt$_2$Si$_2$ presented here reveals that the crystal electric field picture developed by Nieuwenhuys [86] to describe this material is not valid. Instead, UPt$_2$Si$_2$ has to be discussed as a delocalized f electron system, that is Fermi surface properties determine its physics. This situation closely resembles the case of the hidden order material URu$_2$Si$_2$, which initially was also discussed in terms of a crystal electric field model. It

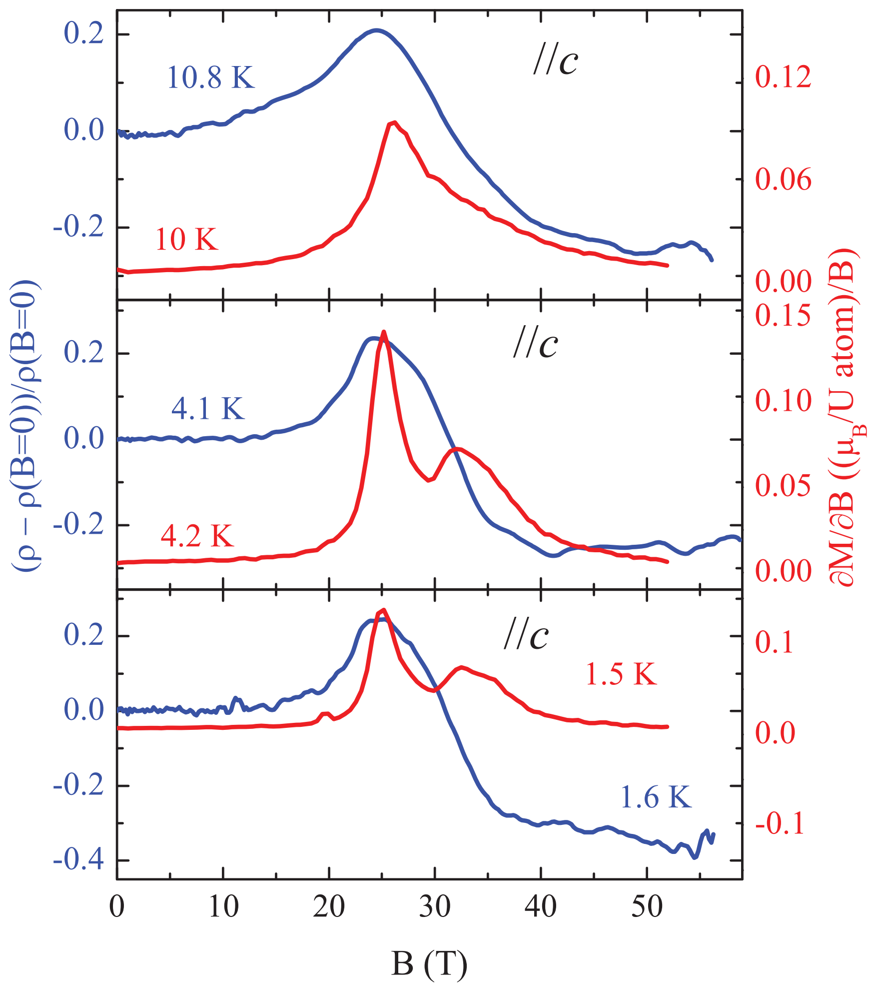

Figure 5.27: Field dependence of the normalized magnetoresistivity $\frac{\rho-\rho(B=0)}{\rho(B=0)}$ and the susceptibility of UPt_2Si_2 with the magnetic field applied parallel to the c axis.

was revealed later that this picture is inadequate and that URu_2Si_2 should be treated as an itinerant f electron system [103, 104].

The multitude of analogies between UPt_2Si_2 and URu_2Si_2, the most remarkable one is the similarity of their complex high magnetic field phase diagrams, which are not understood until now, suggest that UPt_2Si_2 might be a key to understand the exotic properties of hidden order/heavy fermion superconductor

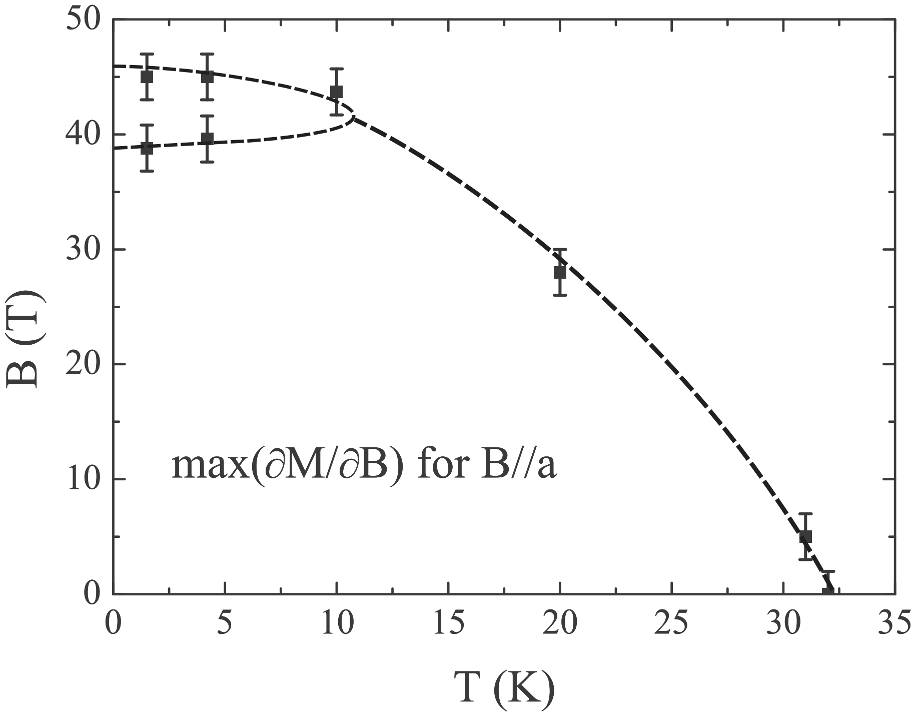

Figure 5.28: Proposed magnetic phase diagram $B//a$ of UPt$_2$Si$_2$ obtained from the maximum in $\partial M/\partial B$. The dashed lines suggest the proposed evolution of the phase boundaries, for details see text.

URu$_2$Si$_2$. To achieve this, further investigations, and in particular high field measurements ought to be carried out on UPt$_2$Si$_2$ in the future.

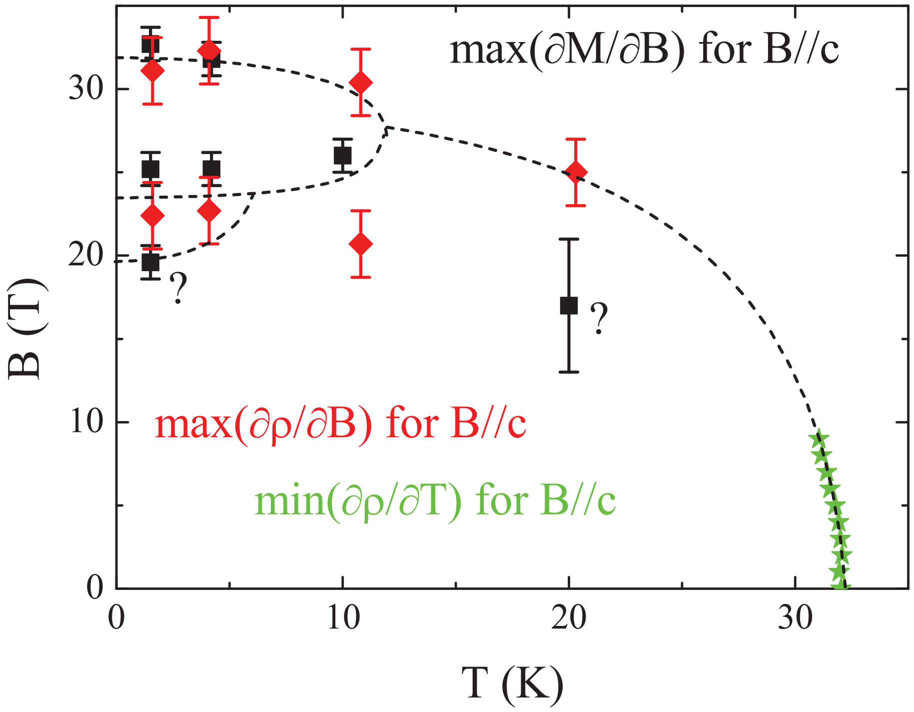

Figure 5.29: Proposed magnetic phase diagram $B//c$ of UPt_2Si_2 obtained from the maxima in $\partial M/\partial B$ (black) and in $\partial\rho/\partial B$ (red), as well as the minima in $\partial\rho/\partial T$ (green). The dashed lines suggest the proposed evolution of the phase boundaries, for details see text.

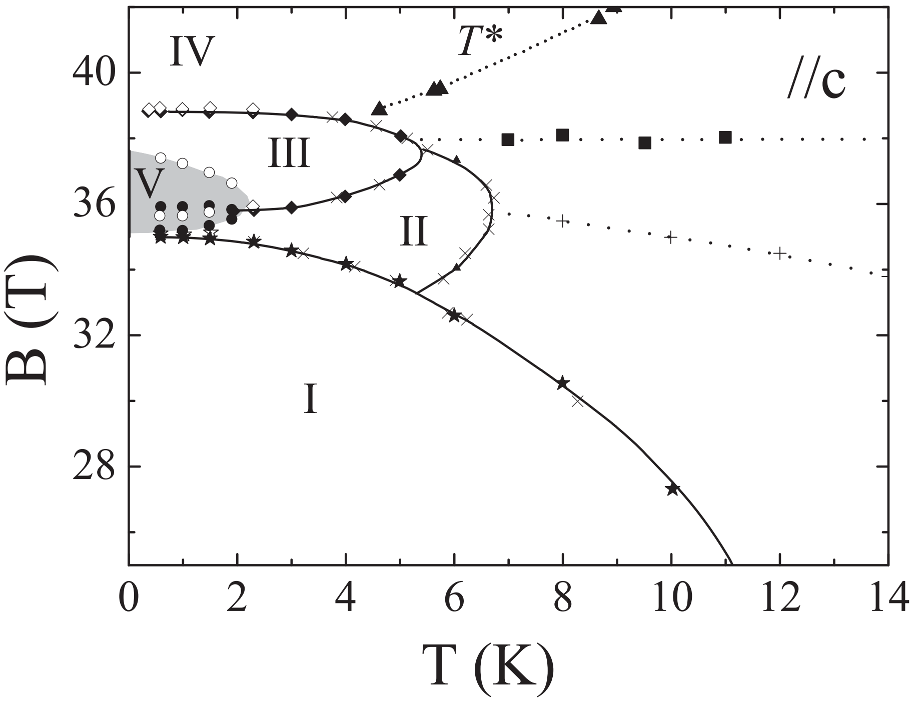

Figure 5.30: Magnetic phase diagram for $B//c$ of tetragonal URu$_2$Si$_2$ after Ref. [90], for details see text.

6 Ground state properties of U($\mathrm{Pd}_{1-x}\mathrm{Pt}_x$)$_3$

6.1 Introduction

Actinide and rare earth systems are of special interest, as their f-electron shells exhibit various local degrees of freedom, which are based on the dipolar, quadrupolar, octupolar etc. character of the f-electronic shells. In consequence, in localized f-electron systems the f-orbitals carry the potential to exhibit long-range order of various types. For many of these ordering phenomena the question occurs if the ordering can be suppressed by an external control parameter. This in turn directly leads to the question if such a suppression of an ordered state to $T = 0\,\mathrm{K}$ leads to quantum critical behavior in a way as observed experimentally for magnetic ordering [27–29].

In many heavy fermion systems long-range dipolar ordering, (*viz.*, here magnetic ordering) has been observed, but examples for long-range quadrupolar ordering in metallic materials are very rare. In magnetically ordered systems, the magnetic dipole moments form an ordered structure. As the name indicates, for the quadrupolar case the electric quadrupolar moments are responsible for the ordering. In contrast to dipolar ordering where the ordering parameter is directly accessible with neutron scattering, in quadrupolar ordered systems it is difficult to determine the ordering parameter. Higher order multipole ordering is only directly accessible with x-ray resonant scattering.

Another way to gain information on the nature of the ordered quadrupolar ground state is to observe the associated phase transition, *e.g.*, with specific heat measurements, even though a direct determination of the ordering parameter is not possible. However, to study the evolution of the phase transition associated to quadrupolar ordering by the variation of an external parameter, measurements of bulk properties are a suitable tool.

In this situation, to study the influence of an external parameter on quadrupolar ordering and on the physical properties, a material is needed for which long-range quadrupolar ordering is established.

6.2 UPd$_3$: An archetypical quadrupolar ordered system

As one of the rare metallic examples which exhibits long-range quadrupolar ordering UPd$_3$ has been intensively studied for more than 30 years, *e.g.* [105–112]. The material crystallizes in the double-hexagonal close-packed (dhcp) crystal structure (space group $P6_3/mmc$) as shown in Fig. 6.1, with lattice parameters $a = 5.73\,\text{Å}$, $c = 9.66\,\text{Å}$ at room temperature [113]. In this structure, the B plane is situated between the hexagonal planes A, hence the B plane has hexagonal symmetry. Conversely, the A planes are stacked within a sequence BAC, which locally represents a cubic symmetry, hence the A plane can be treated in a quasi-cubic approximation. In order to illustrate the quasi-cubic symmetry, the A plane is depicted in Fig. 6.2.

In the course of the years, and with improving sample quality, in total four phase transitions at $T_0 = 7.8\,\mathrm{K}$, $T_{+1} = 6.9\,\mathrm{K}$, $T_{-1} = 6.7\,\mathrm{K}$ and $T_2 = 4.4\,\mathrm{K}$ have been identified at low temperatures [108, 109, 114–121]. By now, it has been demonstrated that the transition at $T_0 = 7.8\,\mathrm{K}$ is into an antiferroquadrupolar ordered (AFQ) structure (order parameter Q_{zx}), which is associated with a periodic lattice distortion and a doubling of the dhcp unit cell, see Fig. 6.3 [112]. The transitions at T_{+1} and T_{-1} are also of quadrupolar origin, the transition at T_{-1} is accompanied by another lattice distortion (space group $P\bar{3}m1$) [117, 121]. The transition at lowest temperatures (T_2) is into an antiferromagnetically ordered state with a very small ordered magnetic moment of $\sim 10^{-2}\,\mu_{\mathrm{B}}/\mathrm{U\,atom}$ in zero magnetic field.

There are several alloying studies to investigate the development of the localized character and the influence of doping on the quadrupolar phases. In one such study substitution of U by Np has been investigated [122]. The transition temperatures are not very sensitive to Np alloying, with the phase diagram summarized in Fig. 6.4 (from Ref. [122]). With a small amount of Np alloying (up to $5\,\%$) the lower transition temperatures T_{-1} and T_2 are reduced, contrary to T_0 which is increased.

In contrast to Np alloying, UPd$_3$ is much more sensitive to Pt doping. Zo-

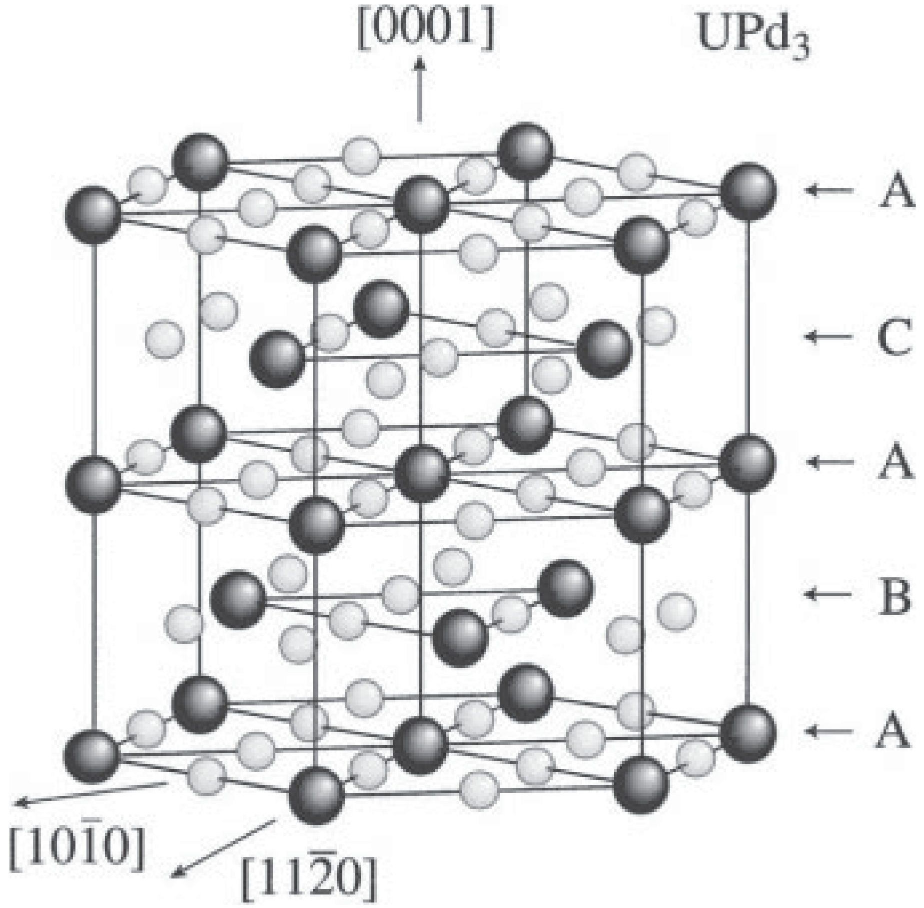

Figure 6.1: Double-hexagonal structure (space group $P6_3/mmc$) of UPd$_3$, from Ref. [114].

chowski *et al.* [121] have shown by thermal expansion measurements of single crystalline material along the c axis, that a small amount of $5\,\%$ Pd substitution by Pt is completely suppressing the antiferroquadrupolar and antiferromagnetic ordering. However, Zochowski *et al.* [121] did not carry out further alloying experiments with amounts $< 5\,\%$ Pt, and thus have not identified the critical composition x in U(Pd$_{1-x}$Pt$_x$)$_3$ of a zero temperature phase transition.

On the other side of the U(Pd$_{1-x}$Pt$_x$)$_3$ phase diagram the heavy fermion ($\gamma = 440\,\mathrm{mJ/K^2molU}$) superconductor UPt$_3$ is located. UPt$_3$ has been studied extensively for many years (for reviews see Refs. [6, 99, 123]). It crystallizes in a hexagonal closed-packed structure (space group $P6_3/mmc$; lattice constants $a = 5.764\,\mathrm{Å}$ and $c = 4.899\,\mathrm{Å}$ at room temperature), corresponding to a stacking of only AB planes. The distance between the U atoms $a_{\mathrm{U-U}}$ is $4.132\,\mathrm{Å}$ in UPt$_3$ and $4.106\,\mathrm{Å}$ in UPd$_3$ which is far beyond the Hill limit (3.5 Å

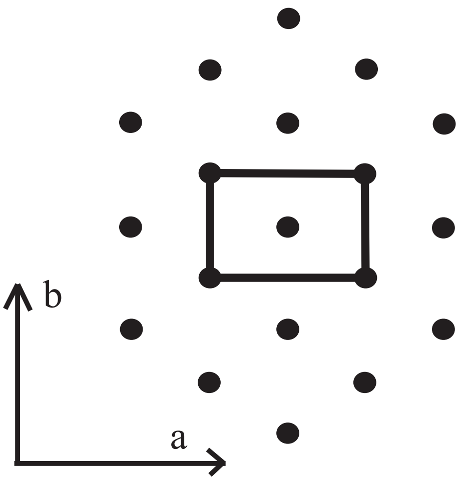

Figure 6.2: Illustration of the hexagonal A plane of UPd_3 to illustrate the local quasi-cubic symmetry.

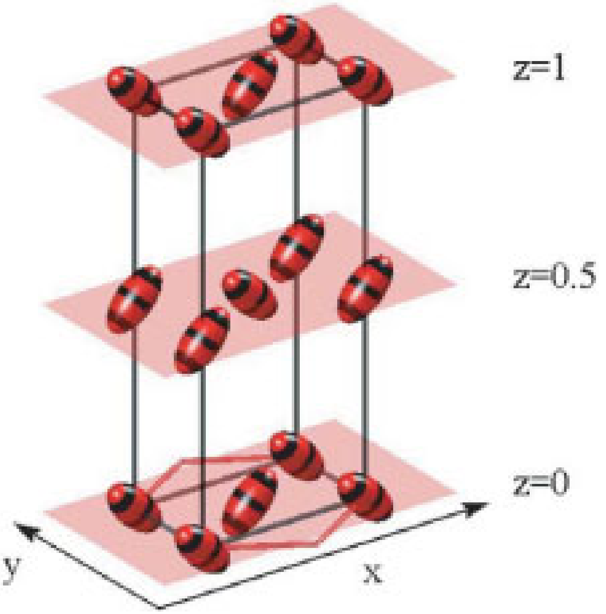

Figure 6.3: The Q_{zx} AFQ structure with antiphase stacking along the z axis in UPd_3 at $T_{+1} < T < T_0$ in an orthorhombic unit cell. The U $5f$-quadrupoles on the quasicubic sites are represented schematically by ellipsoids; figure taken from Ref. [112]

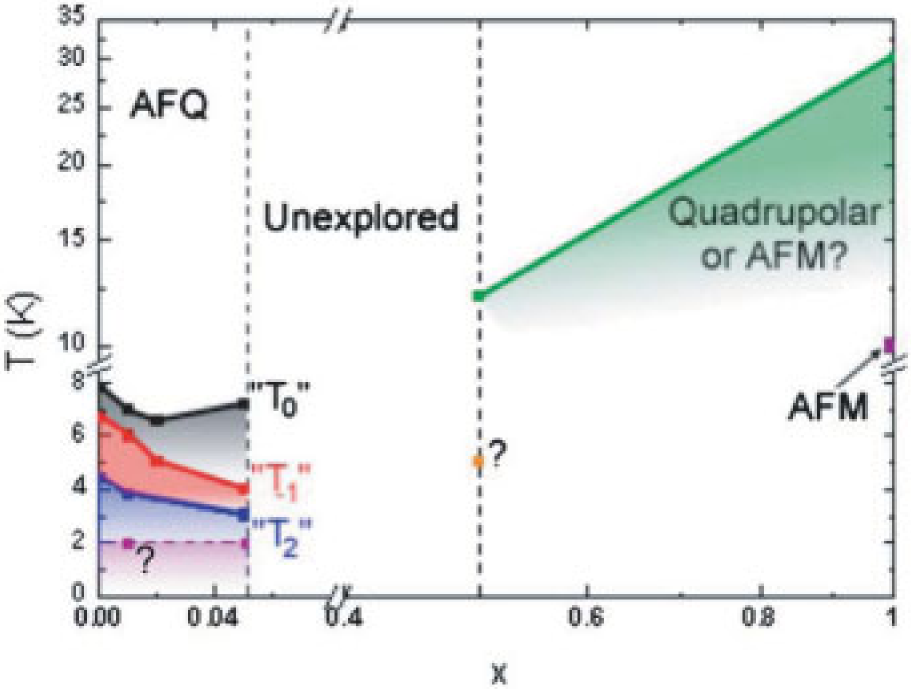

Figure 6.4: Magnetic phase diagram of U$_{1-x}$Np$_x$Pd$_3$ as a function of x, from Ref. [122].

for uranium [124]). The Hill limit denotes the distance beyond which the overlap of the f-orbitals is to small to form f-bands and the f-electrons become localized. In the normal state above the superconducting critical temperature $T_{\mathrm{C}} = 0.5\,\mathrm{K}$ UPt$_3$ appears to exhibit Fermi liquid behavior up to a temperature of about $1.5\,\mathrm{K}$ [6]. Up to $T_{\mathrm{N}} \sim 6\,\mathrm{K}$ a small moment antiferromagnetic phase (SMAF) ($\mu_{\mathrm{ord}} = 0.02\,\mu_{\mathrm{B}}/\mathrm{U\,atom}$) is observed.

In the phase diagram of U(Pd$_{1-x}$Pt$_x$)$_3$ the evolution from double-hexagonal closed-packed structure (UPd$_3$) to hexagonal closed-packed structure (UPt$_3$) is suspended by an intermediate phase ($0.42 < x < 0.67$) characterized by a 10-layer stacking sequence along the c-axis [125].

Various studies on U(Pt$_{1-y}$Pd$_y$)$_3$ [126–130] have been performed to clarify the behavior of the superconducting phase in UPt$_3$ with Pd alloying. The phase diagram of U(Pt$_{1-y}$Pd$_y$)$_3$ for $0 \leq y \leq 0.1$ as taken from Ref. [128] is depicted in Fig. 6.5. The physical properties of UPt$_3$ are extremely sensitive to small amounts of Pd doping. The superconducting phase of UPt_3 is suppressed with only $\sim 0.6\,\%$ of Pd doping, see Fig. 6.5. Contrary to the superconducting phase, the small moment antiferromagnetic phase is more stable with Pd doping and exists till at least $y = 0.01$ [129]. In addition, the superconducting phase is replaced by a conventional large moment antiferromagnetic phase (LMAF) ($\mu_{\mathrm{ord}} = 0.63 \pm 0.05\,\mu_{\mathrm{B}}/\mathrm{U\,atom}$ for $y = 0.05$) [128]. The critical point of superconductivity coincides with the magnetic critical point at $y = 0.006$, reflecting a competition between superconductivity and antiferromagnetic order.

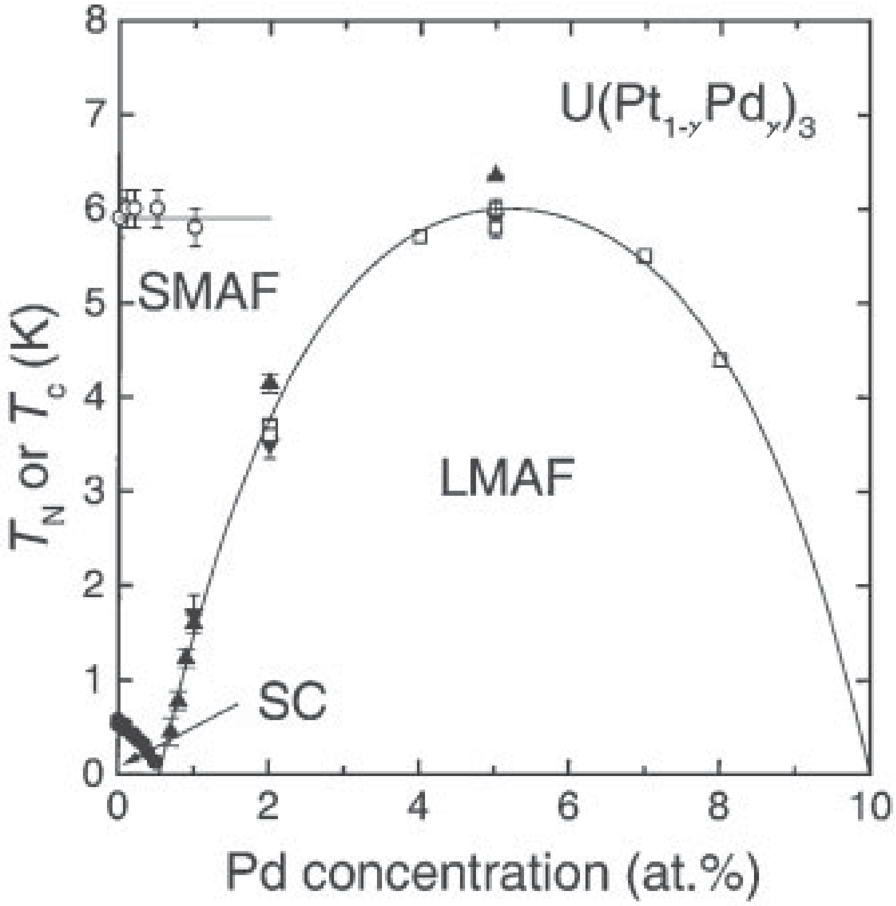

Figure 6.5: The magnetic phase diagram of $U(Pt_{1-y}Pd_y)_3$, as taken from Ref. [128].

As the U atoms are carrying the magnetic moment in UPt_3, it is surprising that substitution of the non-magnetic Pd ion for the heavier isoelectronic Pt ion has such a strong influence on the physical properties. In this situation, an analogous study of the influence of a small amount of Pt in UPd_3 appears very promising, but is lacking so far. Therefore, in this work the physical properties of single crystals U($\mathrm{Pd}_{1-x}\mathrm{Pt}_x$)$_3$ with $x = 0.005$ and $x = 0.01$ have been examined and the essentials of the magnetic phase diagram established.

The samples U($\mathrm{Pd}_{1-x}\mathrm{Pt}_x$)$_3$ investigated in this work are bar shaped single crystals produced in the UK and provided by K. A. McEwen, University College London. Other parts of the crystals are studied by microscopic techniques such as neutron and x-ray scattering.

6.3 Bulk properties of U($\mathrm{Pd}_{1-x}\mathrm{Pt}_x$)$_3$

6.3.1 Specific heat

Specific heat measurements have been employed to determine the ground state properties of U($\mathrm{Pd}_{1-x}\mathrm{Pt}_x$)$_3$. The heat capacity measurements have been performed by using a standard heat pulse technique in a Quantum Design Physical Property Measurement System with a ^{3}He insert[1].

The specific heat c_p and c_p/T *vs.* temperature T of U($\mathrm{Pd}_{1-x}\mathrm{Pt}_x$)$_3$ with $x = 0.005$ and $x = 0.01$ in fields up to $B = 9\,\mathrm{T}$ applied parallel to the a axis are depicted in Fig. 6.6. Further, in Fig. 6.7 the temperature dependence of $c_{\mathrm{p,mag}}/T$ of U($\mathrm{Pd}_{1-x}\mathrm{Pt}_x$)$_3$ with $x = 0$, 0.005 and 0.01 is shown. The data for the sample with $x = 0$ have been provided by H. C. Walker, University College London, and are published in Ref. [112].

In Fig. 6.7, for all data $x = 0$, 0.005 and 0.01 the non-magnetic phonon contribution has been subtracted by using ThPd$_3$ as a phonon blank, with the ThPd$_3$ data taken from Ref. [105]. For $T \leq 20\,\mathrm{K}$ the specific heat c_p of ThPd$_3$ can be fitted with the polynomial of 5th degree:

$$c_\mathrm{p} = 1.5 \cdot 10^{-3} T + 5.01 \cdot 10^{-4} T^3 + 2.04 \cdot 10^{-7} T^5 \mathrm{J} \cdot \mathrm{mole}^{-1} \cdot \mathrm{K}^{-1} \qquad (6.1)$$

The fit is included as a solid line in Fig. 6.6. The fit also is in good agreement with the heat capacity measurements of ThPd$_3$ provided by H. C. Walker and published in Ref. [112].

---

[1] The samples had a rather large mass of $46.88\,\mathrm{mg}$ ($x = 0.01$) and $54.61\,\mathrm{mg}$ ($x = 0.005$), resulting in a long measuring time. The access to a ^{3}He specific heat measurement set up was limited, therefore only low temperature data could be taken and the sample $x = 0.005$ measurement at $B = 9\,\mathrm{T}$ is uncompleted.

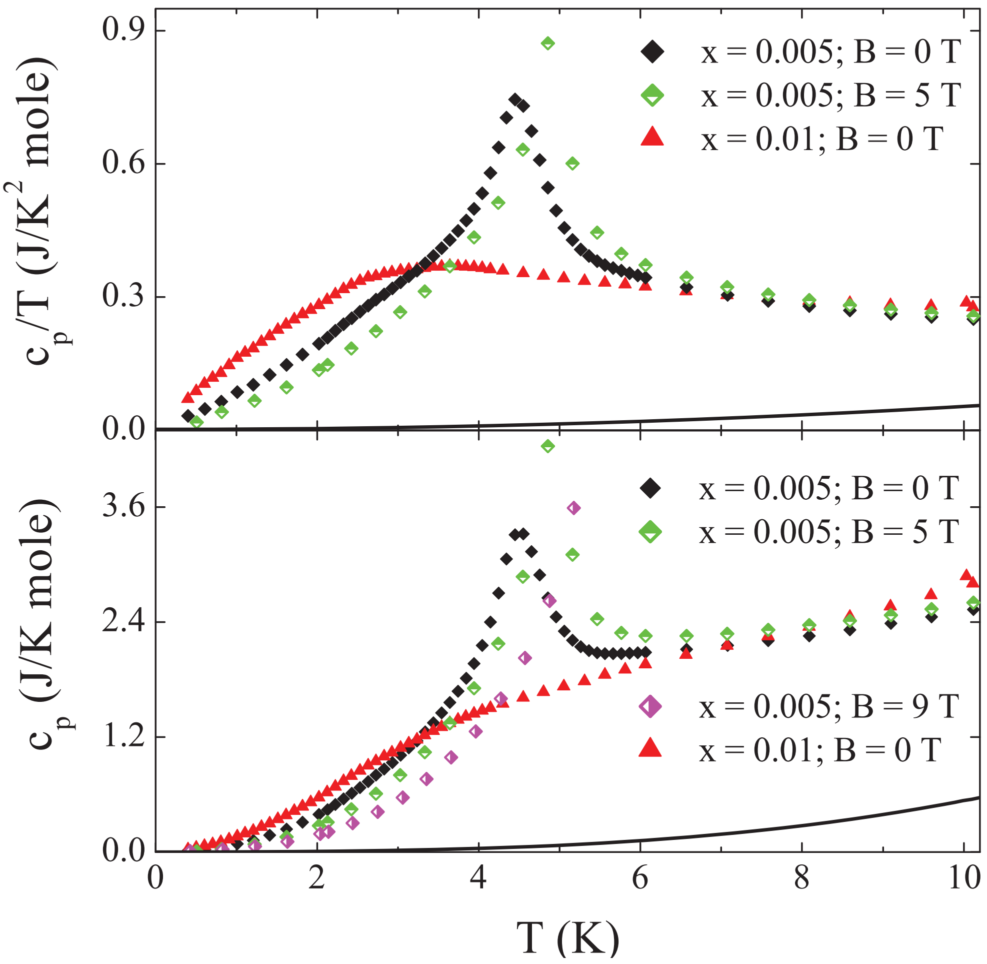

Figure 6.6: Specific heat c_p and c_p/T of U(Pd$_{1-x}$Pt$_x$)$_3$, $x = 0.005$ and 0.01, in fields up to $B = 9\,\mathrm{T}$. The magnetic field was applied parallel to the a axis. The solid line is representing a fit of the ThPd$_3$ data used for the phonon correction, for details see text.

In the heat capacity of U(Pd$_{1-x}$Pt$_x$)$_3$, $x = 0$, the transitions at $T_{-1} = 6.7\,\mathrm{K}$ and $T_2 = 4.4\,\mathrm{K}$ are clearly observable, while the transition at T_{+1} [109] cannot be resolved. No clear peak structure is observed at $T_0 = 7.8\,\mathrm{K}$, although there is a broad specific heat anomaly in this range. For $x = 0.005$ the transition at T_{-1} is still present but shifted to a lower temperature of $T_{-1} = 4.5\,\mathrm{K}$. Further, the lowest transition T_2 is only present as a broad shoulder at $\sim 2.5\,\mathrm{K}$. In the data for $x = 0.01$ the transition at T_{-1} becomes very broad and is shifted further towards lower temperatures, $T_{-1} \sim 2.7\,\mathrm{K}$, while T_2 is not observable anymore.

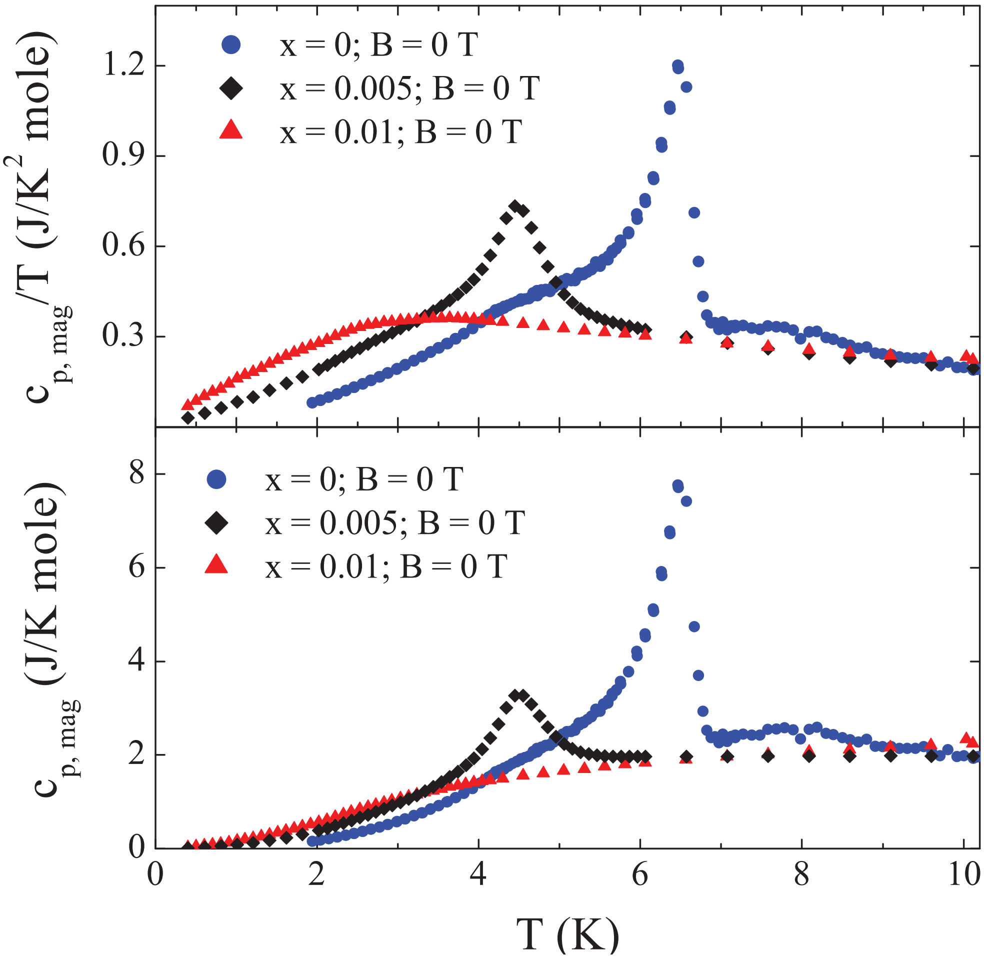

Figure 6.7: Temperature dependence of $c_{\mathrm{p,mag}}$ and $c_{\mathrm{p,mag}}/T$ of U(Pd$_{1-x}$Pt$_x$)$_3$ with $x = 0$, 0.005 and 0.01. The data for pure UPd$_3$ are taken from Ref. [112], for details see text.

From the specific heat data the magnetic entropy was determined using

$$S_{\mathrm{mag}} = \int_0^T \frac{c_{\mathrm{p,mag}}/T}{T} \mathrm{d}T \tag{6.2}$$

and is depicted in the Figs. 6.8 and 6.9. For S_{mag} displayed in Fig. 6.8 the low temperature specific heat $c_{\mathrm{p,mag}}$ has been extrapolated to $T = 0\,\mathrm{K}$, and subsequently the magnetic entropy has been determined. In contrast, for S_{mag} in Fig. 6.9 the integration has been started at $T = 2\,\mathrm{K}$, in order to check that the extrapolation is adequate. Qualitatively, both procedures reveal the same entropic behavior, thus it is ensured that the extrapolation to low temperatures is appropriate.

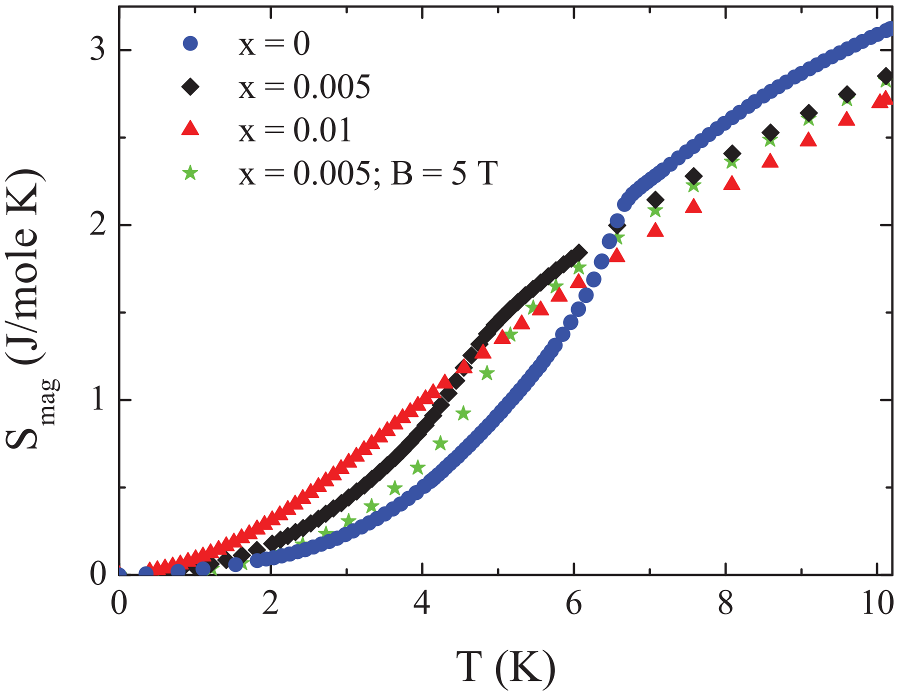

Figure 6.8: Temperature dependence of the magnetic entropy S_{mag} of U(Pd$_{1-x}$Pt$_x$)$_3$ with $x =$ 0; 0.005 and 0.01. In the calculation the integration of the specific heat has been started at $T = 0\,\text{K}$ by extrapolating $c_{\text{p,mag}}$ to zero temperature.

From the figures it is seen that the magnetic entropy S_{mag} is shifted to lower temperature with increasing Pt doping. Quantitatively, at T_{-1} for $x = 0.005$ only $70\,\%$ and for $x = 0.01$ only $30\,\%$ of the entropy is reached, if compared to pure UPd$_3$. The lacking entropy, together with the broadening in $c_{\text{p,mag}}/T$ possibly reflects short range antiferroquadrupolar ordering in the sample $x = 0.01$, likely together with a distribution of transition temperatures in the present sample. This suggestion could possibly be verified with x-ray resonant scattering experiments where one would expect a broadening of charge peaks associated to the AFQ phase.

In Fig. 6.10 the magnetic specific heat $c_{\text{p,mag}}$ and $c_{\text{p,mag}}/T$ in zero magnetic field and in a magnetic field of $B = 5\,\text{T}$ applied parallel to the a axis are presented for U(Pd$_{1-x}$Pt$_x$)$_3$, $x = 0.005$. It can be observed that the transition at T_{-1} shifts to higher temperatures with increasing magnetic field, see Figs. 6.6

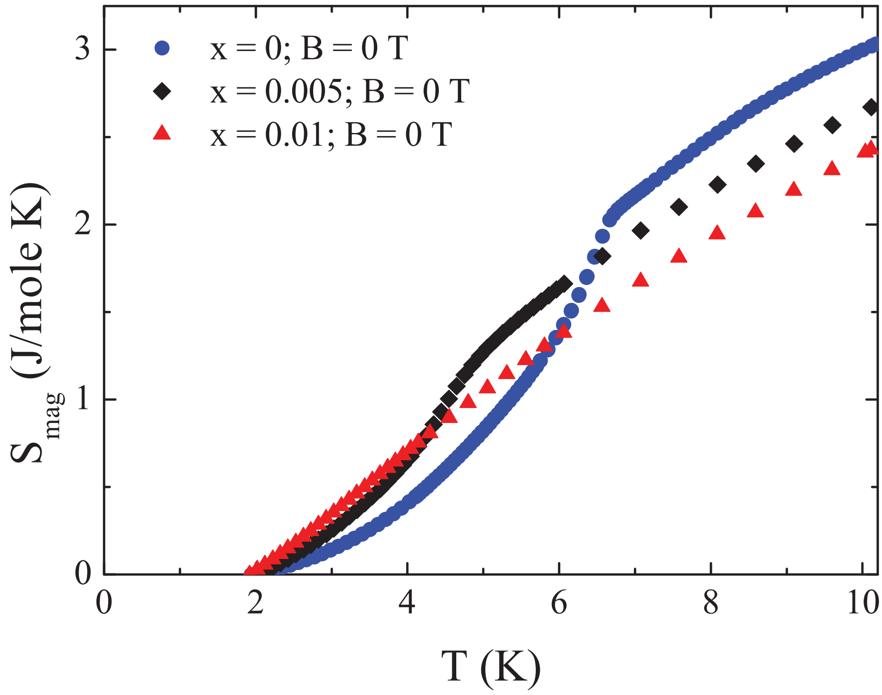

Figure 6.9: Temperature dependence of the magnetic entropy $S_{\rm mag}$ of U(Pd$_{1-x}$Pt$_x$)$_3$ with $x = 0$, 0.005 and 0.01. In the calculation the integration of the specific heat has been started at $T = 2\,\mathrm{K}$ as for pure UPd$_3$ no data below $2\,\mathrm{K}$ were available.

and 6.10. The transition at T_2 is not unambiguously observable in the heat capacity data in an applied magnetic field. Qualitatively, this behavior resembles that observed for UPd$_3$, as reported in Ref. [114], and reflects the AFQ nature of the phase below T_{-1}.

In order to further characterize the ground state properties of U(Pd$_{1-x}$Pt$_x$)$_3$, resistivity and susceptibility measurements in applied magnetic fields have been carried out. From these measurements a magnetic phase diagram will be obtained for the sample $x = 0.005$ and compared to the sample of pure UPd$_3$.

6.3.2 Resistivity

Specific heat experiments have been performed in applied magnetic field to gain information on the magnetic phase diagram. However, resistivity mea-

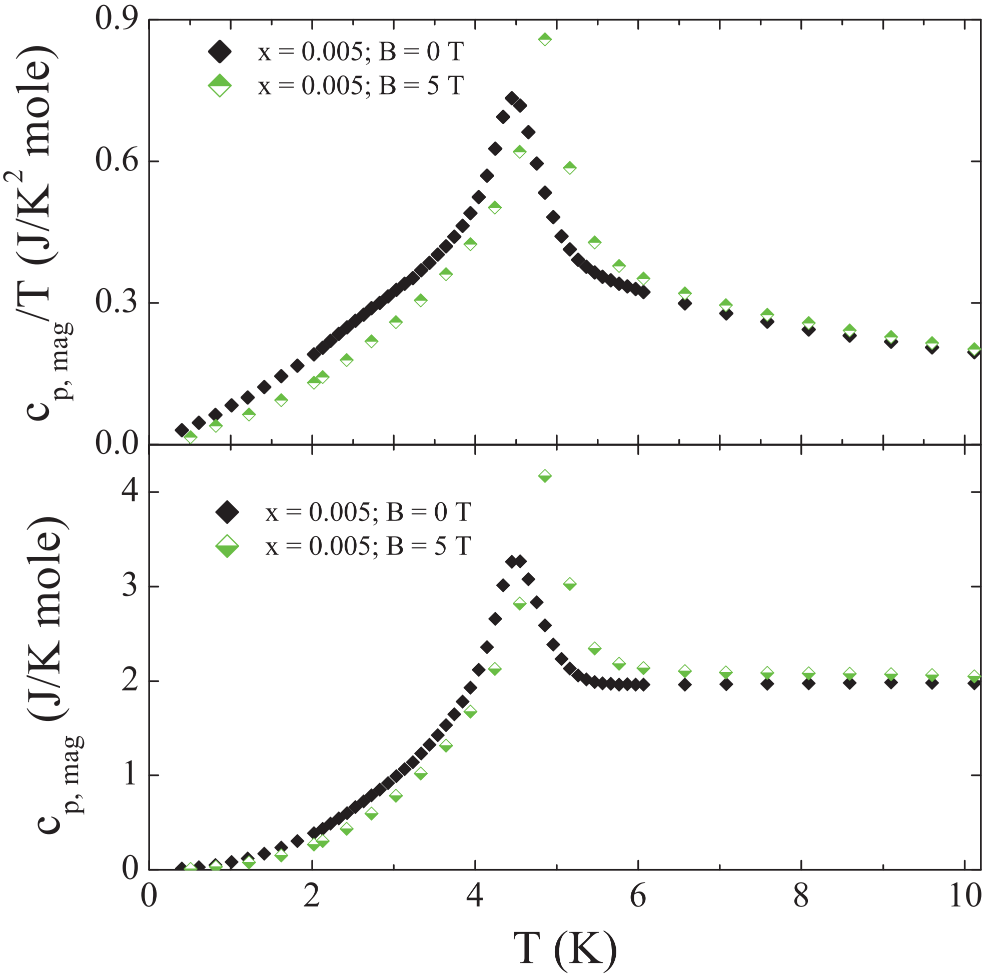

Figure 6.10: Temperature dependence of $c_{\mathrm{p,mag}}$ and $c_{\mathrm{p,mag}}/T$ of U(Pd$_{1-x}$Pt$_x$)$_3$ with $x = 0.005$ in zero magnetic field and in an applied magnetic field of $B = 5\,\mathrm{T}$ applied along the a axis, for details see text.

surements in magnetic fields are less time consuming, and can also provide enough information to determine the phase diagram. Therefore, corresponding experiments have been carried out, with the normalized low temperature resistivity $\rho(T)/\rho_{10\mathrm{K}}$ of U(Pd$_{1-x}$Pt$_x$)$_3$, $x = 0.005$ and 0.01, depicted in Fig. 6.11.

Qualitatively, the derivative of the resistivity $d\rho/dT$ resembles the magnetic specific heat $c_{\mathrm{p,mag}}$. Again, only for U(Pd$_{1-x}$Pt$_x$)$_3$, $x = 0.005$, the transitions at T_{-1} and T_2 are clearly resolvable, while for $x = 0.01$ only a broad maximum is observed in $d\rho/dT$ indicative of a smeared out transition in this sample. Therefore, electronic transport measurements in applied magnetic fields $B//a$

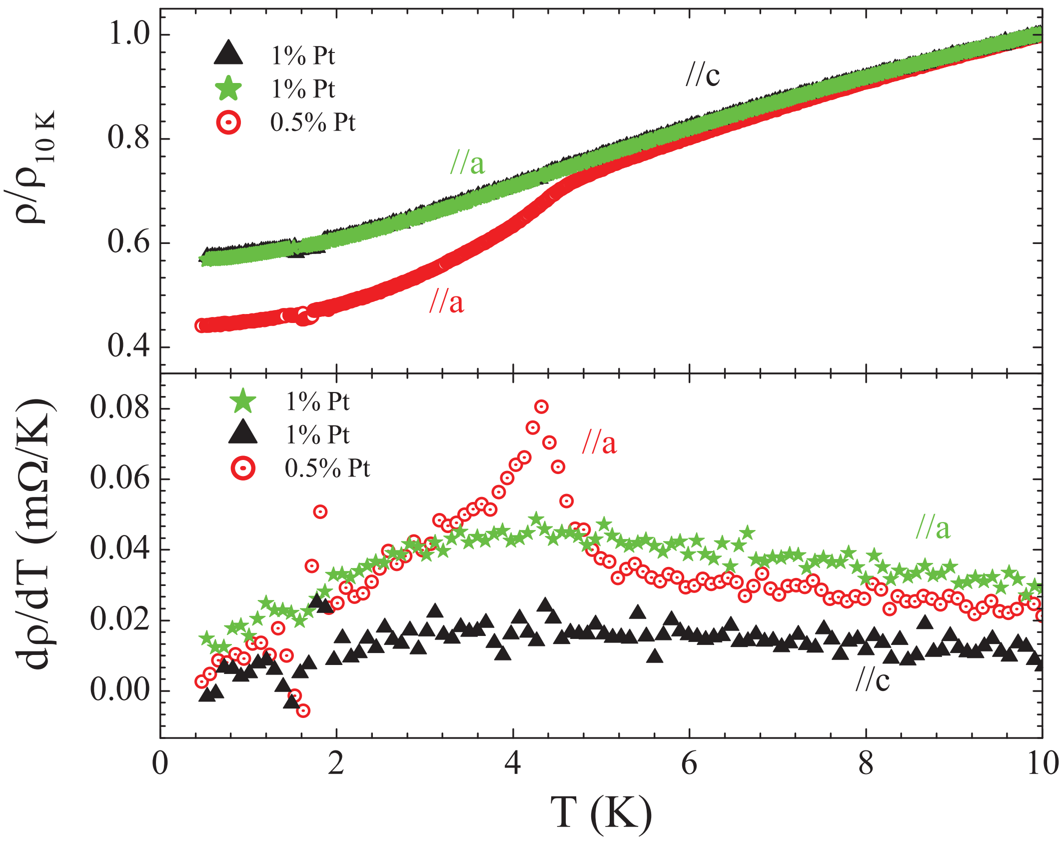

Figure 6.11: Temperature dependence of the normalized resistivity $\rho/\rho_{10\mathrm{K}}$ of U(Pd$_{1-x}$Pt$_x$)$_3$, $x = 0.01$ along the a (green stars) and c (black triangles) direction and $x = 0.005$ along the a direction (red circles).

have been carried out[2] on U(Pd$_{1-x}$Pt$_x$)$_3$, $x = 0.005$. Resistivity measurements in ^{4}He show a larger signal-to-noise ratio than those measured in a ^{3}He setup. Hence, detailed measurements of the resistivity in an applied magnetic field $B = 0\,\mathrm{T} - 9\,\mathrm{T}$ have been carried out using a standard four point technique in a ^{4}He cryostat and are depicted in Fig. 6.12.

According to Fisher-Langer theory [131], for a second order phase transition the specific heat c_p is proportional to the derivative of the electrical resistivity $d\rho/dT$. Fisher and Langer calculated the resistivity for a magnetic transition assuming a lattice of spins $\boldsymbol{S}_i$ at positions $\boldsymbol{R}_i$ and a single band of conduction electrons. The fluctuations are assumed to be slow enough that inelastic scattering does not have to be considered.

---

[2] Unfortunately, no resistive bar for measurements along the c axis was available.

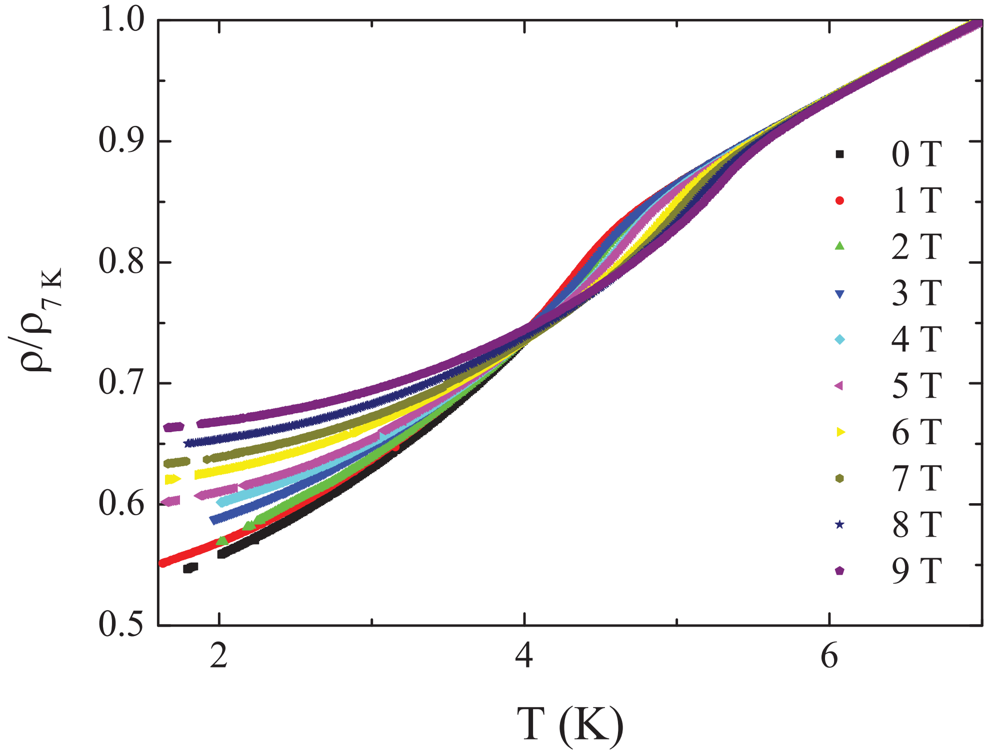

Figure 6.12: Temperature dependence of the resistivity ρ of U(Pd$_{1-x}$Pt$_x$)$_3$, $x = 0.005$, in various magnetic fields applied along the a direction.

In order to test if Fisher-Langer theory is applicable for U(Pd$_{1-x}$Pt$_x$)$_3$, $x = 0.005$, the derivative $d\rho/dT$ of the electrical resistivity and the specific heat c_p in $B = 0\,\mathrm{T}$ and $5\,\mathrm{T}$ of U(Pd$_{1-x}$Pt$_x$)$_3$, $x = 0.005$ are depicted in Fig. 6.13.

Overall, the derivative $d\rho/dT$ of the electrical resistivity exhibits the same features as the specific heat c_p, a finding that might be indicative of the transition at T_{-1} being of second order. Only, a small shift ($\sim 0.2\,\mathrm{K}$) between specific heat and $d\rho/dT$ is observed, which is not fully understood. Altogether, it implies that the quantity $d\rho/dT$ provides a suitable tool to determine the transition temperatures in U(Pd$_{1-x}$Pt$_x$)$_3$, $x = 0.005$.

Analogous to the magnetic specific heat $c_\mathrm{p,mag}$, the transition at T_2 is broadened in the derivative of the resistivity $d\rho/dT$ of U(Pd$_{1-x}$Pt$_x$)$_3$, $x = 0.005$. To accurately determine T_2 additional methods in analyzing the experimental data have been tried, such as the calculation of the second derivative $d^2\rho/dT^2$

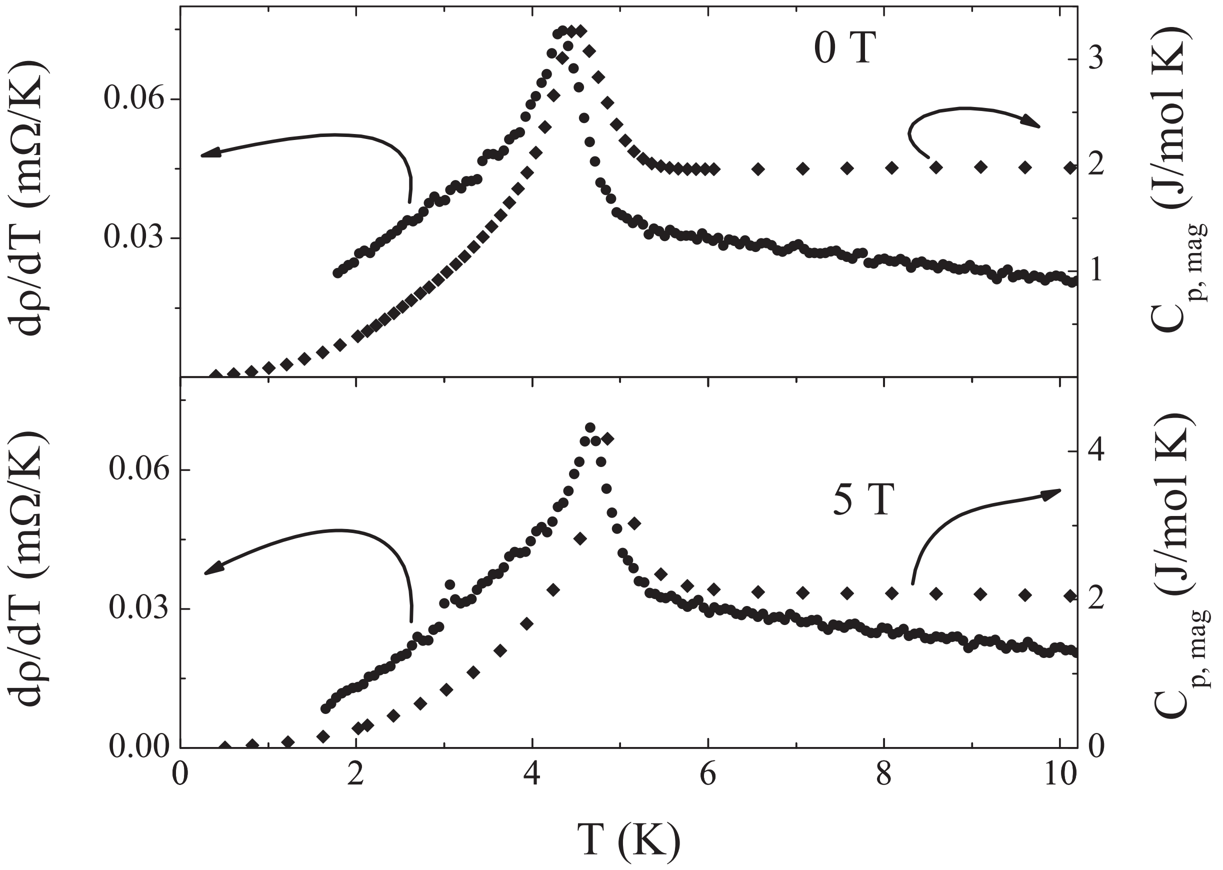

Figure 6.13: Temperature dependence of $d\rho/dT$ and $c_{\mathrm{p,mag}}$ of U(Pd$_{1-x}$Pt$_x$)$_3$, $x = 0.005$, in zero magnetic field and in $5\,\mathrm{T}$. The magnetic field was applied along the a direction.

and the quantity $1/Td\rho/dT$. In the second derivative $d^2\rho/dT^2$ the maximum of the broad anomaly in $d\rho/dT$ occurs as a zero crossing. In contrast, the quantity $1/Td\rho/dT$ should be proportional to $c_{\mathrm{p,mag}}/T$. Therefore, T_2 is determined as the shoulder in $1/Td\rho/dT$ and from the kink in the second derivative $d^2\rho/dT^2$. To illustrate these analyzing procedure both quantities $d^2\rho/dT^2$ and $1/Td\rho/dT$ are depicted in Fig. 6.14.

6.3.3 Susceptibility

As the final step to establish the magnetic phase diagram $B//a$ of U(Pd$_{1-x}$Pt$_x$)$_3$, $x = 0.005$, the temperature dependent susceptibility has been measured in various magnetic fields, both, in a vibrating sample magne-

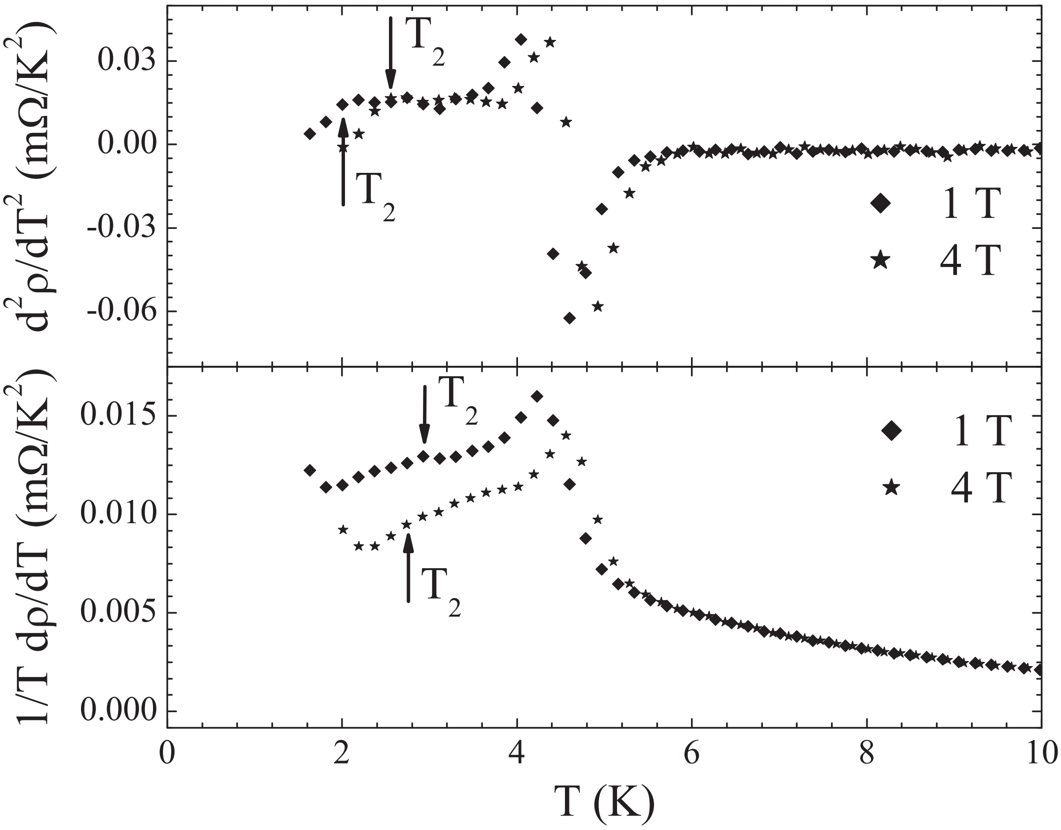

Figure 6.14: Temperature dependence of $1/T d\rho/dT$ and $d^2\rho/dT^2$ of U(Pd$_{1-x}$Pt$_x$)$_3$, $x = 0.005$, in $B = 1\,\mathrm{T}$ and in $4\,\mathrm{T}$. The magnetic field was applied along the a direction.

tometer ($B//a$) and in a commercial SQUID ($B//c$), this in collaboration with M. Bartkowiak, Forschungszentrum Dresden. In addition, U(Pd$_{1-x}$Pt$_x$)$_3$, $x = 0.01$, has been measured in a commercial SQUID for both directions in low magnetic fields $B//a$ and $B//c$. The low field ($x = 0.005$ in $B = 0.1\,\mathrm{T}$ and $x = 0.01$ in $B = 0.01\,\mathrm{T}$) measurements up to room temperature for both samples are depicted in the Figs. 6.15 and 6.16, respectively. Overall, the susceptibility χ closely resembles the behavior reported for pure UPd$_3$ [132].

Further, in Fig. 6.17 the low temperature region of the susceptibility χ in $B = 0.01\,\mathrm{T}$ of U(Pd$_{1-x}$Pt$_x$)$_3$, $x = 0.005$ and 0.01, is enlarged. Again, for both samples the behavior qualitatively resembles that of UPd$_3$. Only the transition temperatures are lower than for the pure sample.

Since from susceptibility measurements alone a distinction between T_{-1} or

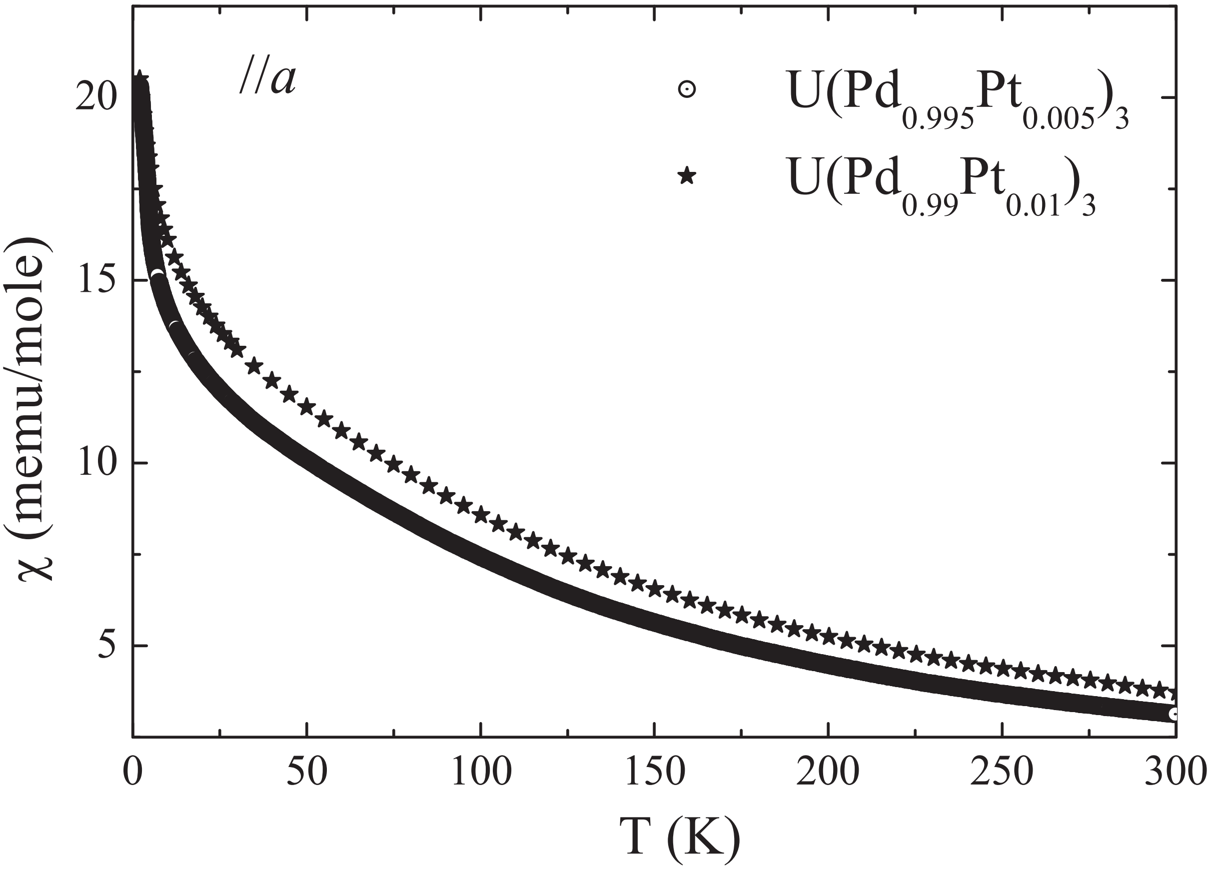

Figure 6.15: Temperature dependent susceptibility of U(Pd$_{1-x}$Pt$_x$)$_3$, $x = 0.005$ (red circles) and $x = 0.01$ (green stars), with the magnetic field B applied parallel to the a axis, for details see text.

T_{+1} cannot be made unambiguously, in the following the upper transition obtained from χ is labeled T_1. For $B//a$, the antiferroquadrupolar transition at T_1 appears as an inflection point in the susceptibility, while for $B//c$ it appears as a maximum in χ. Further, T_2 cannot be determined from these susceptibility data. From our data T_1 = 4.6 K (2.1 K) for $x = 0.005$ ($x = 0.01$) is extracted. (arrows in Fig. 6.17).

Further, and quite surprisingly, in the low temperature susceptibility χ of U(Pd$_{1-x}$Pt$_x$)$_3$, $x = 0.005$, for $B//a$ a difference between zero field cooled (ZFC) and field cooled (FC) measurement is observed below $T \sim 3 - 4\,\mathrm{K}$ (Fig. 6.18). This difference cannot be an experimental artifact, as it is not observed for measurements $B//c$ using the same experimental setup (Fig. 6.19).

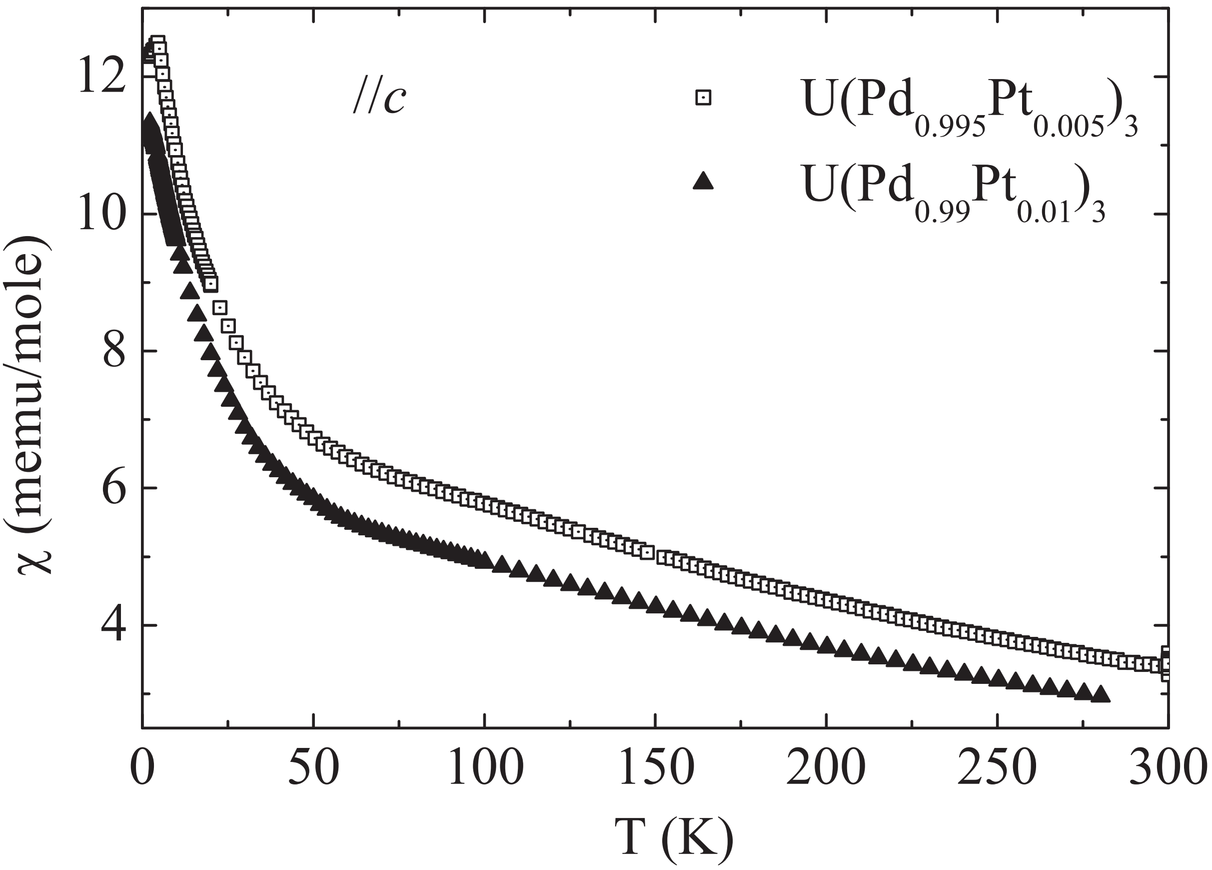

Figure 6.16: Temperature dependent susceptibility of U(Pd$_{1-x}$Pt$_x$)$_3$, $x = 0.005$ (blue squares) and $x = 0.01$ (black triangles), with the magnetic field B applied parallel to the c axis, for details see text.

For pure UPd$_3$, no ZFC-FC susceptibility data have been published so far, and therefore it is not possible to compare our finding with the behavior of the pure system. However, the temperature at which the FC-ZFC splitting starts is around T_2. Further, differences between FC and ZFC measurement can often be associated to domain formation in a magnet. Hence, the splitting might possibly be attributed to pinned antiferromagnetic and/or antiferroquadrupolar domains. If this would be the case, by measuring the susceptibility in FC and ZFC mode would give another measure for T_2. Further, if the concept of pinned domains is adequate, with the reduced amount of impurities in UPd$_3$, in comparison to U(Pd$_{1-x}$Pt$_x$)$_3$, $x = 0.005$, it should result in a reduced absolute value of the difference between FC and ZFC measurement in UPd$_3$, as compared to the sample $x = 0.005$.

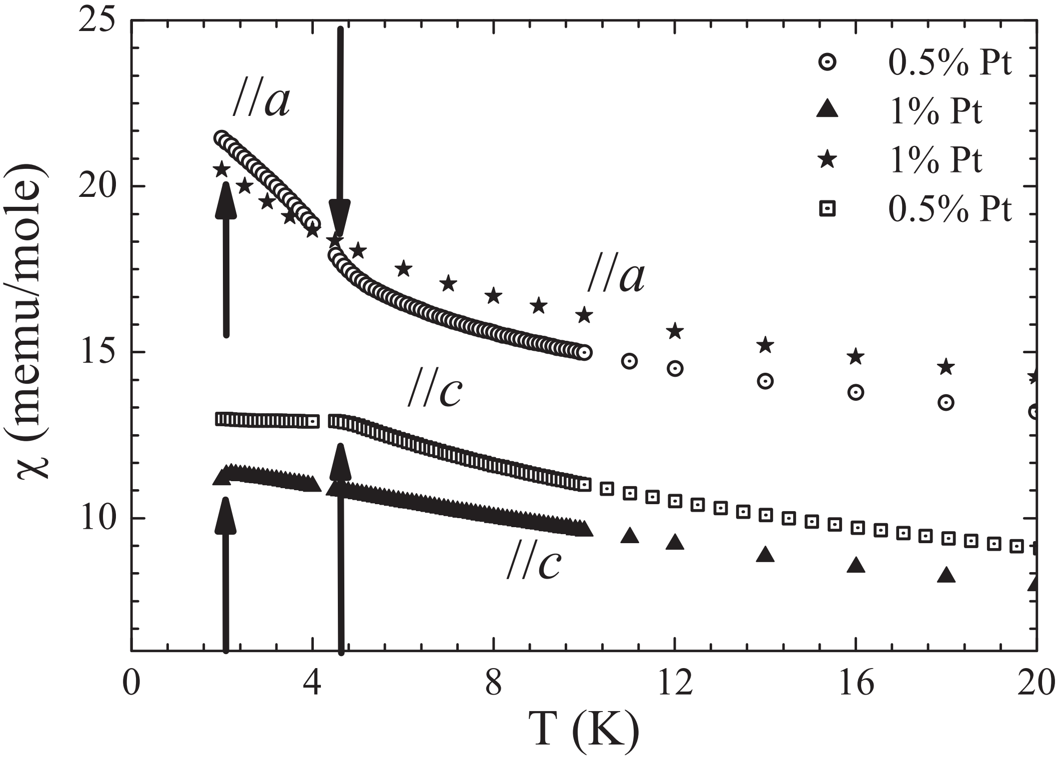

Figure 6.17: Low temperature susceptibility of U(Pd$_{1-x}$Pt$_x$)$_3$, $x = 0.005$ and 0.01, for fields B applied parallel to the a and c axes, respectively. T_1 is marked by an arrow, for details see text.

6.4 Conclusion

Using the specific heat, resistivity and susceptibility data a phase diagram of U(Pd$_{1-x}$Pt$_x$)$_3$ can be constructed, see Fig. 6.20. In both alloyed samples $x = 0.005$ and 0.01 the observable transition temperatures are shifted very strongly to lower temperatures, compared to UPd$_3$. In fact, while for $x = 0.005$ both T_1 and T_2 leave a clear signature in the data, for $x = 0.01$ the transition at T_2 is not observable anymore, while that at T_1 is very much broadened.

Using a linear extrapolation scheme in Fig. 6.20 it appears that T_2 is suppressed to zero for a Pt concentration of $x = 0.012$ in U(Pd$_{1-x}$Pt$_x$)$_3$, while T_{-1} is suppressed to zero for $x = 0.017$. In other words, the characteristic temperatures of quadrupolar ordering in UPd$_3$ react in an even more drastic fashion to Pt doping than the superconducting transition temperature in UPt$_3$ upon Pd doping.

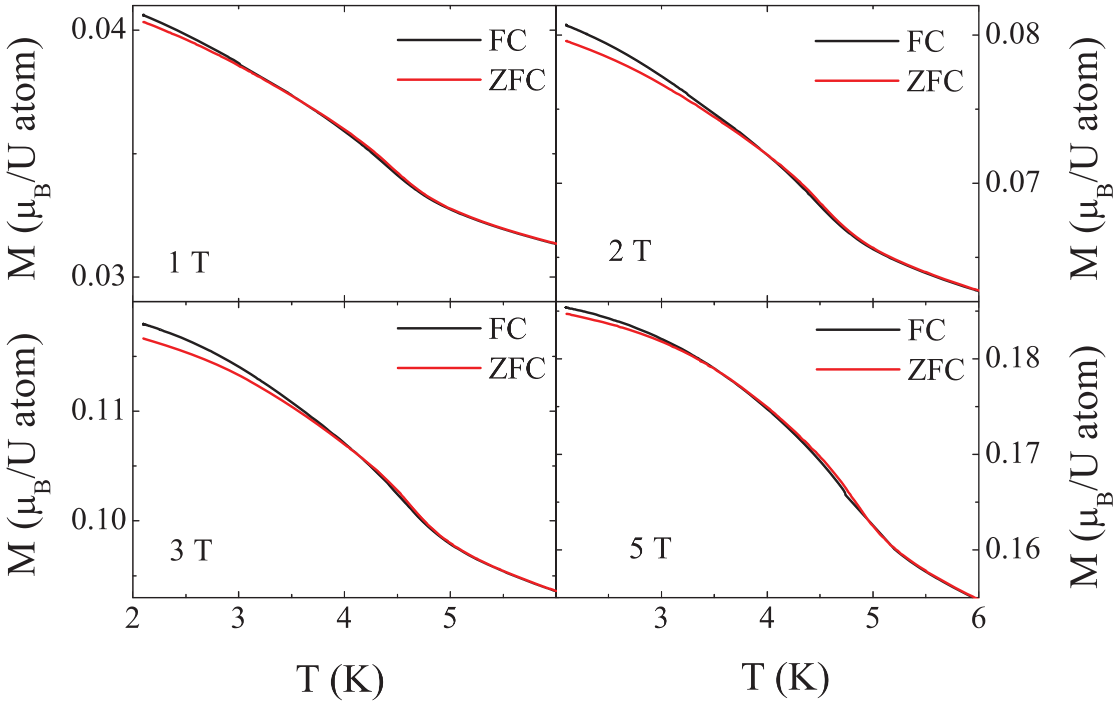

Figure 6.18: Low temperature susceptibility of U(Pd$_{1-x}$Pt$_x$)$_3$, $x = 0.005$, in magnetic fields $B//a$ measured in field cooled and zero field cooled mode, for details see text.

Further, the broadening of the antiferroquadrupolar transition with increasing amount of Pt alloying indicates that a small amount of Pt ($\sim 1\%$) is destroying long range quadrupolar ordering in U(Pd$_{1-x}$Pt$_x$)$_3$. Most likely, the sample $x = 0.01$ consists of microscopic clusters of different size with substantially different values T_1, leading to such "smearing out" of the transition. This finding implies that in the phase diagram of U(Pd$_{1-x}$Pt$_x$)$_3$ there is no quantum critical point, but at best (if at all) a region of quantum criticality for $x \sim 0.02$.

A verification of this scenario would require an investigation of a series of Pt doped samples by means of x-ray resonant scattering experiments. A reduced size of the ordered antiferroquadrupolar clusters with increasing amount of Pt doping might be detectable as an increasing peak width in such a x-ray resonant scattering experiment.

The magnetic phase diagram for U(Pd$_{1-x}$Pt$_x$)$_3$, $x = 0.005$ is depicted in

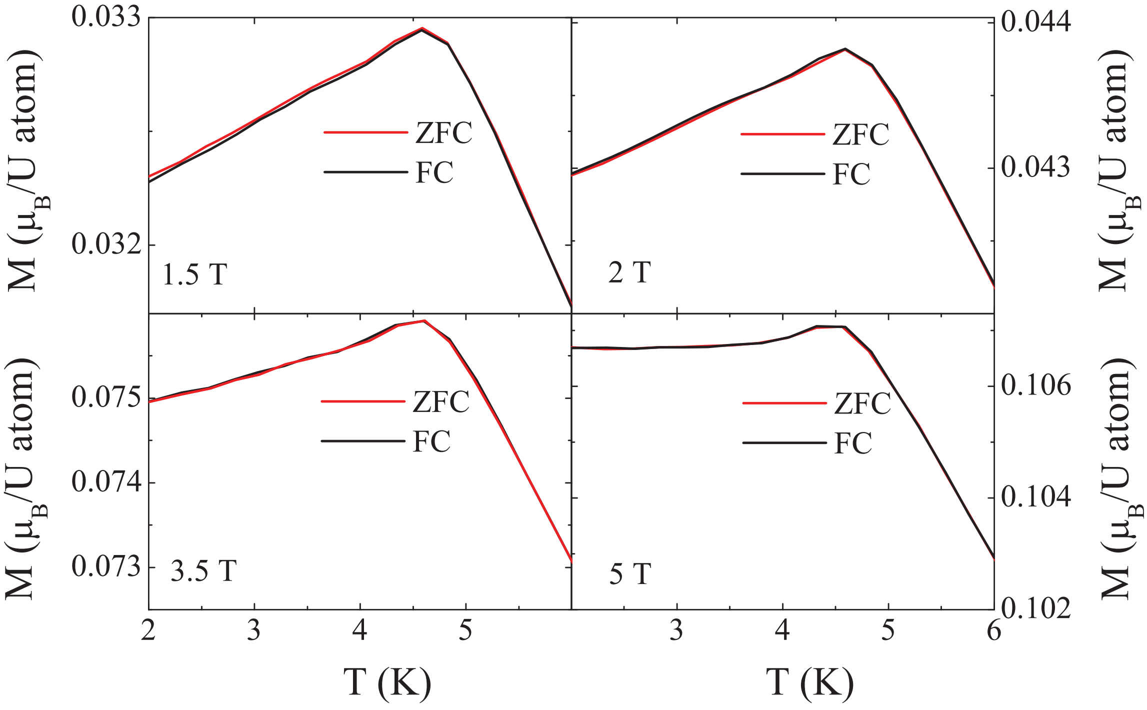

Figure 6.19: Low temperature susceptibility of U(Pd$_{1-x}$Pt$_x$), $x = 0.005$, in magnetic fields $B//c$ measured in field cooled and zero field cooled mode; for details see text.

Fig. 6.21. The transition temperatures T_{-1} and T_2 of U(Pd$_{1-x}$Pt$_x$)$_3$, $x = 0.005$, are indicated as points, the solid and dashed lines represent the behavior of the pure sample UPd$_3$ and are taken from Ref. [114].

From the figure it can be seen that the transition temperatures increase with increasing magnetic field. Qualitatively (that is, aside from a shift to lower temperatures), this behavior of U(Pd$_{1-x}$Pt$_x$)$_3$, $x = 0.005$, follows closely that of UPd$_3$. The increase of transition temperatures in an applied field is a characteristic feature of quadrupolar ordering [114]. It implies that essentially the behavior of U(Pd$_{1-x}$Pt$_x$)$_3$, $x = 0.005$ and $x = 0$, is the same - probably aside from the size of the ordered quadrupolar moment. If the entropy is a measure, the reduction of S_{mag} for $x = 0.005$ by 30 % compared to $x = 0$ would suggest a reduction of the quadrupolar moment by the same order of magnitude. It might be interesting to check this observation by x-ray diffraction studies.

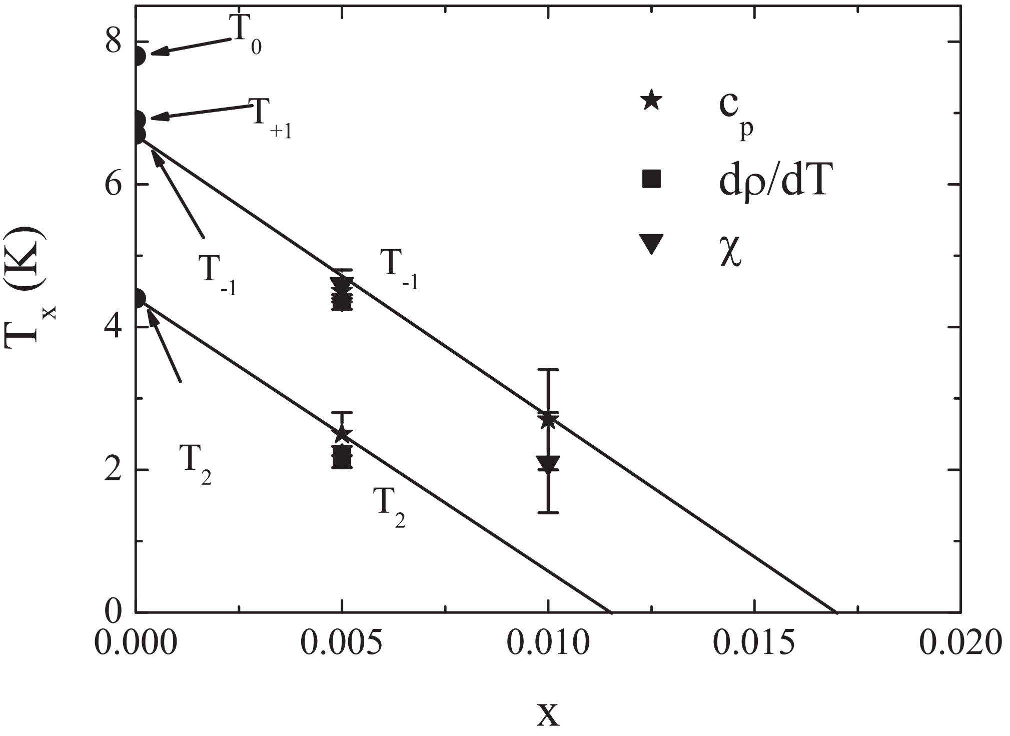

Figure 6.20: Alloying phase diagram of U(Pd$_{1-x}$Pt$_x$)$_3$, with the transition temperatures obtained from heat capacity (stars), resistivity (squares) and susceptibility (triangles) measurements. The data for the pure UPd$_3$ sample (circles) are taken from Ref. [112]. The solid lines are guides to the eyes, for details see text.

In summary, the phase diagram of U(Pd$_{1-x}$Pt$_x$)$_3$, $0 \leq x \leq 0.01$, has been elaborated. A suppression of T_{-1} as well as T_2 with Pt doping has been observed, suggesting a complete suppression of T_{-1} and T_2 at $x = 0.017$ and $x = 0.012$, respectively. Hence, the suppression of quadrupolar ordering does not lead to a quantum critical point, but at best to a broad region of quantum criticality in the phase diagram U(Pd$_{1-x}$Pt$_x$)$_3$.

Furthermore, the magnetic phase diagram of U(Pd$_{1-x}$Pt$_x$)$_3$, $x = 0.005$, has been derived. The principle behavior of U(Pd$_{1-x}$Pt$_x$)$_3$, $x = 0.005$ resembles that of pure UPd$_3$, making the former system to a test material for a deeper understanding of UPd$_3$.

Finally, a splitting in susceptibility measurements between ZFC and FC mode

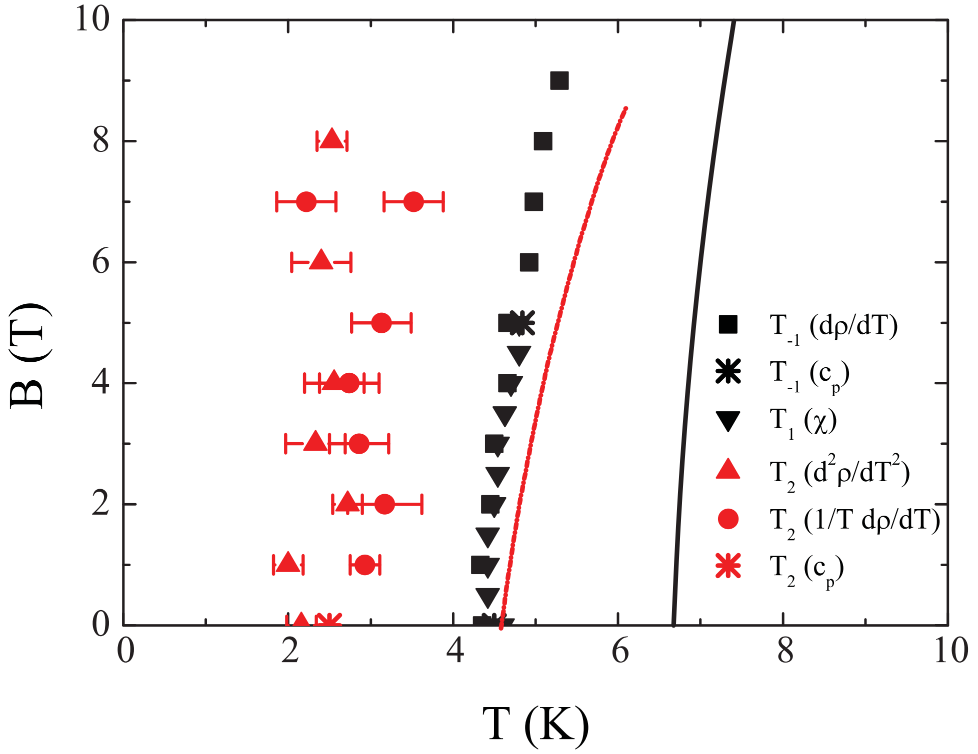

Figure 6.21: Magnetic phase diagram of $U(Pd_{1-x}Pt_x)_3$, $x = 0.005$, with the magnetic field applied in the a direction. T_{-1} has been obtained as a maximum in $\partial\rho/\partial T$, c_p and χ. T_2 was deduced from a maximum in $\partial^2\rho/\partial T^2$, $1/T\partial\rho/\partial T$ and c_p. The black and red solid lines indicate the phase boundaries of T_{-1} and T_2 determined for pure UPd_3 (from Ref. [114]), for details see text.

has been observed for the first time for $U(Pd_{1-x}Pt_x)_3$, $x = 0.005$. The splitting seems to begin at T_2 and would thus indicate the magnetic ordering in combination with the antiferroquadrupolar transition. If this view is correct, measurements in FC and ZFC mode on UPd_3 (and possibly related quadrupolar ordered systems) would give an easily accessible measure for T_2.

7 Quadrupolar *vs.* magnetic order in PrB_6

7.1 Introduction

Because of their simple crystal structure, and in combination with various interesting magnetic and electronic transport properties, rare-earth hexaboride materials are often used as model systems, and have attracted a lot of interest among both, theorists and experimentalists [133–135]. For example, CeB_6 is a dense Kondo material [136], SmB_6 has been discussed in terms of a narrow gap semiconductor [137], while EuB_6 as a low carrier density material is exhibiting ferromagnetic order [138].

The topic of multipolar ordering received renewed attention in recent years since it has been recognized that orbital ordering plays an important role for the magnetic and electronic properties of d- and f-electron systems. In order to better understand the mechanisms associated to such behavior model systems are required. Hence, multipolar ordering is one of the main topics discussed for f-electron systems in recent years [139–143].

In particular, the cubic CaB_6 type RB_6 (R = rare-earth element) compounds often display orbital degeneracies, and therefore these materials can be utilized to study multipolar ordering phenomena. For example, CeB_6 is well known for its unusual type of antiferroquadrupolar ordering. Below the antiferroduadrupolar transition temperatur T_Q and above the antiferromagnetic transition temperature T_N (phase II) in zero magnetic field, an antiferroquadrupolar ordering is observed [144]. In an external magnetic field, in phase II an additional field induced complicated non-collinear antiferromagnetic phase occurs [145]. As well, for the antiferromagnetic compound NdB_6 a two step metamagnetic transition was reported by Awaji *et al.* [146] recently, for which quadrupolar interactions seem to play an important role.

PrB_6 is another compound where the competition between quadrupolar and dipolar ordering may influence the physical properties, although a direct proof is still lacking. Kobayashi *et al.* [147] reported the magnetic phase diagram of PrB_6 and discussed the coexistence of quadrupolar and antiferromagnetic exchange interactions.

PrB_6 crystallizes in the CaB_6 structure with a lattice parameter of $4.133\,\text{Å}$ at room temperature (space group *Pm3m*, unit cell coordinates of Pr: (0 0 0) and B: (x $\frac{1}{2}$ $\frac{1}{2}$); $x \sim$ 0.2 [148]). The PrB_6 crystal structure is depicted in Fig. 7.1.

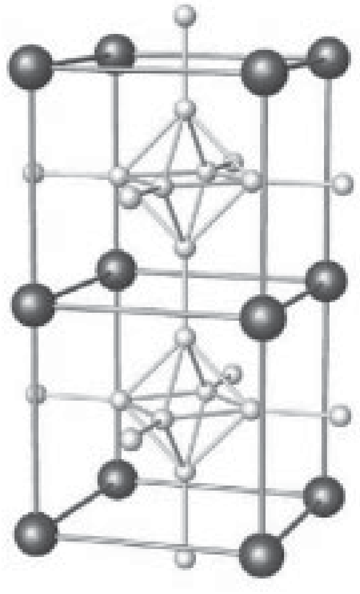

Figure 7.1: Crystal structure of PrB_6, taken from Ref. [149].

PrB_6 exhibits two successive first order phase transitions at low temperatures. The first one is from a paramagnetic to an incommensurate (IC) antiferromagnetic (AFM) phase at $T_N = 7\,\text{K}$, the second one from the IC to a commensurate (C) phase at $T_{IC} = 4.2\,\text{K}$.

The magnetic structure in the C and IC phase was determined by neutron scattering [150]. In the IC phase a double-k structure with an ordering vector of k = $[\frac{1}{4}\frac{1}{4}-\delta\frac{1}{2}]$ with $\delta = 0.05$ has been reported. The double-k structure in the C phase is described by an ordering vector k = $[\frac{1}{4}\frac{1}{4}\frac{1}{2}]$, see Fig. 7.2.

Both, in the C and the IC phase the magnetic structure is of planar type. With

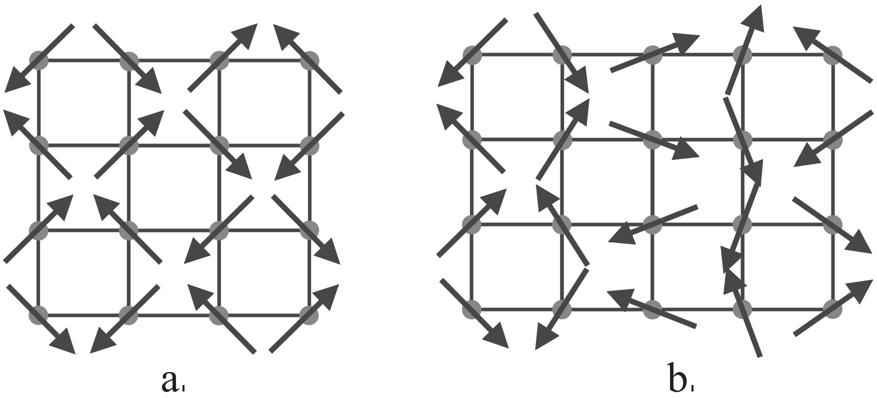

Figure 7.2: Magnetic structure of the C phase (a.) and the IC phase (b.), as seen by viewing it along a cubic main lattice vector.

the cubic symmetry three different antiferromagnetic domains have been observed in the C and the IC phase. As the C phase in $\mathrm{PrB_6}$ is similar to phase III in $\mathrm{CeB_6}$ [145], it suggests that the magnetic behavior in the C phase is dominated by antiferroquadrupolar (AFQ) effects. This idea is supported by the comparatively small ordered moment ($\sim 1.2\,\mu_\mathrm{B}/\mathrm{Pr\,atom}$) as observed in Ref. [150]. This is assumed to be the result of the coexistence of magnetic and quadrupolar interactions. However, the value from Ref. [150] is at odds with earlier neutron scattering experiments, where $\mu_{ord} =\sim\; 1.8\,\mu_\mathrm{B}/\mathrm{Pr}$ has been found in the C phase [151].

The magnetic moment for a free Pr^{3+} ion is $3.20\,\mu_\mathrm{B}$. In $\mathrm{PrB_6}$, the ground state multiplet of the Pr^{3+}ion is split into Γ_5 (triplett)-Γ_3($314\,\mathrm{K}$, doublet)-Γ_4($377\,\mathrm{K}$, triplet)-Γ_1($464\,\mathrm{K}$, singlet) as result of the crystalline electric field, measured by inelastic neutron scattering [152]. In this configuration, for the Γ_5 triplet as ground state the maximum ordered moment is $2.0\,\mu_\mathrm{B}$.

Further, McCarthy *et al.* [145] argued that a lattice distortion is associated to the phase transition into the C phase. However, they could not provide direct evidence because of the resolution limit in their neutron scattering study.

In order to clarify the origin of the complicated magnetic ordering behavior in the C and IC phase and to determine if there are possibly structural phase transitions, it is necessary to investigate the crystal structure in both, C and IC phases, with very high accuracy. Furthermore, direct evidence for the existence of quadrupolar moments in the C phase has not yet been established. Moreover, the driving mechanisms for the transitions in the magnetically ordered states of PrB_6, *i.e.*, quadrupolar versus dipolar ordering effects, have not yet been identified. Also, the value of the magnetic moment has not been determined to high accuracy. In order to contribute to the solution of these open issues, K.A. McEwen, University College London (UCL), has initiated a research program using high resolution resonant x-ray scattering at low temperatures on single crystalline PrB_6. In the following sections some of the results from this study are presented and discussed in the context of quadrupolar ordering in PrB_6.

7.2 Experimental Methods

The single crystal PrB_6 used for these experiments was grown by F. Iga (Hiroshima University) and S. Lee (SungKyunKwan University) at Hiroshima University, using a traveling solvent floating zone method in a mirror furnace equipped with Xe lamps. The sample was cut and aligned to give a face normal to the $[0\,1\,1]$ direction and polished using fine diamond paste. The x-ray scattering experiments were performed in cooperation with H. C. Walker, K. A. McEwen, D. F. McMorrow (all UCL), J.-G. Park, S. Lee (both SungKyunKwan University), and D. Mannix (ESRF) at the XMaS beamline of the European Synchrotron Facility ESRF in Grenoble, France. The sample was mounted in a displex cryostat allowing to adjust temperatures down to $1.7\,\mathrm{K}$. The vertical scattering plane is $[1\,1\,0] - [0\,0\,1]$.

The radiation for the diffractometer is provided by a bending magnet. It is predominantly (to 97.5 %) plane polarised in the horizontal plane. By using an analyzer crystal the non-rotated $\sigma - \sigma$ and the rotated $\sigma - \pi$ components of the scattered x-ray radiation can be separated. The analyzer crystal used in our experiments (*i.e.*, for energies close to the Pr L_{II} edge) was copper $(2\,2\,0)$.

In resonant scattering a core electron is excited to an orbital close to the Fermi energy. In this study on PrB_6 only L_{II} absorption edge processes are used. The main contribution to the resonant process is an electric dipole (E1) transition from the $2p_{1/2}$ orbital to the $5d$ band ($E = 6.444\,\mathrm{keV}$), and an electric quadrupole (E2) transition from the $2p_{1/2}$ to the $4f$-orbitals ($E = 6.437\,\mathrm{keV}$).

The accessible area in reciprocal space for an incident x-ray radiation energy of $E = 6.444\,\mathrm{keV}$ is displayed in Fig. 7.3. As a consequence the reflections that can be investigated here are limited to those indicated in the plot and discussed in the following.

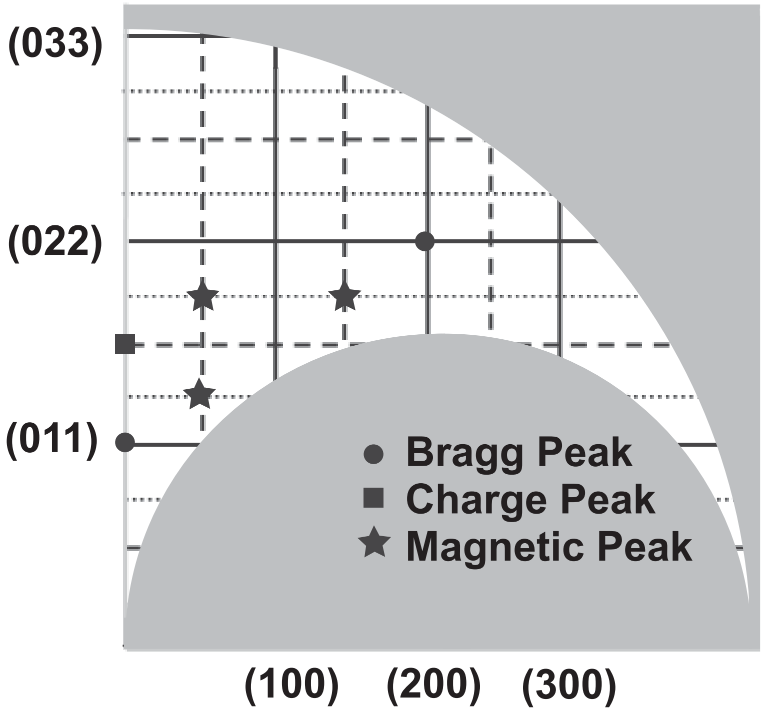

Figure 7.3: . Accessible area in reciprocal space with the investigated reflections for an incident energy of $E = 6.444\,\mathrm{keV}$, for details see text.

7.3 Experimental Results

7.3.1 Structural lattice distortion

As yet, a possible lattice distortion has not directly been detected in neutron scattering experiments because of a limited Q-resolution in these experiments [145]. Hence, in order to verify the presence of such a distortion the $(2\,2\,2)$ and $(0\,1\,1)$ structural peaks have been examined at low temperatures and in all three (paramagnetic, IC, C) phases. The essential observations in our experiments are the same for both Bragg peaks, therefore in the Figs. 7.4 and 7.5 only the data for the $(2\,2\,2)$ peak are presented, which has been measured with higher resolution.

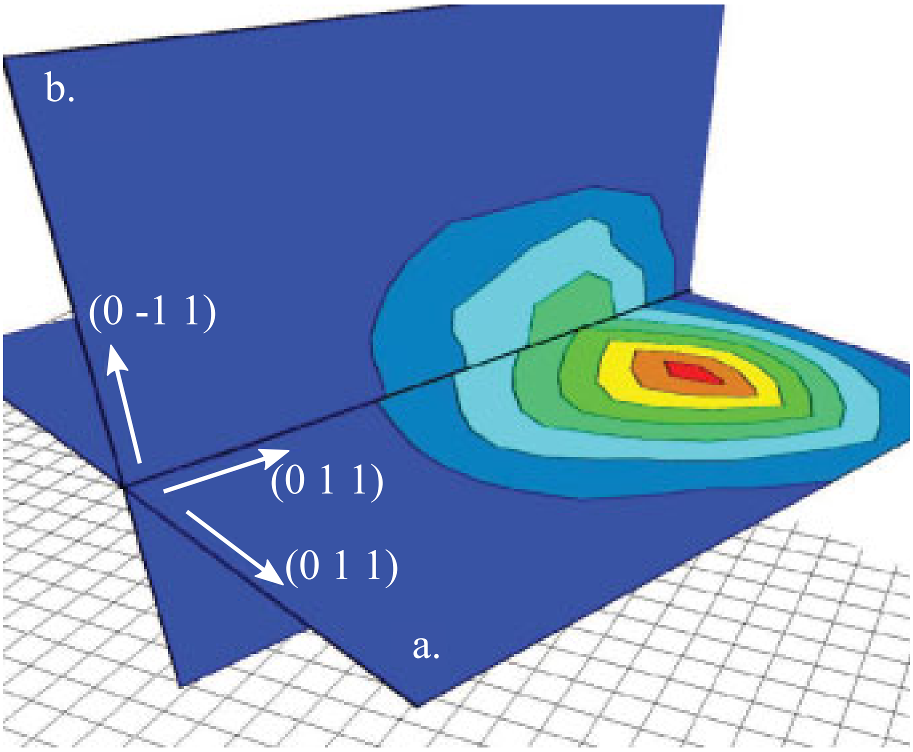

Figure 7.4: . In plane mesh scans on the (2 2 2) peak of PrB$_6$ at $5.5\,\mathrm{K}$ (a.). Corresponding out of plane mesh scans at $5.5\,\mathrm{K}$ (b.), for details see text.

For the labeling of the measurements a simple cubic basis is used, *viz.*, also for the distorted crystal the peak association in reciprocal space is performed in this basis. In general, a reciprocal lattice vector is given by

$$a^* = 2\pi \frac{b \times c}{a \cdot (b \times c)}, \tag{7.1}$$

where a, b, c are the primitive vectors of the real space lattice. The other two primitive vectors of the reciprocal lattice are given by permutation of a, b, c in the numerator.

In the plot, so-called "in plane" scans, *viz.*, two-dimensional cuts through the peak in the [hkl]-plane, with $k = l$ are depicted. The measured area in reciprocal space ranges from $-0.015\,\text{Å}^{-1}$ to $+0.015\,\text{Å}^{-1}$ relative to the center in h-direction, and $-0.006\,\text{Å}^{-1}$ to $0.006\,\text{Å}^{-1}$ relative to the center along kl, respectively.

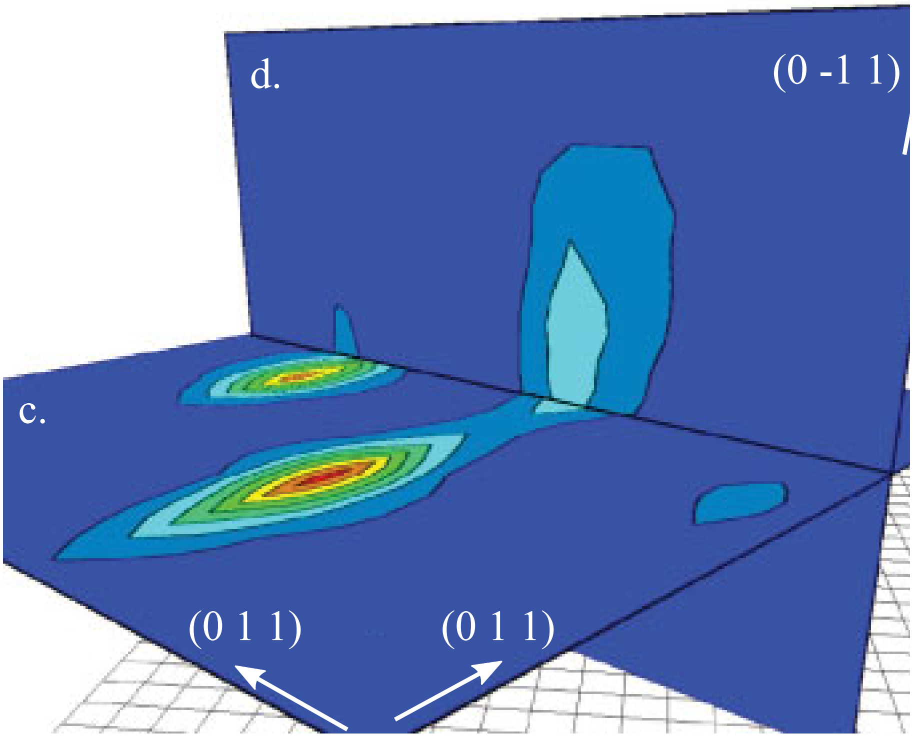

Figure 7.5: In plane mesh scans on the (2 2 2) peak of PrB_6 at $1.7\,\mathrm{K}$ (c.). Corresponding out of plane mesh scans at $1.7\,\mathrm{K}$ (d.), for details see text.

In addition, "out of plane" scans, *i.e.*, mesh scans in $[h\,k\,l]$, with $h = 2 = const.$, and the two-dimensional plane spanned by varying $k = l = 1.9885 - 2.0115$ and $k = 2.02 - 1.98$; $l = 1.98 - 2.02$, are depicted. In the figures, the central areas obtained in these measurements are enlarged for clarity. The different colors indicate counting rates.

In the incommensurate and paramagnetic phases the structural peaks have the same size and the same shape. At these temperatures no splitting of the structural peaks appears. As an example, an in plane scan of the $(2\,2\,2)$ peak at $5.5\,\mathrm{K}$ is shown in Fig. 7.4(a). In contrast, in the commensurate phase a splitting of the structural peaks into four smaller ones is detected. For the $(2\,2\,2)$ peak ($(1\,1\,0)$ peak) a relative splitting $\left(\frac{\Delta d}{d}\right)_{222(110)} = 6.81 \cdot 10^{-4}(1.892 \cdot 10^{-3})$ were found, where d is the d spacing of the peak and Δd is the mean value of the distortion for the four peaks. This is illustrated in Fig. 7.5(c), where the $(2\,2\,2)$ peak measured in plane at $1.7\,\mathrm{K}$ is displayed.

In order to examine the splitting in more detail out of plane scans have been performed. These confirm the splitting in the C phase, as is shown in Figs. 7.4(b) and 7.5(d) for the $(2\,2\,2)$ peak at $5.5\,\mathrm{K}$ and $1.7\,\mathrm{K}$, respectively. To ensure that no peak intensity is missed, additional mesh scans were performed for a very wide range of $0.02\,\text{Å}^{-1}$ around the peak centers, but no additional intensity has been found.

The largely varying intensity of the different split-up Bragg peaks in the C phase, as for instance seen in Fig. 7.5(c) and (d), is reflecting the formation of structural domains, as would be expected to occur for a rhombohedrical distortion of this cubic system. The distribution of the intensity within the splitted peaks is determined by integrating the intensity of every splitted peaks. The full intensity, *i.e.*, $100\,\%$ is given by the sum of the integrated peaks. The three bigger peaks all have roughly $30\,\%$ of the full intensity of the unsplit Bragg peak (see Fig. 7.6: peak *i.*: $30\,\%$, peak *ii.*: $34.8\,\%$, peak *iii.*: $26\,\%$), but the lower peak *iv.* has only about $10\,\%$ of the full intensity (error bars in the determination of the relative intensity about $\pm 5\,\%$).

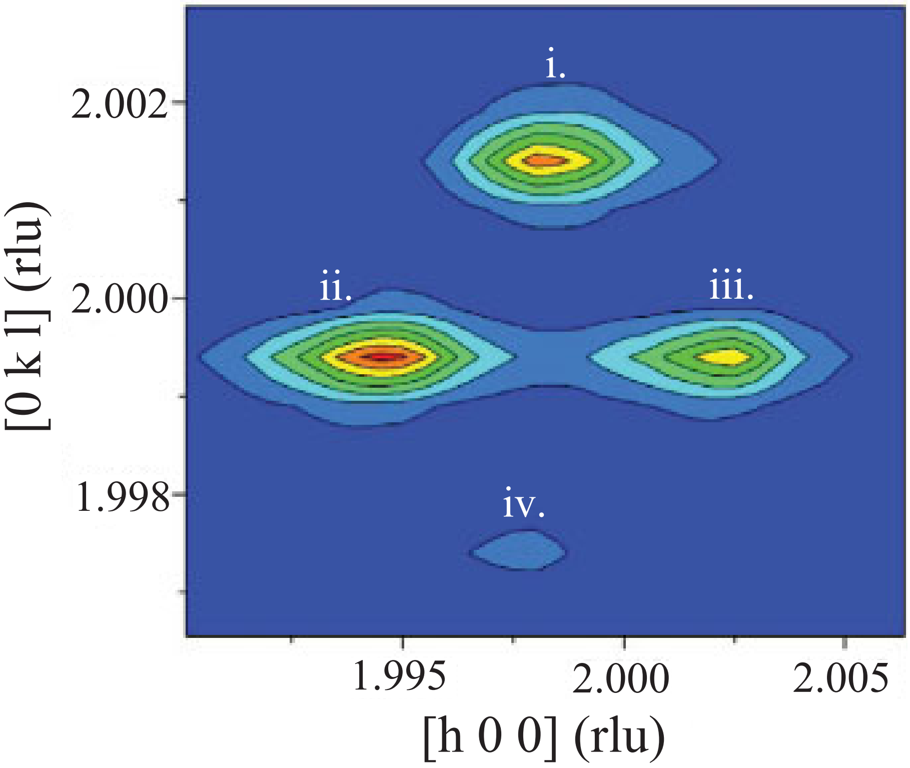

Figure 7.6: In plane scan of the $(2\,2\,2)$ peak at $1.7\,\mathrm{K}$ of PrB_6, for details see text.

To finally verify that the Bragg peak splitting is associated to the transition into the C phase T dependent scans of the $(1\,1\,0)$ peak by varying Θ have been carried out, that is the angle between $(1\,1\,0)$ plane and incoming beam. A typical scan is depicted in Fig. 7.7. From these data the T dependence of the integrated intensities of main and satellite peaks for $(1\,1\,0)$ (see Gaussian peak fits in Fig. 7.7) is derived, which are displayed in Fig. 7.8. From the figure it can be seen that around $5\,\mathrm{K}$ ($\sim T_{IC}$) three peaks appear, indicating the occurrence of a lattice distortion upon transition into the C phase.

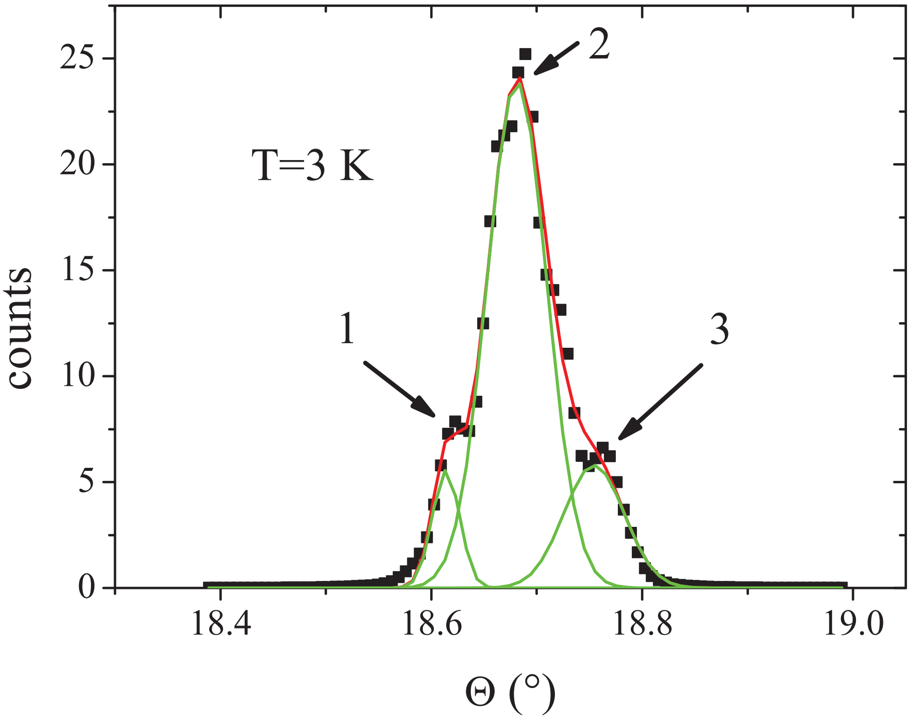

Figure 7.7: A typical scan of the $(1\,1\,0)$ peak including the Gaussian fits used to derive relative peak intensities, for details see text.

A detailed investigation of the position of the $(1\,1\,0)$ Bragg peak, depending on the thermal history is depicted in Fig. 7.9. The position of the single peak in the incommensurate and in the paramagnetic phase, together with the satellite peaks, occurring in the commensurate phase is depicted. The arrows and the numbers are indicating the thermal history. The position of the peak is depending on the thermal history and is not reproducible, indicating hysteresis effects in the lattice distortion. Further, the splitting of the $(2\,2\,2)$ peak, defined as the difference between the original peak position at $T > T_{\mathrm{IC}}$ and that of the

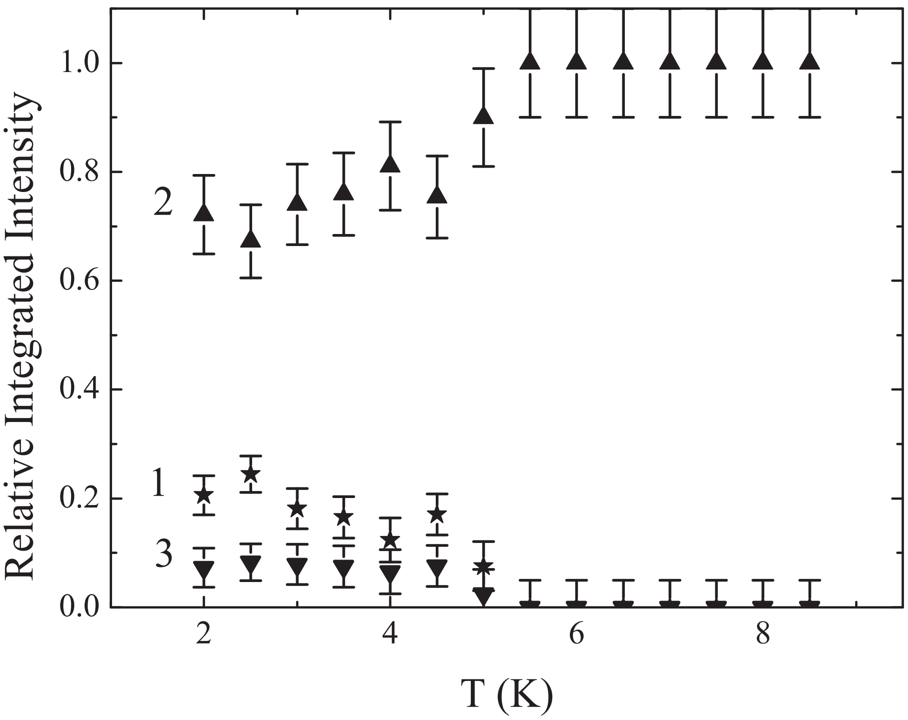

Figure 7.8: Temperature dependence of the relative intensity of the split up $(1\,1\,0)$ Bragg peak lines of PrB$_6$, for details see text.

splitted peaks at $T < T_{\mathrm{IC}}$ is summarized in Tab. 7.1.

The question arises about the crystallographic symmetry of the C phase. If a tetragonal distortion of the cubic lattice is assumed, it implies that only one crystallographic axis, say, the c axis, changes. The cross product and the scalar product both are linear operations. Hence, a change in c is resulting both in a change of the denominator and a change of same magnitude in the numerator. Correspondingly, a^* and b^* both remain constant, while only c^* is changed.

peak	Δh $(\cdot 10^{-3})$	Δk $(\cdot 10^{-3})$	$\Delta l (\cdot 10^{-3})$
i.	-2.3	-2.1	-2.1
ii.	2.3	0.1	0.1
iii.	-5.5	0.1	0.1
iv.	-2	1.9	1.9

Table 7.1: Splitting of the (222) peak given by the difference between the original peak at $T > T_{\mathrm{IC}}$ and the positions of the splitted peaks at $T < T_{\mathrm{IC}}$.

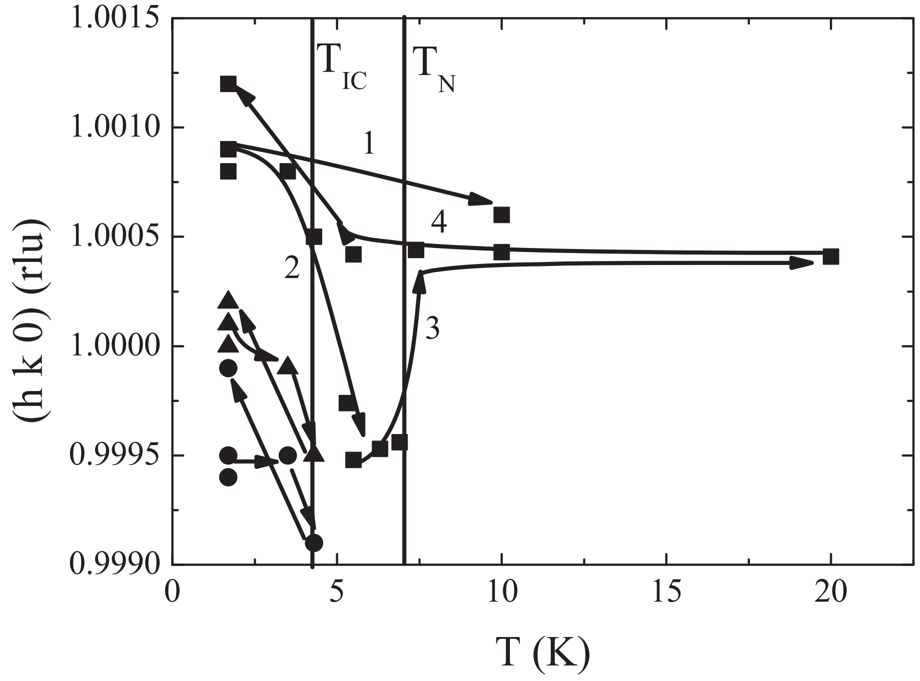

Figure 7.9: Temperature dependence of the position $(0\,k\,l)$ of the $(1\,1\,0)$ Bragg peak of PrB$_6$. The triangles are indicating the position of peak 1, the squares the position of peak 2, and the circles of peak 3. The number of the peaks are defined in Fig. 7.7. The arrows and the red numbers are indicating the thermal history, for details see text.

In other words, for a tetragonal distortion only one of the Miller indices a^*, b^*, c^* should change, as observed for peaks *ii.* and *iii.*. In contrast, all three Miller indices of peaks *iv.* and *i.* are changed, not consistent with a tetragonal distortion. The, from symmetry, expected peaks, where k and l, respectively changes cannot be observed due to the scattering geometry. In the third axis $[0\,\bar{1}\,1]$ a reduction of l (or k) would imply an increase of k (or l). Hence a complete scan in three dimensions would be necessary to detect all reflections associated with the distortion. Due to the enormous amount of measuring time required this was not possible.

However, for a rhombohedral distortion a change in the nominator and the denominator of Eq. 7.1 would occur. The denominator can be written as $a \cdot (b \times c) = b \cdot (c \times a) = c \cdot (a \times b)$. Therefore, the change of the nominator is as big as the change in the cross product in the denominator. The lengths of the primitive vectors stay constant and only the angles between the primitive vectors change but they are all equal. Hence, the Miller indices change by the same value, as observed for peak *i*. For the other peaks no change of the same value in all three Miller indices is observed.

For a monoclinic distortion without a change in the length of the direct lattices, a change in two reciprocal vectors is anticipated for the same reasons as above. This would not be consistent with the measured data. One can speculate that the monoclinic distortion is accompanied with a change in one or more lattice constants, this would only be consistent with peak *iv*.

However, the type of structural distortion cannot be unambiguously concluded. A mixture of distortion types as well as a domain structure is possible. Furthermore, the origin of the distortion is not unambiguously determined, a possible origin is a distortion of the boron octahedra as proposed in CeB_6 [153], but not detected within experimental resolution in neutron scattering experiments [154]. Together with the knowledge of the magnetic structure one can speculate that the lattice distortion is rhombohedral, as illustrated in Fig. 7.10.

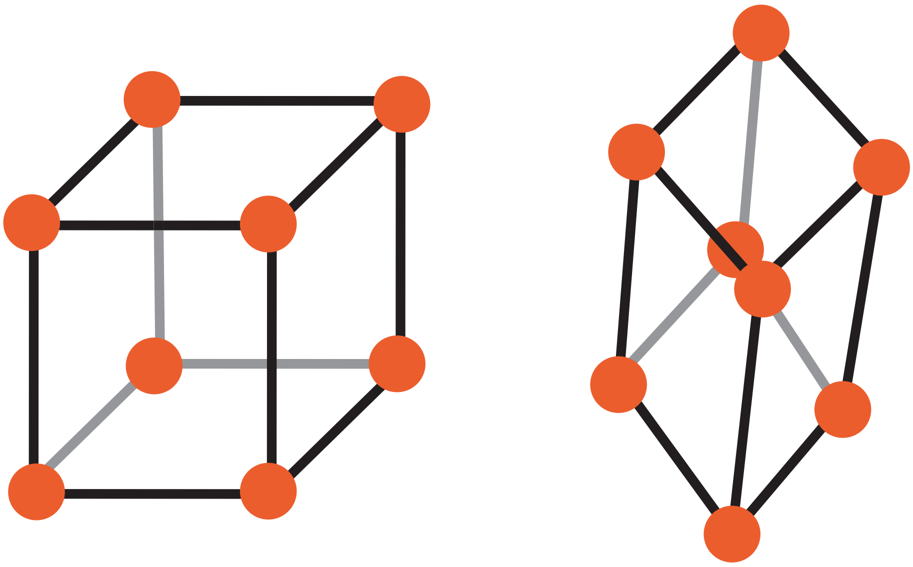

Figure 7.10: Distortion of a cubic lattice to rhombohedral symmetry.

In conclusion, the lattice distortion in PrB_6 associated to the transition into the commensurate phase has been observed directly by high resolution x-ray diffraction. Further, its temperature dependence has been measured. Our observations fully support the speculation from Ref. [145]. At this point, only an unambiguous determination of the symmetry of the distorted low temperature phase remains to be resolved.

7.3.2 Charge peaks

In previous studies on GdB_6, a system closely related to PrB_6, a low temperature lattice distortion has been observed [155, 156], whose nature has not been understood so far. In GdB_6, additional charge peaks with wave vectors of $(0\,0\,\frac{1}{2})$ and $(\frac{1}{2}\,\frac{1}{2}\,0)$ have been detected in the magnetically ordered phases. The question arises if similar charge superstructures appear in PrB_6. Therefore, a systematic search for charge peaks in PrB_6 has been performed.

In this study, a search at various positions in reciprocal space at base temperature ($1.7\,\mathrm{K}$) revealed an additional peak at $(\frac{3}{2}\,\frac{3}{2}\,0)$. Further, areas unsuccessfully scanned include $(\frac{3}{2}\,\frac{3}{2}\,\frac{1}{2})$, $(2\,2\,\frac{3}{2})$ and $(2\,2\,\frac{1}{2})$. For the $(\frac{3}{2}\,\frac{3}{2}\,0)$ peak the absorption energy has been determined by measuring its energy dependence in $\sigma - \sigma$ and $\sigma - \pi$ geometry (Fig. 7.11), respectively, while keeping the wave vector transfer fixed.

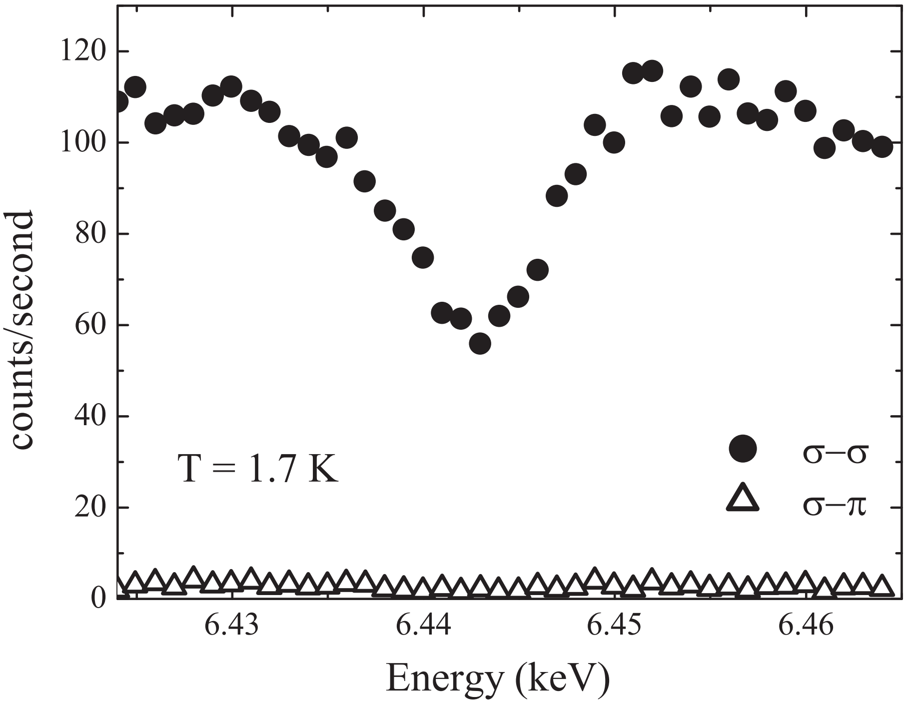

Figure 7.11: Energy scan of the Bragg peak at $(\frac{3}{2}\,\frac{3}{2}\,0)$ in $\sigma - \sigma$ and $\sigma - \pi$ geometry for fixed wave vector transfer of PrB_6 at $1.7\,\mathrm{K}$.

In the $\sigma - \sigma$ data a $\sim 50\%$ suppression of the intensity at resonance is observed, with the resonance energy determined to $6.443\,\mathrm{keV}$. At the resonance the emitted x-rays are radiated into all directions, which accounts for the observed suppression. In contrast, for the $\sigma - \pi$ channel there is essentially no signal. In conclusion the $(\frac{3}{2}\,\frac{3}{2}\,0)$ peak is a pure charge peak. The propagation vector of this lattice distortion in PrB$_6$ is $(\frac{1}{2}\,\frac{1}{2}\,0)$, closely resembling the situation in GdB$_6$ [155, 156]. Subsequently, the T dependence of the $(\frac{3}{2}\,\frac{3}{2}\,0)$ peak has been measured, as shown in Fig. 7.12.

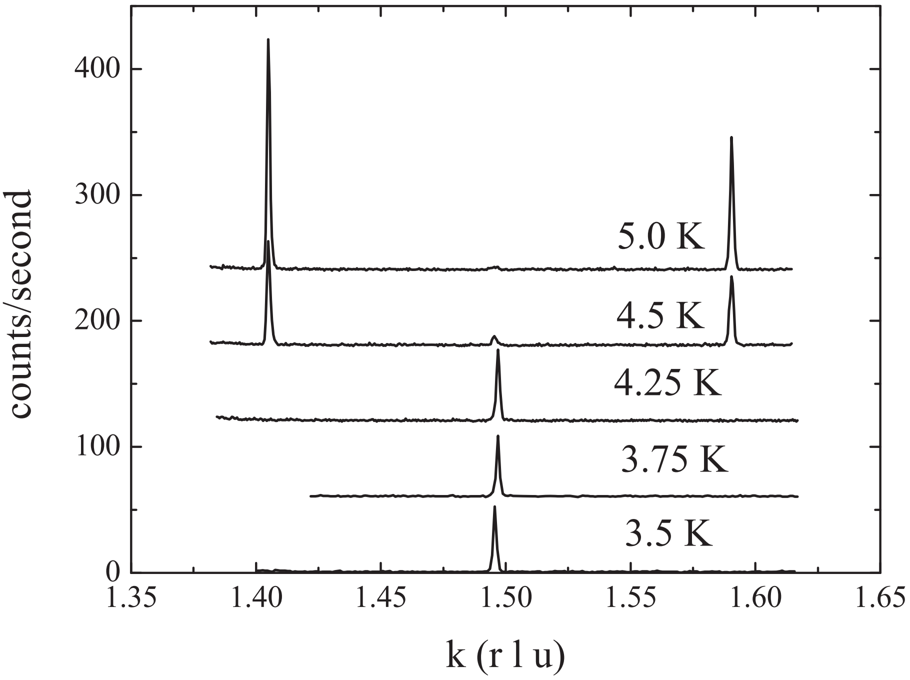

Figure 7.12: k dependent scans in $\sigma - \sigma$ geometry at different temperatures of the $(\frac{3}{2}\,\frac{3}{2}\,0)$ peak of PrB$_6$.

In this figure, k dependent scans in $\sigma - \sigma$ geometry at different temperatures are depicted. The data are shifted by $60\,\mathrm{counts/second}$ against each other for clarity. The $(\frac{3}{2}\,\frac{3}{2}\,0)$ peak splits up upon entering the IC phase, and disappears in the paramagnetic phase. The splitting γ in the incommensurate phase, with the peak positions at $(\frac{3}{2}\,\frac{3}{2} \pm \gamma 0)$, is found to be $\gamma = 2\delta$, with δ characterizing the incommensurability of the magnetic structure. It indicates that there is a close connection between magnetic and charge ordering in PrB$_6$. The doubling of $\gamma = 2\delta$ as incommensurability vector of the charge ordering, in comparision to the incommensurability δ of the magnetically ordered phase reflects the doubling of the unit cell lattice vectors of the antiferromagnetic phase compared to the charge ordered one.

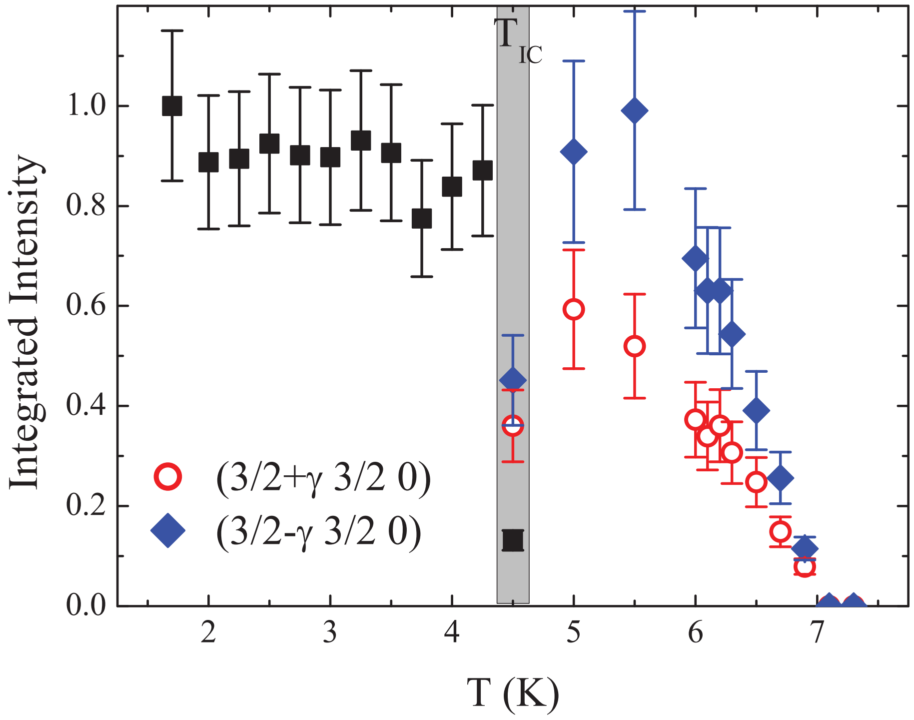

Figure 7.13: The temperature dependence of the integrated intensity of the $(\frac{3}{2}\,\frac{3}{2}\,0)$ and $(\frac{3}{2} \pm \gamma \frac{3}{2}\,0)$ peaks (from Θ scans in the C phase, from k scans in the IC phase). The data in the C phase are scaled by a factor of 0.25.

From the data as in Fig. 7.12 the T dependence of the relative peak intensities of the $(\frac{3}{2}\,\frac{3}{2}\,0)$ and corresponding superstructure $(\frac{3}{2}\,\frac{3}{2} \pm \gamma 0)$ peaks (Fig. 7.13) is derived. From the figure it appears that the transition at T_{IC} is first order. With the accuracy of the temperature control of the cryostat, $\Delta T = \pm 0.1K$, from these data the transition temperature T_{IC} within these limits is determined, a fact indicated by the shaded box in Fig. 7.13. Conversely, due to the lack of thermal hysteresis for the transition at T_N from these data the order of the transition cannot be unambiguously concluded, although specific heat measurements indicate that it is also first order [147, 151]. To determine the nature of the superstructure peaks in GdB$_6$ [156] is has been argued that a scaling with $(Q \cdot \hat{e})$ should be observable (Q: wave vector transfer, $\hat{e}$: unit vector parallel to the distortion). Unlike GdB$_6$, such a scaling could not be found in PrB$_6$. The reason for this different behavior is not understood so far.

In conclusion, a coupling of charge ordering in PrB$_6$ to the magnetically ordered state is found. While there appears to be a clear connection between charge and magnetic incommensurability in the IC phase, the situation is less clear in the C phase.

7.3.3 Magnetic peaks

In order to search for possible scattering contributions from quadrupolar ordering a detailed investigation of the magnetic peaks has been carried out, including azimuthal scans by analyzing the relative scattering strength of the peaks in $\sigma - \sigma$ and $\sigma - \pi$ geometry. Furthermore, with these measurements the magnetic structure can be verified.

In order to find the resonance energies of the different peaks energy scans in $\sigma - \pi$ and $\sigma - \sigma$ geometry have been performed in k space at $(\frac{5}{4}\,\frac{5}{4}\,\frac{1}{2})$, $(\frac{7}{4}\,\frac{7}{4}\,\frac{1}{2})$ and $(\frac{7}{4}\,\frac{7}{4}\,\frac{3}{2})$. The data for $(\frac{5}{4}\,\frac{5}{4}\,\frac{1}{2})$ are depicted in Fig. 7.14, those for $(\frac{7}{4}\,\frac{7}{4}\,\frac{1}{2})$ and $(\frac{7}{4}\,\frac{7}{4}\,\frac{3}{2})$ closely resemble the behavior of the peak at $(\frac{5}{4}\,\frac{5}{4}\,\frac{1}{2})$ and are not shown here.

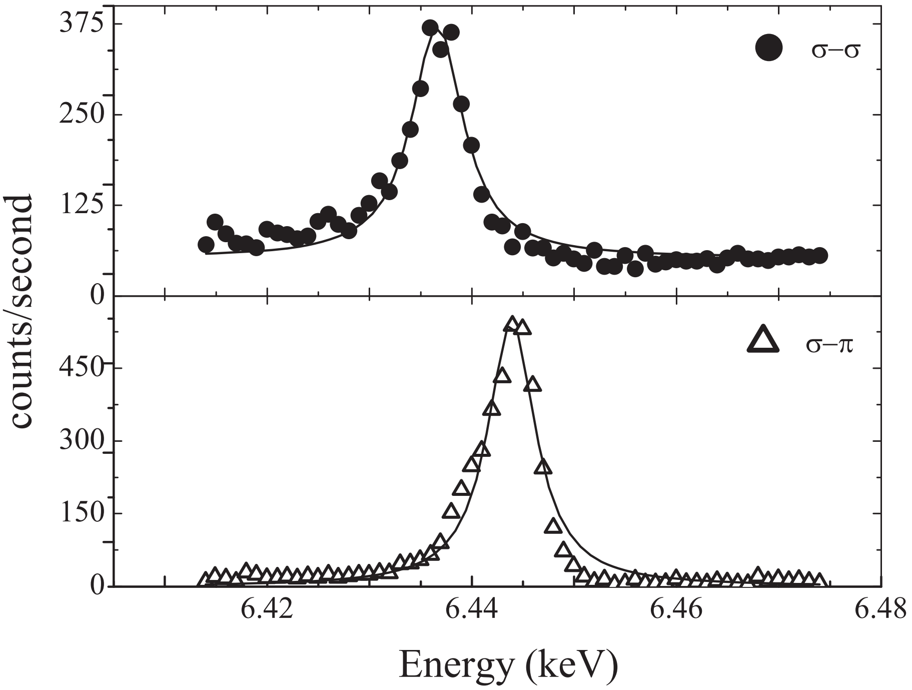

Figure 7.14: Energy scans of the $(\frac{5}{4}\,\frac{5}{4}\,\frac{1}{2})$ peak at $T = 1.7\,\mathrm{K}$ for $\Psi = -75.13$, see Fig. 3.26. The red line in the lower panel and the black line in the upper panel are Lorentzian fits, for details see text.

From the measurements the resonance energies for all three peaks have been determined to $E = 6.444$ keV and $E = 6.437$ keV for $\sigma - \pi$ and $\sigma - \sigma$, respectively. For $\sigma - \pi$ the scattering stems from an E1-term dipole transition, for $\sigma - \sigma$ it is due to a E2-term quadrupole transition, thus for PrB_6 the two transitions are separated by only $7\,\mathrm{eV}$ (Fig. 7.14). The FWHM of the peaks for all measured magnetic k space positions is determined to $\sim 6\,\mathrm{eV}$.

The intensities in the energy scans could not be corrected for crosstalk because the angle between scattered beam and polarizer, Θ_P, depends on the energy. Hence, no corrections for these scans were possible. However, from an analysis of purely structural peaks the crosstalk is estimated to contribute less than 5% to the absolute intensity in $\sigma - \sigma$ geometry. This observation implies that because of this crosstalk between $\sigma - \sigma$ and $\sigma - \pi$ channels measurements in the two geometries affect each other in the peak ranges, limiting the experimental resolution in this study.

Further, the temperature dependence of the $(\frac{7}{4}\,\frac{7}{4}\,\frac{1}{2})$ peak in $\sigma - \pi$ and $\sigma - \sigma$ configuration was measured in detail. The Θ scans were fitted using a Lorentzian, with the integrated intensity from the fits plotted as function of temperature in Fig. 7.15. From the figure a transition temperature of $T_{IC} = 4.3\,\mathrm{K}$ is obtained, in good agreement with the results presented in Secs. 7.3.1 and 7.3.2.

In order to analyze the azimuthal dependence of the scattering the electric dipole (E1) transition is more closely inspected. The peaks discussed in this chapter all are far away from structural Bragg peaks. Hence, the first term in Eq. 3.26 in the dipole scattering amplitude is zero. The scattering amplitude for the first harmonic magnetic satellites is given by the second term in Eq. 3.26. The scattering amplitude for the contribution from a magnetic scattering center is zero in $\sigma - \sigma$, while in $\sigma - \pi$ this scattering amplitude is given by $-iF^{(1)}(z_3 \sin\Theta + z_1 \cos\Theta)$, where z_1 is the component of the magnetic moment in $[1\,1\,0]$ and z_3 the component in $[0\,\overline{1}\,1]$ direction, respectively. As seen in Fig. 7.2 the magnetic moments are pointing along the $[1\,1\,0]$ direction, hence z_3 is zero. The effectively detected magnetic moment is the projection of the moment in the direction of the incident/scattered beam. In an azimuthal scan the sample is rotated around the scattering vector Q. Hence, a variation $z_1 = M \sin\Psi$, where M is denoting the magnetic moment and Ψ the angle of rotation, is expected, resulting in an intensity variation $\sim M^2 \sin^2\Psi$.

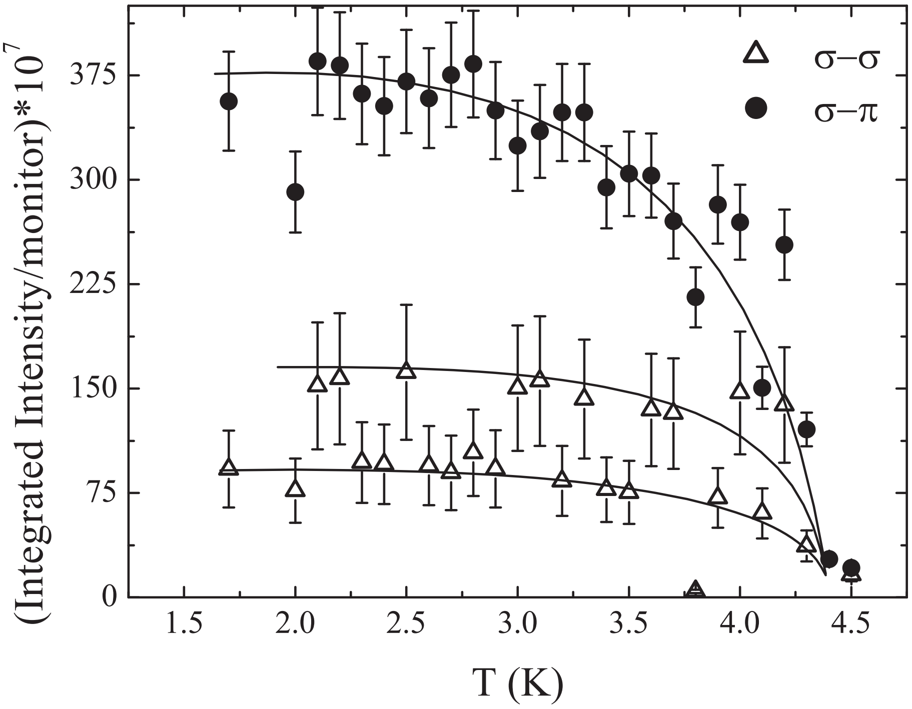

Figure 7.15: Temperature dependence of the $(\frac{7}{4}\,\frac{7}{4}\,\frac{1}{2})$ peak in the C-phase measured in $\sigma - \pi$ and $\sigma - \sigma$ geometry. The solid lines are guides to the eyes.

As shown in Fig. 7.16 in $\sigma - \pi$ configuration the azimuthal angle dependence of the $(\frac{5}{4}\,\frac{5}{4}\,\frac{1}{2})$ peak measured in the C phase at $1.7\,\mathrm{K}$ is well described by a $\sin^2\Psi$ function, compatible with the antiferromagnetic structure of PrB$_6$. At $E = 6.444\,\mathrm{keV}$ in $\sigma - \sigma$ geometry the intensity is about $3.7\,\%$ of that in $\sigma - \pi$ configuration. The crosstalk of the structural $(1\,1\,0)$ peak at this energy has been determined to $3.8\,\%$. Hence the $(\frac{5}{4}\,\frac{5}{4}\,\frac{1}{2})$ peak at $E = 6.444\,\mathrm{keV}$ appears only in $\sigma - \pi$ reflecting the AFM order as discussed above.

The E2 transition appears at a slightly lower energy of $E = 6.437\,\mathrm{keV}$. Its azimuthal angular dependence is included in Fig. 7.16. The intensity is very low (about 1% of the $\sigma - \pi$ channel), however it cannot not be due to feedthrough from the analyzer crystal because of the different energy with respect to the E1 transition. Unfortunately, an accurate analysis of the data is difficult, because of the residual crosstalk limiting the experimental resolution.

Further, in the IC phase a behavior of the azimuthal angular dependence has been found in $\sigma - \pi$ geometry which is similar to the one in the C phase. To illustrate this, the data taken in $\sigma - \sigma$ and $\sigma - \pi$ configuration for the peak

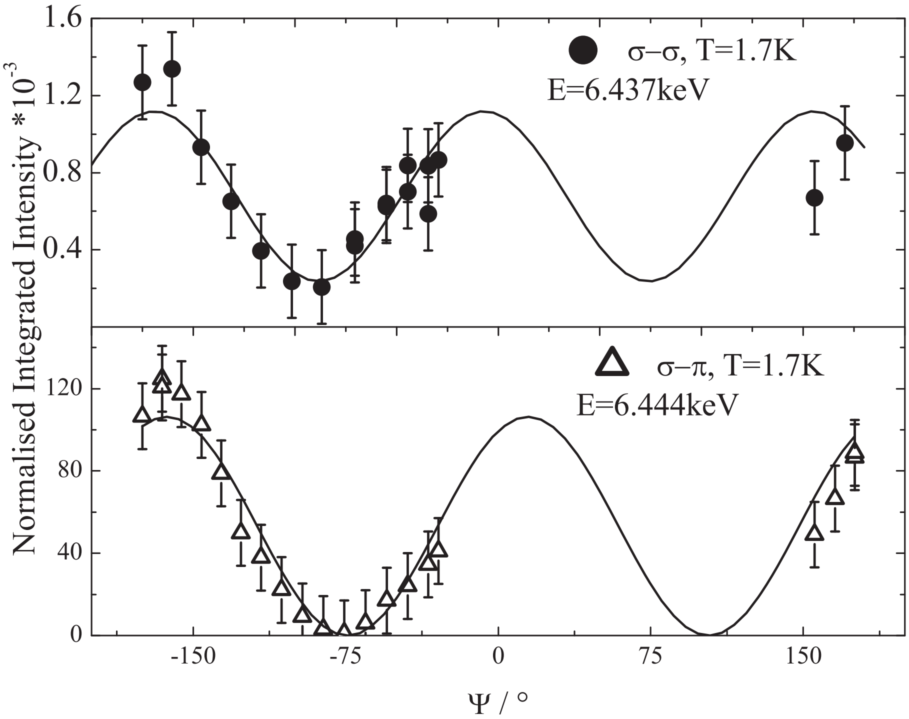

Figure 7.16: Azimuthal angular dependence of the integrated intensity of the $(\frac{5}{4}\,\frac{5}{4}\,\frac{1}{2})$ reflection at $1.7\,\mathrm{K}$ for the $\sigma-\sigma$ scattering component at $E = 6.437\,\mathrm{keV}$ and the $\sigma-\pi$ component at $E = 6.444\,\mathrm{keV}$. Solid lines are the fits with $\cos^2\Psi$ for $\sigma-\sigma$ and $\sin^2\Psi$ for $\sigma-\pi$, for details see text.

at $(\frac{7}{4}\,\frac{7}{4}-\delta\frac{1}{2})$ at $5.25\,\mathrm{K}$ are plotted in Fig. 7.17, which should be compared to Fig. 7.16 ($T = 1.7\,\mathrm{K}$). Again, the intensity of the scattering in $\sigma-\sigma$ is roughly $2\,\%$ of the intensity in $\sigma-\pi$. As well, the intensity of the scattering in $\sigma-\pi$ is well described by a $\sin^2\Psi$ function, reflecting the AFM ordering in the IC phase. The difficulties in accurately analyzing the $\sigma-\sigma$ data are the same as in the C phase discussed above.

Comparing the Figs. 7.16 and 7.17 the minima are not in the same positions, reflecting the different angles between the reciprocal lattice and the magnetic moments in the IC phase and the C phase.

Finally, to complete the study of the azimuthal angular dependence the $(\frac{3}{4}\,\frac{5}{4}\,\overline{\frac{1}{2}})$ peak in the $\sigma-\pi$ configuration is examined (Fig. 7.18). Since, again a $\sin^2\Psi$ behavior is observed, these data represent confirmation of our findings from the other peaks. Altogether, these data are consistent with the magnetic structure proposed in Ref. [145] for the C and IC phases.

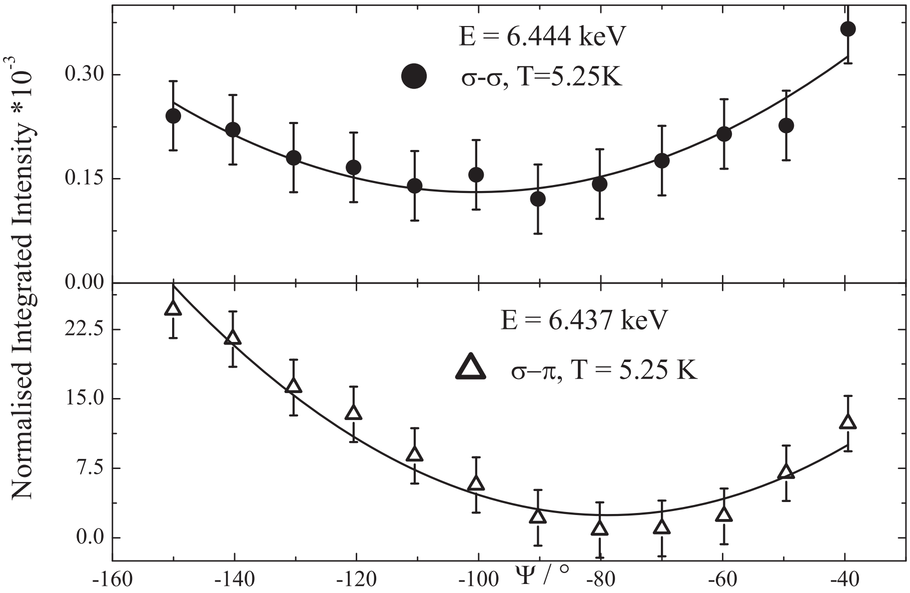

Figure 7.17: Azimuthal angular dependence of the integrated intensity of the $(\frac{7}{4}\,\frac{7}{4}-\delta\frac{1}{2})$ reflection at $5.25\,\mathrm{K}$ for $\sigma-\sigma$ and $\sigma-\pi$ scattering. Solid lines are the fits with $\cos^2\Psi$ for $\sigma-\sigma$ and $\sin^2\Psi$ for $\sigma-\pi$, for details see text.

In conclusion, the magnetic scattering contribution has been identified with the $\sigma-\pi$ data in the C and the IC phase, but no clear evidence of quadrupolar ordering has been found. Further investigations on the origin of the $\sigma-\sigma$ scattering in the E2 channel have to be carried out. For the future, in order to resolve the question of quadrupolar ordering in PrB$_6$ measurements using a better analyzer crystal, yielding a reduction of crosstalk, would be helpful.

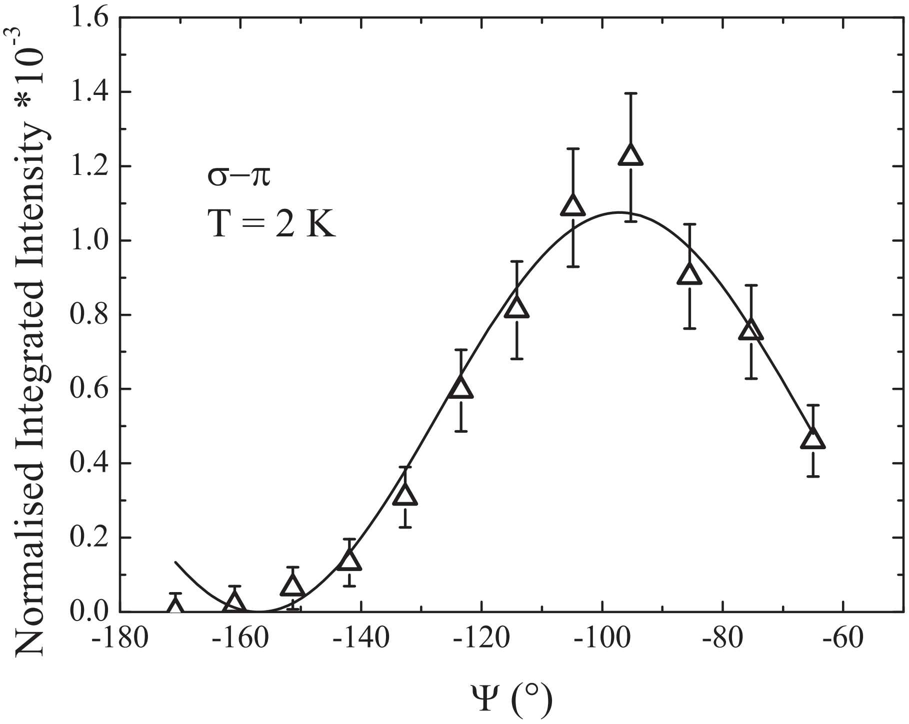

Figure 7.18: Azimuthal angular dependence of the integrated intensity of the $(\frac{3}{4}\,\frac{5}{4}\,\overline{\frac{1}{2}})$ reflection at 2 K for $\sigma - \pi$ scattering. The solid line is a fit with $\sin^2\Psi$ for $\sigma - \pi$, for details see text.

8 Summary

In this thesis, various f-electron systems, ranging in their f-electron character from itinerant to localized, have been investigated by means of bulk and microscopic methods.

The alloying series $\mathrm{CePt_3B_{1-x}Si_x}$ is of interest as it might shed more light onto $\mathrm{CePt_3Si}$, the first heavy fermion superconductor without inversion symmetry. The phase diagram of the alloying series $\mathrm{CePt_3B_{1-x}Si_x}$ has been determined by means of bulk measurements. Furthermore, susceptibility and μSR measurements of $\mathrm{CePt_3B}$ have shown, that the antiferromagnetic order at low temperatures is a bulk property with a magnetic moment of the order of $1\,\mu_\mathrm{B}$. Surprisingly, no magnetic signal has been observed in neutron scattering experiments, an observation that will require further investigation.

The influence of structural disorder on the physical properties of the antiferromagnetic heavy fermion system $\mathrm{UPd_2Sb}$ has been investigated by means of neutron scattering. The unusual semiconductor like behavior of the resistivity could be associated to crystallographic disorder, present in $\mathrm{UPd_2Sb}$. The type of structural disorder has been determined as a kind of phase segregation, with small crystallites embedded in quasi amorphous regions. Furthermore, the antiferromagnetic structure has been determined to consist of ferromagnetically ordered planes, which are antiferromagnetically coupled along the third cubic axis. We have shown that the size of the crystallites affects on the correlation length of the magnetically order phase.

A detailed analysis of structural disorder on the Fermi liquid properties, as observed in the resistivity of $\mathrm{UPd_{2-x}Sn}$, revealed that there is no disorder induced non-Fermi liquid behavior and the Fermi liquid temperature T^* is not significantly altered by structural disorder. In context of the prediction of disorder induced non-Fermi liquid behavior in the vicinity of a QCP by Rosch [23], these observations bring up the question, how to measure the distance to a QCP, *viz.*, what is the meaning of "vicinity to a QCP". Furthermore, the results of the study on the influence of disorder on the coherent state in the Hall effect contradict the predictions of the theory of Fert and Levy [49]. Therefore, new theoretical studies on the anomalous Hall effect in heavy fermion systems are desirable.

The reinvestigation of the resistivity and magnetoresistivity, in combination with new high magnetic field measurements, of UPt_2Si_2 revealed that this compound has to be discussed as an itinerant f-electron system. New field induced phases have been found, bearing resemblance to the the hidden order/heavy fermion superconductor URu_2Si_2. It suggests that UPt_2Si_2 might be a key to understand the exotic properties of the hidden order/heavy fermion superconductor URu_2Si_2. To achieve this, further investigations, and in particular additional high field measurements ought to be carried out on UPt_2Si_2 in the future.

UPd_3 is one of the rare examples of metallic, quadrupolar ordered systems. In this study, for the first time a phase diagram of $U(Pd_{1-x}Pt_x)_3$ has been determined by means of specific heat, susceptibility, and resistivity. A small amount of $\sim 1\%$ Pt doping destroys long range quadrupolar ordering in UPd_3, implying that the quadrupolar phases in UPd_3 are even more sensitive to Pt doping than the superconducting phase in UPt_3 to Pd doping. Because of substantial broadening of the quadrupolar transitions with Pt alloying, most likely no quadrupolar QCP exists in the phase diagram.

Furthermore, the magnetic phase diagram of $U(Pd_{1-x}Pt_x)_3$, $x = 0.005$, has been derived. The principle behavior of $U(Pd_{1-x}Pt_x)_3$, $x = 0.005$ in a magnetic field is the same as observed for UPd_3, aside from a shift of the transitions to lower temperatures and a reduction of the entropy S_{mag} associated to the quadrupolar phase transition, and which possibly might indicate a reduction of the quadrupolar moment. A splitting of the susceptibility between FC and ZFC mode at low temperatures has been observed for the first time in $U(Pd_{1-x}Pt_x)_3$, $x = 0.005$. We speculate that the splitting provides an easy avenue to determine the associated transition temperature T_2. In order to fully resolve the open questions of the quadrupolar properties of $U(Pd_{1-x}Pt_x)_3$, resonant x-ray experiments would be desirable.

The resonant x-ray experiments on the rare earth hexaboride PrB_6 revealed a splitting of the structural peaks in the antiferromagentic commensurate phase. Furthermore, a charge peak in the commensurate phase has been observed, which splits in the incommensurate phase and vanishes in the paramagnetic phase. A detailed investigation of the magnetic peaks could verify the earlier proposed magnetic structure, while no unambiguous evidence for quadrupolar ordering has been found.

In conclusion, the investigations presented in this thesis reveal that the heavy fermion related systems investigated in this study have a pronounced itinerant character. Both, UPd_2Sn and UPd_2Sb are well understood within an itinerant approach, and even UPt_2Si_2, which was considered a prime example of a local moment U-based antiferromagnet, is more adequately described within an itinerant Fermi surface picture. Furthermore, in UPd_3, again considered to be an archetypical localized system, Fermi surface effects seems to play an important role. This is indicated by the suppression of the entropy with $0.5\,\%$ of Pt doping and a complete elimination of the quadrupolar ordering with only $\sim 1.5\,\%$ Pt content. Only PrB_6 is a localized system with the physical properties being well described in a crystal electric field scheme. In conclusion, with this study, it appears that Fermi surface effects ought to be emphasized if a detailed understanding of heavy fermion related materials should be attained.

Bibliography

[1] Q. Si, S. Rabello, K. Ingersent, and J. L. Smith, Nature **413**, 804 (2002).

[2] P. Coleman, C. Pepin, Q. Si, and R. Ramazashvili, J. Phys. Condens. Matter **13**, R723 (2001).

[5] E. Miranda, V. D. ć, and G. Kotlinar, J. Phys.: Condens. Matter **8**, 9871 (1996).

[3] G. R. Stewart, Rev. Mod. Phys. **73**, 797 (2001).

[4] H. v. Löhneysen, J. Phys.: Condens. Matter **8**, 9689 (1986).

[6] R. Joynt and L. Taillefer, Rev. Mod. Phys. **74**, 235 (2002).

[7] P. Chandra, P. Coleman, J. A. Mydosh, and V. Tripathi, Nature **471**, 831 (2002).

[8] K. Andres, J. E. Graebner, and H. R. Ott, Phys. Rev. Lett. **35**, 1979 (1975).

[9] F. Steglich, J. Aarts, C. D. Bredl, W. Lieke, D. Meschede, W. Franz, and J. Schäfer, Phys. Rev. Lett. **43**, 1892 (1979).

[10] G. R. Stewart, Z. Fisk, J. O. Willis, and J. L. Smith, Phys. Rev. Lett. **52**, 679 (1984).

[11] G. R. Stewart, Z. Fisk, and M. S. Wire, Phys. Rev. B **30**, 482 (1984).

[12] J. Kondo, Progress of Theoretical Physics **32**, 37 (1964).

[13] K. G. Wilson, Rev. Mod. Phys. **47**, 773 (1975).

[14] S. Doniach, Physica B **91**, 231 (1977).

[15] S. Doniach, *Valence Instabilities and Related Narrow Band Phenomena*, Plenum, New York (1993).

[16] P. Nozières and A. Blandin, J. Phys. (Paris) **41**, 193 (1980).

[17] D. L. Cox, Phys. Rev. Lett. **59**, 1240 (1987).

[18] O. O. Bernal, D. E. MacLaughlin, H. G. Lukefahr, and B. Andraka, Phys. Rev. Lett. **75**, 2023 (1995).

[19] A. H. C. Neto, G. Castilla, and B. A. Jones, Phys. Rev. Lett. **81**, 3531 (1998).

[20] A. H. C. Neto and B. A. Jones, Phys. Rev. B **195**, 14975 (2000).

[21] D. R. Grempel and Q. Si, Phys. Rev. Lett. **91**, 026401 (2003).

[22] L. Zhu, M. Grast, A. Rosch, and Q. Si, Phys. Rev. Lett. **91**, 066404 (2003).

[23] A. Rosch, Phys. Rev. Lett. **82**, 4280 (1999).

[24] A. Rosch, A. Schröder, O. Stockert, and H. v. Löhneysen, Phys. Rev. Lett. **79**, 159 (1997).

[25] P. Gegenwart, Q. Si, and F. Steglich, Nature Physics **4**, 186 (2008).

[26] A. Schröder, G. Aeppli, R. Coldea, M. Adams, O. Stockert, H. Löhneysen, E. Bucher, R. Ramazashvili, and P. Coleman, Nature **407**, 351 (2000).

[27] S. R. Julian, C. Pfleiderer, F. M. Grosche, N. D. Mathur, G. J. McMullan, A. J. Diver, I. R. Walker, and G. G. Lonzarich, J. Phys.: Condens. Matter **8**, 9675 (1996).

[28] F. M. Grosche, P. Agarwal, S. R. Julian, N. J. Wilson, R. K. W. Haselwimmer, S. J. S. Lister, N. D. Mathur, F. V. Carter, S. S. Saxena, and G. G. Lonzarich, J. Phys.: Condens. Matter **12**, L533 (2000).

[29] N. D. Mathur, F. M. Grosche, S. R. Julian, I. R. Walker, D. M. Freye, R. K. W. Haselwimmer, and G. G. Lonzarich, Nature **364**, 39 (1998).

[30] R. J. Elliott and M. F. Thorpe, J. Appl. Phys. **39**, 802 (1968).

[31] P. M. Levy, Phys. Rev. **135**, A155 (1964).

[32] P. Morin and D. Schmitt, *Handbook on Ferromagnetic Materials, Vol. 5*, Elsevier, Amsterdam (1990).

[33] K. Kubo and T. Hotta, Phys. Rev. B **72**, 144401 (2005).

[34] S. Süllow, G. J. Nieuwenhuys, A. A. Menovsky, and J. A. Mydosh, Physica B **199 & 200**, 644 (1994).

[35] E. Bauer, G. Hilscher, H. Michor, C. Paul, E. W. Scheidt, A. Gribanov, Y. Seropegin, H. Noël, M. Sigrist, and P. Rogl, Phys. Rev. Lett. **92**, 027003 (2004).

[36] P. W. Anderson, Phys. Rev. B **30**, 4000 (1984).

[37] N. Metoki, K. Kaneko, T. D. Matsuda, A. Galatanu, T. Takeuchi, S. Hashimoto, T. Ueda, R. Settai, Y. Onuki, and N. Bernhoeft, J. Phys.: Condens. Matter **16**, L207 (2004).

[38] T. Takeuchi, S. Hashimoto, T. Yasuda, H. Shishido, T. Ueda, M. Yamada, Y. Obiraki, M. Shiimoto, H. Kohara, T. Yamamoto, K. Sugiyama, K. Kindo, T. D. Matsuda, Y. Haga, Y. Aoki, H. Sato, R. Settai, and Y. Onuki, J. Phys.: Condens. Matter **16**, L333 (2004).

[39] M. M. Salomaa and G. E. Volovik, Rev. Mod. Phys. **59**, 533 (1987).

[40] H. Shimahara, Phys. Rev. B **62**, 3524 (2000).

[41] O. Sologub, J. Hester, P. Salamakha, E. Leroy, and C. Godart, J. Alloys Comp. **337**, 10 (2002).

[42] R. Lackner, M. Sieberer, H. Michor, G. Hilscher, E. Bauer, P. S. Salamakha, O. L. Sologub, and S. . K. Hiebl , J. Phys.: Condens. Matter **17**, S905 (2005).

[43] I. A. Campbell and A. Fert, in *Ferromagnetic Materials, Vol. 3*, North-Holland Publ. Co., Amsterdam (1982).

[44] N. H. Andersen and H. Smith, Phys. Rev. B **19**, 384 (1979).

[45] N. H. Anderson, *Crystalline Electric Field and Structural Effects in f-electron Systems*, Plenum, New York (1980).

[46] N. Mott, *Metal-Insulator Transitions*, Taylor&Francis, London, New York, Philadelphia (1997).

[47] P. W. Anderson, Phys. Rev. **109**, 1492 (1958).

[48] N. F. Mott and W. D. Twose, Adv. Phys. **10**, 107 (1961).

[49] A. Fert and P. Levy, Phys. Rev. B **36**, 1907 (1987).

[50] J. Schoenes and J. J. M. Franse, Phys. Rev. B **33**, 5138 (1986).

[51] H. Kontani and K. Yamada, J. Phys. Soc. Jpn. **63**, 2627 (1994).

[52] A. Otop, S. Süllow, M. B. Maple, A. Weber, E. W. Scheidt, T. J. Gortenmulder, and J. A. Mydosh, Phys. Rev. B **72**, 024457 (2005).

[53] L. Berger, Phys. Rev. B **11**, 4559 (1970).

[54] M. A. Continentino, S. N. de Medeiros, M. T. D. Orlando, M. B. Fontes, and E. M. Baggiio-Saitovitch, Phys. Rev. B **64**, 012404 (2001).

[55] M. J. Besnus, A. Braghta, N. Hamdaoui, and A. Meyer, J. Mag. Mag. Mat. **104-107**, 1385 (1992).

[56] G. L. Squires, *Introduction to the theory of thermal neutron scattering*, Cambridge University Press, Cambridge (1978).

[57] J. E. Sonier, *Muon Spin Rotation/Relaxation/Resonance (μSR)*, unpublished.

[58] S. J. Blundell, Contemp. Phys. **40**, 175 (1999).

[59] F. de Bergevin and M. Brunel, Phys. Lett. **A39**, 141 (1972).

[60] J. P. Hill and D. F. McMorrow, Acta Cryst. **A52**, 236 (1996).

[61] T. Takabatake, H. Kawanaka, H. Fujii, Y. Yamaguchi, J. Sakurai, Y. Aoki, and T. Fujita, J. Phys. Soc. Japan **58**, 1918 (1989).

[62] T. Endstra, S. A. M. Mentink, G. J. Nieuwenhuys, J. A. Mydosh, and K. H. J. Buschow, J. Phys.: Condens. Matter **2**, 2447 (1990).

[63] T. Takabatake, H. Fuji, S. Miyata, H. Kawanaka, Y. Aoki, T. Suzuki, T. Fujita, Y. Yamaguchi, and J. Sakurai, J. Phys. Soc. Jpn. **59**, 16 (1990).

[64] C. Seaman, N. R. Dilley, M. C. deAndrade, J. Herrmann, M. B. Maple, and Z. Fisk, Phys. Rev. B **53**, 2651 (1996).

[65] T. Takabatake, H. Iwasaki, H. Fuji, S. Ikeda, S. Nishigori, Y. Aoki, T. Suzuki, and T. Fujita, J. Phys. Soc. Japan **61**, 778 (1992).

[66] Y. Maeda, T. Takabatake, Y. Bando, H. Fujii, K. Oda, K. Sugiyama, K. Kindo, K. Izawa, T. Suzuki, T. Fujita, and Y. Morii, Physica B **223 & 224**, 228 (1996).

[67] P. J. Webster, K. R. A. Ziebeck, S. L. Town, and M. S. Peak, Philos. Mag. B **49**, 295 (1984).

[68] A. U. B. Wolter, A. Bosse, D. Baabe, I. Maksimov, D. Mienert, H.-H. Klauss, F. J. Litterst, D. Niemeier, R. Michalak, C. Geibel, R. Feyerherm, R. Hendrikx, J. A. Mydosh, and S. Süllow, Phys. Rev. B **66**, 174428 (2002).

[69] E. Miranda, V. Dobrosavljević, and G. Kotliar, Phys. Rev. Lett. **78**, 290 (1997).

[70] Z. Zolnierek, J. Magn. Magn. Matter. **76 & 77**, 231 (1988).

[71] J. C. Slater, J. Chem. Phys. **41**, 3199 (1964).

[72] F. M. Mulder, A. Drost, R. C. Thiel, and E. Frikkee, Phys. Rev. Lett. **77**, 3477 (1996).

[73] I. Ishii, H. Higaki, T. Takabatake, H. Goshima, T. Fujita, T. Suzuki, and K. Katoh, Phys. Rev. B **68**, 144413 (2003).

[74] C. Rossel, M. S. Torikachvili, J. W. Chen, and M. B. Maple, Solid State Commun. **60**, 563 (1986).

[75] M. Marezio, D. E. Cox, C. Rossel, and M. B. Maple, Solid State Commun. **67**, 831 (1988).

[76] K. Izawa, T. Suzuki, T. Fujita, Y. Maeda, T. Takabatake, and H. Fujii, J. Phys. Soc. Japan **65**, 3260 (1996).

[77] I. Maksimov, F. J. Litterst, H. Rechenberg, M. A. C. de Melo, R. Feyerherm, R. W. A. Hendrikx, T. J. Gortenmulder, J. A. Mydosh, and S. Süllow, Phys. Rev. B **67**, 104405 (2003).

[78] K. Gofryk, D. Kaczorowski, and A. Czopnik, Solid State Commun. **133**, 625 (2005).

[79] N. Ashcroft and N. Mermin, *Solid State Physics*, Saunders College Publishing, New York (1976).

[80] *FullProf Manual, http://www.ill.eu/sites/fullprof.*

[81] I. Maksimov, F. J. Litterst, S. Süllow, R. Feyerherm, and J. A. Mydosh, Acta Phys. Pol. **34**, 967 (2003).

[82] V. H. Tran, F. Steglich, and G. Andre, Phys. Rev. B **65**, 134401 (2001).

[83] A. Otop, S. Süllow, E. W. Scheidt, and J. A. Mydosh, Phys. Rev. B **77**, 045121 (2008).

[84] A. Otop, Ph.D. thesis, TU Braunschweig (2006).

[85] S. Süllow, A. Otop, A. Loose, J. Klenke, O. Prokhnenko, R. Feyerherm, R. W. A. Hendrikx, J. A. Mydosh, and H. Amitsuka, J. Phys. Soc. Japan **77**, 024708 (2008).

[86] G. J. Nieuwenhuys, Phys. Rev. B **35**, 5260 (1987).

[87] T. Endstra, G. J. Nieuwenhuys, A. A. Menovsky, and J. A. Mydosh, J. Appl. Phys. **69**, 4819 (1991).

[88] C. H. Booth, S.-W. Han, S. Süllow, and J. A. Mydosh, J. Magn. Magn. Mater. **272**, 941 (2004).

[89] S. Süllow, I. Maksimov, A. Otop, F. J. Litterst, A. Perucchi, L. Degiorgi, and J. A. Mydosh, Phys. Rev. Lett. **93**, 266602 (2004).

[90] M. Jaime, K. H. Kima, N. Harrison, G. Jorge, G. S. Boebinger, and J. A. Mydosh, J. Alloys Compd. **369**, 33 (2004).

[91] A. A. Menovsky, A. C. Moleman, C. E. Snel, T. J. Gortenmulder, H. J. Tan, and T. T. M. Palstra, J. Cryst. Growth **79**, 316 (1986).

[92] H. Ptasiewicz-Bak, J. Leciejewicz, and A. Zygmunt, Solid State Commun. **55**, 601 (1985).

[93] R. A. Steeman, E. Frikkee, S. A. M. Mentnik, A. A. Menovsky, G. J. Nieuwenhuiys, and J. A. Mydosh, J. Phys.: Condens. Matter **2**, 4059 (1990).

[94] H. Amitsuka, private communication (2002).

[95] B. J. Hickey, D. Greig, and M. A. Howson, J. Phys. F **16**, L13 (1986).

[96] H. H. Boghosian and M. A. Howson, Phys. Rev. B **41**, 7397 (1990).

[97] P. Oppeneer, private communication (2008).

[98] S. A. M. Mentink, T. E. Mason, S. Süllow, G. J. Nieuwenhuys, A. A. Menovsky, J. A. Mydosh, and J. A. A. J. Perenboom, Phys. Rev. B **53**, R6014 (1996).

[99] G. Zwicknagl, A. N. Yaresko, and P. Fulde, Phys. Rev. B **65**, 081103(R) (2002).

[100] G. Zwicknagl, A. N. Yaresko, and P. Fulde, Phys. Rev. B **68**, 052508 (2003).

[101] A. U. B. Wolter, Ph.D. thesis, TU Braunschweig (2006).

[102] H. Amitsuka, T. Sakakibara, K. Sugiyama, T. Ikeda, Y. Miyako, M. Date, and A. Yamagishi, Physica B **177**, 173 (1992).

[103] N. Harrison, M. Jaime, and J. A. Mydosh, Phys. Rev. Lett. **90**, 096402 (2003).

[104] K. H. Kim, N. Harrison, M. Jaime, G. S. Boebinger, and J. A. Mydosh, Phys. Rev. Lett. **91**, 256401 (2003).

[105] K. Andres, D. Davidov, P. Dernier, F. Hau, W. A. Reed, and G. J. Nieuwenhuys, Solid State Commun. **28**, 405 (1978).

[106] H. R. Ott, K. Andres, and P. H. Schmidt, Physica B **102**, 148 (1980).

[107] M. Yoshizawa, B. Lüthi, T. Goto, T. Suzuki, B. Renker, A. de Visser, P. Frings, and J. J. M. Franse, J. Magn. Magn. Mater. **52**, 413 (1985).

[108] U. Steigenberger, K. A. McEwen, J. L. Martinez, and D. Fort, J. Magn. Magn. Mater. **108**, 163 (1992).

[109] N. Lingg, D. Maurer, V. Müller, and K. A. McEwen, Phys. Rev. B **60**, R8430 (1999).

[110] T. Ito, H. Kumigashira, S. Souma, T. Takahashi, Y. Haga, Y. Tokiwa, and Y. Onuki, Phys. Rev. B 66 **66**, 245110 (2002).

[111] S. Heathman, M. Idiri, J. Rebizant, P. Boulet, P. S. Normile, L. Havela, V. Sechovský, and T. L. Bihan, Phys. Rev. B **67**, 180101 (2003).

[112] H. C. Walker, K. A. McEwen, D. F. McMorrow, S. B. Wilkins, F. Wastin, E. Colineau, and D. Fort, Phys. Rev. Lett. **97**, 137203 (2006).

[113] T. J. Heal and G. I. Williams, Acta Cryst. **8**, 494 (1955).

[114] Y. Tokiwa, K. Sugiyama, T. Takeuchi, M. Nakashima, R. Settai, Y. Inada, Y. Haga, E. Yamamoto, K. Kindo, H. Harima, and Y. Onuki, J. Phys. Soc. Japan **70**, 1731 (2001).

[115] D. F. McMorrow, K. A. McEwen, U. Steigenberger, H. M. Rønnow, and F. Yakhou, Phys. Rev. Lett. **87**, 057201 (2001).

[116] W. J. L. Buyers, A. F. Murray, T. M. Holden, E. C. Svensson, P. de V. DuPlessis, G. H. Lander, and O. Vogt, Physica B (Amsterdam) **102**, 291 (1980).

[117] M. B. Walker, C. Kappler, K. A. McEwen, U. Steigenberger, and K. N. Clausen, J. Phys. Condens. Matter **6**, 7365 (1994).

[118] K. A. McEwen, U. Steigenberger, K. N. Clausen, J. Kulda, J.-G. Park, and M. B. Walker, J. Magn. Magn. Mater. **177–181**, 37 (1998).

[119] S. W. Zochowski, M. de Podesta, C. Lester, and K. A. McEwen, Physica B (Amsterdam) **206–207**, 489 (1995).

[120] K. A. McEwen, M. Ellerby, and M. de Podesta, J. Magn. Magn. Mater. **140–144**, 1411 (1995).

[121] S. W. Zochowski and K. A. McEwen, Physica B (Amsterdam) **199–200**, 416 (1994).

[122] H. C. Walker, K. A. McEwen, P. Boulet, E. Colineau, J.-C. Griveau, J. Rebizant, and F. Wastin, Phys. Rev. B **76**, 174437 (2007).

[123] D. V. Efremov, N. Hasselmann, E. Runge, P. Fulde, and G. Zwicknagl, Phys. Rev. B **69**, 115114 (2004).

[124] H. H. Hill, *Plutonium 1970 and other Actinides*, Metallurgical Society of the American Institute of Mechanical Engineers (1970).

[125] K. A. McEwen, W. G. Stirling, C. K. Loong, G. H. Lander, and D. Fort, J. Magn. Magn. Mater. **76 & 77**, 426 (1988).

[126] G. R. Stewart and A. L. Giorgi, J. Low Temp. Phys. **59**, 185 (1985).

[127] A. de Visser, J. C. P. Klaasse, M. van Sprang, J. J. M. Franse, A. Menovsky, T. T. M. Palstra, and A. Dirkmaat, Phys. Lett. A **113**, 489 (1986).

[128] A. de Visser, M. J. Graf, P. Estrela, A. Amato, C. Baines, D. Andreica, F. N. Gygax, and A. Schenck, Phys. Rev. Lett. **85**, 3005 (2000).

[129] R. J. Keizer, A. de Visser, M. J. Graf, A. A. Menovsky, and J. J. M. Franse, Phys. Rev. B **60**, 10527 (1999).

[130] A. de Visser, A. Menovsky, and J. J. M. Franse, Physica B **147**, 81 (1987).

[131] M. E. Fisher and J. S. Langer, Phys. Rev. Lett. **20**, 665 (1968).

[132] K. A. McEwen, J.-G. Park, A. J. Gipson, and G. A. Gehring, J. Phys.: Condens. Matter **15**, S1923 (2003).

[133] N. E. Sluchanko, V. V. Glushkov, S. V. Demishev, A. A. Pronin, A. A. Volkov, M. V. Kondrin, A. K. Savchenko, and S. Kunii, Phys. Rev. B **64**, 153103 (2001).

[134] V. M. Pereira, J. M. B. L. dos Santos, E. V. Castro, and A. H. C. Neto, Phys. Rev. Lett. **93**, 147202 (2004).

[135] R. G. Goodrich, N. Harrison, and Z. Fisk, Phys. Rev. Lett. **97**, 146404 (2006).

[136] A. Takase, K. Kojima, T. Komatsubara, and T. Kasuya, Solid State Commun. **36**, 461 (1980).

[137] P. S. Riseborough, Phys. Rev. B **68**, 235213 (2003).

[138] S. Süllow, I. Prasad, M. C. Aronson, J. L. Sarrao, Z. Fisk, D. Hristova, A. H. Lacerda, M. F. Hundley, A. Vigliante, and D. Gibbs, Phys. Rev. B **57**, 5860 (1998).

[139] P. Link, J. M. Mignot, T. Matsumura, and T. Suzuki, Phys. Rev. Lett. **80**, 4779 (1998).

[140] M. Hiroi, S. Kobayashi, M. Sera, N. Kobaysashi, and S. Kunii, Phys. Rev. Lett. **81**, 2510 (1998).

[141] H. Amitsuka, M. Sato, M. Metoki, M. Yokoyama, K. Kuwahara, S. Kawarazaki, S. Sakakibara, T. Miyako, and J. A. Mydosh, Phys. Rev. Lett. **83**, 5114 (1999).

[142] H. Yamauchi, H. Ondera, K. Ohoyama, T. Onimaru, M. Kosaka, M. Ohashi, and Y. Yamaguchi, J. Phys. Soc. Jpn. **68**, 2057 (1999).

[143] P. Santini and G. Amoretti, Phys. Rev. Lett. **85**, 2188 (2000).

[144] V. P. Plakhty, L. P. Regnault, A. V. Goltsev, S. V. Gavrilov, F. Yakhou, J. Flouquet, C. Vettier, and S. Kunii, Phys. Rev. B **71**, 100407 (2005).

[145] J. M. Effantin, J. Rossat-Mignod, P. Burlet, S. Kunii, and T. Kasuya, J. Magn. Magn. Mater. **47-48**, 145 (1985).

[146] S. Awaji, N. Kobayashi, S. Sakatsume, S. Kunii, and M. Sera, J. Phys. Soc. Jpn. **68**, 2518 (1999).

[147] S. Kobayashi, M. Sera, M. Hiroi, T. Nishizaki, N. Kobayashi, and S. Kunii, J. Phys. Soc. Jpn. **70**, 1721 (2001).

[148] H. Hein, L. Gmelin, R. J. Meyer, E. H. E. Pietsch, and E. Fluck, *Gmelin handbook of inorganic and organometallic chemistry; C 11a, compounds with boron*, Berlin: Verl. Chemie (1990).

[149] C. H. Booth, J. L. Sarrao, M. F. Hundley, A. L. Cornelius, G. H. Kwei, A. Bianchi, Z. Fisk, and J. M. Lawrence, Phys. Rev. B **63**, 224302 (2001).

[150] P. Burlet, J. M. Effantin, J. Rossat-Mognod, S. Kunii, and T. Kasuya, J. Phys. (Paris) **C 8**, 459 (1988).

[151] C. M. McCarthy, C. W. Tompson, R. J. Graves, H. W. White, Z. Fisk, and H. R. Ott, Solid State Commun. **36**, 861 (1980).

[152] M. Loewenhaupt and M. Prager, Z. Phys. B **62**, 195 (1986).

[153] R. Shiina, O. Sakai, H. Shiba, and P. Thalmeier, J. Phys. Soc. Jpn. **67**, 941 (1998).

[154] O. Zaharko, P. Fischer, A. Schenck, S. Kunii, P.-J. Brown, F. Tasset, and T. Hansen, Phys. Rev. B **68**, 214401 (2003).

[155] R. M. Galera, D. P. Osterman, J. D. Axe, S. Kunii, and T. Kasuya, J. Appl. Physics **63**, 3580 (1988).

[156] D. F. McMorrow, K. A. McEwen, J.-G. Park, S. Lee, D. Mannix, F. Iga, and T. Takabatake, Physica B **345**, 66 (2004).

Curriculum Vitae

Personal Data

Name	Matthias Bleckmann
Date / place of birth	23.05.1979 / Herford

Education

1985-1989	Primary school Mennighüffen-Ost, Löhne
1989-1998	Städtisches Gymnasium Löhne (High school)
June 1998	Abitur

Civilian Service

10/1998 – 11/1999	Diakonisches Werk (Bad Oeynhausen)

Academic studies

10/1999 – 11/2004	Technical University of Braunschweig Degree in physics (*Diplom*, 2004) Subject of diploma thesis: *"Kalorimetrische Untersuchungen an der ferromagnetisch gekoppelten bimetallischen Kettenverbindung* $MnNi(NO_2)_4(en)_2$*; en=Ethylendiamin"*

Current Position

since 11/2004	Research assistant at the Institute for Condensed Matter Physics, Technical University of Braunschweig Supervisor: Prof. Dr. Stefan Süllow, TU Braunschweig

Veröffentlichungen allgemeiner Art

Publikationen:

- R. Feyerherm, M. Bleckmann, A. Honecker, S. Süllow *Antiferromagnetism, ferromagnetic 1D fluctuations and two energy scales in* $MnNi(NO_2)_4(en)_2$ *(en = ethylenediamine)* in preperation

Braunschweig, 15.11.2008

Thanks

I sincerely wish to express my gratitude to everybody who contributed to the completion of this thesis.

First of all, I would like to thank my supervisor Prof. Stefan Süllow for giving me the opportunity to work on a fascinating branch of solid state physics in the inspiring scientific environment of Braunschweig, London, Sapporo and Rio de Janeiro. I am deeply indebted to Prof. Stefan Süllow for his constant support, for being always accessible, and for numerous scientific discussions. Further, I am particularly happy that Prof. Andreas Eichler agreed to referee this thesis, for which I want to thank him.

I would like to thank all my colleagues, present and past, for contributing to a pleasant working environment, for their friendliness and help, and for plenty of stimulating discussions. Many thanks to: Ali, Anja, Anna, Christopher, Daniela, Dirk, Frauke, Hanno, Jan, Josefin, Markus, Teresa, Sascha, Silja.

I would like to thank Prof. Keith McEwen, for giving me the opportunity to work at the UCL in London and for the introduction to the fascinating topic of x-ray resonant scattering. I would like to thank Dr. Helen Walker, Prof. Des McMorrow, Dr. Danny Mannix, Prof. J.-G. Park, Dr. S. Lee and Prof. McEwen for the nice atmosphere during the x-ray resonant scattering experiments.

I would like to thank Prof. Hiroshi Amitsuka, for providing a motivating, friendly work atmosphere in Sapporo and introducing me into Japanese culture. The group of Prof. Amitsuka, for explaining me the Japanese way of life and supporting me with managing my daily life. It was a a successful and pleasant time with all of them.

I would like to thank Prof. Elisa Baggio-Saitovitch, for giving me the opportunity to work in the wonderful city of Rio de Janeiro. Furthermore, I would like to thank the group of Prof. Baggio-Saitovitch, for giving me a warm and pleasant welcome and showing me some nice places in this vibrant city.

I am very grateful to Dr. Marek Bartkowiak for the fruitful collaboration and his support on the high magnetic field investigations in Dresden. It was always a pleasure to work with you.

I would like to thank Dr. Norbert Stüßer and Dr. Alexandra Buchsteiner for their support and the discussions concerning the neutron scattering experiments at BENSC.

I would also like to thank Dr. Harison Rakoto for the efficient cooperation on the high field magnetization measurements in Toulouse.

Furthermore, thanks to Dr. Michael Baenitz from MPI Dresden for giving me measurement time at the PPMS.

I would like to thank Dr. Dirk Menzel for giving me sufficient measurement time at the SQUID magnetometer.

I am very grateful to Robert and Arno for their technical support.

Anja, Daniela, Jan, Dirk, and Hanno have shared the tedious task of proofreading this thesis, for which I am deeply indebted to them.

It is with particular pleasure that I express my deeply-felt gratitude to my parents for their continual encouragement and kind support in any situation beyond the realm of physics.

Last but not least, I am deeply grateful to my girlfriend Steffi, who gave me inspiration, moral support and love while I was writing this thesis.